Development of AlGaN nanostructures for the fabrication of electron pumped UV lasers

Sergi Cuesta Arcos

THÈSE

Pour obtenir le grade de

DOCTEUR DE L'UNIVERSITÉ GRENOBLE ALPES

École doctorale : PHYS - Physique
Spécialité : Nanophysique
Unité de recherche : PHotonique, ELectronique et Ingéniérie QuantiqueS

Développement de nanostructures à base d'AlGaN pour la fabrication lasers UV à pompage électronique

Development of AlGaN nanostructures for the fabrication of electron pumped UV lasers

Présentée par :

Sergi CUESTA ARCOS

Direction de thèse :

Eva MONROY DIRECTRICE DE RECHERCHE, Université Grenoble Alpes	Directrice de thèse

Rapporteurs :

PETER JAMES PARBROOK
Professeur, University College Cork
JULIEN BARJON
Professeur des Universités, UNIVERSITE DE VERSAILLES - SAINT QUENTIN

Thèse soutenue publiquement le **13 décembre 2022**, devant le jury composé de :

PETER JAMES PARBROOK Professeur, University College Cork	Rapporteur
JULIEN BARJON Professeur des Universités, UNIVERSITE DE VERSAILLES - SAINT QUENTIN	Président
CHRISTOPHE DURAND Maître de conférences HDR, UNIVERSITE GRENOBLE ALPES	Examinateur
MARIA VLADIMIROVA Directeur de recherche, CNRS DELEGATION OCCITANIE EST	Examinatrice
SIRONA VALDUEZA-FELIP Professeur associé, Universidad de Alcalá	Examinatrice
BASTIEN BONEF Ingénieur, ALEDIA	Examinateur

Acknowledgements

This PhD thesis is the result of my research in the "Nanophysique et Semiconducteurs (NPSC)" group, at the "Institute de Recherche Interdisciplinaire de Grenoble (IRIG)", part of the "Commissariat à l'énergie atomique et aux énergies alternatives (CEA)" in Grenoble, France. During these years, I have had the opportunity to live in "the capital of the French Alps", work with a dynamic and talented team, and meet wonderful people along the way. I would like to devote some time to thank the people who have contributed to making this work possible.

First and foremost, I would like to express my most sincere appreciation and gratitude to my PhD supervisor, **Eva Monroy**. Her inestimable support and guidance, in addition to her contagious enthusiasm and positive energy, showed me that it is possible to work hard while enjoying the journey in the process. I have learnt a lot from her, both scientifically and personally. It was a pleasure and an honor for me to work with someone whom I regard as a great researcher and a great person. I will always cherish these years, and I hope our paths can cross again in the future.

I would like to express my gratitude to **Jean-Michel Gerard** (former director of PHELIQS) and **Manuel Houzet** (director of PHELIQS), as well as to **Régis André** and **Bruno Gayral** (heads of NPSC), for welcoming me into the group and extending any kind of support I needed. Thanks also to **Luigia Indorato** for her unparalleled help with the administrative procedures of CEA.

Next, I would like to thank **Yoann Curé**, **Yann Genuist**, **Fabien Jourdan** and **Jean Dussaud** for their constant technical support with the MBE and other equipment necessary to perform my work. Special thanks to **Edith Bellet-Amalric** for her training and constant support to perform (and to understand!) the XRD measurements. Thanks also to **Fabrice Donatini** for his support with the cathodoluminescence set-up, and **Catherine Bougerol** for the TEM images provided. I want to deeply thank **Le Si Dang** for the fruitful discussions on the optical properties, as well as **Lou Denaix**, for providing her support in the optical measurements during her master's internship. It was a great experience to work with them.

I would like to extend my gratitude to our great external collaborators, whose extraordinary work contributed immensely to my research. Special thanks to **Stephen T. Purcell** and his group at Université Lyon 1, for building the electron beam set-up and for welcoming me in their lab every time I came to Lyon to perform the measurements. My deepest gratitude also goes to **Florian Castioni**, from LETI, and his wonderful TEM images and EDX studies, which became extremely handy to interpret my results. Thanks also to **Eric Delamadeleine** for his help with the DBR.

I want to thank the jury members of my PhD defense, for accepting the invitation to evaluate my work and coming all the way to Grenoble (even against the snow!) to attend the dissemination in person. Thanks to **Julien Barjon** and **Peter J. Parbrook**, reviewers of this manuscript, for their time to read my work and their constructive comments. Also, thanks to **Christophe Durand**, **Maria Vladimirova**, **Sirona Valdueza-Felip** and **Bastien Bonef** for their interesting questions and examination.

I was very lucky to be surrounded by a group of wonderful colleagues who became like a little family in Grenoble, both inside and outside the lab, and with whom I shared lots of memories. Thanks to **Jane, Rémy, Alex, Anjali, Thibaut, Vincent, Jesús, Zijie, Elçin, Lucie, Francis, Jonathan, Matteo, Rana, Sylvain, Corentin, Ioanna, Anh, Saptarshi, Raouia,**

José, Ali, Akanksha, Mada, Romy, Marion, Saransh, Maria, Ghenwa, Yassine, Danylo, Raphael. They really made my PhD experience more enjoyable, and I am leaving with good friends that I am sure I will meet again.

Last but not least, a big thanks to my family and friends. Thanks to my friends **Akash, Roger, Isma, Marta, David, Alba, Laura, Gabi, Marcel, Xavi, Mario, Chema** and **Eric**. Special thanks to my partner, **Cantia**, for her unconditional support and being a daily motivation for me. Finally, I am deeply grateful to **my parents** and my brother **Pau** for always encouraging me to pursue my goals, providing all the help and support whenever is needed. I am certain that I could not become the person I am now without them.

Moltes gràcies / Muchas gracias!

Glossary

AFM	atomic force microscopy
BIC	bottom inner cladding
BOC	bottom outer cladding
CCD	charge-coupled device
CL	cathodoluminescence
CNT	carbon nanotube
DAP	donor-acceptor pair
DBR	distributed Bragg reflector
EDX	energy dispersive X-ray spectroscopy
EQE	external quantum efficiency
FIB	focus ion beam
FWHM	full width half maximum
GRINSCH	graded-index separate confinement heterostructure
HAADF	high angle annular dark field
HR	high resolution
ICP	inductively coupled plasma
IQE	internal quantum efficiency
LD	laser diode
LED	light emitting diode
MBE	molecular beam epitaxy
ML	monolayer
MOVPE	metal organic vapor phase epitaxy
MQW	multi quantum well
OCF	optical confinement factor
PAMBE	plasma assisted molecular beam epitaxy
PECVD	plasma enhanced chemical vapor deposition
PL	photoluminescence
QCSE	quantum confinement Stark effect
QD	quantum dot

QW	quantum well
RF	radio frequency
RHEED	reflection high-energy electron diffraction
RIE	reactive ion etching
RMS	root mean square
RSM	reciprocal space map
SCH	separate confinement heterostructure
SEM	scanning electron microscopy
TEM	transmission electron microscopy
TIC	top inner cladding
TOC	top outer cladding
UHV	ultra-high vacuum
UV	ultraviolet
VCSEL	vertical cavity surface emitting lasers
VSL	variable stripe length
WPE	wall-plug efficiency
XRD	X-ray diffraction

Table of Contents

Chapter 1
Context and motivation

This chapter aims to provide a general context on the UV laser technology and III-nitrides materials, in order to introduce the motivation and targets of this work. At the end of the chapter, I briefly describe the structure of this manuscript.

1.1 A brief introduction to III-N for UV technology

III-nitride semiconductors (GaN, AlN, InN, and their compounds) are direct band gap materials that can cover a wide spectral range, from the infrared (≈ 0.65 eV for InN) to the ultraviolet (6.2 eV for AlN). This feature, in addition to their high mechanical and thermal stability [1], makes them suitable materials for the fabrication of optoelectronic [2–5] and high power devices [6–9]. The first polycrystalline growth of AlN and GaN was described in 1907 [10] and 1932 for GaN [11], respectively. We find the first reports on the synthesis of III-nitrides by metalorganic vapor phase epitaxy (MOVPE) [12] and molecular beam epitaxy (MBE) [13] dating back to the 1970s, but device fabrication was hindered by the poor material quality. A breakthrough came in 1986, when Amano *et al.* [14] proposed the use of an AlN buffer layer prior to the growth of GaN, which successfully reduced the defect density. Three years later, the same team also achieved the p-type GaN by doping with Mg [15]. All this progress culminated with the demonstration of the first efficient blue light emitting diode (LED) in 1994 [16] and laser diode (LD) in 1996 [17]. The impact was such that the Nobel Prize in Physics 2014 was awarded to Isamu Akasaki, Hiroshi Amano and Shuji Nakamura "for the invention of efficient blue light-emitting diodes which has enabled bright and energy-saving white light sources" [18]. Since then, blue and white LEDs have led to a change of paradigm in the lighting industry. Despite these tremendous achievements, most of the spectral range that III-N emitters should be able to cover has not been exploited. Material issues have delayed the extension of this technology towards the green and ultraviolet domains.

Ultraviolet (UV) radiation is the region of the electromagnetic spectrum between visible and x-ray radiation, in the range of 400 – 100 nm. UV light was discovered in 1801 by Johann Wilhelm Ritter when he noticed that invisible light darkened silver-chloride even faster than violet radiation, hence the name "ultraviolet" [19]. Since its discovery, numerous have been its applications due to its ability to induce chemical reactions and excite fluorescent materials. Some examples have been summarized in Figure 1.1, including medical diagnostics, disinfection of various surfaces, water purification, gas sensing and UV curing.

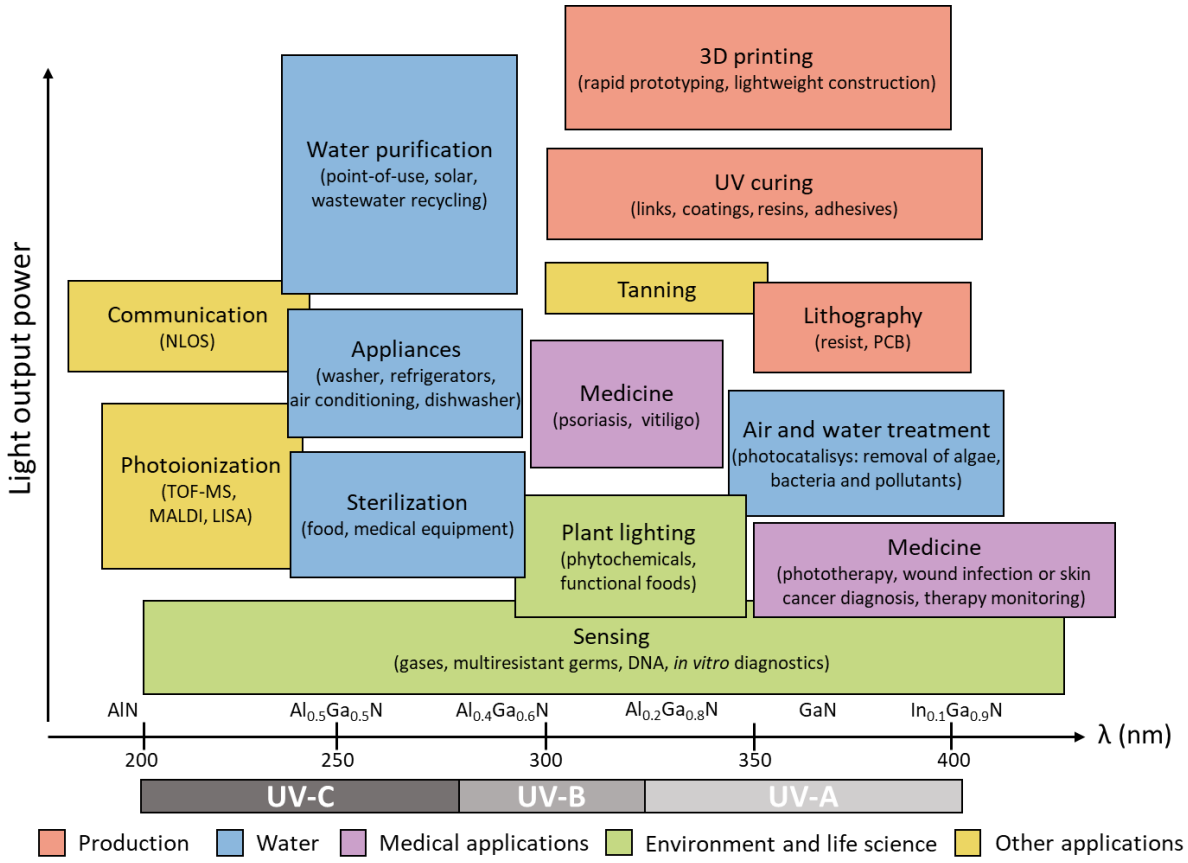

Figure 1.1. *Schematic with the main applications of UV emitters. Abbreviations stand for: LISA, Laser Interferometer Space Antenna; MALDI, matrix-assisted laser desorption/ionization; NLOS, non-line-of-sight; PCB, printed circuit boards; TOF-MS, time-of-flight mass spectrometry. (Modified from ref. [2,20])*

The electromagnetic spectrum of UV radiation can be subdivided in a number of ranges, according to the International Organization for Standardization (ISO 21348) [21]. The most common division is presented in Table 1.1.

Table 1.1. *Classification of UV wavelength spectrum.*

	Wavelength range (nm)
UV-A	400-315
UV-B	315-280
UV-C	280-200
Vacuum UV	200-100

The development of III-nitride based UV emitters has gained considerable momentum, although the efficiency and maximum power of UV light emitting devices are still modest in comparison with their visible counterparts.

UV lasers have gained interest due to their potential applications in Lidar remote detection, non-line of sight communication [22], biotechnology [23], or 3D printing [24]. The principles of

laser (acronym for "light amplification by stimulated emission of radiation") date back to 1917, when Albert Einstein derived the existence of absorption, spontaneous emission, and stimulated emission of electromagnetic radiation from Planck's law [25]. From this concept, the first practical application of stimulated emission was a microwave radiation amplifier that was named after maser (acronym for "microwave amplification by stimulated emission of radiation), first built in 1953 by Charles H. Townes. In parallel, Nikolay Basov and Aleksandr Prokhorov worked on a multilevel quantum oscillator that facilitated population inversion [26]. These achievements culminated in 1960 with the invention of an "optical maser" named as laser, and in 1964, the Nobel Prize in Physics was awarded to the above mentioned physicist "for their fundamental work in the field of quantum electronics, which has led to the construction of oscillators and amplifiers based on the maser-laser principle" [27].

Since their invention, considerable progress has been made in the laser domain. In the case of III-nitrides, the GaN blue laser diode (405 nm) have become a standard for data storage (Blue-ray technology). However, UV laser diodes are still in early stages of development. Due to the difficulty of dealing with ultra-wide-bandgap materials, efficient UV LDs are limited to emission wavelengths above 370 nm [28], and for a long time the shortest emission wavelength was 326 nm [28]. However, recently edge emitting LDs demonstrated emission at 298 nm (UV-B) [29] and 271.8 nm (UV-C) [30] at room temperature. Figure 1.2 presents a summary of data from recent literature on UV III-nitride-based LDs. The graph reveals that the challenges for UV lasers strongly depend on the emission wavelength and composition. Thus, the lasing threshold current density exhibits a strong increase for devices with shorter emission wavelength than 370 nm [31]. This marks the transition from GaN-based lasers, which are already commercially available, to lasers based on AlGaN heterostructures, which lead to high tensile strain when grown on GaN substrates [28]. Thus, in this latter case, strain relief techniques are required to avoid the formation of cracks in the laser heterostructure. AlN native substrates have been continuously improving during the last few years [32–35]. However, the lack of high quality lattice-matched substrates makes difficult the growth of medium AlGaN composition lasers for the UV-B, since they match neither GaN (tensile strain) nor AlN (compressive strain) substrates [36]. Finally, efficient carrier injection and confinement, as well as low resistivity p-AlGaN layers with large Al content (>70%), pose very difficult challenges for the realization of UV-C lasers. The ionization energy of Mg acceptors in AlGaN increases with the aluminum content, leading to very low conductivity [3]. The resulting high lasing threshold leads to a reduction of the device lifetime, due to Joule heating. A very recent result reported by Nagoya University, is an AlGaN-based UV laser diode operating at 5 °C with a threshold current of 3.7 kA/cm^2 [37]. This reduction of threshold was the result of improvements in the design, which incorporates polarization doping for the p-type layers and a complex top structure to compensate the optical modal loss [38–40].

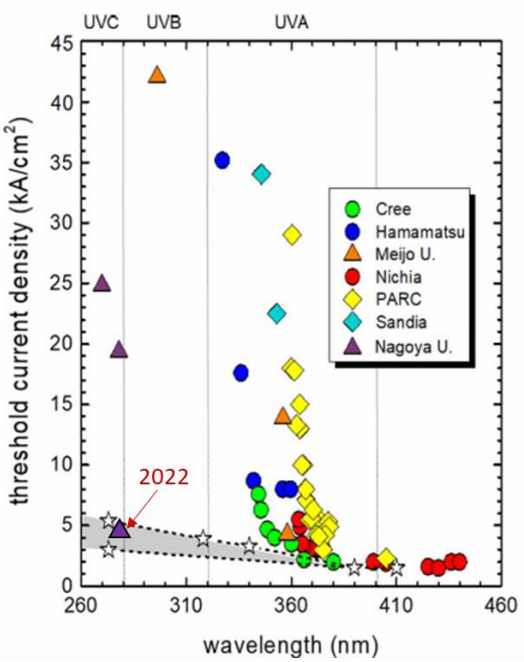

Figure 1.2. *Previously published threshold current densities of III-nitride based laser diodes as a function of their emission wavelength. (Reproduced from [3], with data added from [37])*

Alternatives to electrical injection include optically pumped and electron beam pumped lasing, which obviate the need of contacts or high conductivity cladding layers. Optically pumped lasers with emission wavelengths from 310 nm to 237 nm have been demonstrated over the past years, with lasing threshold power densities reaching < 10 kW/cm² [41–43]. Some advanced laser structures have also been explored in the range between 400 nm and 310 nm, such as vertical cavity surface emitting lasers (VCSELs) [44,45] or distributed feedback (DFB) laser diodes [46]. Another alternative currently under development are polariton lasers [47,48], which use exciton-polariton interaction in micro-cavities to achieve lasing emission. Lasing thresholds are hundreds of times lower than conventional lasers, despite their output powers being much lower [49,50].

1.2 Motivation and targets

As we have seen in the previous section, the challenges for realizing p-type AlGaN cladding layers with high conductivity are a hindrance that limit the performance of UV lasers. The shortest commercial UV LDs emit at 375 nm (Nichia). Due to these problematics, the commercial ultraviolet spectral range is currently covered by gas lasers (ArF, XeF, KrF) or lasers based on frequency conversion (Nd:YAG). However, these light sources are bulky, inefficient and inflexible in wavelength. AlGaN has the potential to overperform these lasers and offer a competitive alternative in the market. An alternative strategy to pump AlGaN heterostructures is using a high-energy electron beam excitation to generate electron-hole pairs that can circumvent many of the

issues encountered in conventional p-n junction configurations. This technique does not require any contacting or doping in the structure. In addition, it provides efficient and homogeneous carrier injection even in wide active zones, which is not possible in laser diodes due to the asymmetric transport properties of electrons and holes. Therefore, electron beam pumping offers a larger degree of freedom for the heterostructure design.

As mentioned above, optically pumped lasers are another alternative to consider. Under these conditions, doping and contacting is not required either. However, it requires to locate the active media as close to the surface as possible to ensure the collection of generated carriers. Compared with optical pumping, electron beam pumping offers the possibility to make devices more compact (smaller pumping source), and the ability of the electron beam to penetrate deeper into the structure provides an additional degree of freedom in the design of the optical cavity, and reduces surface-related loses. Furthermore, electron beam pumping is adapted to a large spectral range, since the electron-hole pair generation is done by impact-ionization. Instead, in the case of optical pumping, the wavelength of the output laser must be longer than the wavelength of the pumping in order to generate electron-hole pairs by photon absorption.

Currently, and to the best of my knowledge during the writing of this manuscript, there is only one demonstration of In-free AlGaN/GaN heterostructure UV electron beam pumped laser, reported by Hayashi *et al.* [51]. A separate confinement heterostructure (SCH) containing a 10-period GaN/AlGaN multi-quantum well (MQW) displayed stimulated emission around 353 nm with a threshold power density ≈ 230 kW/cm^2 at 107 K, under pulsed electron beam excitation operating at 15 kV. There has not been any demonstration of laser emission from electron beam pumped AlGaN-based lasers at room temperature at the time of writing this manuscript.

The motivation of this work rises from the high demand of efficient UV lasers compared with the low offer available. The **aim of this work is to contribute to the development of AlGaN/GaN based electron beam pumped UV laser technology**, a recent field of research with plenty of potential to compete with current commercial lasers. Electron beam pumped AlGaN/GaN lasers, offer an alternative path towards the achievement of efficient solid-state lasers that can cover the whole UV spectral range. Within this context, the **main targets of the work** were:

- Understanding the mechanisms and parameters governing the performance of these devices.
- Develop a first heterostructure emitting in the UV-A that acts as the active media of a UV laser that operates at low acceleration voltages (≤ 10 kV).
- Optimize the structure to improve the efficiency and the lasing threshold.
- Use the knowledge acquired to design prototypes to extend the work towards shorter wavelengths.

This work is part of the ANR-UVLASE project, which aims to develop a new compact UV-laser technology based on the excitation of an AlGaN MQW nanostructure by a shaped electron beam from a high-current cathode, such as those based on carbon nanotubes (CNT). First, we target a proof-of-principle demonstration of an electron beam pumped UV laser emitting at 350 nm. Figure 1.3 presents a schematic of the initial prototype of the device. This project is in collaboration between CEA/IRIG/PHELIQS, my hosting lab, in charge of the growth, characterization and fabrication of the active medium; CNRS/Institut Néel, in charge of simulations and characterization; and CNRS/Université Claude Bernard Lyon I/ILM, in charge of the electron beam technology.

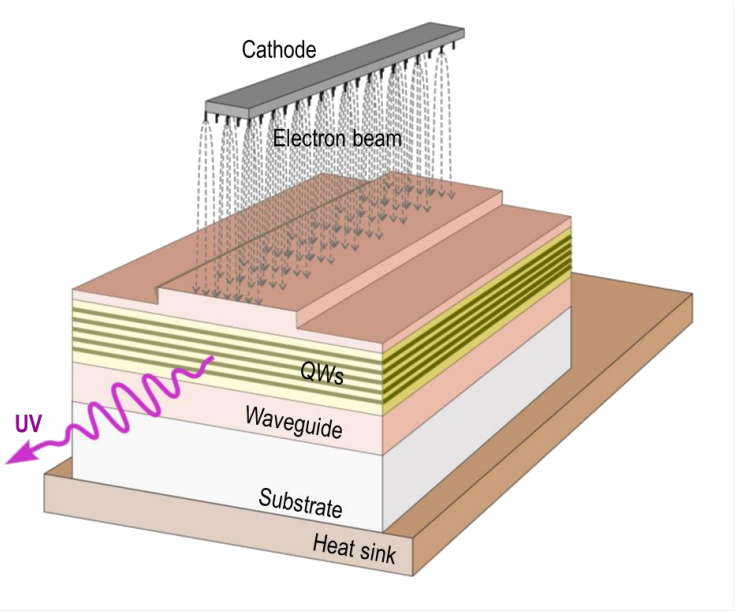

Figure 1.3. *Schematic description of the initial device protoype, including a planar cathode and a semiconductor dice with a multimode waveguide containing the MQW active region.*

Within this framework, **my tasks** were the following:

- Design of the MQW heterostructure, including the optical waveguide, by simulation tools (COMSOL, nextnano3, CASINO).
- Epitaxial growth of the heterostructures by plasma-assisted molecular beam epitaxy (PAMBE).
- Optical characterization of the heterostructures by photoluminescence (PL) and cathodoluminescence (CL), plus collaborating in the structural characterization by electron microscopy, atomic force microscopy (AFM) and x-ray diffraction (XRD).
- Fabrication of laser cavities from the heterostructures in cleanroom facilities, including lithography, metal deposition and reactive ion etching.

1.3 Organization of the manuscript

This manuscript starts by the introductory pages of **Chapter 1**, where I offer a general and brief historical overview to the III-nitride UV technology during the last decades, which justifies the motivation and targets of this work.

Chapter 2 is dedicated to introduce in detail the concepts that are important for this work. In particular, I present the properties of III-nitride materials, with an emphasis on GaN, AlN and their ternary alloy AlGaN, followed by the fundamentals of laser physics. The last two sections are devoted to introducing electron beam pumping and its particularities, together with a brief review of the state of the art of this technology applied to semiconductor lasers.

Chapter 3 introduces all the experimental methods and tools used during this work, describing the different techniques and their operation conditions. This chapter includes the epitaxial growth, characterization techniques, simulation tools and clean-room fabrication procedures.

Chapter 4 presents the main device designs for UV-A laser emission and their justification in terms of electrical and optical properties. Then, I describe the growth conditions of the main samples for each design, together with their structural characterization. Finally, the as-grown samples are characterized optically in terms of emission under optical and electron beam pumping, to extract internal quantum efficiency and optical gain. The suitability of the designs/samples as active medium for electron beam pumping lasers is discussed.

Chapter 5 is dedicated to the fabrication of optical cavities from the samples described in Chapter 4, and the characterization of their lasing emission under optical pumping. First, cavities are fabricated by mechanical cleaving. Then, in order to reduce the lasing threshold, a two-step etching process is developed to obtain smoother and vertical cavity facets. We report lasing emission for both cases and we discuss the benefits of the two-step process for the laser performance. In addition, in this chapter, I discuss the observed decorrelation between the lasing threshold and the internal quantum efficiency in our samples, and I perform an estimation of the lasing threshold under electron beam pumping.

Chapter 6 describes our first steps towards the achievement of UV-C AlGaN-based electron beam pumped lasers. In this chapter, I present new designs targeting shorter wavelengths and the last experimental results including the growth of separate confinement heterostructures on bulk AlN.

Chapter 7 contains the general conclusions extracted from this work, how they relate to our initial targets, and a discussion on future prospects on this research field.

Chapter 2
Introduction to III-nitride semiconductors and e-beam pumped lasers

This chapter introduces III-nitride materials and electron beam pumped lasers. First, we present the structural and electronic properties of III-N semiconductors, and we discuss the formation of heterostructures. Then, we describe the principles of lasing and electron beam pumping, and describe the design and operation of an electron beam pumped laser. The chapter concludes with a summary of the state of the art of III-N electron beam pumped lasers.

Part of this chapter is published as a review paper: "Electron beam pumped light emitting devices", S. Cuesta et al., J. Phys. D: App. Phys. 55, 273003 (2022) [52].

2.1 III-nitride materials

III-nitride materials are compound semiconductors that consist of group III metals (particularly Al, Ga and In) and the group V element N. Their binary compounds are GaN, AlN and InN, and by combining them, it is possible to synthesize their ternary and quaternary compounds. In this project, we will focus on GaN, AlN and their ternary alloy AlGaN.

2.1.1 Crystal structure

III-nitride semiconductors (GaN, AlN, InN and their alloys) can adopt three types of crystalline configurations, namely wurtzite (α-phase), zinc blende (β-phase) and rock salt (γ-phase), as illustrated in Figure 2.1. The wurtzite and zinc-blende phases can be obtained through epitaxial growth techniques. In contrast, the rock-salt phase can only be synthesized at high pressure [53].

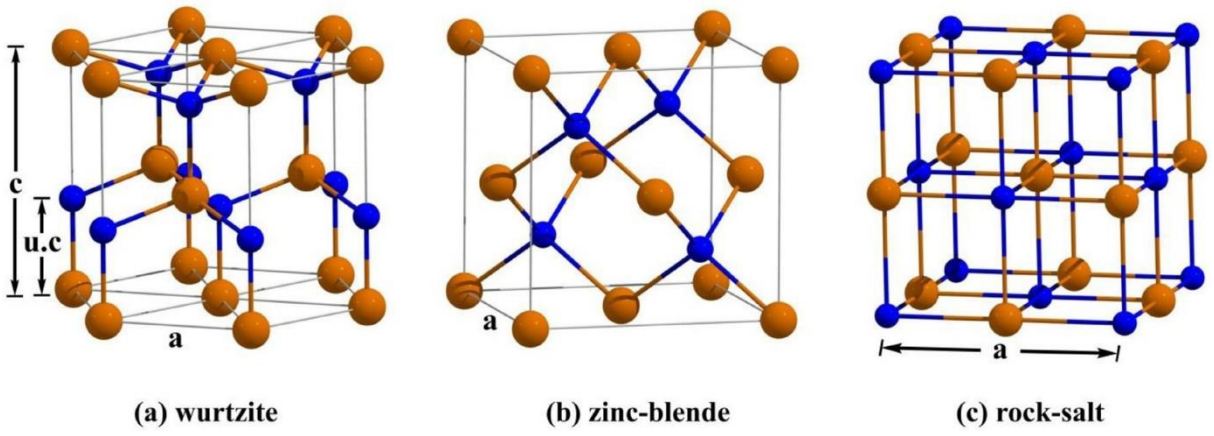

Figure 2.1. *Schematic representation of (a) wurtzite, (b) zinc blende and (c) rock salt structures. The orange and blue spheres indicate metal and N atoms, respectively. [54]*

In order to understand the geometry of the unit cells, the hexagonal and cubic systems are illustrated in Figure 2.2.

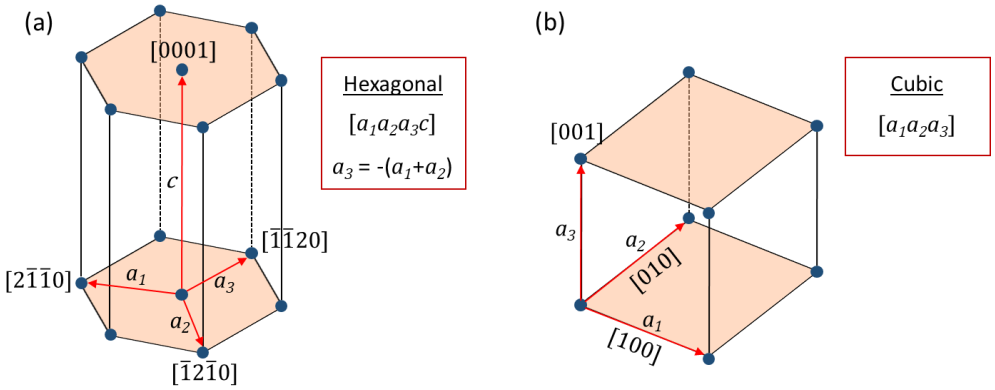

Figure 2.2. *(a) Hexagonal unit cell with base vectors a_1, a_2, a_3 and c. (b) Cubic unit cell with base vectors a_1, a_2 and a_3.*

The directions and crystallographic planes in a hexagonal symmetry are described using the Miller-Bravais indices, which are four integers generally denoted by the letters *h k i l*. The first three indices represent the basal axes a_1, a_2 and a_3, while the fourth index represents the vertical *c* axis. Note that the first three indices form an angle of 120° between each other, satisfying the relation $i = -(h+k)$, as illustrated in Figure 2.2(a). In the case of cubic symmetry, the notation uses three integers denoted by *h k l*. The three indices represent the basal axes a_1, a_2 and a_3, which are perpendicular to each other, as illustrated in Figure 2.2(b).

The wurtzite structure presents hexagonal symmetry and it consists of two hexagonal sublattices of metal (Al, Ga, In) and nitrogen (N) atoms, respectively, shifted by $u = \frac{3}{8}c$ along the [0001] direction, as shown in Figure 2.1(a). The zinc blende structure shows a cubic symmetry, and it consists of two interpenetrating face-centered cubic sublattices shifted by $\frac{\sqrt{3}}{4}$[111] with respect to each other, as shown in Figure 2.1(b). In wurtzite and zinc blende configurations, each atom is tetrahedrally coordinated. The wurtzite structure can be generated from zinc blende by rotating adjacent tetrahedra around their common bonding axis along [111] by an angle of 60° with respect to each other.

In this work, we focus on the wurtzite phase, which is the most thermodynamically stable configuration. The lattice parameters that define the wurtzite unit cell are the edge of the hexagon (a), the height of the hexagon (c) and the anion-cation bond length (u) along the [0001] direction. For an ideal wurtzite crystal, the c/a and the u/c ratios are 1.633 and 0.375, respectively. However, even in bulk materials, these ratios deviate from their ideal values. Table 2.1 describes the lattice parameters of bulk wurtzite III-nitrides.

Table 2.1. *Lattice parameters of bulk GaN, AlN and InN at room temperature.*

	GaN	**AlN**	**InN**
***c* (Å)**	5.185	4.982	5.703
***a* (Å)**	3.189	3.112	3.545
c/a	1.626	1.6	1.608
u/c	0.377	0.382	0.377
References	[55,56]	[55,56]	[56]

In the case of ternary alloys, the lattice parameters can be calculated by linear interpolation from binary compounds following Vegard's law:

$$a_{Al_xGa_{(1-x)}N} = a_{AlN}x + a_{GaN}(1-x) \tag{2.1}$$

In the wurtzite geometry, the planes perpendicular to the [0001] axis or *c*-direction are called "polar planes", denoted as {0001} plane family or *c*-plane (orange in Figure 2.3), and they have only group III metal or N atoms in their surface. The planes parallel to the *c*-direction are called "non-polar planes", and they contain an equal number of metal and N atoms on their surfaces. The most important families of non-polar planes are the {1-100} *m*-plane (green in Figure 2.3) and the {11-20} *a*-plane (blue in Figure 2.3). The rest of the surfaces that form an angle other than 0° or 90° with the c-axis are called "semi-polar planes", e.g. the {11-22} plane family (purple in Figure 2.3). The preferential orientation used for GaN epitaxy is the *c*-plane, with a well-established knowledge of the epitaxial mechanisms.

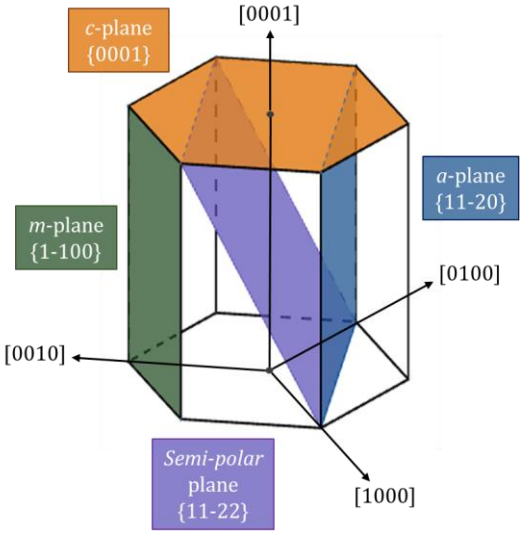

Figure 2.3. *Schematic view of the main polar, non-polar and semi-polar planes.*

The hexagonal wurtzite structure is asymmetric in the [0001] and [000-1] directions. The axis sign is determined by the orientation of the vector associated to the metal-nitrogen bond along the <0001> axis. The [0001] direction is arbitrarily defined by the vector pointing from a metal atom to a nitrogen atom, as illustrated in Figure 2.4. We denote the material as metal-polar if grown along [0001] and nitrogen-polar if grown along [000-1].

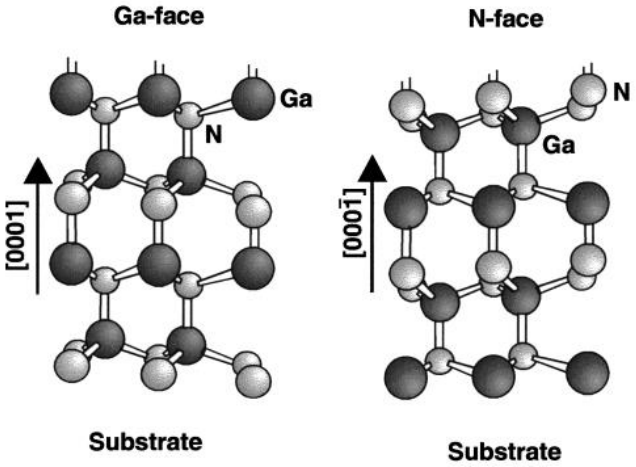

Figure 2.4. *Schematic drawing of the crystal structure of Ga-polar and N-polar wurtzite GaN. [57]*

The polarity strongly affects the surface morphology [58], chemical reactivity, optical properties [59] and growth features of the material [60]. The choice of polarity depends on the nature of the substrate and the growth conditions. Usually, Ga-face GaN is preferred as it offers higher chemical stability and it is easier to control the surface morphology during the epitaxial growth.

2.1.2 Elastic properties

III-nitride layers are commonly synthesized on c-plane oriented templates, using sapphire, SiC or Si as substrates. The lattice mismatch between the layer and the template, together with thermal expansion effects, imposes an in-plane stress on the epitaxial layer, which can affect the optical and electronic properties of the material. When growing along the <0001> axis, the lattice mismatch between the substrate and the epilayer is given by

$$f = \frac{a_{sub} - a_{epi}}{a_{sub}} \tag{2.2}$$

where a_{sub} and a_{epi} refer to the in-plane lattice parameter of the substrate and the relaxed material of the epitaxial layer, respectively.

For small stress, the lattice reacts elastically through a shape deformation (strain), leading to pseudomorphic growth. The strain can be either tensile for $f > 0$, or compressive for $f < 0$ (see

Figure 2.5). When the accumulated elastic energy exceeds a certain value, relaxation occurs plastically via formation of dislocations or cracks, leading to metamorphic growth.

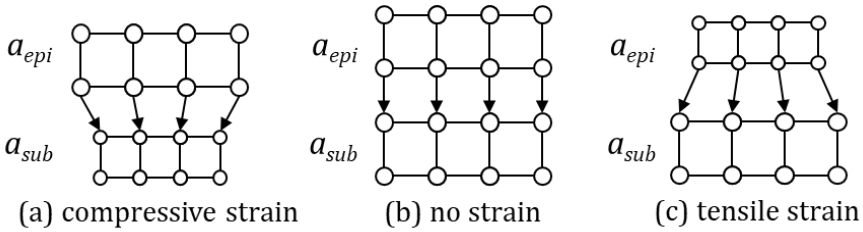

(a) compressive strain (b) no strain (c) tensile strain

Figure 2.5. *Schematic illustrating the strain as a function of the lattice mismatch.*

In the linear elasticity regime, Hooke's law describes the relation between the stress (σ_{ij}) applied to the material and the strain (ε_{kl}):

$$\sigma_{ij} = \sum_{kl} C_{ijkl}\,\varepsilon_{kl} \tag{2.3}$$

where C_{ijkl} is the fourth order elastic tensor. To simplify the notation, we introduce the indices {1, 2, 3, 4, 5, 6} to substitute indices {*xx, yy, zz, yz, zx, xy*}:

$$\begin{aligned} \varepsilon_1 &= \varepsilon_{xx} & \sigma_1 &= \sigma_{xx} \\ \varepsilon_2 &= \varepsilon_{yy} & \sigma_2 &= \sigma_{yy} \\ \varepsilon_3 &= \varepsilon_{zz} & \sigma_3 &= \sigma_{zz} \\ \varepsilon_4 &= \varepsilon_{yz}, \varepsilon_{zy} & \sigma_4 &= \sigma_{yz}, \sigma_{zy} \\ \varepsilon_5 &= \varepsilon_{zx}, \varepsilon_{xz} & \sigma_5 &= \sigma_{zx}, \sigma_{xz} \\ \varepsilon_6 &= \varepsilon_{xy}, \varepsilon_{yx} & \sigma_6 &= \sigma_{xy}, \sigma_{yx} \end{aligned}$$

For hexagonal crystal symmetry, the elastic tensor matrix contains six elastic modules, five of which are independent, as given in equation (2.4):

$$C_{ij} = \begin{pmatrix} C_{11} & C_{12} & C_{13} & 0 & 0 & 0 \\ C_{12} & C_{11} & C_{13} & 0 & 0 & 0 \\ C_{13} & C_{13} & C_{33} & 0 & 0 & 0 \\ 0 & 0 & 0 & C_{44} & 0 & 0 \\ 0 & 0 & 0 & 0 & C_{44} & 0 \\ 0 & 0 & 0 & 0 & 0 & \frac{1}{2}(C_{11} - C_{12}) \end{pmatrix} \tag{2.4}$$

The elastic stiffness constant can be found experimentally performing Brillouin or Raman scattering. However, due to the difficulties of growing high quality crystals, we can find some discrepancies between the theoretical and experimental values, as summarized in Table 2.2.

During the epitaxial growth of thin films on the (0001) plane, the in-plane stress is uniform ($\sigma_{11} = \sigma_{22} = \sigma$) and there is no stress along the [0001] *c*-axis. In this configuration of biaxial stress, equation (2.3) can be simplified as:

$$\begin{pmatrix} \sigma \\ \sigma \\ 0 \end{pmatrix} = \begin{pmatrix} C_{11} & C_{12} & C_{13} \\ C_{12} & C_{11} & C_{13} \\ C_{13} & C_{13} & C_{33} \end{pmatrix} \begin{pmatrix} \varepsilon_1 \\ \varepsilon_2 \\ \varepsilon_3 \end{pmatrix} \tag{2.5}$$

Due to symmetry, the strain components ε_1 and ε_2 are equal such that:

$$\varepsilon_1 = \varepsilon_2 = \varepsilon_{xx} = -(a_{epi} - a_{sub})/a_{sub} \tag{2.6}$$

As consequence, the biaxial stress induces also a strain component ε_3, along the *c*-axis, opposite to ε_1 and ε_2:

$$\varepsilon_3 = \varepsilon_{zz} = -2(C_{13}/C_{33})\varepsilon_1 \tag{2.7}$$

Table 2.2. *Theoretical and experimental stiffness constant for GaN, AlN and InN in GPa.*

	C_{11}	C_{12}	C_{13}	C_{33}	C_{44}	References
GaN	396	144	100	392	91	[61] The.
	367	135	103	405	95	[62] The.
	374	106	70	379	101	[63] Exp.
	390	145	106	398	105	[64] Exp.
AlN	398	140	127	382	96	[61] The.
	396	137	108	373	116	[62] The.
	411	149	99	389	125	[65] Exp.
	410	140	100	390	120	[66] Exp.
InN	271	124	94	200	46	[61] The.
	223	115	92	224	48	[62] The.
	225	109	108	265	55	[67] Exp.

2.1.3 Spontaneous and piezoelectric polarization

An intrinsic property of III-nitride materials is the presence of polarization in the crystal. The nitrogen atoms are more electronegative than the metal atoms, thus converting the cation-anion bond into an electrostatic dipole. Due to the lack of symmetry of the wurtzite structure, this charge distribution is not fully compensated along the [0001] direction, leading to spontaneous polarization (P_{sp}). The values of spontaneous polarization for III-nitride materials are described in Table 2.3, using different approximation methods.

Table 2.3. *Calculation of spontaneous polarization for wurtzite GaN, AlN and InN.*

	GaN	AlN	InN
P_{sp} (C/m²) [68]	-0.029	-0.081	-0.032
P_{sp} (C/m²) [69]	-0.032	-0.100	-0.041
P_{sp} (C/m²) [69]	-0.034	-0.090	-0.042

When applying mechanical stress to the system, an additional piezoelectric component of the polarization (P_{pz}) appears. Therefore, the total polarization of the system is the sum of both spontaneous and piezoelectric polarization. The piezoelectric polarization can be calculated from the following equation:

$$P_{pz} = \begin{pmatrix} 0 & 0 & 0 & 0 & e_{15} & 0 \\ 0 & 0 & 0 & e_{15} & 0 & 0 \\ e_{31} & e_{31} & e_{33} & 0 & 0 & 0 \end{pmatrix} \begin{pmatrix} \varepsilon_1 \\ \varepsilon_2 \\ \varepsilon_3 \\ \varepsilon_4 \\ \varepsilon_5 \\ \varepsilon_6 \end{pmatrix} \tag{2.8}$$

where e_{ij} are the piezoelectric coefficients of the material and ε_{ij} form the stress tensor. The values of the piezoelectric coefficients for III-nitride materials are summarized in Table 2.4.

Table 2.4. *Calculation of piezoelectric coefficients for wurtzite GaN, AlN and InN.*

	GaN	AlN	InN
e_{31} (C/m²) [68]	-0.49	-0.60	-0.57
e_{33} (C/m²) [68]	0.73	1.46	0.97
e_{15} (C/m²) [70]	-0.30	-0.48	-

2.1.4 Band structure

The electronic band structure of a semiconductor describes what energy ranges can be occupied by electrons. It can be obtained from the Schrödinger equation and it is represented as energy $E(k)$ as a function of the wavevector $\vec{k}$ = (k_1, k_2, k_3). The band structures for GaN and AlN are presented in Figure 2.6 (a) and (b), respectively. Considering the Brillouin zone, which is a unit cell in the reciprocal space, we find critical points of high symmetry labelled as Γ, A, H, K, L and M, being Γ the center of the Brillouin zone (k = 0). The energy distribution along the paths connecting these points describe all the possible occupations in the space. The energy band gap of a semiconductor is defined as the difference between the highest energy point in the occupied valence band and the lowest energy point in the unoccupied conduction band. When these two

extremes converge in the same symmetry point, the band gap is direct; otherwise, the band gap is indirect. In the case of III-N, the band gap is direct and located at the Γ point.

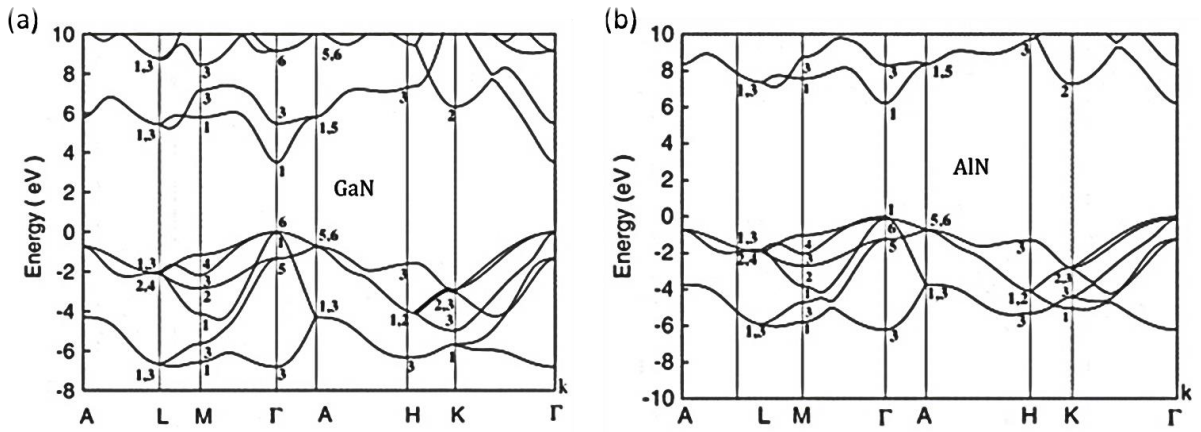

Figure 2.6. *Band structure of wurtzite (a) GaN and (b) AlN. [71]*

From the band structure, it is interesting to see that the valence band is split into three subbands due to the spin-orbit coupling and the static electric field produced by the spontaneous polarization (crystal field). These are called heavy hole (HH), light hole (LH) and crystal field hole (CH) subbands. These three subbands are illustrated in Figure 2.7, which is a zoomed image of the valence band maximum at Γ point.

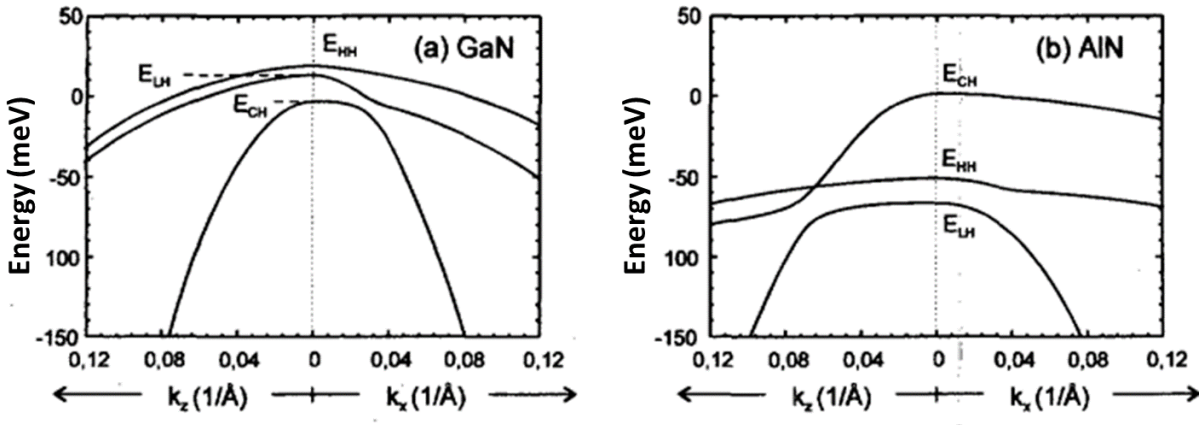

Figure 2.7. *Valence band energy levels HH, LH and CH around the Γ point for wurtzite (a) GaN and (b) AlN. [72]*

An effective mass approximation can be used to describe the band at the Γ point as a parabola. In this approach, the motion of both electrons and holes can be expressed as the motion of free particles with an effective mass m^*. The Schrödinger equation can be solved with a one-electron Hamiltonian, neglecting the electron-hole interaction and assuming a small electric field. The effective mass values of electrons and holes for GaN and AlN are summarized in Table 2.5.

The semiconductor band gap is a crucial parameter to understand the optoelectronic behavior of the material. The gap energy varies with temperature due to the lattice expansion and the

derived electron-lattice interaction. The evolution of the band gap energy with temperature can be modelled by the Varshni equation [73]:

$$E_g(T) = E_g(T=0) - \frac{\alpha T^2}{\beta + T} \tag{2.9}$$

where α is the Varshni coefficient, β is the Debye coefficient. These parameters were found empirically and their values are reported in Table 2.5.

The band gap of ternary compounds (i.e. AlGaN) can be approximated by quadratic interpolation of the band gaps of the corresponding binary compounds:

$$E_g{}^{Al_xGa_{(1-x)}N} = xE_g{}^{AlN} + (1-x)E_g{}^{GaN} - x(1-x)b \tag{2.10}$$

where b is a bowing parameter that accounts for the deviation from the linear interpolation between the two binary compounds. The reported values of b for AlGaN are in the range of 0-1.5 eV, since the strain state can also influence the bowing parameter [74–76]. In this work, we used b = 0.62 eV [77] for our calculations.

Table 2.5. *Band gap at T = 0 K, effective mass (m_0 being the electron mass in vacuum) and band parameters of wurtzite GaN and AlN.*

Parameters (units)	Symbol	GaN	AlN
Band gap (eV)	E_g	3.51 [56]	6.23 [56]
Electron effective mass	m_e^*	0.2 m_0 [78]	0.27 m_0 [79]
Hole effective mass	m_h^*	1.25 m_0 [80]	1.44 m_0 [81]
Varshni coefficient (meV/K)	α	0.59 [82]	1.999 [56]
Debye coefficient (K)	β	600 [82]	1429 [56]

2.1.5 III-nitride heterostructures

III-nitride compounds offer enormous opportunities in the optoelectronic field, due to their band gaps being able to embrace a vast part of the electromagnetic spectra. Figure 2.8 shows a diagram with the band gap energy of III-nitrides as a function of their lattice parameter. The band gap of ternary alloys results from the interpolation of the binary compounds, as stated in equation (2.10). The spectral range covers wavelengths from the infrared to the ultraviolet.

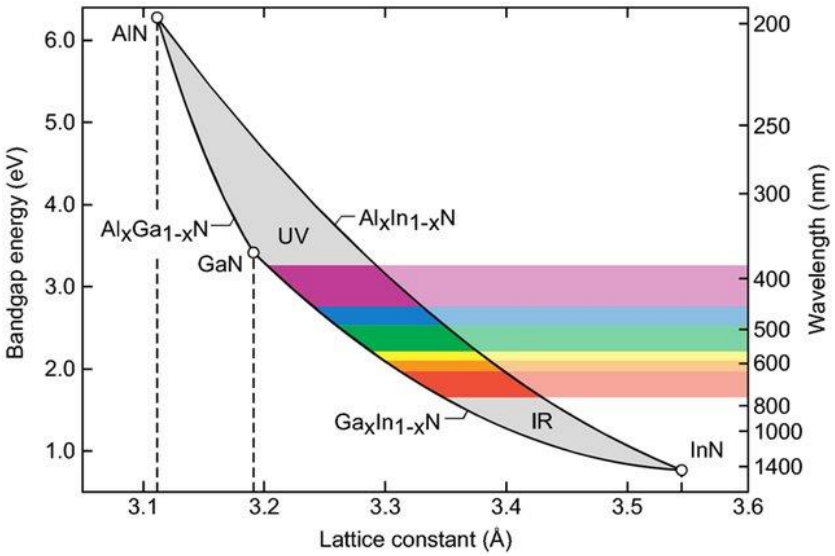

Figure 2.8. *III-N materials band gap as a function of the lattice parameter. [83]*

The advances in epitaxial deposition techniques permit the fabrication of heterostructures, which opens the path towards band gap engineering. When putting two materials with different band gap together, there are three possibilities of alignment of band gap minima along the growth direction depending on the conduction band offset, named type I, II and III (see Figure 2.9). In the case of III-nitrides, heterostructures are mostly type I, and in particular, the conduction band offset in the AlN/GaN system is ≈ 1.8 eV [84].

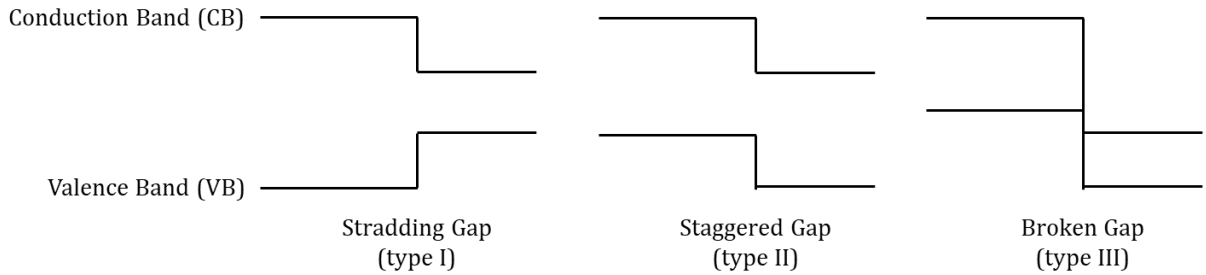

Figure 2.9. *Schematic description of the three types of band edge profile at heterojunctions.*

The concept can be taken further to produce heterostructures like quantum wells (QWs), where quantum confinement generates quantified electron levels. However, as stated in section 2.1.3, III-nitrides present spontaneous polarization whose value differ between materials. Therefore, the discontinuity of polarization vector at the heterointerface between two different materials results in a fixed charged sheet (+/- σ) at the interface. The fixed charges generate an internal electric field (E) that bend the band structure, as illustrated in Figure 2.10(a) for an AlGaN/GaN/AlGaN heterostructure grown along the [0001] polar direction. In this configuration, the polarization in GaN is weaker than in AlN, thus generating an internal electric field along the [0001] direction. As a result, the electron and hole wave functions get spatially separated. The overlap between both functions is lower than in a symmetric well, thus reducing the probability of radiative recombination. In addition, the band-to-band transition is shifted towards lower

energies (red shift). The consequences of the band bending are called quantum confinement Stark effect (QCSE); they must be considered carefully when designing devices using polar materials. In contrast, in heterostructures grown on non-polar planes such as the *m*- or the *a*-direction, the polarization is perpendicular to the growth direction. Hence, all the dipoles are compensated and there is no fixed charge at the heterointerfaces. This means that, in a QW, the electron and hole wave functions are aligned, as illustrated in Figure 2.10(b).

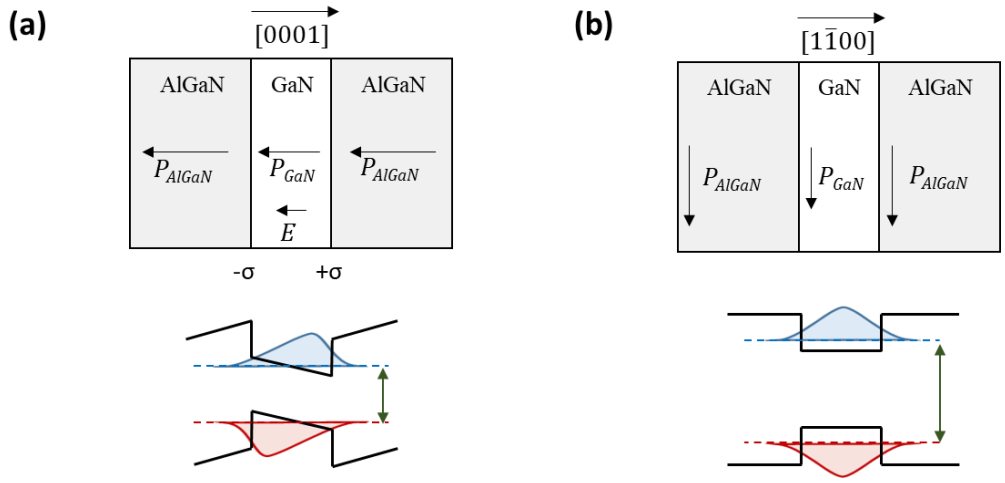

Figure 2.10. *Schematic of AlGaN/GaN/AlGaN heterostructure with energy band structure for growth along (a) the polar c-direction and (b) the non-polar m-direction. The band diagram represents one period in a GaN/AlGaN infinite superlattice.*

2.2 Fundamentals of laser

A semiconductor laser is a solid-state device that consists of a semiconductor gain medium inserted in an optical cavity. Optical amplification results in stimulated emission, which requires a situation of population inversion and gain regime. These conditions can be attained through electrical injection, electron beam pumping or optical pumping. In this section, the basics of laser physics are introduced, highlighting figures of merit such as threshold and gain.

2.2.1 Spontaneous and stimulated emission

Let us consider a semiconductor, with the conduction band and the valence band separated by the band gap energy E_g (see Figure 2.11). A photon with energy $h\nu$ equal or higher to E_g that separates the two levels can be absorbed to promote one electron from the valence to the conduction band, generating an electron-hole pair. The resulting hole will relax towards the valence band edge (fundamental level) and the electron will relax towards the conduction band edge (excited state). If no more excitation occurs, and neglecting non-radiative recombination, the

electron and hole will recombine emitting a photon with energy E_g and random phase and direction. This phenomenon is known as spontaneous emission.

However, if there is an electron in the excited state and a photon with energy $h\nu$ arrives, a new radiative recombination process can occur, stimulated emission, which consists in the emission of a photon of energy E_g induced by a photon of the same energy. In this case, the two photons are coherent, with the same frequency, direction and phase.

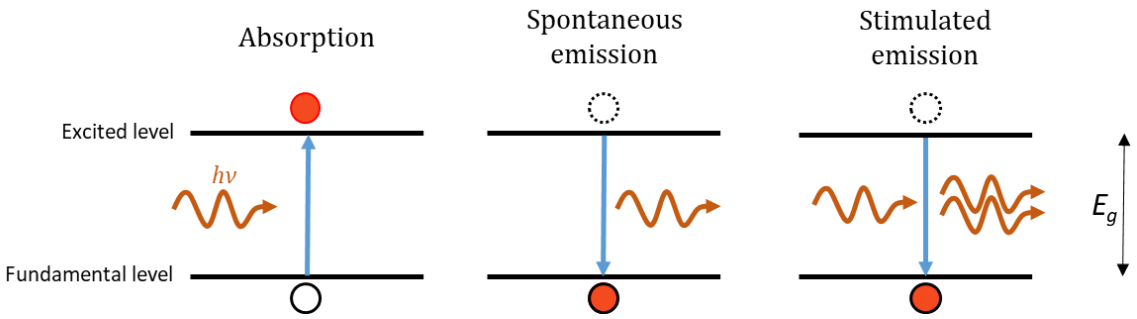

Figure 2.11. *Schematic of the three mechanism of interaction between a photon and a two level system.*

In a two level system with N_1 carriers in the fundamental state (level 1) and N_2 carriers in the excited state (level 2), excited with energy density $u(v)$, the transition probability rates of the above-described phenomena can be described as follows

$$Spontaneous\ emission\ rate:\ R_{sp} = AN_2$$

$$Stimulated\ emission\ rate:\ R_{st} = B_{21}N_2 \cdot u(v)$$

$$Absorption\ rate:\ R_{abs} = B_{12}N_1 \cdot u(v)$$

where A and B are Einstein coefficients. Since absorption and stimulated emission are inverse processes, $B_{12} = B_{21} = B$. Therefore, the population of carriers in each level determines the dominant process. When the excitation is low, the number of carriers in the excited state is small ($N_2 < N_1$) so the probability of absorption is larger than the probability of stimulated emission. On the other hand, under high excitation density, a high number of carriers are promoted to excited states. When $N_2 > N_1$, the probability of stimulated emission becomes higher than the probability of absorption. This regime is known as population inversion, and it is one of the conditions to generate lasing. In practice, it is not possible to achieve population inversion in a two-level system in thermal equilibrium, limited to the condition where $N_2 = N_1$. Lasers usually work with a 4-level system, but in this explanation we considered a two-level system for simplicity.

2.2.2 Threshold and gain

A scheme of an optical cavity of length L is presented in Figure 2.12. Two mirrors limit the cavity, with reflectivity R_1 and R_2. If we consider a photon that starts at the center of the cavity with initial intensity I_0, the light intensity after one round trip in the cavity is given by

$$I = I_0 e^{2L(g-\alpha_i)} R_1 R_2 \tag{2.11}$$

where g is the net gain and α_i are the internal losses, related to phenomena of scattering or absorption of the light.

The lasing threshold is the lowest excitation level at which the laser output is dominated by stimulated emission instead of spontaneous emission. Therefore, the threshold is the excitation level at which gain compensates optical losses. At the threshold ($I = I_0$), equation (2.11) becomes

$$e^{2L(g_{th}-\alpha_i)} R_1 R_2 = 1 \tag{2.12}$$

where g_{th} is the net gain at the threshold. Therefore, we can write

$$g_{th} = \alpha_i + \frac{1}{2L} ln \frac{1}{R_1 R_2} = \alpha_i + \alpha_m \tag{2.13}$$

where α_m are the losses related to the mirrors of the cavity. Therefore, in order to obtain lasing emission, the net gain must be greater than the sum of all the optical losses. The net gain, also called modal gain, results from the product of the material gain ($g_{material}$) and the optical confinement factor (Γ or OCF) of the cavity:

$$g = \Gamma g_{material} \tag{2.14}$$

The material gain is an intrinsic property from each material. However, the optical confinement factor depends on the cavity design.

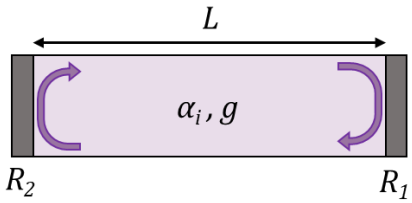

Figure 2.12. *Schematic of a laser cavity of length L, with internal losses α_i and net gain g. The mirrors at each side of the cavity have reflectivity R_1 and R_2, respectively.*

The threshold power density, P_{th}, i.e. the pumping power density that is necessary to inject in the device so that the stimulated emission becomes dominant, is proportional to g_{th} such that

$$P_{th} = kg_{th} = k\left(\alpha_i + \frac{1}{2L} ln \frac{1}{R_1 R_2}\right) \quad (2.15)$$

For electron beam pumping, $P_{th} = V_a \times I_{th}$, where V_a is the acceleration voltage and I_{th} is the current density at threshold conditions. V_a defines the penetration depth of the electrons into the structure. Consequently, the depth location of the gain medium in the device will determine the optimum V_a to maximize the carrier density in the active region. With this optimum value of V_a, the excitation power can be tuned by increasing the current density injected in the semiconductor.

In semiconductor lasers, the threshold was empirically observed to increase exponentially with temperature, following [85]

$$I_{th} = I_0 \exp\left(\frac{T}{\theta}\right) \quad (2.16)$$

where I_0 is the threshold at T = 0 and θ is a fitting coefficient, generally in the range of 50-110 K.

2.3 Introduction to electron beam pumping

Electron beam pumped lasers are clean and energy-efficient light emitting devices that can provide high light output and long service life. When exciting with an electron beam, electron-hole pairs are created by impact-ionization processes in the semiconductor, which obviates the need for doping or contacts. This approach is promising to be implemented in those spectral ranges where electrical injection is problematic, and it is compatible with ultra-wide band gap materials such as AlN.

2.3.1 Electron beam pumping principle

The working principle of electron beam pumped light emitting devices differs from the electrical current injection in the conventional light emitting diodes (LEDs) and laser diodes (LDs). Figure 2.13 presents a simplified diagram to compare the two approaches. LEDs and LDs, described in Figure 2.13(a), consist in a p-doped region and an n-doped region heterostructure. At equilibrium, the band structure of both regions align such that the Fermi level matches in the two sides of the junction. When the p-type region is positive biased with respect to the n-type region (forward bias), electrons from the n-side and holes from the p-side are injected into the junction, where they recombine with an energy equivalent to the band gap. In contrast, in an electron beam pumped source there is no need for a p-n junction to drive electrons and holes. In this latter case, the light emitting device consists of a vacuum tube that contains an electron gun, which serves as cathode, and a cathodoluminescent element, which is the anode. The operating

mechanism is described in Figure 2.13(b) in two steps. First, electrons are accelerated from the cathode to the anode by an acceleration voltage (V_a), and they generate electron-hole pairs in the semiconductor material at the anode due to their collision with bonding electrons in the valence band. Then, the excited electrons will relax to their original state by radiative recombination, emitting a photon with energy equivalent to the band gap.

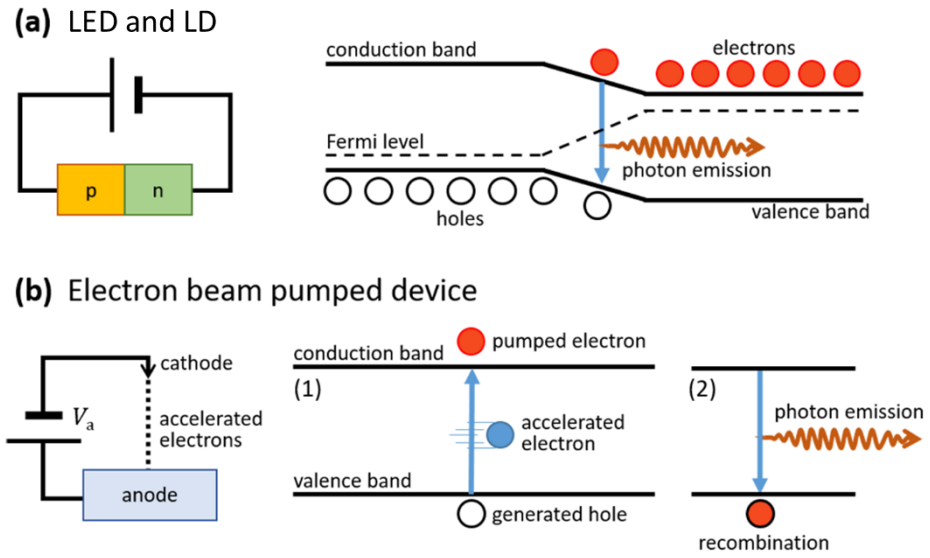

***Figure 2.13**. (a) Operating principle of LEDs and LDs. On the left side, polarization scheme. On the right side, band diagram. Under positive bias, electrons and holes are injected into the depletion region and recombine emitting photons. (b) Operating principle of an electron beam pumped source. On the left side, polarization scheme. On the right side, band diagram describing the process in two steps: (1) accelerated electrons injected from the cathode generate electron-hole pairs by impact-ionization, and (2) the electron-hole pairs recombine emitting photons.*

2.3.2 Efficiency

The performance of a light emitting device is characterized by its external quantum efficiency (EQE). The EQE is the ratio of the number of photons emitted by the device (N_{out}^{photon}) to the number of electrons injected into the device ($N_{in}^{carriers}$). The EQE can be decomposed in the product of three terms (see Figure 2.14):

(i) Carrier injection efficiency (η_{inj}): ratio of the number of carriers that reach the active media ($N_{active}^{carriers}$) to the number of electrons injected into the device ($N_{in}^{carriers}$).

(ii) Radiative recombination efficiency (η_{rad}): ratio of the number of photons generated by recombination (N_{active}^{photon}) to the number of carriers that reach the active media ($N_{active}^{carriers}$).

(iii) Light extraction efficiency (η_{ext}): ratio of the number of photons emitted by the device (N_{out}^{photon}) to the number of photons generated (N_{active}^{photon}). Indicates how many photons are able to come out of the structure.

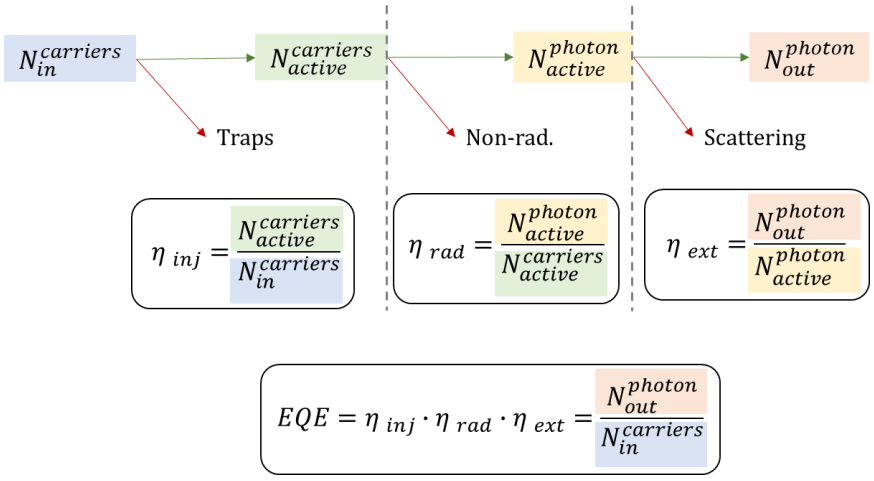

Figure 2.14. *Schematic to summarize the EQE calculation and its factorization.*

The product of the injection efficiency and the recombination efficiency is typically referred to as internal quantum efficiency (*IQE*). Another term that can describe the performance of a device is the wall-plug efficiency (*WPE*), also known as power efficiency or conversion efficiency, which is the ratio of the radiant flux (i.e. the total radiometric optical output power, P_{out}, measured in watts) to the electrical input power, i.e. the efficiency of converting electrical power into optical power:

$$WPE = \frac{P_{out}}{I \cdot V} \tag{2.17}$$

where I is the operating current and V is the operating voltage. In the case of LEDs and LDs, the *EQE* and the *WPE* can be related by the following equation [2,3]:

$$WPE = EQE \cdot \eta_{el} = EQE \frac{\hbar\omega}{e \cdot V} \tag{2.18}$$

where $\hbar\omega$ is the emitted photon energy, e the electron charge, and η_{el} the electrical efficiency, which is the ratio of the mean energy of the photons emitted and the total energy that an electron acquires from the power source. In the case of cathodoluminescent emitters, η_{el} is the ratio between the energy of the emitted photon and the energy required to create an electron-hole pair, which depends on the semiconductor band gap energy, E_G. Consequently, *WPE* is generally written as:

$$WPE = EQE \cdot \eta_{el} = EQE \frac{\hbar\omega}{\beta E_G} \tag{2.19}$$

where β is a material-dependent coefficient associated with the band structure.

This coefficient β is the ratio between the average energy required to create one electron-hole pair and the band gap energy, and is generally taken as $\beta \approx 3$ [86]. In other words, it takes approximately 3 times the band gap energy to generate an electron-hole pair. This sets an upper limit of 33% to the *WPE*. It has been shown that that $\beta \approx 3$ for direct-band-gap materials where the effective masses of electron and hole are approximately equal, but theoretical calculations predict lower values $\beta \approx 1.5\text{-}2$ in wide band gap materials with $m_h^* > m_e^*$ [87,88]. The value of β is relatively independent of the emission wavelength, so that the wavelength dependence of the *WPE* of electron beam pumped devices is given by the *EQE*.

2.3.3 Electron beam penetration depth

When exposing a semiconductor material to an electron beam, incident electrons lose energy when they penetrate the semiconductor due to scattering by interaction with valence and core electrons. The penetration depth of the electron beam (R_e) can be estimated using an empirical expression [86]:

$$R_e = \frac{4.28 \times 10^{-6}}{\rho} V_a^{1.75} \tag{2.20}$$

where ρ is the material density (in g/cm^3) and V_a is the acceleration voltage (in kV). This simple equation was improved by Everhart and Hoff [89], who developed more accurate calculations leading to the Monte Carlo simulations used nowadays. Figure 2.15 presents Monte Carlo simulations on the trajectory of the electrons injected in GaN ($\rho = 6.15$ g/cm^3) and AlN ($\rho = 3.23$ g/cm^3), for various values of V_a. For simplicity, we assume a focused electron beam impinging on the sample surface, although the shape of the beam has little effect on the penetration depth of the electrons.

The results in Figure 2.15 illustrate the effect of the material density and acceleration voltage. Higher density leads to an acceleration of the scattering events, so that the penetration depth of the electron beam decreases, following equation (2.20). On the other hand, increasing the acceleration voltage results in an enhancement of the penetration depth. Therefore, a key factor for maximizing the conversion energy is implementing an active region that overlaps with the expected electron trajectories at the required acceleration voltage. This is more challenging in the case of a laser structure, where the gain media is located in an optical cavity, and the ensemble should adapt to the electron penetration depth.

For a certain design of the multilayer stack that constitutes the semiconductor active region, there will be an optimum acceleration voltage for maximum carrier collection. At that voltage, the output power can be tuned by varying the electron beam current, which is almost independent

from the penetration depth. Therefore, a high-brightness electron source can deliver high excitation power density, even for laser architectures that require low acceleration voltages.

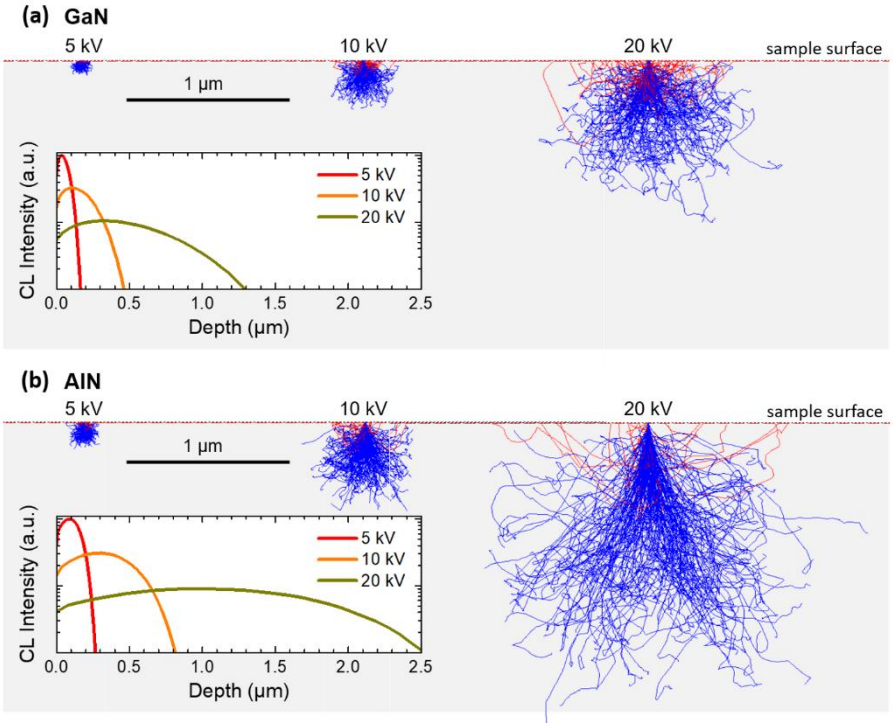

Figure 2.15. *Monte Carlo simulations of the electron trajectory in (a) GaN and (b) AlN for V_a = 5 kV, 10 kV and 20 kV. The trajectories of absorbed electrons appear in blue and those of backscattered electrons are depicted in red. The inset plots represent the electron energy loss, i.e. the distribution of the cathodoluminescence emission intensity, as a function of the penetration depth in both materials.*

2.4 Electron beam pumped semiconductor lasers

Electron beam pumped lasers are an interesting substitute for laser diodes in certain spectral windows, particularly in the UV range, with the capacity to deliver high power (up to ≈ 100 W) in both longitudinal and transversal laser configurations. The direct injection of carriers into the active medium completely obliterates the necessity of implementing contacts or inserting doped layers, which is appealing for materials with doping issues like III-nitrides or II-oxides. Furthermore, the carrier injection depth that can be controlled through the acceleration voltage, grants an additional degree of freedom for the design of the optical cavity. Efficiencies exceeding 20% have been demonstrated using bulk semiconductors with high acceleration voltages (20-50 kV). Progress in cathode research has allowed implementing compact high-current-density electron guns operating at relatively low acceleration voltage (1-10 kV), more adapted for the use of semiconductor anodes consisting of separate confinement heterostructures (particularly in the UV range) and the development of handheld devices.

In this section, we provide a brief review of the research on electron beam pumped semiconductor lasers.

2.4.1 Device geometry

Electron beam pumped semiconductor lasers can be fabricated in different configurations, with mainly two highlighted geometries: longitudinal and transversal [90,91]. In longitudinally pumped lasers, similar to vertical-cavity surface-emitting lasers (VCSEL), the laser emission propagates perpendicular to the semiconductor wafer. In general, the electron beam is parallel to the laser beam, as illustrated in Figure 2.16 (a), although it is also possible to pump at a certain angle. The semiconductor is usually pumped through one of the mirrors of the optical resonator. This geometry enables testing the sample on-wafer before manufacturing, and was originally considered for the fabrication of displays. However, the distribution of gain is strongly inhomogeneous along the axis of the optical cavity and the size of the gain region is limited by the penetration depth of the electron beam into the semiconductor.

In transverse lasers, also named edge-emitting lasers, light is emitted through the edge of the sample, almost parallel to the surface of the wafer. The electron beam impinges perpendicular to the wafer surface, as shown in Figure 2.16 (b). The cavity length is defined by cleaved or etched and chemically polished mirrors. In this case, the distribution of the electron beam over the irradiated surface can be homogeneous, if properly designed. Therefore, the distribution of the gain can also be homogeneous along the cavity axis, but it is inhomogeneous in the transverse direction. This geometry is more conventional today, presenting better efficiency and higher output power than the longitudinal configuration. In this thesis, the laser samples will be designed to operate in transverse configuration.

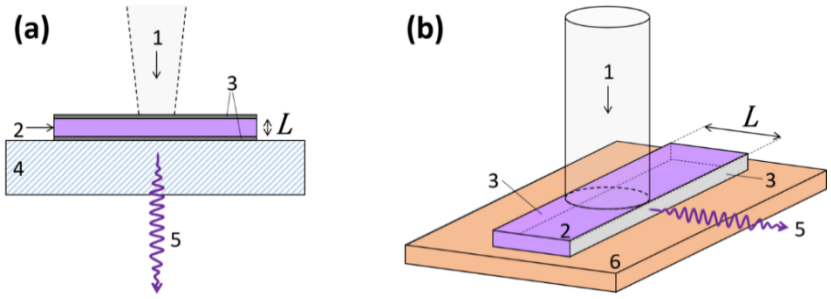

Figure 2.16. *Geometry of laser cavities: (a) Longitudinal and (b) transversal configuration. L represents the cavity length. 1– electron beam, 2– active media, 3– mirrors, 4– substrate (window), 5– laser beam, 6– substrate (heatsink).*

Heat management is a relevant issue to take into account in the fabrication of electron beam pumped laser devices. As a reminder from section 2.3.2, the average energy required to create an electron-hole pair in the semiconductor is roughly three times the band gap energy [86], and the remaining two-thirds of the injected power are converted into heat. To evacuate heat from the active region, it is particularly important to control the shape of the beam. For instance, in transverse lasers, a ribbon-shaped beam can increase the efficiency and reduce overheating due to electron loses.

2.4.2 Historical introduction and state of the art

The first stimulated emission from semiconductors under electron beam pumping was achieved at the Lebedev Physics Institute (USSR) in December 1963 by Nobel Laureate Nikolai G. Basov, using CdS single crystals cooled with liquid helium [92]. Basov already predicted [93]: "This type of excitation will evidently make it possible to create sources of coherent emission working in the far ultraviolet range." In May 1964, Benoit à la Guillaume and Debever at Ecole Normale Superieure (France) achieved laser action in InAs single crystals cooled at ≈ 20 K [94]. During the following years, these reports motivated efforts to demonstrate lasing in some of the most common III-V and II-VI semiconductors with electron beam excitation.

Still in 1964, Hurwitz and Keyes demonstrated the feasibility of the electron beam pumped GaAs laser in the infrared (842 nm) [95] at liquid helium temperature. A p-type GaAs crystal was cleaved to obtain two parallel facets, creating a 210 μm long cavity. Experiments were performed under a pulsed electron beam operated at 50 kV (penetration depth ≈ 5-10 μm), with a pulse duration of 0.2 μs and a repetition rate of 1 kHz. The excitation beam was focused into a spot with a diameter of ≈ 0.5 mm on the cleaved facet. Two years later, Hurwitz demonstrated red (685 nm) CdSe and green (491 nm) CdS lasers with efficiencies close to 30% [96], as well as ZnS lasers operating in the UV (329 nm) [97], all of them at liquid nitrogen temperature. The experiments were performed in cleaved crystals with optical cavity lengths in the range of 40-500 μm. The electron beam, with a diameter of 0.5 mm, was pulsed with a pulse duration of 100-200 ns and a repetition rate of 60 Hz. The emitted light was collected from the same direction of the excitation beam incidence. The laser threshold was found at 1.5 A/cm^2 for CdSe under 20 kV, and 400 mA/cm^2 for ZnS under 26 kV.

Following the research line of Hurwitz, in 1966, Nicoll et al. [98] reported lasing at liquid nitrogen temperature in ZnO emitting at 375 nm with an efficiency of 0.1%. The amplified stimulated emission was achieved at 15 kV with a threshold of ≈ 3 A/cm^2, under the excitation of an electron gun emitting 0.3 μs pulses with a repetition rate of 700 Hz. The spot size was 200 μm, equivalent to the cavity length that was formed by cleaving two parallel faces.

The above-mentioned experiments demonstrated lasing emission under electron beam pumping for different bulk semiconductor materials. This technology evolved rapidly in the Soviet Union, reaching the state of a commercial product in the form of sealed electron beam tubes [99], to be used in displays. Researchers demonstrated that the lasers could operate in cw mode, or emit picosecond pulses at a repetition frequency of tens of gigahertz. In pulsed regime, they could deliver peak output powers of tens of megawatts. The average output power could reach tens of Watts and the efficiency could reach ≈ 10%. A review of this research was published by O. V. Bogdankevich [100].

In the 80's, advances in epitaxial processes paved the way to new configurations for both II-VI and III-V compounds, including GaAs-based heterostructures [101–104] or ZnSe thin films and ZnSe/ZnSSe superlattices grown on GaAs [105,106]. To this point, electron beam pumped lasers were operating at high acceleration voltages (typically around 40 kV) and with very high current injection density (tens of A/cm^2). A reduction of threshold was obtained by replacing bulk or semi-bulk active regions with waveguided heterostructures incorporating quantum wells. The use of a graded-index separate confinement heterostructure (GRINSCH), where the active quantum wells are embedded in a waveguide with graded heterointerfaces, was a major step ahead towards efficient devices. Applying the concept to the ZnCdSe/ZnSe (emission at 478 and 505 nm) and CdTe/CMnTe (753 nm and 763 nm) material systems reduced the required acceleration voltage below 10 kV and the threshold current below 1 A/cm^2 [107,108]. Therefore, the pumping conditions became compatible with compact cold electron sources, such as microtip arrays [109].

In the last decades, researchers of the Moscow State Institute of Radio Engineering, Electronics and Automation (Russian Technological University) in collaboration with the Ioffe Institute in St. Petersburg developed a research program to demonstrate electron beam pumped green lasers using ZnSe-based separate confinement heterostructures in the transversal configuration [110–115]. Using a single CdSe quantum dot layer as emitting element (wavelength = 535 nm) embedded in a complex ZnMgSSe/ZnSSe/ZnSe waveguide, they reported a room-temperature lasing threshold as low as 0.4-0.5 A/cm^{-2} at an acceleration voltage of 8-9 kV [112]. However, the design was not optimized in terms of conversion efficiency, since the maximum efficiency was obtained for an acceleration voltage around 17-21 V, i.e. with the electron beam penetrating more than 1 μm into the semiconductor, which was well beyond the waveguide core (0.2 μm top cladding + 0.2 μm waveguide core) [113]. This misalignment resulted in important carrier injection losses. By enlarging the core of the waveguide to 0.65 μm and increasing the number of quantum dot layers to ten, the emission efficiency was boosted to 8.5% and they could demonstrate a peak output pulsed power of 12 W per facet at room temperature (pulse duration ≈ 50 ns, repetition rate ≈ 10 Hz) [113]. Extracting even more power at 535 nm was possible by

further enlarging the waveguide core (up to ≈ 2 μm) and by implementation of a multi-element laser array [114], as depicted in Figure 2.17. In this configuration, the maximum output pulsed power was 630 W (31 W per laser element) with an efficiency of 5% per facet, obtained for an acceleration voltage of 24 kV (pulse duration ≈ 0.5 μs). The concept was extended to "true green" devices (λ = 547 nm), attaining peak pulsed output power of 80-100 W (≈ 3 W per laser element) at room temperature, with an acceleration voltage of only 5.6 kV (pulse duration ≈ 1 μs, repetition rate ≈ 10 Hz) [115]. The sample architecture and the threshold dependence with the acceleration voltage are illustrated in Figure 2.18.

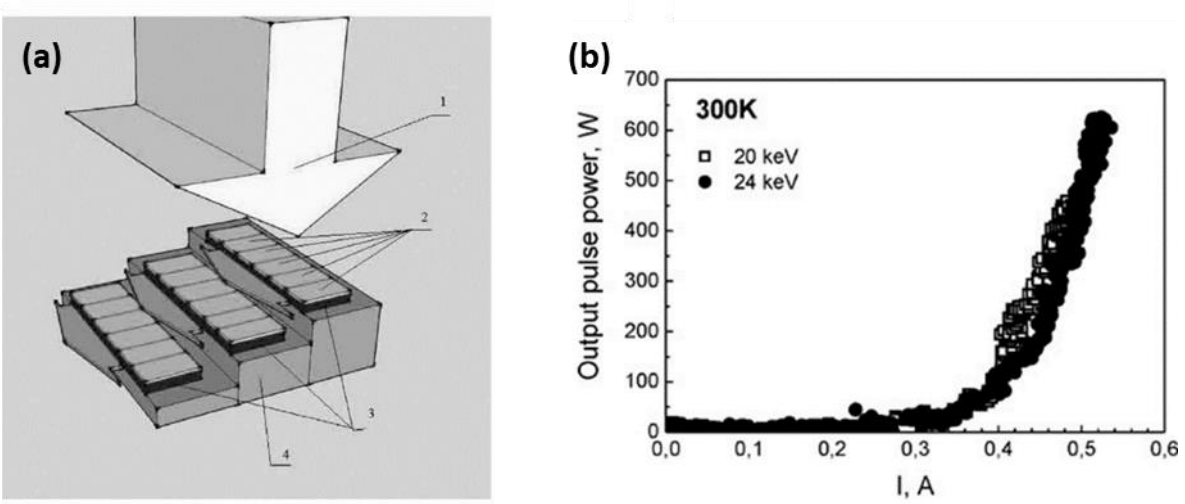

Figure 2.17. *(a) Sketch of the ZnSe-based laser array: 1–electron beam, 2–laser elements, 3–laser bars, 4–heat sink. (b) Dependence of the output pulse power on the electron beam current for different acceleration voltages: 20 kV (open squares) and 24 kV (circles). The data corresponds to a 26-element laser array. [Reproduced from reference [114]]*

On the other hand, another international consortium explored electron beam pumped ZnSe-based lasers in a longitudinal configuration [116,117], more adequate for laser projection applications. The study covered blue (λ = 462 nm, quantum well material = ZnSe) and green (λ = 530 nm, quantum well material = ZnCdSSe) lasers. The highest efficiency corresponds to devices with an active region consisting of a 10 λ (blue) or 20 λ (green) cavity containing 20 quantum wells, with both bottom and top distributed Bragg reflectors (DBRs) fabricated *ex-situ* by dielectric deposition [117]. The lower room temperature lasing thresholds were 60 A/cm^2 (blue) and 14 A/cm^2 (green) using an acceleration voltage of 42 kV. For the same acceleration voltage, the maximum output power was 3.3 W (laser efficiency = 5%) and 5.9 W (laser efficiency = 10.4%) for the blue and green devices, respectively.

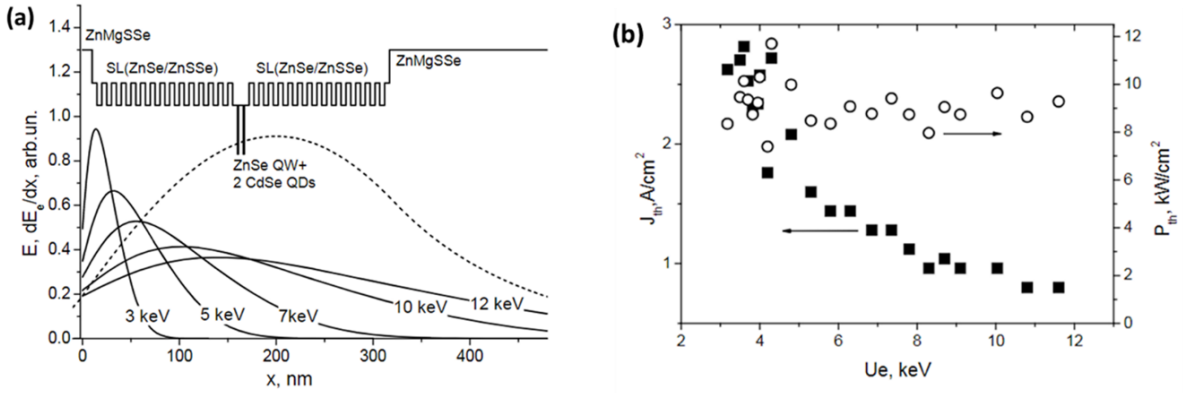

Figure 2.18. *Electron beam pumped laser based on a CdSe/ZnSe nanostructure with ZnMgSSe confinement layers: (a) Schematic energy band diagram and spatial distribution of the electron energy loss in ZnSe for electron acceleration voltages of 3, 5, 7, 10 and 12 kV. The dotted line represents the spatial distribution of the fundamental waveguide mode. (b) Dependence of the threshold current density (black squares) and threshold power density (open circles) on electron energy. [Reproduced from reference [115]]*

A selection of electron beam pumped laser reports has been summarized in Table 2.6.

Table 2.6. *Summary of operation parameters of electron beam pumped semiconductor lasers: operation wavelength (λ), temperature (T) and acceleration voltage (V_a), threshold current density (I_{th}) and threshold power density (P_{th}).*

	Material	λ (nm)	T (K)	V_a (kV)	I_{th} (A/cm²)	P_{th} (kW/cm²)	Ref.
II-VI	CdS	491	77	20 kV	1.5	30	[96]
		525	300	40 kV	4	160	[118]
	CdSe	685	77	20 kV	1.5	30	[96]
		690	100	35 kV	3	105	[119]
	ZnS	329	77	26 kV	0.4	10.4	[97]
		330	80	75 kV	70	5,250	[120]
	ZnO	375	77	15 kV	3	45	[98]
	ZnSe	450	100	40 kV	12	480	[119]
		450	15	20 kV	4	80	[105]
		493	300	15 kV	3	45	[110]
		462	300	37 kV	57	2,100	[117]
		547	300	11.5 kV	0.8	9	[115]
	ZnSe/ZnSSe	454	100	35 kV	2.5	87	[106]
		474	300	35 kV	12	420	[106]
	CdTe	763	90			2	[107]
	ZnCdSe/ZnSe	478	83			4-20	[108]
		484	300	40 kV	50	2,000	[121]
		490	80	40 kV	10	400	[122]
		490	300	40 kV	50	2,000	[122]
	ZnCdSSe	530	300	37 kV	37	1,370	[117]
	ZnSe/CdSe	494	300	15-18 kV	0.7	9-14	[111]
	CdSe/ZnSe	535	300	8-9 kV	0.4-0.5	3-5	[112]
	Cd(Zn)Se/ZnMgSSe	542	300			10.4	[113]
	ZnCdSe/ZnSSe	542	300	40 kV	8	320	[116]
III-V	GaAs	841	4			50	[95]
		821	20	33 kV	1.75	58	[123]
		825	90			1	[107]
	GaInP/AlGaInP	643	300	40 kV	10	400	[124]
	InGaN/GaN	402	100	35 kV	60	2,100	[125]
		409	300	150 kV	250	37,500	[125]
	AlGaN/InGaN/GaN	430	300			144	[126]
		385	77	18 kV	5	90	[127]
	GaN/AlGaN	353	107			230	[51]

2.4.3 III-nitride electron beam pumped lasers

In 1997, the first nitride-based electron-beam pumped laser was demonstrated by Kozlovsky et al. [125] using a 30-period InGaN/GaN MQW embedded in an AlGaN/GaN waveguide, which was pumped in the transversal configuration and displayed laser emission at 409 nm. Cavities with a length around 0.15 mm were defined by cleaving and operated at a high pumping power of 2 MW/cm^2 at 80K and more than 37 MW/cm^2 at 300 K (quasi-cw excitation with an acceleration voltage of 35 kV). More recently, new heterostructures designed specifically for electron beam pumping (5-period InGaN/GaN MQW in an $Al_{0.2}Ga_{0.8}N/Al_{0.1}Ga_{0.9}N$ waveguide, mechanically cleaved 0.5-1.2 mm long cavities, transversal configuration) have been able to reduce the threshold for lasing (λ = 429 nm) down to 100 kW/cm^2 at room temperature [126]. They used an acceleration voltage of 9 kV, with a pulse duration of 300 ns and a repetition rate of 1.5 Hz.

Below 370 nm, AlGaN must replace GaN in the contact layers of laser diodes, hence current injection becomes a major problem. AlGaN p-type doping is particularly challenging [128,129], and the high Mg density required to achieve p-type conductivity degrade the material quality and can result in absorption losses. Also the activation energies of n-type dopants (Si, Ge) increase with the Al mole fraction [130–132], solubility issues have been raised [133], and some theoretical calculations predict a DX transition at high Al concentrations [134]. Therefore, the use of electron beam pumping appears as an interesting alternative for the implementation of AlGaN-based UV lasers.

The first demonstration of a III-nitride based laser working under electron beam pumping in the UV range was reported by Hayashi et al. in 2017 (see Figure 2.19) [51]. It was the first In-free GaN/AlGaN electron beam pumped laser: the active region consisted of a 10-period $GaN/Al_{0.07}Ga_{0.93}N$ MQW in an $Al_{0.15}Ga_{0.85}N/Al_{0.07}Ga_{0.93}N$ waveguide. The cavity was a 50 µm square mesa defined by a combination of dry and wet etching. The device displayed laser emission at 353 nm at 107 K under a pump power of 230 kW/cm^2 (acceleration voltage = 15 kV, pulse duration = 20 ns, repetition rate = 3 MHz), about 4 times larger power density than the optical pumping threshold (55 kW/cm^2 using a pulsed Nd-YAG laser).

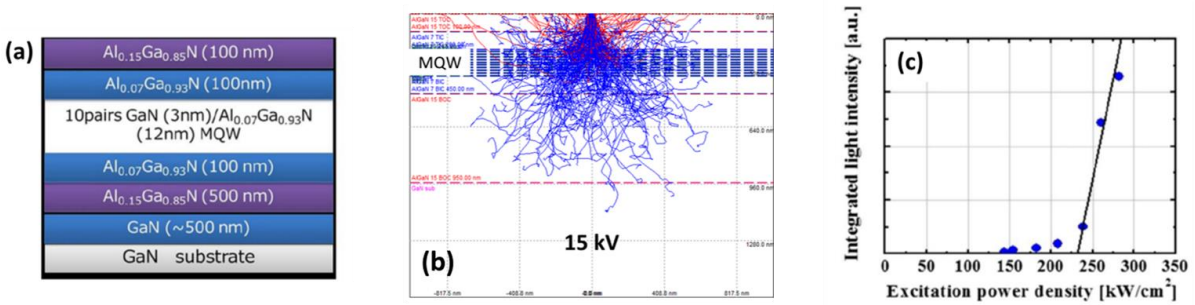

Figure 2.19. *(a) Schematic view of the sample structure. (b) Trajectory of the electron beam for an acceleration voltage of 15 kV (Monte Carlo simulations). (c) Integrated light intensity of the emission spectra as a function of the excitation power density. (taken from the work of Hayashi et al. [51])*

The same year, Wunderer et al. [127] reported an electron beam pumped UV laser consisting of an active InGaN MQW embedded in a GaN/AlGaN waveguide, with dry-etched ridge and mirror facets. Their measurements were performed at 77 K under pulsed excitation (pulse duration = 5 µs, repetition rate = 1 kHz). Lasing was demonstrated in the 375 nm to 385 nm range for resonator cavities with a length of 50 to 600 µm (see Figure 2.20). Their lowest threshold was at 174 µA with an acceleration voltage of 18 kV, which would correspond to a power density threshold around 160 kW/cm² for a 50-µm-diameter beam spot.

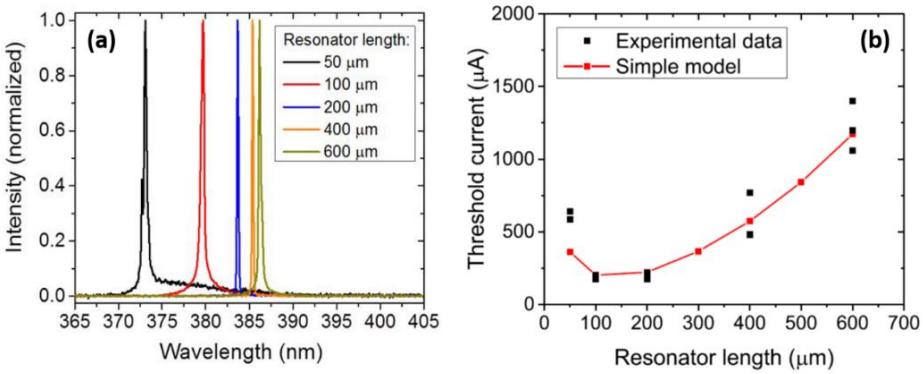

Figure 2.20. *(a) Shift of the laser emission wavelength for different cavity lengths. (b) Variation of the threshold current as a function of the resonator length. (taken from the work of Wunderer et al. [127])*

There are also designs of III-nitride electron beam pumped lasers in the longitudinal configuration [135,136]. Chen et al. [136] proposed a structure based on an AlGaN λ-cavity on an epitaxially-grown AlN/$Al_{0.47}Ga_{0.53}N$ DBR and completed *ex situ* with a dielectric DBR. However, such a device has not been experimentally demonstrated so far.

The feasibility of pumping III-nitrides with electrons has been proved in the above mentioned reports. However, there are still important issues to address. At the moment of writing this thesis and to the best of my knowledge, no demonstration of room temperature operation for AlGaN-based electron beam pumped UV laser has been reported. In this work, we try to make some progress in the research of e-beam pumped AlGaN based UV lasers, towards the achievement of room temperature operation and high efficiency device.

Chapter 3
Experimental methods

This chapter introduces the experimental methods that were used during my PhD thesis. First, it presents a general description of epitaxial growth by plasma assisted molecular beam epitaxy, to later focus on the materials of this work, namely GaN, AlN and AlGaN. The second part of the chapter describes the characterization techniques, including both structural and optical characterization. The last two sections contain a brief overlook to the simulation tools and cleanroom techniques or equipment for device fabrication.

3.1 Epitaxial growth

The concept of "*epitaxy*" is defined as the deposition of a material on a crystalline substrate, where the crystallographic arrangement of the deposited material (called epitaxial film/layer) is aligned with that of the substrate. Its etymological meaning comes from Greek, and it can be translated as "arranged upon". When the deposited material is the same as the substrate, the process is called *homoepitaxy*. Otherwise, the process is called *heteroepitaxy*.

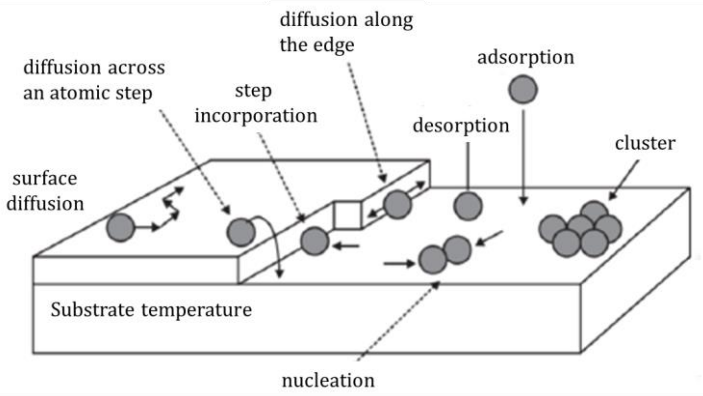

Figure 3.1. *Atomistic processes occurring on the surface during epitaxial growth.*

The growth progression depends on the properties of the materials but also on the adatom kinetics [137–139], affected mainly by the substrate temperature. The various atomistic processes that can take place at the growing surface are described in Figure 3.1, namely adsorption, diffusion, nucleation, step incorporation and desorption. The growth modes resulting from these processes are the following:

- *Multi-layer growth*: When the adatom diffusion length is short, it results in the nucleation of multi-layered clusters, ultimately forming a rough surface.

- *Layer-by-layer growth*: When the adatom diffusion length is longer, the increased diffusion length results in the nucleation of monolayer (ML) clusters, with atomic layers completed one by one.
- *Step-flow growth*: When the diffusion length is even longer, the adatoms have enough mobility to reach the step edges, which are often energetically favorable incorporation sites, and grow monolayers in a staggered way.

In the case of heteroepitaxy, the atomistic processes still hold. However, the epitaxy is also largely influenced by the lattice mismatch between the two materials, surface free energy and dislocation formation energy. This results in three possible growth modes [140,141], illustrated in Figure 3.2:

- *Franck van der Merve* (*FM*) *growth mode*: Adatoms attach preferentially to the surface sites due to comparable lattice constants (low lattice misfit), resulting in an atomically smooth surface. It is a 2D or planar growth mode. Misfit dislocations might appear to release strain above a certain critical thickness.
- *Volmer-Weber* (*VM*) *growth mode*: Adatom-adatom interactions are stronger than adatom-surface interactions due to a huge lattice misfit, resulting in three-dimensional clusters. It is a 3D growth, also called island growth mode.
- *Stranski-Krastanov* (*SK*) *growth mode*: A mediate lattice misfit starts with a strained layer-by-layer growth until the height is higher than the critical thickness resulting in relaxation of the layer and generating three-dimensional islands. It is a combination of 2D and 3D growth, also called layer plus island growth mode. Continuation of the growth leads to the formation of misfit dislocations (*MD*).

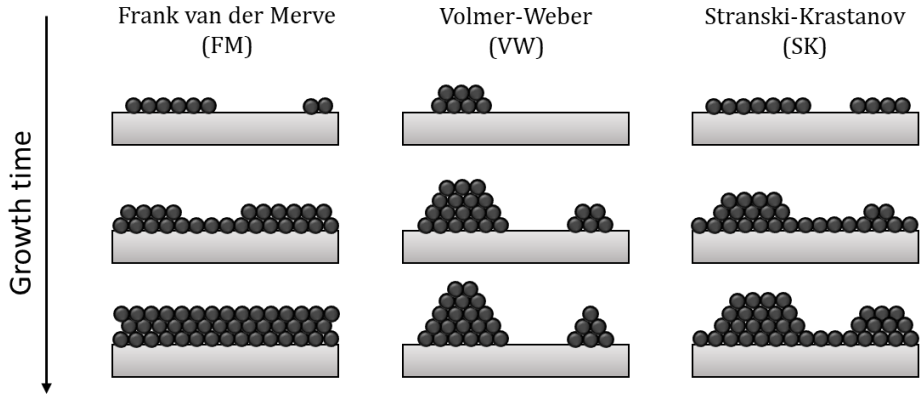

Figure 3.2. *Schematic of heteroepixaxial growth mode.*

Epitaxial growth can be performed by various techniques [142], including metalorganic vapor phase epitaxy (MOVPE), liquid phase epitaxy (LPE), hydride vapor phase epitaxy (HVPE), and molecular beam epitaxy (MBE). The latest is the method used in this work, due to its many benefits. The growth by MBE is carried out at low temperature (compared with other techniques

such as MOVPE) and under a relatively low growth rate (generally, less than 1 ML/s), resulting in an excellent control over the layer thickness and great surface and interface morphology. Furthermore, the growth in MBE is performed under an ultra-high vacuum (UHV) environment, which offers the possibility to follow-up the growth process in-situ real-time with techniques like reflection high-energy electron diffraction (RHEED).

3.1.1 Plasma-assisted molecular beam epitaxy

Molecular beam epitaxy was invented in the late 1960s at the Bell Telephone Laboratories by A. Y. Cho and J. R. Arthur [143]. The technique consist in the thermal evaporation or sublimation of the desired materials, providing an atomic or molecular beam that impinges on the substrate. It requires UHV ($P \leq 10^{-9}$ Torr as base vacuum, $P \leq 10^{-5}$ Torr during growth) to ensure that the mean free path of the precursor molecules is much longer than the distance between the substrate and the source cells, and to prevent contamination from external elements.

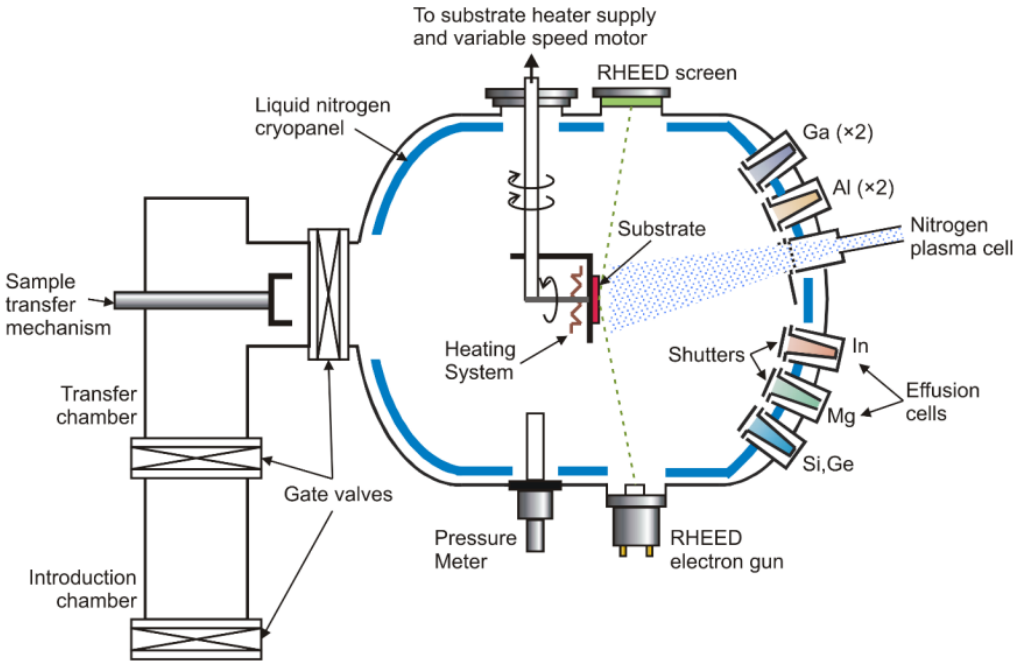

Figure 3.3. *Schematic of the PAMBE used in this work (taken from [144]).*

Figure 3.3 presents the schematic of the MBE used in this work. The system consists of three chambers separated by gate valves: introduction chamber, transfer chamber and growth chamber. Samples are loaded into the system through the introduction chamber at atmospheric pressure and under nitrogen flux, to be then evacuated down to 10^{-8} Torr. After that, the samples are transferred to the transfer chamber, which is constantly kept at 10^{-9} Torr by an ionic pump. This chamber works as a buffer between the introduction chamber, which is often exposed to atmospheric conditions, and the growth chamber that requires always UHV conditions. In particular, the growth chamber is evacuated down to 10^{-11} Torr by a cryogenic pump combined

with a cryogenic cooling system with liquid nitrogen flowing through the chamber walls. During the growth, the pressure of the chamber rises to 5-8 × 10^{-6} Torr due to the nitrogen flux. The samples transferred into the growth chamber are mounted onto a 4-axis manipulator and adjusted to the growth position. The substrate holder allows heating the sample at the desired temperature, and rotate in-plane, which is useful to obtain homogeneous deposition. To be compatible with the manipulator, the substrates are previously glued on a molybdenum sample holder (molyblock) with molten indium.

For the growth of III-nitrides, the metallic III elements (In, Ga, and Al) and doping elements (Si, Ge, Mg) are obtained from high-purity solid metals loaded in effusion cells, which consist of a crucible surrounded by heating coils, as depicted in Figure 3.4. By raising up the temperature of the effusion cells, the precursors are evaporated generating the molecular flux. Thus, the flux can be tuned by modifying the cell temperature. An accurate regulation of the cells temperatures is achieved through proportional-integral-derivative (PID) controllers. A mechanical shutter in front of each effusion cell is used to start or interrupt the beam flux at will.

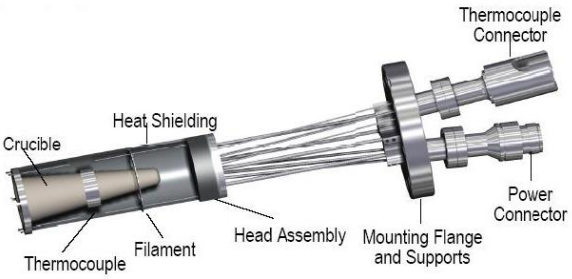

Figure 3.4. *Schematic of an effusion cell (taken from [144]).*

In contrast, the nitrogen molecule (N_2) cannot be thermally dissociated into mono-atomic nitrogen (N). There are two possibilities to obtain active N atoms: from an NH_3 source, in which the bond of nitrogen is weaker than that in N_2, or by using a radio-frequency plasma cell. In our case, we use the second approach, where active nitrogen is obtained by cracking high-purity molecular nitrogen (6N5) with a radio-frequency source. This technique is known as *plasma-assisted MBE* (PAMBE). Our MBE is equipped with an automatic N plasma source HD25 supplied by Oxford Applied Research, illustrated in Figure 3.5. The plasma is monitored through an optical detector, and the flux of active nitrogen is controlled by tuning the radio-frequency power.

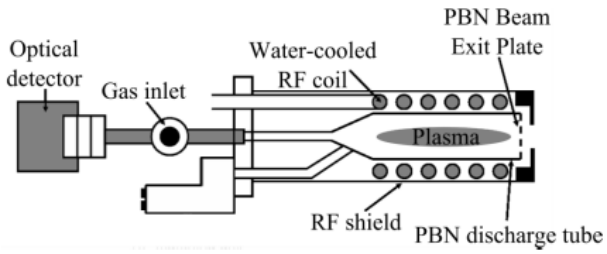

Figure 3.5. *Schematic of the nitrogen plasma cell (taken from [144]).*

3.1.2 Reflection high energy electron diffraction

The UHV environment during the growth in PAMBE makes it possible to monitor the morphology and crystal structure of the growing surface in-situ and real-time by reflection high energy electron diffraction. RHEED is a characterization technique where electrons are emitted from a hot filament and accelerated under high-voltage (in our case, current = 1.5 A and acceleration voltage = 32 kV). The electron beam strikes the sample at a small grazing angle, and the diffracted beam impinges on a fluorescent phosphor screen mounted on the opposite side. A schematic description of the RHEED measurement principle is shown in Figure 3.6. The image displayed on the screen is the Fourier transform of the lattice interacting with the beam. It corresponds to the intersection of the reciprocal lattice rods with the Ewald sphere of radius $k_i = \frac{2\pi}{\lambda}$ where λ is the wavelength of the electron (λ = 0.124 Å).

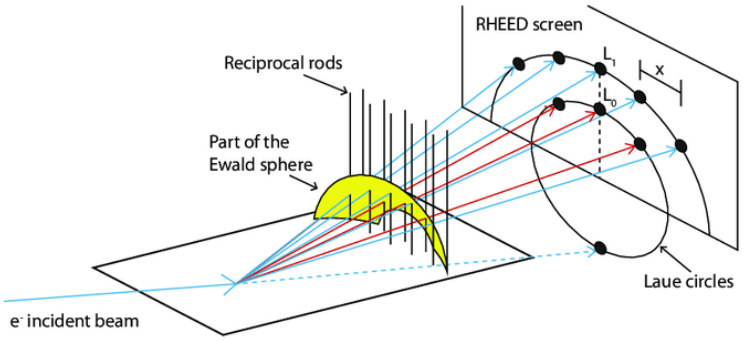

Figure 3.6. *Schematic description of the RHEED principle.*

Observing the pattern, the 2D or 3D nature of the surface morphology and a qualitative estimation of the crystal quality can be obtained. A summary with different cases are described in Figure 3.7. In an ideal atomically smooth and single crystalline surface, the crystal lattice would correspond to perpendicular rods. This would lead to a RHEED pattern consisting of infinitesimal spots aligned on a radial arc. However, due to instrumental divergence and non-idealities of the surface, the thickness of the Ewald sphere is not zero and a streaky pattern is observed [145]. In the case of a polycrystal, the Ewald sphere is intersected everywhere, leading to a ring-shaped pattern, sign of grains with different orientations. In the case of rough surfaces, the beam is diffracted by the vertical planes leading to a spotty pattern. Finally, in the presence of islands (i.e. nanowires or quantum dots), additional lines appear due to the diffraction on the island facets. One can reduce the explanation to a simplistic statement: 2D surfaces will present streaky patterns, while any 3D geometry will lead to spotty patterns.

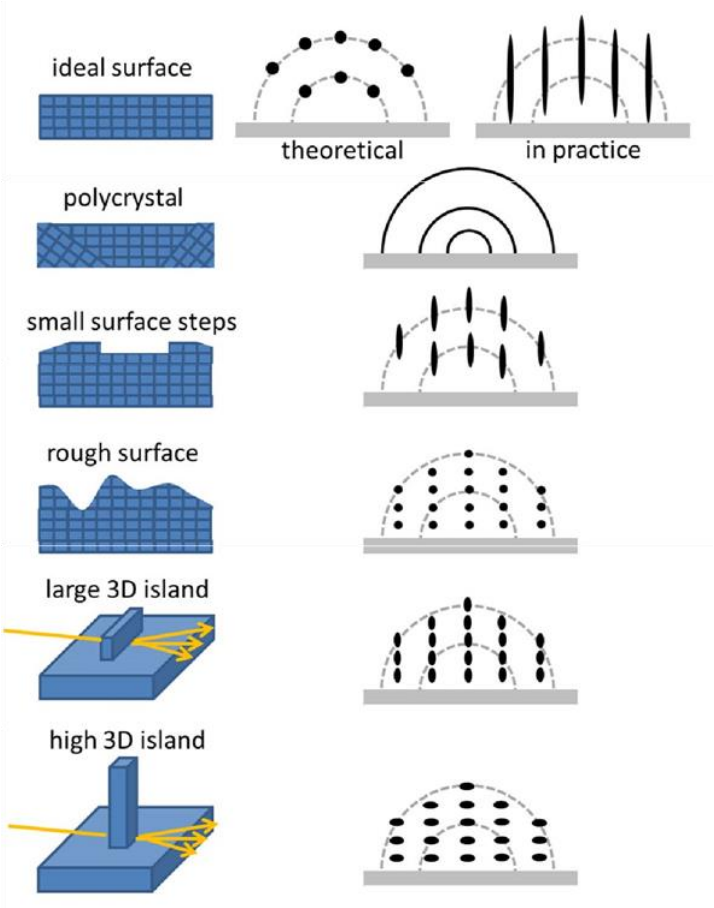

Figure 3.7. *Schematic of RHEED patterns for different surface morphologies (taken from [146]).*

The RHEED intensity can also provide information about the growth rate under layer-by-layer growth conditions [147,148]. The time-dependent variation in the density of atoms at the growth front results in an oscillatory variation of the RHEED intensity. We define the coverage of atoms on the surface as θ, being minimum (θ = 0) when n^{th} layer is complete and being maximum (θ = 1) when the $n+1^{th}$ layer is complete, leading again to a smooth surface. Figure 3.8 illustrates such variation, starting at minimum coverage θ = 0. For intermediate coverage (θ = 0.5), the roughness is maximum and the intensity decreases to lowest. At θ = 0.75, the intensity recovers as the space between the nucleating sites gets covered. The surface flattens again at θ = 1, recovering the maximum RHEED intensity and the process repeats cyclically as the growth continues. A single RHEED oscillation corresponds to the growth of a monolayer. During the operation of the PAMBE, the calibration of the growth rate and the control of the 2D surface morphology are performed by studying the described RHEED features.

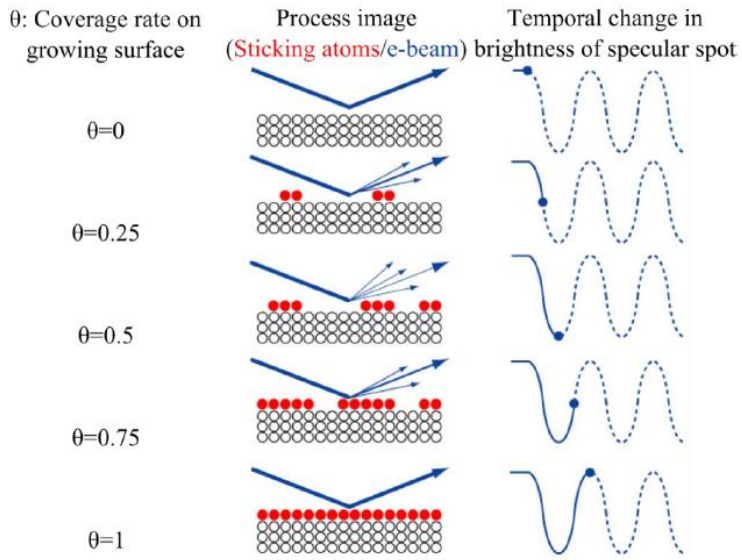

Figure 3.8. *Schematic description of the RHEED intensity behavior as a function of the surface coverage (taken from [144]).*

3.1.3 Growth of GaN (0001)

The synthesis of high-quality III-N planar structures is extremely important for the development of high-performance optoelectronic devices based on these materials. Thus, it is crucial to understand the mechanisms involved. The growth of 2D polar GaN structures by PAMBE has been intensively investigated [149–151]. The model that better explains what processes can undergo a Ga atom in a PAMBE during the growth, leading to the formation of a GaN layer [152], is described in Figure 3.9. The impinging N atoms adhere to the growing surface in which we call adsorption. The impinging Ga atoms are also adsorbed, but there are two possible states. In the first one, the Ga adatom can fall into a weakly bound physisorbed state, where the electronic structure of the adatom is barely changed and it can be easily thermally desorbed from the surface. In the second case, the adatom can be transferred to a chemisorbed state through the formation of new chemical bounds with the surface. These two states are reversible: one physisorbed adatom can be transferred to chemisorbed state and vice versa. However, it is in the chemisorbed state when a Ga atom can meet an N atom and form a GaN layer.

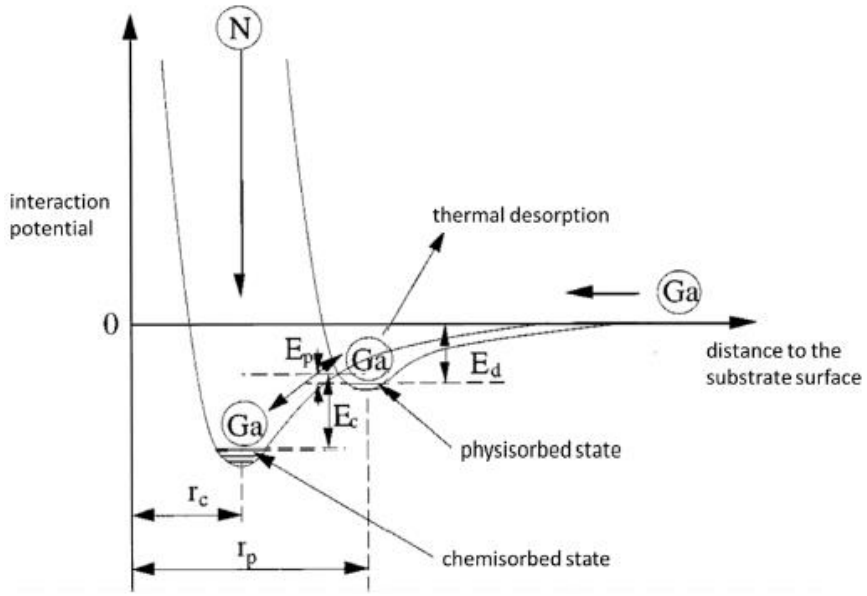

Figure 3.9. *Schematic representation of the process during the formation of a GaN layer (taken from [153]).*

The growth kinetics are determined by the metal-to-nitrogen flux ratio (III/V ratio) and the substrate temperature. The GaN deposition under N-rich conditions occurs in a SK growth mode, with a RHEED pattern that becomes spotty after a few nanometers due to the roughening of the growth front. On the other hand, an excessive Ga-rich condition would lead to the formation of metal droplets on the surface that degrades the surface morphology. Therefore, to obtain smooth 2D GaN layers, it is necessary to work under slightly Ga-rich conditions [154]. In particular, we use a Ga bilayer regime, with the Ga distribution illustrated in Figure 3.10. The first layer of adsorbed Ga is in a physisorbed state, aligned with the underlying substrate while the second one is liquid. This bilayer minimizes the (0001) surface energy and postpones the elastic relaxation of the layers, hence obtaining a smooth GaN growth front [151,155].

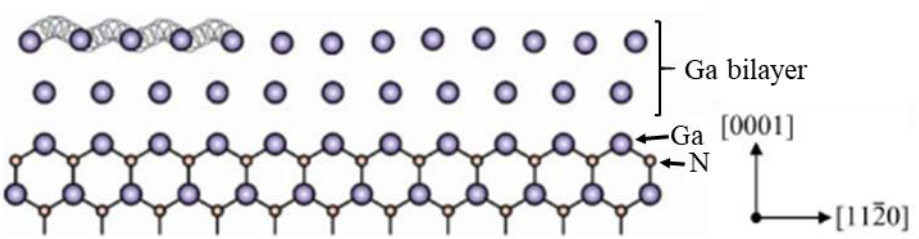

Figure 3.10. *Schematic representation of the Ga bilayer model (modified from [156]).*

For a certain Ga flux, the amount of Ga adsorbed on the epilayer surface can be quantified by analyzing the Ga desorption transients using RHEED [149]. For this measurement, the GaN surface is firstly exposed for a few seconds to a Ga flux and N flux simultaneously to grow GaN. Then, both fluxes are interrupted and the RHEED intensity is recorded during the Ga desorption from the synthesized GaN surface. The experiment is repeated at a constant substrate temperature (T_S) and

fixed N flux, while changing the Ga flux. After processing the data, four different regimes can be distinguished, as presented in Figure 3.11 for T_S = 720 °C:

- *Regime A*: For Ga flux Φ_{Ga} < 0.3 ML/s, the Ga coverage on the surface is negligible, N-rich conditions.
- *Regime B*: For 0.3 ML/s < Φ_{Ga} < 0.35 ML/s, there is less than 1ML of Ga on the surface.
- *Regime C*: For 0.35 ML/s < Φ_{Ga} < 0.475 ML/s, there is a bilayer of Ga (≈ 2.4 ML) on the surface.
- *Regime D*: For Φ_{Ga} > 0.475 ML/s, the system reach the Ga accumulation regime, leading to the formation of metal droplets on the surface.

The atomic force microscopy images confirm that the optimum growth conditions for obtaining a smooth surface is the Ga bilayer regime, corresponding to regime C.

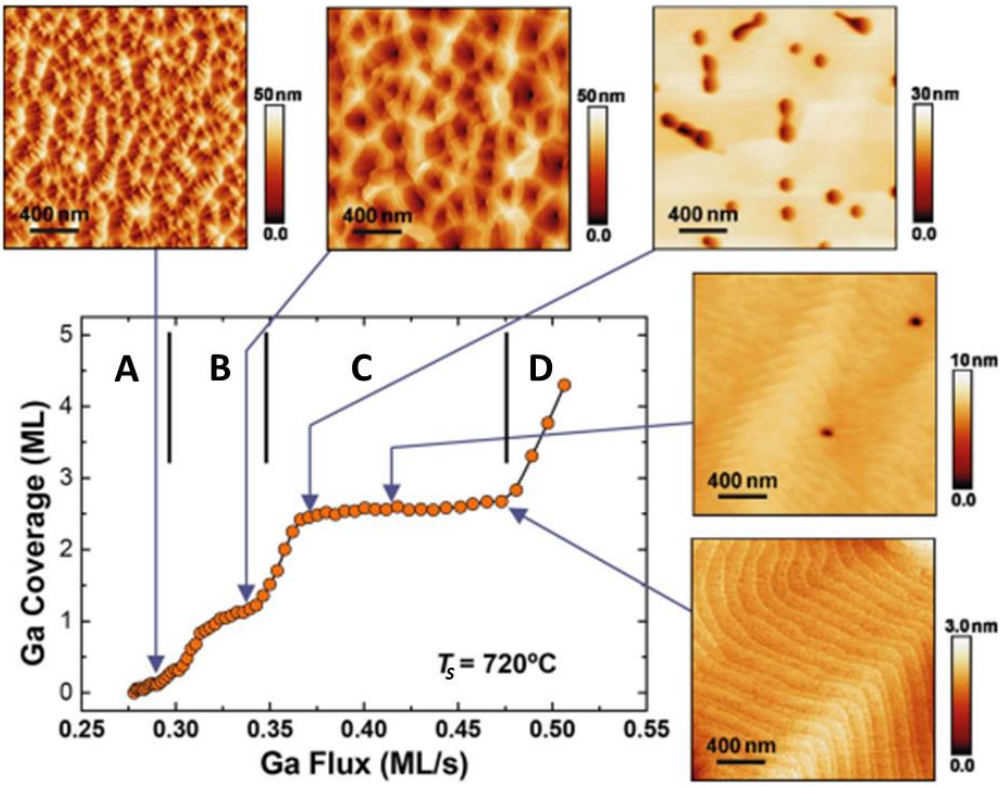

Figure 3.11. *Ga coverage on top of GaN (0001) surface as a function of the Ga flux, with four distinguished regimes: (A) N-rich conditions; (B) Ga excess ≤ 1 ML; (C) Ga bilayer; (D) accumulation of Ga droplets. Atomic force microscopy images show the resulting surface morphology for each regime. (modified from [157]).*

The above-mentioned experiment was performed at a fixed temperature, but varying the substrate temperature might affect the Ga desorption characteristics, thus changing the four regimes boundaries. Figure 3.12 illustrates the dependence of the Ga flux with the substrate temperature for a Ga-polar GaN epilayer. To conserve a certain amount of Ga on the surface, the Ga flux must be increased as the substrate temperature is raised.

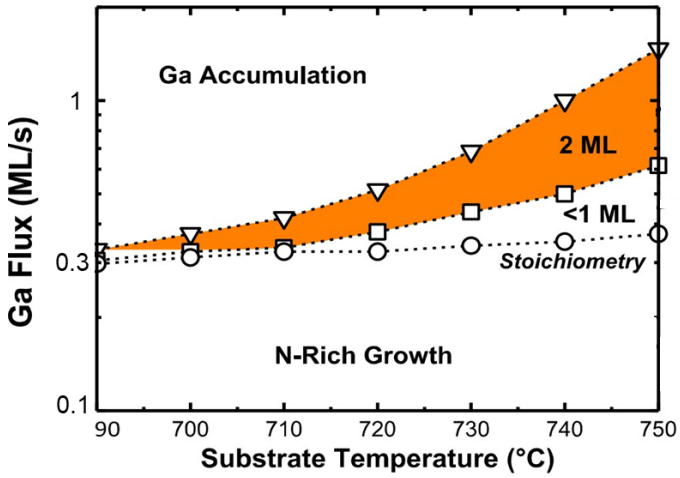

Figure 3.12. *Ga coverage regimes as a function of both the impinging Ga flux and the substrate temperature (taken from [158]).*

3.1.4 Growth of AlN (0001)

The 2D growth of smooth c-plane AlN layers also requires metal rich conditions, as in the case of 2D GaN. The excess of Al on top of the epilayer can be noticed by two shadow lines in the RHEED pattern along the <11-20> azimuth, as shown in Figure 3.13. These extra lines in the pattern are the evidence of metal Al, which has a smaller lattice constant than AlN. This Al excess cannot be desorbed at the standard growth temperatures for GaN (T_S ~700 °C). Therefore, to eliminate the accumulation of Al, a growth interruption under N is required to capture the excess of Al forming AlN on the surface. The time to consume all the Al excess can be monitored from the RHEED pattern, being all the Al consumed when the shadow lines disappear. The computed time can be used to calculate the Al cell temperature that provides Al:N stoichiometric growth conditions (III/V ratio = 1).

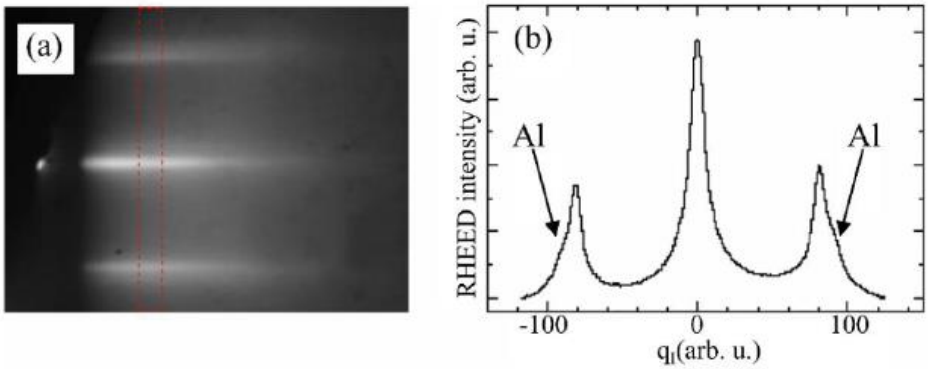

Figure 3.13. *(a) RHEED image of an Al-rich AlN surface (azimuth <11-20>). (b) Intensity profile along the a-direction of the region marked in (a). The arrows indicate the shadow streaks due to Al excess.*

3.1.5 Growth of AlGaN (0001)

Similar to their binary compounds, the growth of 2D AlGaN requires metal-rich conditions [159,160]. In the case of a ternary alloy such as AlGaN, some additional difficulties are triggered by the different Ga – N and Al – N binding energies, resulting in different mobility of Al and Ga adatoms on the growing surface. The Ga – N bond is much weaker than the Al – N bond [161], which results in a preferential Al incorporation in the AlGaN alloy in the presence of Ga. At the standard growth temperatures of AlGaN (T_S ~ 650-700 °C), the incorporation probability of Al is equal to 1. Figure 3.14 presents the incorporation probability of Al and Ga as a function of the group-III flux (the sum of Ga and Al fluxes) under constant N flux. Three regimes can be distinguished: *(i)* under N-rich conditions, the incorporation probability of Ga is constant due to the excess of N, but always lower than Al; *(ii)* in group-III rich regime, the formation of a Ga bilayer on the surface is observed, leading to optimum growth conditions; *(iii)* when the group-III flux is excessive, the Ga droplet accumulation regime is reached. Note that the Ga incorporation probability is reduced as the III/N ratio becomes larger, since the incorporation of Ga depends on the active nitrogen not consumed by the Al.

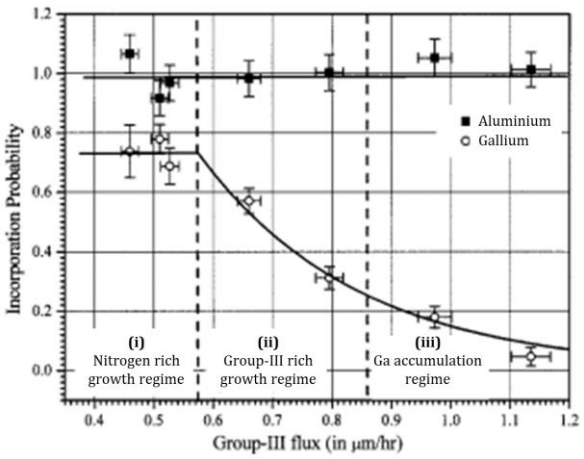

Figure 3.14. *Incorporation probabilities of Al and Ga atoms as a function of the group-III flux for AlGaN films grown at 750 °C. (modified from [159]).*

This feature must be taken into account when growing AlGaN. Thus, the Al/N flux ratio is fixed to match the required Al content, and the Ga flux is used in excess to obtain a self-surfactant effect that favors 2D growth. However, for contents of Al > 40%, the substrate temperature must be reduced to maintain a 2D growth in order to balance the diffusion between Al, Ga and N.

3.1.6 Substrates

In this work, we used two different kinds of substrates: sapphire-based templates and bulk substrates. The former were used for calibration and characterization purposes. For the

fabrication of laser structures, bulk substrates were chosen in order to minimize the density of structural defects. GaN substrates were used for samples designed to emit in the UV-A with low Al concentration, thus lattice parameter closer to GaN than AlN. AFM images from the GaN substrates used in this work are depicted in Figure 3.15. For samples emitting in the UV-C, with high Al molar fraction, AlN substrates were chosen.

(i) **Sapphire-based templates:** Sapphire (Al_2O_3) is widely used as foreign substrate for GaN and AlN, in spite of their lattice mismatch (30% with GaN). However, GaN(0001) is grown on c- sapphire with an in-plane rotation of 30°, reducing the lattice mismatch to 13.9%.

The GaN-on-sapphire templates used in this thesis were provided by LUMILOG, and they consist of 4-µm-thick GaN(0001) on c-sapphire deposited by MOVPE. The dislocation density is $\approx 10^8$ cm^{-2} and the top epilayer presents a smooth surface with root mean square (RMS) roughness around 0.66 nm. The templates were non-intentionally doped, and they presented n-type conduction, with carrier density around 10^{17} cm^{-3}.

The AlN-on-sapphire substrates used in this thesis were provided by DOWA, consisting of 1.0 ± 0.1 µm-thick AlN(0001) on c-sapphire deposited by MOVPE. The dislocation density is $\approx 10^9$ cm^{-2} and the top epilayer presents a smooth surface with RMS roughness around 0.42 nm.

(ii) **Free-standing bulk substrates:** GaN substrates are obtained from GaN boules grown by HVPE on sapphire substrates. The free-standing GaN substrates used in this work were provided by NANOWIN, with a dislocation density lower than 10^6 cm^{-2} and RMS roughness around 0.18 nm. They were n-type doped, to reach a carrier concentration around 5×10^{17} cm^{-3}.

In the case of AlN, the fabrication of high-quality free-standing substrates has progressed a lot recently in spite of being still under development [33,162]. The AlN substrates used in this work were provided by HEXATECH. They are obtained from AlN boules grown by physical vapor transport (PVT), using previously grown AlN seeds. They present a dislocation density of 10^3 cm^{-2} and RMS roughness around 0.1 nm.

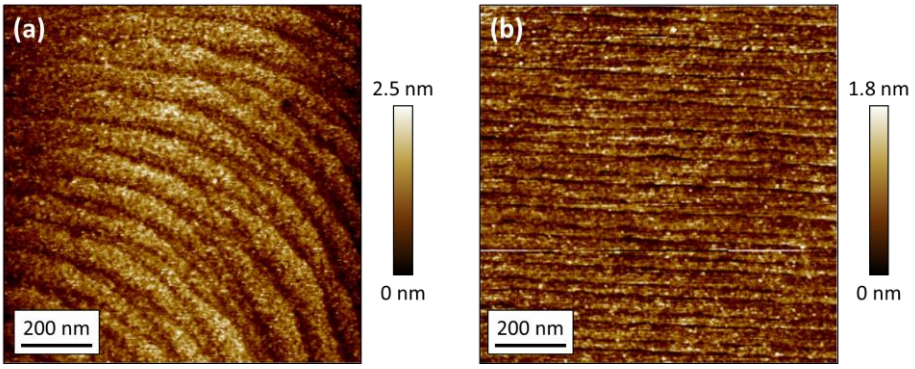

Figure 3.15. *AFM images of (a) GaN-on-sapphire template and (b) GaN free-standing substrates.*

3.2 Characterization techniques

This section introduces the characterization techniques used during this work. The techniques used for structural characterization are X-ray diffraction (XRD), scanning electron microscopy (SEM), transmission electron microscopy (TEM) and atomic force microscopy (AFM). For optical characterization, I describe here photoluminescence (PL) and cathodoluminescence (CL). During my PhD, I have used all these techniques by myself, except for the TEM.

3.2.1 X-ray diffraction

X-ray diffraction (XRD) is a versatile characterization technique which provides structural information about crystalline structures. In this work, it was used to determine the period of our superlattices, to estimate the strain state of the multilayer stack and to assess the alloy composition and the crystalline quality of our samples. We performed θ-2θ scans, ω-scans and reciprocal space maps (RSMs). For theoretical calculations we used GlobalFit2 from Rigaku Co.

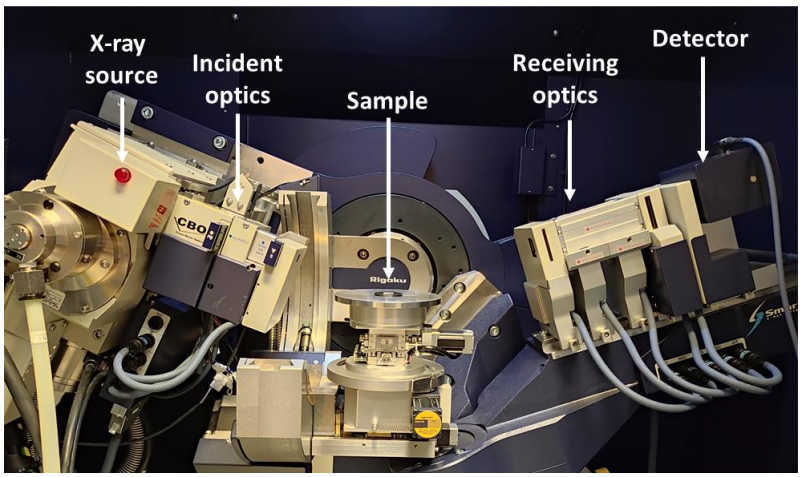

Figure 3.16. *Image of the Rigaku Smartlab diffractometer with one of the configurations used in this work.*

In this work, we used a Rigaku Smartlab X-ray diffractometer, depicted in Figure 3.16. It consists in three parts: x-ray beam generator (source), sample holder (goniometer), and x-ray detector. In this system, the x-ray excitation is obtained from the $k_{\alpha 1}$ emission line of Cu (λ_{XRD} = 0.154056 nm). The source consists in an evacuated tube in which electrons are emitted from a heated tungsten filament and accelerated by an electric potential of 40 kV to impinge on a Cu target. The emitted x-ray beam is collected and converted into a parallel beam by a parabolic mirror (<0.06° divergence). To measure high resolution XRD (HR-XRD), we used a monochromator consisting of 4 Ge crystals (Ge(220)×4) between the source and the sample. The resulting beam presents a divergence of 0.0033° and a wavelength spread of $\Delta\lambda_{XRD}/\lambda_{XRD}$ = 2.2 × 10^{-5}. For quick measurements where high resolution is not required, a 2-Ge-crystal monochromator (Ge(220)x2) was used.

Since the sample surface might be tilted with respect to the crystallographic planes, we first need to align the desired sample plane family with the optical axis of the set-up. To do so, the sample is mounted on a goniometer that offers four possible angular rotation mechanism, namely ω, 2θ, φ and χ, described in Figure 3.17. The angle ω is the angle between the incident x-ray beam and the sample surface, 2θ is the angle between the incident beam and the reflected beam from the surface, φ is the rotation angle around the z-axis and χ is the rotation angle perpendicular to the z-axis. To minimize the background noise, the sample is placed on a monocrystalline Si plate.

The detector has an aperture of 2°, which can be reduced by inserting slits to improve the resolution of the diffracted beam. For HR-XRD, a 0.228 collimator or a Ge(220)x2 analyzer are placed between the sample and the detector to improve the angular precision of the diffracted beam.

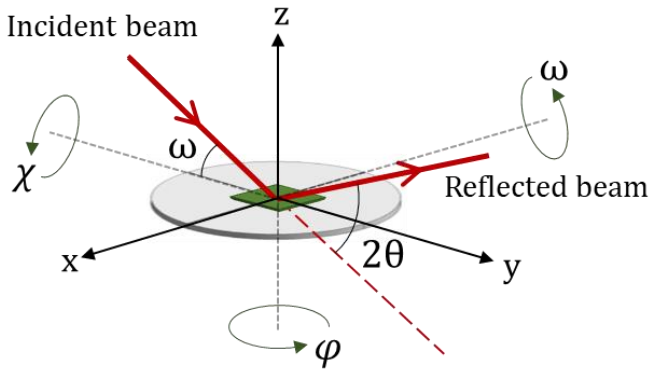

Figure 3.17. *Schematic representation of the axis and angles available in the goniometer to align the sample.*

XRD uses the constructive interference of the monochromatic x-ray diffracted by the crystalline structure at specific angles, following Bragg's law:

$$2d \sin\theta = n\lambda_{XRD} \tag{3.1}$$

where n is an integer which indicates the order of reflection, λ_{XRD} is the wavelength of the x-ray, d is the distance between reflecting planes, and θ is the angle of incidence between the beam and the crystallographic plane. From this equation, we can extract the lattice parameter of a crystal, which corresponds to the distance d. Furthermore, the period of a MQW (P_{MQW}) can be obtained from the angular separation of two satellite peaks in the θ-2θ scans:

$$P_{MQW} = \frac{\pm n\lambda_{XRD}}{2(\sin\theta_{\pm n} - \sin\theta_0)} \tag{3.2}$$

where θ_0 and $\theta_{\pm n}$ are the zero-order and the ±n-order MQW satellite angle position. The evaluation of the stain state of the layers and the alloy composition required of reciprocal space maps to extract the various lattice parameters using also Bragg's law. Finally, the crystalline quality of the planar structures were qualitatively deduced from the ω-scans, also called rocking curves. Broader rocking curves are generally attributed to poorer crystal quality.

3.2.2 Scanning electron microscopy

Scanning electron microscopy (SEM) is a characterization technique based in the interaction between a scanning electron beam and the sample surface that allows imaging at the nanometric scale and get morphological information. In contrast with conventional optical microscopy, a much higher resolution is achieved due to the shorter effective wavelength of the electrons. The interaction of the electron beam with the specimen results in the generation of several secondary particles that are characteristic from the sample, as seen in Figure 3.18, e.g. backscattered electrons, secondary electrons, x-ray, photons and phonons.

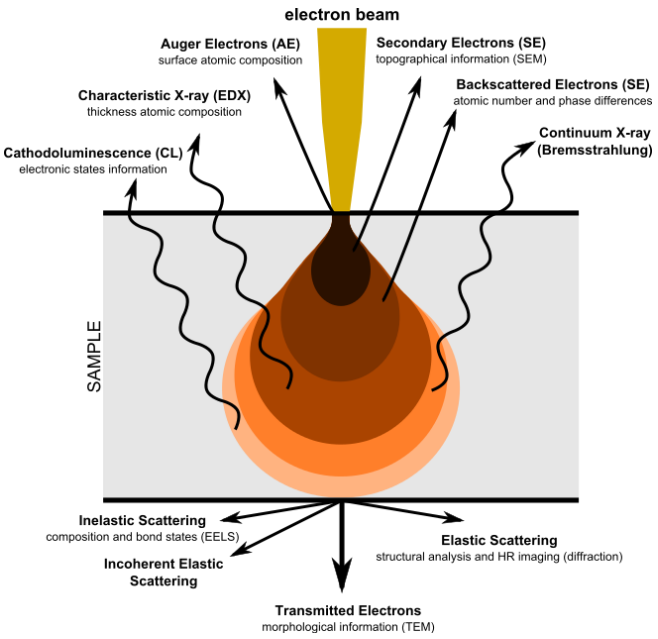

Figure 3.18. *Signals resulting from the interaction between the electron beam and the specimen [163].*

In this work, we have used a Zeiss Ultra 55 to image the nanostructures. The electron beam was operated between 3-8 kV. An in-lens detector was used to collect the secondary electrons emitted from the sample surface. The secondary electrons are generated from the impact of the electron beam on electrons in the valence or conduction band, that through inelastic scattering, they can get enough energy to become free electrons. Due to their little energy, only surface electrons can leave the sample and reach the detector, while inner secondary electrons are reabsorbed by surrounding atoms. Secondary electrons are very sensitive to the topography, providing information on the sample surface morphology.

3.2.3 Transmission electron microscopy

In transmission electron microscopy (TEM), the image is the result of electrons traversing the sample, which must be thin enough to allow high yield electron transmission. In this work, thin lamellas were extracted from samples with a Ga^+ ion beam in a focused ion beam (FIB) SEM Zeiss Crossbeam 550, using the usual lift-out technique [164]. The voltage was progressively decreased from 30 kV to 2 kV in order to reduce beam damage and to obtain a sample thickness of about 70 nm. The specimens were prepare by Florian Castioni (CEA-LETI) or Vincent Grenier (CEA-IRIG-PHELIQS).

The TEM analysis was performed on a probe-corrected FEI Titan Themis microscope operated at 200 kV by Florian Castioni (CEA-LETI) or Catherine Bougerol (Institut Néel-CNRS). They used mainly two techniques:

- *High-resolution TEM (HR-TEM)*: A parallel electron beam is formed and the transmitted beam is collected and imaged on the camera. Generally, heavier atoms and thicker regions appear darker due to the electron loss. With this technique, the resolution can reach atomic scale and we can address the morphology and defect contrast of the sample. However, no direct interpretation of the images can be done in terms of chemical composition because of the influence of the sample thickness, defocus and diffraction contrast.
- *High angle annular dark field scanning TEM (STEM-HAADF)*: A focused electron beam is scanned over the sample. The electrons scattered over relatively large angles are collected on an annular detector. In this technique, the contrast in the image is directly related to the chemical nature of the atoms (proportional to their atomic mass). The influence of diffraction contrast is drastically reduced and high-resolution imaging at atomic scale is achievable. A qualitative interpretation is directly possible from the image.

3.2.4 Atomic force microscopy

Atomic force microscopy (AFM) is a type of scanning probe microscopy (SPM) characterization technique, where a physical probe is used to scan the sample surface. The AFM instrument allows to perform force measurements (i.e. Young modulus or stiffness), topographic imaging, current mapping or nano-manipulation. In this work, we have used a Veeco Dimension 3100 AFM system to examine the surface morphology of the samples.

The schematic of the AFM set-up is described in Figure 3.19. The silicon probe tip is integrated into a cantilever that is sensitive to the forces between the sample and the tip. This tip, usually made of Si or Si_3N_4, has a couple of microns length and less than 10 nm diameter. The force applied by the cantilever on the sample is kept constant thanks to a feedback system, which can change the location of the tip through a piezoelectric. Therefore, the movement of the tip follows the surface morphology. The movement of the cantilever changes the trajectory of the laser reflected on it. Thus, the variation of the laser spot on the photodetector can be used to trace the sample topography.

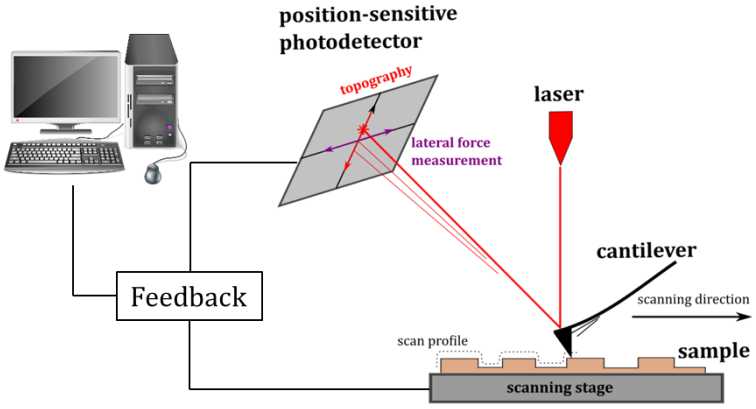

Figure 3.19. *Schematic of the AFM system (modified from [165]).*

As shown in Figure 3.20, there are three different modes to operate the AFM: contact mode, non-contact mode and tapping mode. The interacting force between the tip and the sample depends directly on the distance between them [166]. All the AFM measurements in this PhD have been made by tapping mode.

- *Contact mode*: The tip is brought very close to the sample surface, keeping the repulsive force constant. As a consequence, the measurement is done with huge frictional and adhesive forces that can damage the sample and result in a distorted image.
- *Non-contact mode*: The tip is kept a few hundreds of angstroms away from the sample surface and is made to oscillate at large amplitude and near the resonant frequency. The changes in the amplitude of oscillation due to attractive Van der Waals force gives information about the topography of the sample. However, it provides low resolution and the image can be hampered by natural oscillations.
- *Tapping mode*: This mode combines the advantages of the previous two. The tip is made to oscillate near the resonant frequency closer to the sample. It avoids surface damage issues and provides better resolution.

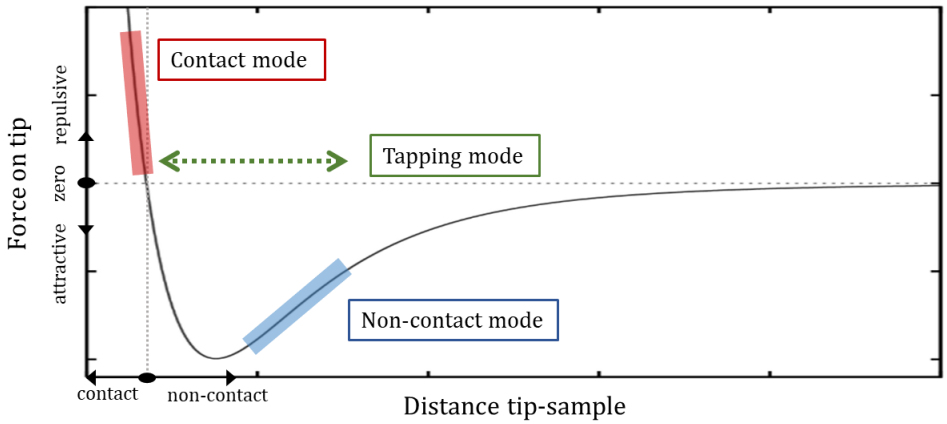

Figure 3.20. *Variation of the force with the tip-sample distance in the different AFM operation modes.*

In this work, AFM experiments were performed in the tapping mode, using TESPA-V2 tips from Bruker. The tip specifications are described in Figure 3.21.

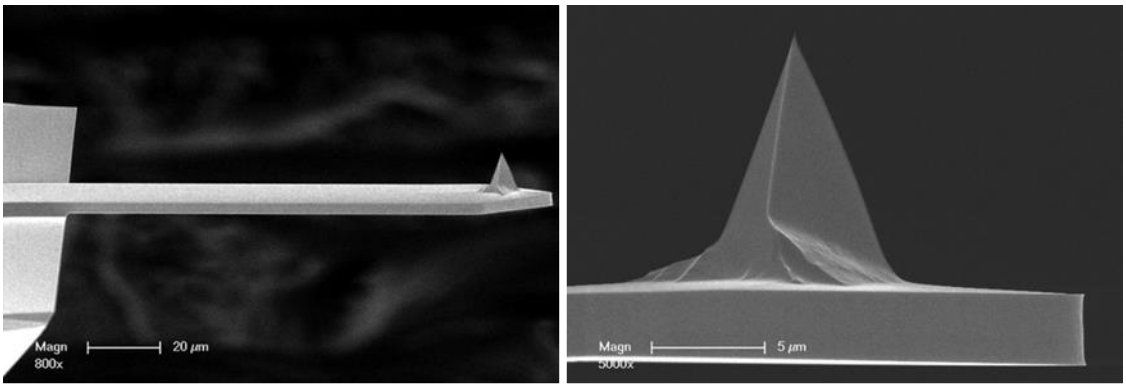

Geometry	Tip Radius (nm)
Rectangular	Nom: 7
	Max: 10
Frequency (KHz)	**Length (µm)**
Nom: 320	Nom: 123
Min: 270	Min: 120
Max: 370	Max: 125
Spring Const (N/m)	**Width (µm)**
Nom: 37	Nom: 40
Min: 19	Min: 37
Max: 55	Max: 42

Figure 3.21. *SEM images and specifications of the AFM tips used during this work.*

3.2.5 Photoluminescence

Photoluminescence (PL) is the phenomena that describes the light emission from a material when excited with light. PL spectroscopy is a characterization technique that provides information about the optical and electronic properties and the material quality of the sample by analyzing its characteristic emitted light under optical excitation. The working principle is based on the radiative recombination of electron-hole pairs generated from the absorption of incident photons. Figure 3.22 describes different processes that can take place [167]. First, the sample is excited with an incident photon whose energy must be larger than the material band gap in order to promote an electron from the valence band to the conduction band, creating an electron-hole pair (process (a)). Since the energy absorbed is larger than the band gap, the electron is pumped to an excited energy state, from which it will relax to the lower energy state of the conduction band by releasing energy in the form of phonons i.e. vibration modes of the crystal (process (b)). In general, this relaxation process is much faster than the radiative rates. From here, there are several recombination paths depending on the nature of the semiconductor material and the

presence of impurities. The simplest radiative recombination is the band-to-band transition between a free electron from the conduction band and a free hole from the valence band (process (c)). In this case, the energy of the photon emitted is equivalent to the band gap energy. However, donor and acceptor states can appear within the band gap due to either unintentional lattice defects/impurities or intentionally generation by doping. These intermediate states give rise to new recombination paths like donor-bound electron to free hole (process (d)), free electron to acceptor-bound hole (process (e)) and donor-bound electron to acceptor-bound hole, also known as donor-acceptor pair recombination (process (f)). Note that in these cases, the energy of the emitted photon does not correspond to the band gap, and the difference in energy is compensated by non-radiative relaxation. Each emission is specific from its recombination path and it carries a characteristic energy. Therefore, PL always probes the lower energy states, not necessarily the band-to-band transition.

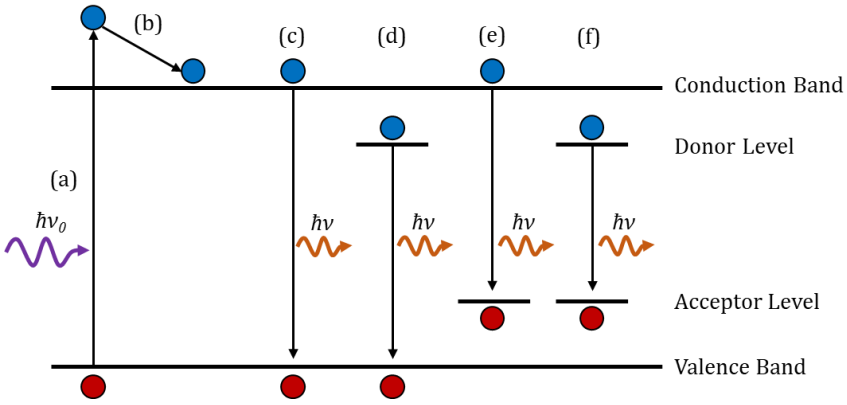

Figure 3.22. *Processes involved in photoluminescence of semiconductors: (a) photon absorption to generate an electron-hole pair, (b) non-radiative relaxation to the band edge, (c) band-to-band radiative recombination, (d) donor electron to free hole radiative recombination, (e) free electron to acceptor hole radiative recombination, (f) donor electron to acceptor hole radiative recombination.*

In the case of III-N materials, the photoluminescence is generally excitonic. An exciton is an electron-hole pair which are bounded by Coulomb attraction. In this way, the electron and the hole move in the crystal as a single entity [168], in contrast with an ordinary electron-hole pair, which are unbound and each particle can move independently. Due to the electrostatic attraction, the recombination energy of a free exciton is slightly lower than the recombination energy of an unbound electron-hole pair:

$$E_{FX} = E_g - E_b \tag{3.3}$$

where E_g is the band gap energy and E_b is the binding energy, which can be calculated from the hydrogen atom model with the following expression:

$$E_b = \frac{e^4 \mu}{2h\varepsilon^2} \frac{1}{n^2} \tag{3.4}$$

where μ is the reduced mass of the electron-hole system, h is the Planck's constant, ε is the dielectric constant from the material, e is the electron charge and n is the quantic number of the energy level. In the case of GaN, the exciton binding energy results in 25 meV [169,170]. This energy value is similar to the thermic energy (kT) at room temperature (≈ 26 meV), reason why excitons are extremely stable in nitrides even at room temperature, being excitonic recombination the dominant process in these materials. Bound excitons are those who are attached to an acceptor or a donor, which introduces an additional energy shift.

In this thesis, photoluminescence spectroscopy has been used to address various properties of our samples. Figure 3.23 describes the two main set-ups that were built during this work. In both set-ups, the PL emission was collected with a Jobin-Yvon HR460 monochromator and a liquid nitrogen cooled UV enhanced charge-coupled device (CCD).

- **Set up A:** This set-up was used to characterize the PL emitted perpendicular from the sample surface. The light source was either a pulsed Nd:YAG laser (λ = 266 nm, repetition rate = 8 kHz, pulse width = 0.5 ns) or a continuous wave frequency-doubled solid-state laser (λ = 244 nm). The beam was focused on a spot of ≈100 μm. The optical power of the beam impinging on the sample was tuned with a variable optical filter, and monitored with a retractable power meter located in front of the sample holder. The sample was glued on a He cold-finger cryostat that could be moved precisely along three axes to examine any point of the sample surface.
- **Set up B:** This set-up was used to measure lasing thresholds, by pumping normal to the sample surface and collecting the emission from the edge, parallel to the surface. The light source was the Nd:YAG laser from set up A (λ = 266 nm, repetition rate = 8 kHz, pulse width = 0.5 ns), which was focused with a cylindrical lens to obtain a stripe with a width of ≈100 μm. The stripe beam shape was characterized in length and width, presenting a Gaussian pattern as illustrated in Figure 3.24. In order to perform an homogeneous excitation, the sample was centered at the maximum of the Gaussian. The sample was glued on a sample holder that could be moved along three axes with micro positioners. For temperature dependent measurements, the sample holder was inserted into a He cold-finger cryostat. The optical power of the beam was tuned with a variable optical filter and monitored with a retractable power meter located in front of the sample holder.

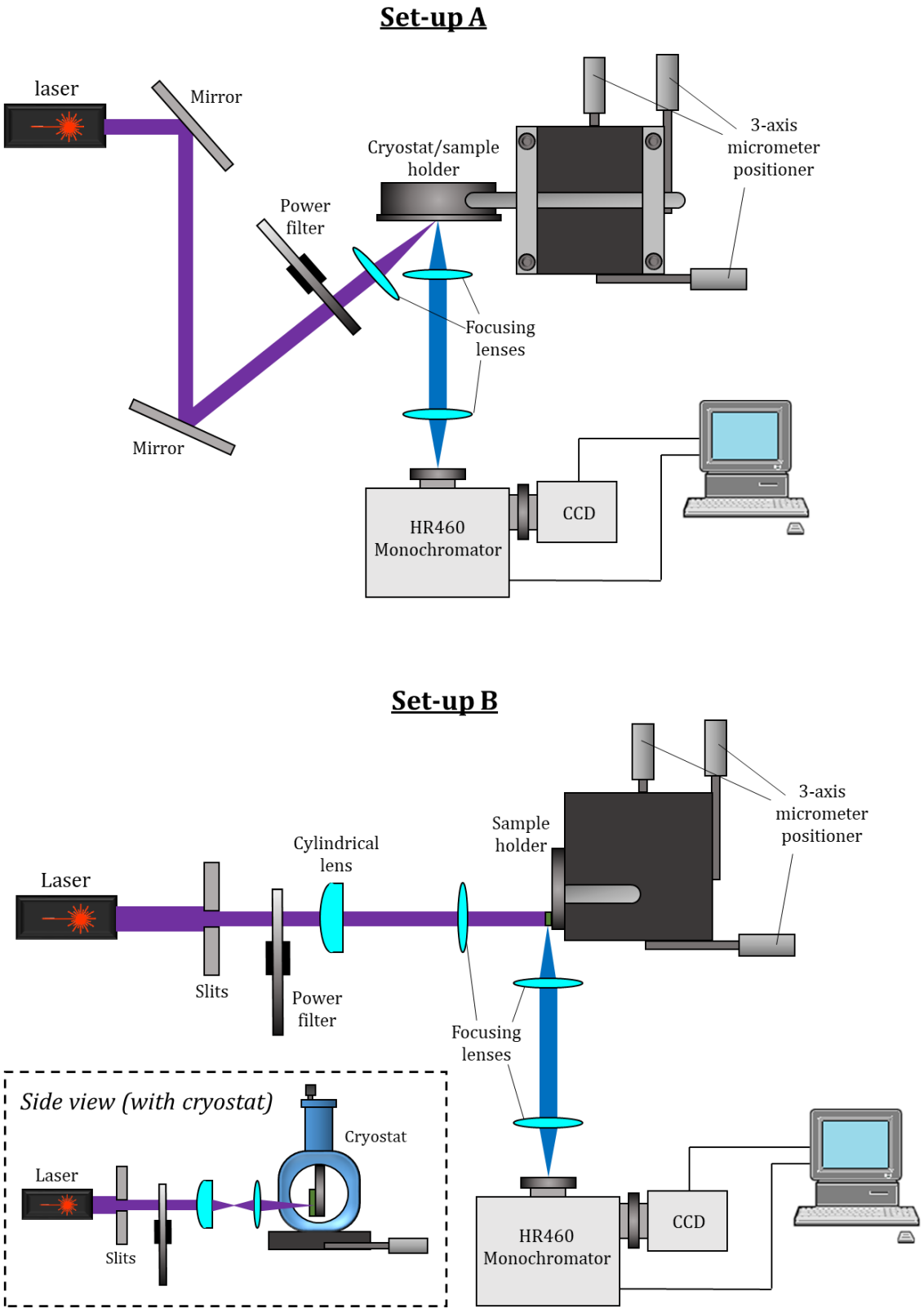

Figure 3.23. *Schematics of the PL set-ups used in this work. Set-up A was designed to measure PL emission perpendicular to the sample surface. Set-up B was used to measure photoluminescence or lasing emission from the sample edge. The inset in Set-up B shows the side view of the set-up, to describe the stripe-shaped beam focusing.*

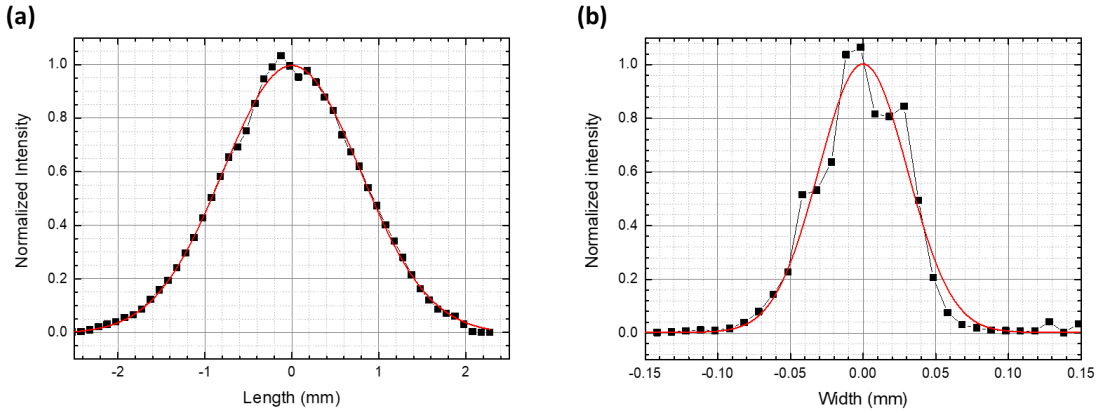

Figure 3.24. *(a) Length and (b) width of the stripe-shaped beam. Black squared dots are experimental data and the red curve is a Gaussian fit.*

3.2.6 Cathodoluminescence

Cathodoluminescence (CL) is the phenomena that describes the light emission from a material when excited with an electron beam source. CL spectroscopy is a characterization technique that provides information about the optical properties and the material quality of the sample by analyzing its characteristic emitted light under electron beam excitation. The working principle is based on the radiative recombination of electron-hole pairs generated by impact ionization, as explained in detail in section 2.3.1.

The CL set-up used in this work consists in a SEM (model FEI Quanta 200) coupled to an optical spectrometer, so that it is possible to image the sample while exciting with the same electron beam. A parabolic mirror is placed between the sample and the electron beam tube, as described in Figure 3.25. The mirror has a tiny hole to let the electron beam pass through. The sample is placed at the focal point of the mirror by micro positioners with 3 nm resolution. The mirror reflects the emission from the sample in a parallel beam that is focused onto a Jobin Yvon HR460 monochromator, which projects the photons to a CCD detector. In our measurements, we scan an area of 2x2 μm^2 for different acceleration voltages ranging from 5 to 20 kV, at an injection current approximately constant ($I \approx 100$ pA).

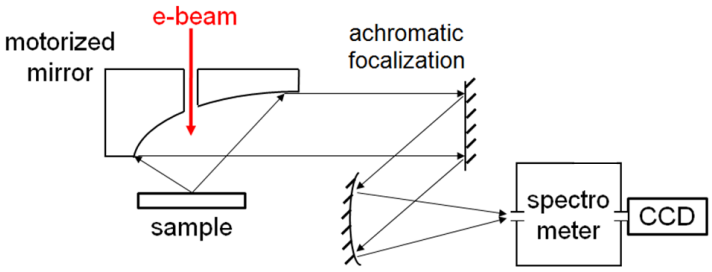

Figure 3.25. *Schematic of the CL set-up used in this work.*

3.3 Simulations

During this work, the design of laser cavities and the interpretation of the experimental results were supported by simulations. I have performed simulations on NextNano³, COMSOL and CASINO to address different aspects of the laser heterostructures. In this section, I discuss briefly the application of these simulation tools.

3.3.1 Nextnano

Table 3.1. *Input parameters used for nextnano³ simulations.*

Parameters (units)	Symbol	GaN	AlN
Lattice constant (Å)	a	3.189 [56]	3.112 [56]
	c	5.185 [56]	4.982 [56]
Spontaneous polarization (C/m²)	P_{SP}	-0.029 [171]	-0.081 [171]
Piezoelectric constant (C/m²)	e_{31}	-0.49 [68]	-0.60 [68]
	e_{33}	0.73 [68]	1.46 [68]
	e_{15}	-0.30 [172]	-0.48 [172]
Elastic constant (GPa)	c_{11}	390 [173]	396 [56]
	c_{12}	145 [173]	137 [56]
	c_{13}	106 [173]	108 [56]
	c_{33}	398 [173]	373 [56]
Band gap at 0 K (eV)	E_g	3.51 [56]	6.23 [56]
Electron effective mass	m_e^*	0.20 [56]	0.32 [56]
Heavy hole effective mass	$m_{hh\perp}^*$	1.60 [78]	10.42 [174]
	$m_{hh\parallel}^*$	1.10 [78]	3.53 [174]
Light hole effective mass	$m_{lh\perp}^*$	0.15 [78]	0.24 [174]
	$m_{lh\parallel}^*$	1.10 [78]	3.53 [174]
Crystal field hole effective mass	$m_{ch\perp}^*$	1.10 [78]	3.81 [174]
	$m_{ch\parallel}^*$	0.15 [78]	0.25 [174]
Dielectric constant	ε	10 [171]	8.5 [171]
Deformation potential	a_{c1}	-4.6 [175]	-4.5 [176]
	a_{c2}	-4.6 [175]	-4.5 [176]
	D_1	-1.7 [175]	-2.89 [175]
	D_2	6.3 [175]	4.89 [175]
	D_3	8.0 [175]	7.78 [175]
	D_4	-4.0 [175]	-3.89 [175]
	D_5	-4.0 [175]	-3.34 [175]
	D_6	-5.66 [175]	-3.95 [175]
Luttinger parameters	A_1	-5.947 [177]	-3.86 [56]
	A_2	-0.528 [177]	-0.25 [56]
	A_3	5.414 [177]	3.58 [56]
	A_4	-2.512 [177]	-1.32 [56]
	A_5	-2.510 [177]	-1.47 [56]
	A_6	-3.202 [177]	-1.64 [56]

NextNano[3] is a commercial software for the simulation of electronic and optoelectronic properties of semiconductor nanodevices created by Nextnano GmbH, a start-up from the Technical University of Munich. In practice, it is a self-consistent Schrödinger-Poisson equation solver written in Fortran or C++. In this work, we used a model based on the 8-band k·p perturbation theory for calculating the quantum levels for electrons and holes. We also used the simulations to study the electronic band structure of the multilayered heterostructures. A detailed explanation of the models can be found in ref. [178]. For simplicity, the nanostructure was simulated in 1D (growth direction) due to the symmetry in the other two directions. Note that Coulomb interactions are not taken into account.

The material parameters given in the software can be modified by the user. The input parameters for GaN and AlN in this work were taken from Kandaswamy et al. [157] and are summarized in Table 3.1.

3.3.2 COMSOL

COMSOL Multiphysics is a commercial finite-element analysis software that allows creating physics-based models and solving them mathematically. In this work, it was used to study the optical confinement in the laser waveguide. The sample geometries were reconstructed along the growth direction in a 2D representation. The structure was sandwiched between a 2-µm-thick substrate and a 300-nm-thick layer of air. As boundary conditions, the active area was defined as a perfect electric conductor, the electric field was defined as zero at the top and bottom edge of the air and substrate layers, respectively, and periodic conditions were applied at the lateral edges of the geometry due to the in-plane symmetry of the 2D layers. The model space is discretized in finite elements with a user-defined mesh, with element size between 0.5 and 1 nm.

The simulation solves the three components of the electric field vector from the Maxwell equations assuming that the field varies sinusoidally in time at a known angular frequency $\omega = 2\pi f$, being f the frequency of the light emitted by the QW. With these assumptions, the equation to be solved is the following

$$\nabla \times \left(\mu_r{}^{-1} \nabla \times \vec{E}\right) - \frac{\omega^2}{{c_0}^2}\left(\varepsilon_r - \frac{i\sigma}{\omega \varepsilon_0}\right)\vec{E} = 0 \qquad (3.5)$$

where $\vec{E}$ is the electric field vector, μ_r is the relative permeability, ε_r is the relative permittivity, σ is the electrical conductivity, c_0 is the speed of light in vacuum and ε_0 is the vacuum permittivity. Considering $\sigma = 0$ and $\mu_r = 1$, equation (3.5) simplifies to

$$\nabla \times \left(\nabla \times \vec{E}\right) - {k_0}^2 \varepsilon_r \vec{E} = 0 \tag{3.6}$$

with $k_0 = \frac{\omega}{c_0}$ being the wavenumber. The relative permittivity can be calculated from the real and imaginary components of the refractive indices for each material as $\varepsilon_r = (n - ik)^2$. The values of refractive indices were extracted from [179,180].

3.3.3 CASINO

CASINO is a software designed to perform quantum Monte Carlo simulations on the energy, distribution and trajectory of electrons impinging a material. In this work, it was used to calculate the penetration depth and energy distribution of the electron beam cannon into the laser samples. Layers of the stack are defined in thickness, density and composition. For this work, the density values taken were 6.15 g/cm^3 for GaN and 3.26 g/cm^3 for AlN [181]. The density of their ternary alloys were obtained from linear interpolation. The conditions of the electron beam can be tuned in terms of radius, acceleration voltage and number of electrons impinging. Further details on this software can be found in references [182–185].

3.4 Clean-room fabrication

During this PhD, the fabrication of defined laser nano-cavities was performed in the PTA cleanroom of CEA by a series of microfabrication techniques, which are briefly discussed in this section, namely optical lithography, metal deposition and inductively-coupled-plasma reactive ion etching (ICP-RIE).

3.4.1 Optical lithography

Lithography is a fabrication process that consist in projecting an image into a photosensitive emulsion, called photoresist, coated onto a substrate by using photons. In this work, it was used to define specific cavity patterns in the heterostructures. The equipment used was a SUSS MicroTech MJB4 mask aligner, which incorporates a UV lamp (365 nm filtered at 6 mW/cm^2) and allows aligning the sample and the mask with a resolution of 2 µm in soft contact mode. The samples were covered with the selected photoresist by spin-coating, to be later exposed to UV light that will change the polymer chemical structure, thus its chemical properties. A predefined patterned mask was used to block the light in certain regions of the photoresist, so that only unmasked regions were exposed to light. Finally, the sacrificial parts were lifted off with a

developer solvent. There are two types of photoresist according to their behavior when exposed to light, as depicted in Figure 3.26, namely positive photoresist and negative photoresist.

- *Positive photoresist*: The material that is exposed to light becomes soluble to the photoresist developer.
- *Negative photoresist*: The material that is exposed to light becomes insoluble to the photoresist developer.

In this work, we used a reversible photoresist (AZ5214E), which can be used either as positive or negative photoresist, according to the chosen preparation process.

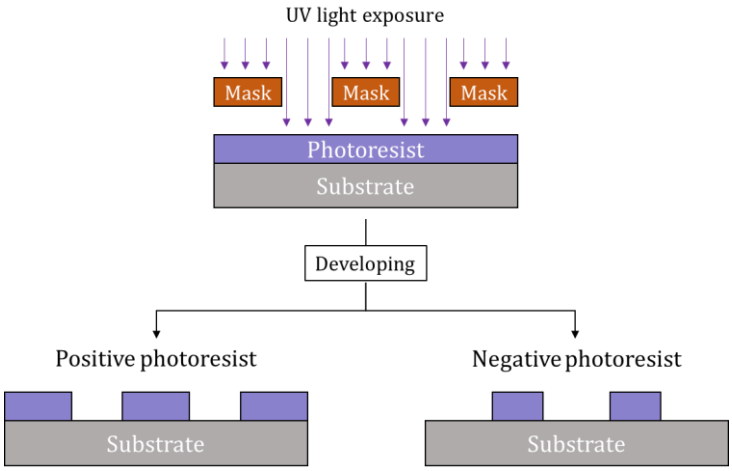

Figure 3.26. *Schematic diagram showing the two types of photoresist used in optical lithography.*

3.4.2 Deposition of metals and dielectrics

In some microfabrication processes, it is necessary to deposit thin layers of metal with a precise thickness, for instance, for implementing contacts in electronic devices. In this thesis, we deposited thin layers of metal (i.e. Ti, Au, Ni) that work as a markers and hard mask for following etching processes. For this purpose, a metal evaporator MEB550 from Plassys was used. In this technique, a high-power electron gun (10 kW) evaporates metal atoms from bulk material under high vacuum conditions ($\approx 10^{-6}$ Torr) that are deposited on the chosen substrate. We are able to measure the in-situ thickness of the deposited film using a quartz microbalance, which provides a mass variation per unit area by measuring the change in frequency of a quartz crystal resonator.

In addition, the deposition of thin films of SiO_2 was also required during the course of this work. In this case, the deposition was performed by plasma enhanced chemical vapor deposition (PECVD) technique in a Corial D250L. The film of SiO_2 is obtained from fluxes of SiH_4, N_2O and Ar, at a deposition temperature of 280 ^oC. The depositions of SiO_2 thin layers during this work were performed by Delphine Constantin.

3.4.3 Reactive ion etching

Etching consist in removing layers from a wafer. Thanks to the masking process, some areas of the sample can be defined and protected during the etching, leading to the formation of a patterned nanostructure. There exist two types of etching processes: dry etching and wet etching.

- *Dry etching*: It consists in removing material by exposing it to a bombardment of ions, usually a plasma of reactive atoms. The reaction that takes place can be due to high kinetic energy of particle beams (physical dry etching), chemical reaction (chemical dry etching) or a combination of both.
- *Wet etching*: It consists in removing material by dipping it in liquid chemicals or etchants. In general, a wet etching process involves multiple chemical reactions.

ICP-RIE is a dry etching technique involving plasma that combines both physical and chemical mechanisms. In a RIE process, cations are produced from reactive gases, which are accelerated with high energy and chemically react with the material. An ICP system generates the plasma by induction with radio frequency (RF) excitation, controlled by two parameters: ICP power and RF power. The final thickness of the etched structures were measured by profilometry. Figure 3.27 presents a schematic of the ICP-RIE chamber. In this work, etching techniques have been used to fabricate microcavities in our samples. Specifically, an Oxford Plasmalab100 ICP etcher was used for dry etching processes.

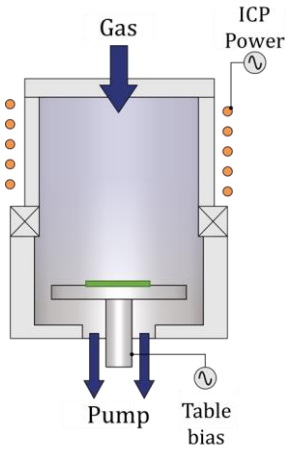

Figure 3.27. *Schematic of the ICP-RIE chamber.*

Chapter 4
AlGaN/GaN heterostructures for electron beam pumped UV-A lasers

This chapter describes the design and growth conditions of four AlGaN/GaN heterostructures (two separate confinement heterostructures and two graded-index separate confinement heterostructures), proposed to obtain laser emission around 360 nm. Characterization through x-ray diffraction (XRD) and transmission electron microscopy (TEM) is presented to validate their structure and crystalline quality. The spontaneous emission is analyzed by cathodoluminescence and photoluminescence, including an exhaustive study on the internal quantum efficiency. Finally, an assessment of the net optical gain is presented.

COMSOL simulations were performed by me, with the support of Yoann Curé and Gilles Nogues. TEM measurements were performed by Florian Castioni or Catherine Bougerol, in specimens prepared by Florian Castioni and Vincent Grenier, respectively. XRD measurements were also performed by me with the training and support from Edith Bellet-Amalric. I was also in charge of the epitaxial growth and nextnano simulations, under the supervision of Eva Monroy. On the cathodoluminescence and photoluminescence measurements, I had the support from Fabrice Donatini and Lou Denaix, respectively. The gain measurements were performed by Quang Mihn Thai (Univ. Claude Bernard Lyon 1).

Some of the results presented in this chapter have been published in:

(1) "AlGaN/GaN asymmetric graded-index separate confinement heterostructures designed for electron-beam pumped UV lasers", S. Cuesta et al. Opt. Express 29, 13084-13093 (2021) [186]

(2) "Development of AlGaN/GaN heterostructures for e-beam pumped UV lasers", S. Cuesta Arcos et al. Proc. SPIE 11686, Gallium Nitride Materials and Devices XVI, 116860S (2021) [187]

(3) "Decorrelation of internal quantum efficiency and lasing threshold in AlGaN-based separate confinement heterostructures for UV emission", S. Cuesta et al. Appl. Phys. Lett. 119, 151103 (2021) [188]

(4) "Optical net gain measurement on $Al_{0.07}Ga_{0.93}N$/GaN multi-quantum wells", Q. M. Thai, S. Cuesta et al. Opt. Express 30(14), 25219-25233 (2022) [189]

4.1 Design of the AlGaN/GaN heterostructures

To obtain high-performance semiconductor lasers, it is critical to understand the optical and electrical properties of the material, which must be taken into consideration for the device design. In this section, I present the main AlGaN/GaN architectures that were considered in this work for the fabrication of electron beam pumped UV-A lasers.

4.1.1 Separate confinement heterostructures

Figure 4.1 presents the general sample structure considered in this work, based in a separate confinement heterostructure (SCH). The active region consist of a number of GaN QWs (multi-

quantum well, MQW) embed in AlGaN. For the samples described in this chapter, the active region consists of 10 QWs, unless indicated. The number of QWs was chosen in order to obtain high output power and take the maximum profit from the electron injection. The active region is located within two AlGaN cladding layers acting as a waveguide. In the figure, the layers have been labelled, starting from the GaN substrate and following the growth direction, as bottom outer cladding layer (BOC), bottom inner cladding layer (BIC), multi quantum well (MQW), top inner cladding layer (TIC) and top outer cladding layer (TOC).

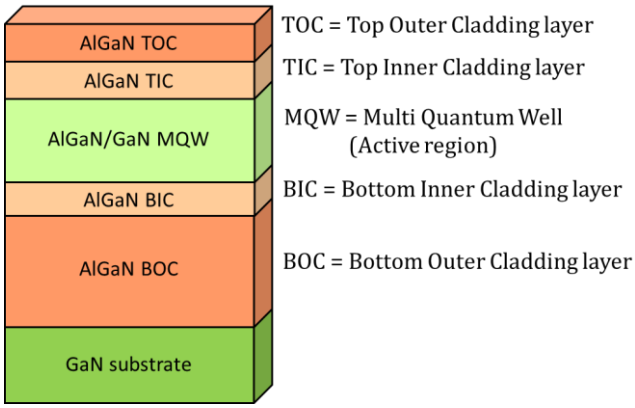

Figure 4.1. *General scheme of a separate confinement heterostructure containing a MQW.*

Table 4.1 describes two SCH designs developed in this work, to operate under electron beam pumping with an acceleration voltage of 10 kV and to emit around λ = 360 nm (labelled SCH-D1) and at λ = 350 nm (labelled SCH-D2), respectively.

Table 4.1. *Description of the designs under study in terms of thickness and Al content on the layers, following the general design in Figure 4.1.*

	SCH-D1	**SCH-D2**
TOC	50 nm $Al_{0.15}Ga_{0.85}N$	50 nm $Al_{0.2}Ga_{0.8}N$
TIC	67 nm $Al_{0.07}Ga_{0.93}N$	67 nm $Al_{0.1}Ga_{0.9}N$
MQW	10×(3 nm GaN/12 nm $Al_{0.07}Ga_{0.93}N$)	10×(1.5 nm GaN/11 nm $Al_{0.1}Ga_{0.9}N$)
BIC	40 nm $Al_{0.07}Ga_{0.93}N$	40 nm $Al_{0.1}Ga_{0.9}N$
BOC	400 nm $Al_{0.15}Ga_{0.85}N$	400 nm $Al_{0.2}Ga_{0.8}N$
Targeted wavelength	360 nm	350 nm

The design of the structures was carried out taking into account both optical and electrical considerations. In particular, three main requirements must be addressed when defining the multilayer ensemble:

(i) *Waveguide design*: The bottom cladding layer must be thick enough to prevent waveguide losses through the absorbing GaN substrate. The Al concentration in the cladding layers defines the inner reflection, thus, the optical confinement factor.

(ii) *Penetration depth:* The penetration depth of the electron beam in the structure imposes a limit to the thickness of the upper layers.

(iii) *Emission wavelength:* The MQW must emit at the targeted wavelength, defining the QW thickness and Al concentration in the barriers.

The above-mentioned conditions must be fulfilled at the same time. When addressing these requirements, we must keep in mind also the limitations imposed by the difference in lattice mismatch between layers, which sets a maximum to the layer thickness and alloy compositions.

(i) Waveguide design

Compared to lamps or LEDs, lasers demand an extra degree of complexity in their structures, because of the need to confine light in a cavity. In this work, we use a ridge waveguide, which is induced thanks to the difference in refractive indices between cladding layers. Note that, following Fresnel equations [190], to enhance the confinement of the light generated in the active region, the refractive index of the outer layer must be lower than the refractive index of the inner layer. In other words, due to AlN presenting lower refractive index than GaN [179,180], the molar fraction of Al in the AlGaN outer layers must be higher than the molar fraction in the inner layers. However, when designing the structure, the difference between Al concentrations should be minimized in order to decrease the lattice mismatch during the epitaxial growth.

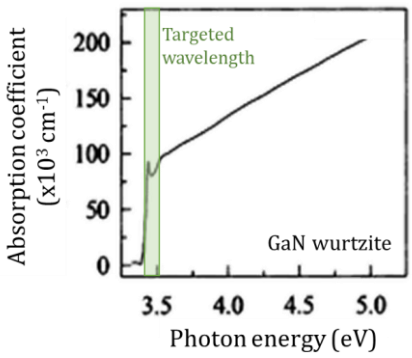

Figure 4.2. *Absorption spectrum of GaN (modified from [191]).*

The design tries to maximize the overlap of the fundamental optical mode with the active region. In addition, the waveguide must prevent that the optical mode leaks towards areas of the sample where absorption is dominant. For instance, the bulk GaN substrate behaves as absorbing media at the targeted wavelengths (see Figure 4.2). Therefore, a thick bottom cladding layer is desirable to prevent that the optical mode spreads towards the GaN substrate. However, a thick bottom cladding can lead to severe cracking of the epilayer, due to tensile stress. We have found

that a BOC layer with a thickness of 400 nm provides enough insulation from the substrate, as illustrated by theoretical calculations in Figure 4.3(a) for SCH-D1 and Figure 4.3(b) for SCH-D2. The optical confinement factor (OCF) for each design, i.e. the overlap between the optical mode and the 10 GaN QWs, is 7% and 4.1% for SCH-D1 and SCH-D2, respectively. Note that the thickness of the QWs in SCH-D2 is half that of the QWs in SCH-D1, which explains the lower OCF for the second design. These values represent an improvement with respect to the ≈ 6% reported by Hayashi *et al.* [51] for a QW thickness equivalent to SCH-D1.

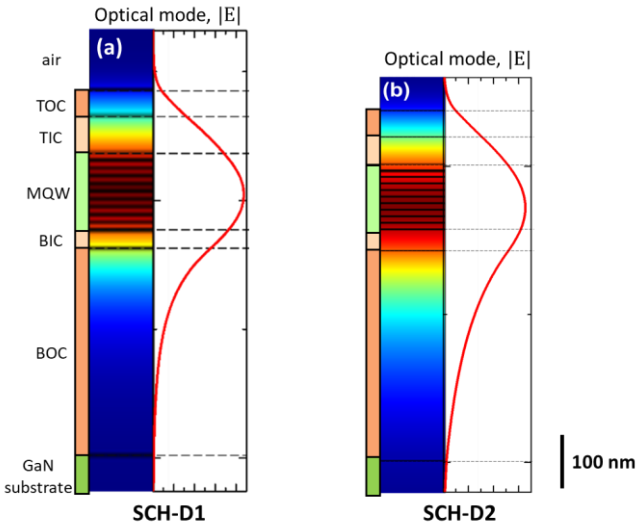

Figure 4.3. *Simulation of the first optical mode distribution through the (a) SCH-D1 and (b) SCH-D2.*

(ii) Electron penetration

As a reminder from section 2.3.3, the acceleration voltage is directly related to the penetration length of the electrons. The choice of operation voltages seeks reducing the spread of the profile of generated electron-hole pairs in the material, to maximize the amount of carriers that are collected and recombine radiatively in the active region. This should facilitate attaining the condition of population inversion. In view of the targeted wavelength ($\lambda \approx 360$ nm), the optimum thickness of the core of the waveguide will be around λ/n, where n is the refractive index of the layers. Keeping in mind the refractive index of GaN in the near-UV is around 2.4, the core will have a thickness around 150 nm. Therefore, looking back at Figure 2.15, we have made a choice of targeting operation at 7-10 kV. The thickness of the top cladding layers must be adapted to the acceleration voltage, so that the active region is located at the optimum depth to maximize the charge transfer.

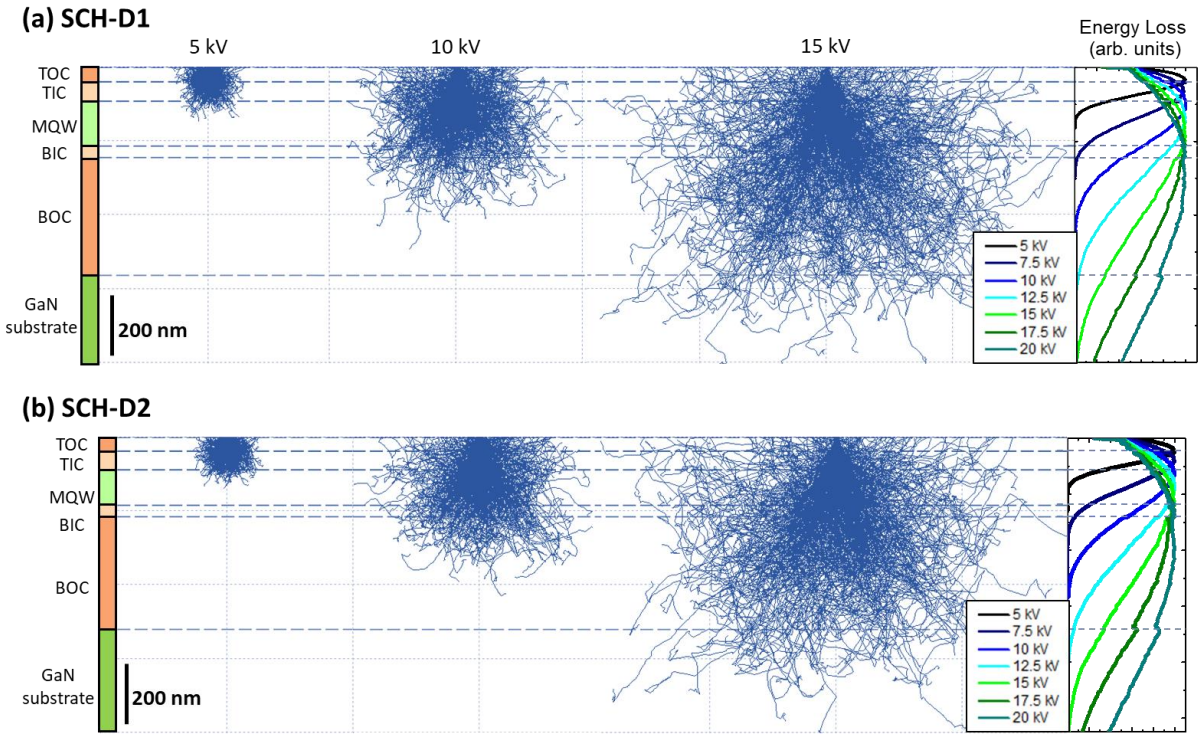

Figure 4.4. *Simulation of the electron beam trajectory through the (a) SCH-D1 and the (b) SCH-D2 at different acceleration voltages. The right panel shows the electron energy loss profile for various acceleration voltages.*

Figure 4.4 shows CASINO simulations of the electron beam penetration into SCH-D1 and SCH-D2 at acceleration voltages between 5 and 15 kV. The calculation shows that the MQW is placed so that the overlap with the electron beam is maximized at 10 kV, so that, at this acceleration voltage, most of the generation is contained within the inner claddings. In comparison, the bombardment at 5 kV is not enough to reach the MQW, whereas the injection at 15 kV mostly spreads into the BOC layer, reaching even the GaN substrate. For further evidence, the overlap between the generation profile and the MQW region as a function of the acceleration voltage is presented in Figure 4.5(a).

Keeping the acceleration voltage at 10 kV, we have studied the variation of the overlap of the optical mode with the MQW region as a function of the total top cladding thickness (i.e. the thickness of the TIC+TOC, whose thicknesses were modified proportionally when varying the total top cladding thickness), with the results summarized in Figure 4.5(b). For thicker top layers, the MQW is located deeper into the structure and the percentage of electrons that can reach it decreases. On the contrary, shortening the top layers thickness down to a total of 50 nm can slightly increase the overlap. However, such a change has detrimental consequences for the optical confinement. Therefore, we decided that the values stated in Table 4.1 represent a good compromise between all previously stablished conditions.

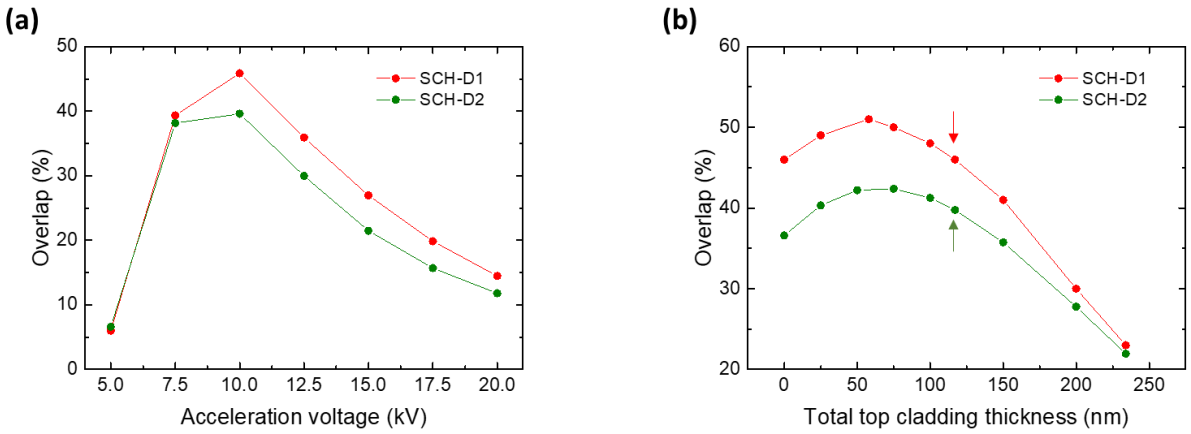

Figure 4.5. *(a) Overlap between the MQW and the electron energy loss profile at different acceleration voltages. (b) Overlap between the MQW and the electron energy loss profile at 10 kV for different top cladding layers thickness (i.e. TOC+TIC total thickness, with each layer thickness varying proportionally). Arrows mark the total top cladding thickness chosen in our designs.*

(iii) Emission wavelength tunability

The emission wavelength can be shortened by reducing the width of the QW, due to the higher confinement and reduced quantum confined Stark effect. Figure 4.6(a) and (b) presents simulated band diagrams for SCH-D1 and SCH-D2, respectively, indicating the first quantum confined states for electrons and holes with blue and red dashed lines, respectively. From the simulation, which considers a lattice temperature of 300 K, the band gap of the GaN in the QWs is E_g = 3.45 eV in both samples. However, the transition energy is larger than that in both cases.

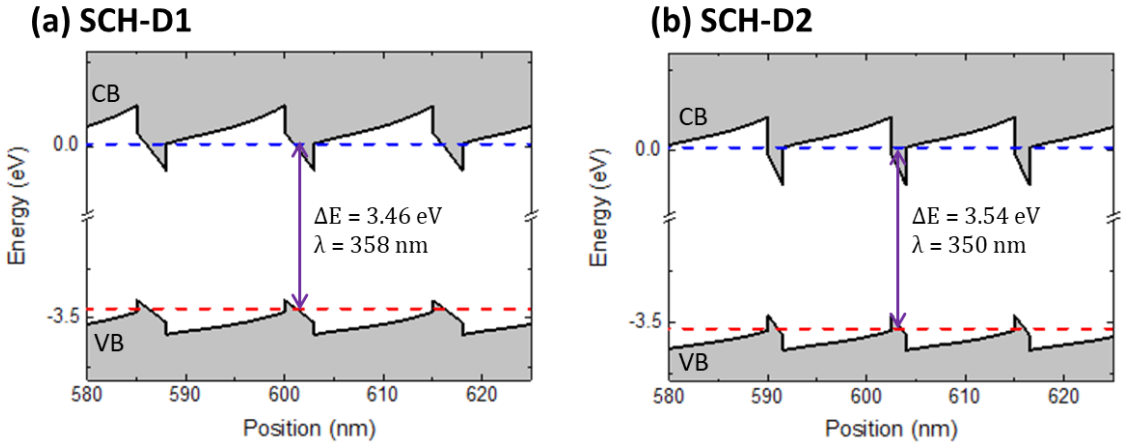

Figure 4.6. *Simulated band diagram for (a) SCH-D1 and (b) SCH-D2. Dashed lines represent the first quantum confined levels for electrons (blue) and holes (red).*

4.1.2 Graded-index separate confinement heterostructures

In order to promote the carrier diffusion from claddings towards the MQW, we modified the original SCH-D2 design to implement a graded-index separate confinement heterostructure (GRINSCH). With this concept, the interfaces between inner and outer AlGaN cladding layers become compositionally graded. Consequently, the diffusion of electrons is promoted while the waveguiding properties of the structure are preserved [192,193]. GRINSCH designs are generally not used in III-nitride laser diodes since they introduce a perturbation of the doping distribution due to the variation of polarization in the graded layers [194,195]. Increasing the Al mole fraction along the [0001] direction results in n-type doping, whereas decreasing the Al mole fraction along the [0001] leads to p-type doping. If we keep in mind the requirement of higher refractive index in the core of the waveguide, GRINSCH structures are only compatible with the n-layer on top designs, or with structures grown along the N-polar direction. In spite of this limitation, some recent reports are trying to implement an inverted graded layer to obtain p-type conductivity without impurity doping, at the cost of requiring a much more complex waveguide to compensate the additional modal losses [39,40]. However, these restrictions are not relevant in an electron beam pumped device, so that the advantages of the graded index layers can be fully exploited.

The two designs that incorporate graded layers are described in Figure 4.7 and Table 4.2. The first design, labelled "GRINSCH", is a modification of SCH-D2 where the interfaces between inner and outer cladding layers are graded along 40 nm. With respect to SCH-D2, the GRINSCH structure preserves the location of the active region along the growth axis and the waveguide properties. The second design, labelled "a-GRINSCH", is an asymmetric version of GRINSCH, where the top graded layer extends to the edge of the MQW, and the Al molar fraction of the TOC layer is increased to 30%.

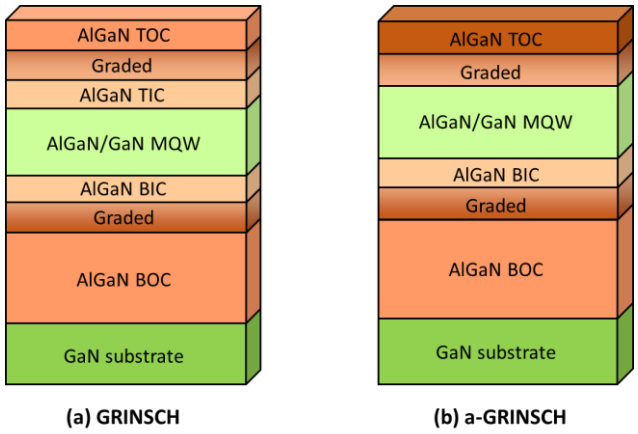

Figure 4.7. *Schematic view of the (a) GRINSCH and (b) a-GRINSCH designs.*

Table 4.2. *Description of the graded designs in terms of thickness and Al content on the layers, following the general design in Figure 4.7.*

	GRINSCH	a-GRINSCH
TOC	30 nm $Al_{0.2}Ga_{0.8}N$	50 nm $Al_{0.3}Ga_{0.7}N$
Graded	40 nm	55 nm
TIC	47 nm $Al_{0.1}Ga_{0.9}N$	-
MQW	10×(1.5 nm GaN/11 nm $Al_{0.1}Ga_{0.9}N$)	10×(1.5 nm GaN/11 nm $Al_{0.1}Ga_{0.9}N$)
BIC	20 nm $Al_{0.1}Ga_{0.9}N$	20 nm $Al_{0.1}Ga_{0.9}N$
Graded	40 nm	40 nm
BOC	380 nm $Al_{0.2}Ga_{0.8}N$	380 nm $Al_{0.2}Ga_{0.8}N$

Figure 4.8 shows the Al concentration profile along the growth direction and the simulated band diagram for the SCH-D2, GRINSCH and a-GRISNCH designs. In the case of SCH-D2, depicted in Figure 4.8(a), the difference in spontaneous and piezoelectric polarization between the waveguide core and the outer cladding results in a strong band bending that favors electron accumulation at the TIC/TOC interface and hole accumulation at the BOC/BIC interface (red arrows in the figure). The perturbation of the bands hinders the carrier transfer to the MQW. This problem is corrected in the GRINSCH design, where the graded interfaces inserted between inner and outer cladding layers result in a band diagram with smooth energy transitions at the heterointerfaces (see Figure 4.8(b)). To further reduce the carrier recombination rate in the top cladding layers, we consider the a-GRINSCH design with band diagram depicted in Figure 4.8(c). The purpose of this design is to force carriers generated in the top layers to diffuse towards the active region (see dashed red circle in the figure).

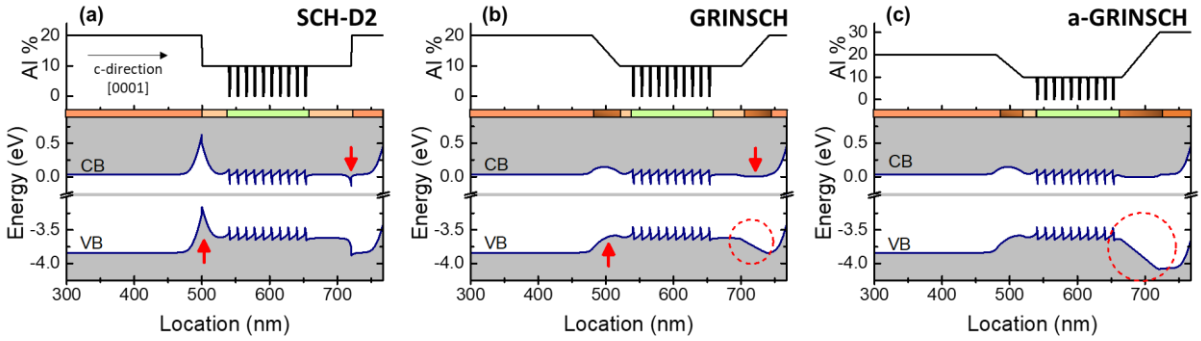

Figure 4.8. *Aluminium concentration along the growth direction and simulated conduction and valence band profile (CB and VB, respectively) for (a) SCH-D2, (b) GRINSCH and (c) a-GRINSCH. Red marks aid to identify the main differences in the band profiles.*

All the modifications introduced in the graded designs are intended to improve the carrier collection with respect to SCH-D2, while preserving the assets of the original design discussed in section 4.1.1: waveguiding capabilities, optimum operation at around 10 kV and targeted emission

wavelength at 350 nm. We have also performed calculations of the OCF and electron penetration depth for the GRINSCH and a-GRINSCH designs, with the results summarized in Figure 4.9. The results are very similar to those obtained for SCH-D2, presenting an OCF of 3.7% and 3.8% for the GRINSCH and a-GRINSCH, respectively. The maximum overlap between the active region and the electron beam occurs around 10 kV.

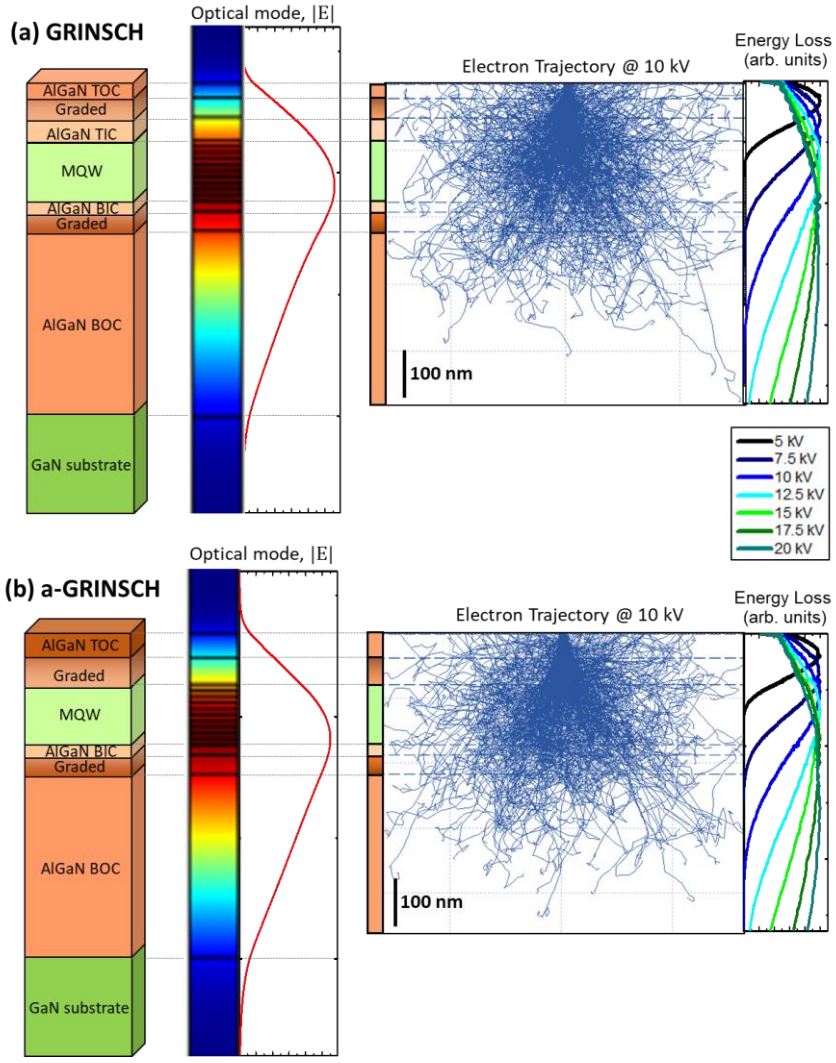

***Figure 4.9**. Simulation of the first optical mode distribution and the electron beam penetration in the (a) GRINSCH and (b) a-GRINSCH designs.*

4.2 Synthesis of the AlGaN/GaN heterostructures

In this section, I describe the synthesis of the AlGaN/GaN heterostructures based on the SCH-D1, SCH-D2, GRISNCH and a-GRINSCH designs. Then, I present the results of their structural characterization, focusing on four samples summarized in Table 4.3. These samples were chosen as the most representative examples for each design.

Table 4.3. *Summary of the samples under study and their corresponding design.*

Sample	Design
E3980	SCH-D1
E3997	SCH-D2
E4025	GRINSCH
E4044	a-GRINSCH

4.2.1 Growth conditions

The heterostructures were synthesized on free-standing, non-intentionally doped, n-type conductive GaN(0001) substrates. Rectangular pieces of ≈ 1 cm × 2 cm were obtained from the original wafer by mechanical cleaving with a diamond tip. The substrate was degreased in organic solvents (dichloromethane, acetone and methanol), mounted on a mollyblock with molten indium, and introduced in the PAMBE chamber described in section 3.1.1.

The epitaxial structures were grown at a substrate temperature T_S = 720 °C, and the growth rate was 0.5 ML/s. The relatively low growth rate allowed a precise control of the growth process. As stated in section 3.1.3, slightly Ga-rich conditions are required to obtain smooth GaN layers. Therefore, before each growth, I calibrated the Ga flux required to attain the Ga bilayer regime by measuring the changes in the RHEED intensity due to the Ga desorption during an interruption of the growth of GaN. The growth of planar AlGaN also requires metal-rich conditions, as stated in section 3.1.5. For low Al concentrations, this can be achieved by fixing the Al/N flux ratio at the required Al content and providing a metal exceed with Ga. The Al flux required for each Al content was calibrated beforehand via RHEED oscillations during the growth of AlN. The Ga flux was kept constant at the value required to grow GaN in the Ga bilayer regime. To maintain the III/N ratio constant, the growth was monitored in real time by RHEED. For the graded layers, the Al flux was increased/decreased linearly along the length of the layer.

4.2.2 Structural characterization

The structural quality of the samples was validated using XRD and STEM. Figure 4.10(a) shows the HRXRD θ-2θ scan around the (0002) reflection of GaN for sample E3980, compared with a theoretical calculation of the diffractogram. The calculation assumed the structure to be pseudomorphic on the BOC layer, which in turn was assumed 50% relaxed on the GaN substrate. There is an excellent agreement between the calculation and the experiment. The most intense peak of the diffractogram is attributed to the GaN substrate, and the second highest, located at slightly higher angles, to the TOC and BOC $Al_{0.15}Ga_{0.85}N$ layers. The reflection from the $Al_{0.07}Ga_{0.93}N$

layers is not resolved due to its proximity to the MQW reflection. The satellites of the MQW reflection allow a precise determination of the MQW period using equation (3.2). For E3980, we obtained a period of 14.1 nm. Figure 4.10(b) presents the XRD θ-2θ scan for samples E3997, E4025 and E4044, which share the same MQW nominal period, compared with the theoretical calculation of the E3997 diffractogram. In this case, the distance between MQW satellite peaks is larger compared to E3980, indicating a shorter period in real space, as expected. The most intense peak corresponds to the reflection of the GaN substrate, and the second highest to the $Al_{0.2}Ga_{0.8}N$ layers. In the case of E4044, an extra peak appear at higher angles, corresponding to the reflection of the $Al_{0.3}Ga_{0.7}N$ TOC layer. The MQW satellites of the three samples are almost aligned due to their almost identical periods, which were calculated to be 11.1 nm for E3997, 10.9 nm for E4025 and 11 nm for E4044.

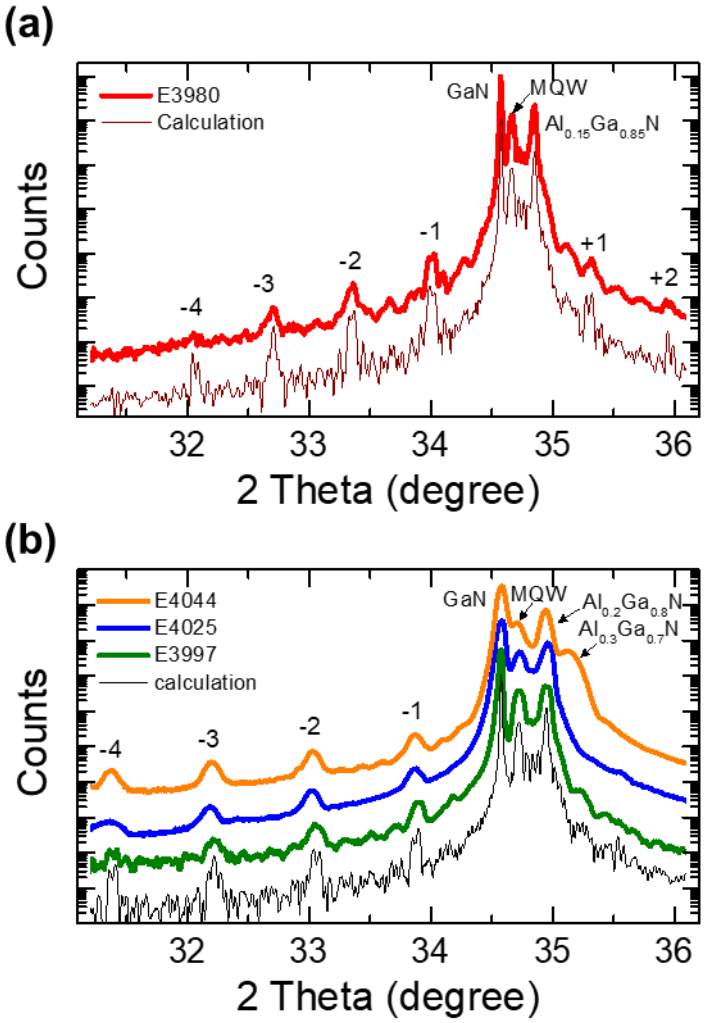

Figure 4.10. *XRD θ-2θ scan around the (0002) reflection of GaN for samples (a) E3980, and (b) E3997, E4025 and E4044. Labels identify the reflections originating from the GaN substrate, the $Al_{0.15}Ga_{0.85}N$, $Al_{0.2}Ga_{0.8}N$ and $Al_{0.3}Ga_{0.9}N$ layers and the MQWs, with several satellites. Experimental results are compared with theoretical calculations of the diffractograms for E3980 and E3997.*

From the periods extracted from the XRD data, we can correct our estimation of the growth rate and calculate the thickness for each individual layer of the samples. Table 4.4 summarizes the real architectures obtained, which slightly differ in thickness from the nominal designs. These measurements were confirmed by HAADF-STEM images, shown in Figure 4.11 for E3997, E4025 and E4044. Clear contrast corresponds to layers with higher Ga concentration. Note the difference between the sharp $Al_{0.2}Ga_{0.8}N/Al_{0.1}Ga_{0.9}N$ interfaces in E3997 (Figure 4.11(a), left panel) and the graded layers in E4025 (Figure 4.11(b), left panel) and E4044 (Figure 4.11(c), left panel). The zoomed images of the MQWs on the right side are consistent with the periods obtained from XRD measurements.

Table 4.4. *Description of the samples under study with the real thickness extracted from XRD and STEM measurements.*

	E3980	**E3997**	**E4025**	**E4044**
TOC	47 nm $Al_{0.15}Ga_{0.85}N$	44.4 nm $Al_{0.2}Ga_{0.8}N$	26.4 nm $Al_{0.2}Ga_{0.8}N$	44.2 nm $Al_{0.3}Ga_{0.7}N$
Graded	-	-	35.2 nm	48.7 nm
TIC	63 nm $Al_{0.07}Ga_{0.93}N$	59.5 nm $Al_{0.1}Ga_{0.9}N$	41.4 nm $Al_{0.1}Ga_{0.9}N$	-
MQW	10×(2.8 nm GaN/ 11.4 nm $Al_{0.07}Ga_{0.93}N$)	10×(1.4 nm GaN/ 9.8 nm $Al_{0.1}Ga_{0.9}N$)	10×(1.3 nm GaN/ 9.7 nm $Al_{0.1}Ga_{0.9}N$)	10×(1.3 nm GaN/ 9.7 nm $Al_{0.1}Ga_{0.9}N$)
BIC	37.6 nm $Al_{0.07}Ga_{0.93}N$	35.5 nm $Al_{0.1}Ga_{0.9}N$	17.6 nm $Al_{0.1}Ga_{0.9}N$	17.7 nm $Al_{0.1}Ga_{0.9}N$
Graded	-	-	35.2 nm	35.4 nm
BOC	376 nm $Al_{0.15}Ga_{0.85}N$	355 nm $Al_{0.2}Ga_{0.8}N$	332 nm $Al_{0.2}Ga_{0.8}N$	334 nm $Al_{0.2}Ga_{0.8}N$

Table 4.5 presents the full width at half maximum (FWHM) of the X-ray ω-scan around the (0002) reflection of the MQWs from E3997, E4025 and E4044, the 3 samples with the same nominal MQW structure. The comparison points to an improvement of the crystalline quality in samples that incorporate graded layers. This result is consistent with the structural studies of Sun *et al*. [192], who showed that such compositionally graded AlGaN layers may serve as a strain transition buffer which blocks threading dislocations.

Table 4.5. *Experimental measurement of the full width at half maximum of the ω-scan of the (0002) X-ray reflection of the MQW (Δω).*

	E3997	**E4025**	**E4044**
Δω	208 arcsec	128 arcsec	158 arcsec

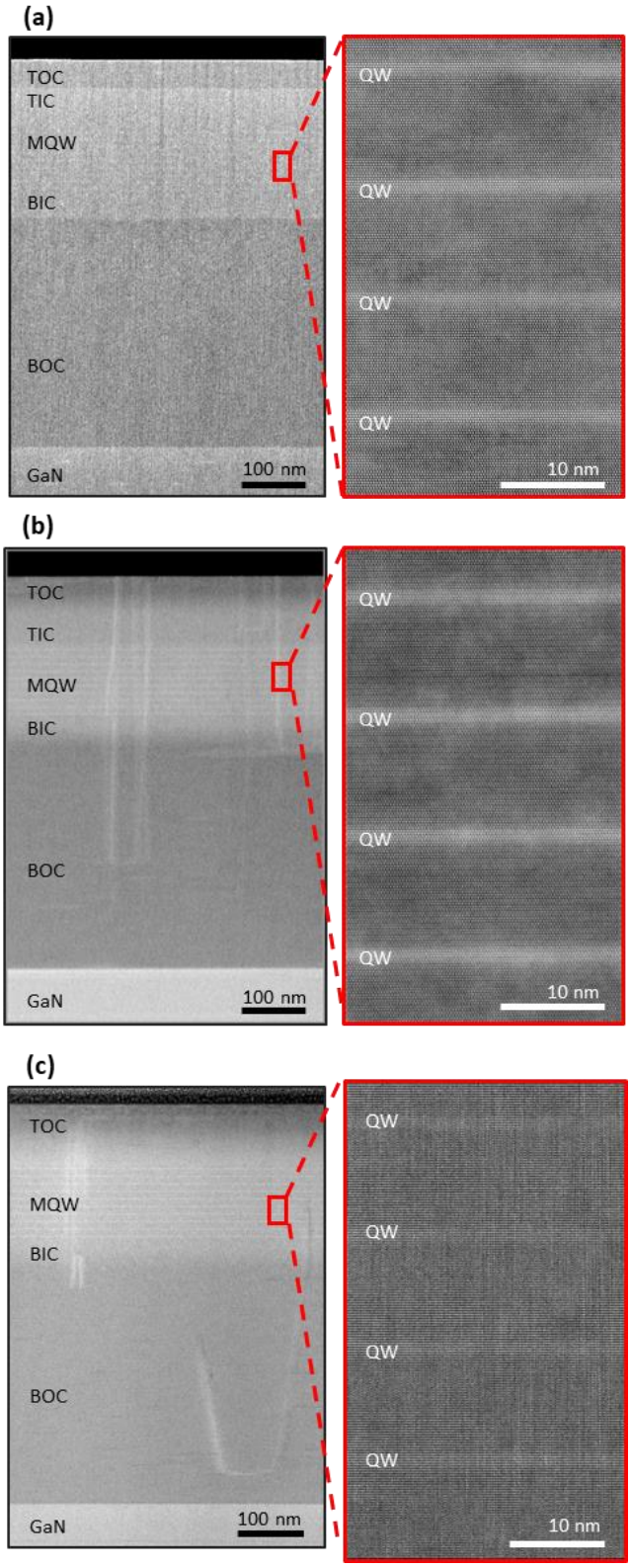

Figure 4.11. *HAADF-STEM images of samples (a) E3997, (b) E4025, (c) E4044, observed along the [11-20] zone axis. A zoomed view of four quantum wells in the MQW is outlined in red.*

To gain further insight into the samples, we performed reciprocal space maps (RSM) around the (10-15) reflection, which can provide information on the Al molar fraction and the strain state of the layers. In the reciprocal space map of sample E3980 in Figure 4.12(a), we can identify the reflection from the $Al_{0.15}Ga_{0.85}N$ claddings, whose location confirms that the Al mole fraction is 0.150 ± 0.005 and the BOC layer is partially relaxed. The reflection of $Al_{0.15}Ga_{0.85}N$ and the satellites of the MQW are vertically aligned, which confirms that the MQW grows pseudomorphically on the bottom cladding layer. Similar situation occurs for samples E3997 and E4044, whose RSMs are presented in Figure 4.12(b) and (c), respectively. In these samples, the reflections of the MQW are aligned with the BOC reflection. From the angular location of the $Al_xGa_{1-x}N$ reflections, we can estimate that the Al molar fraction is 0.23 and 0.34 in the BOC and TOC layers of E4044, respectively, which is slightly higher than the nominal values.

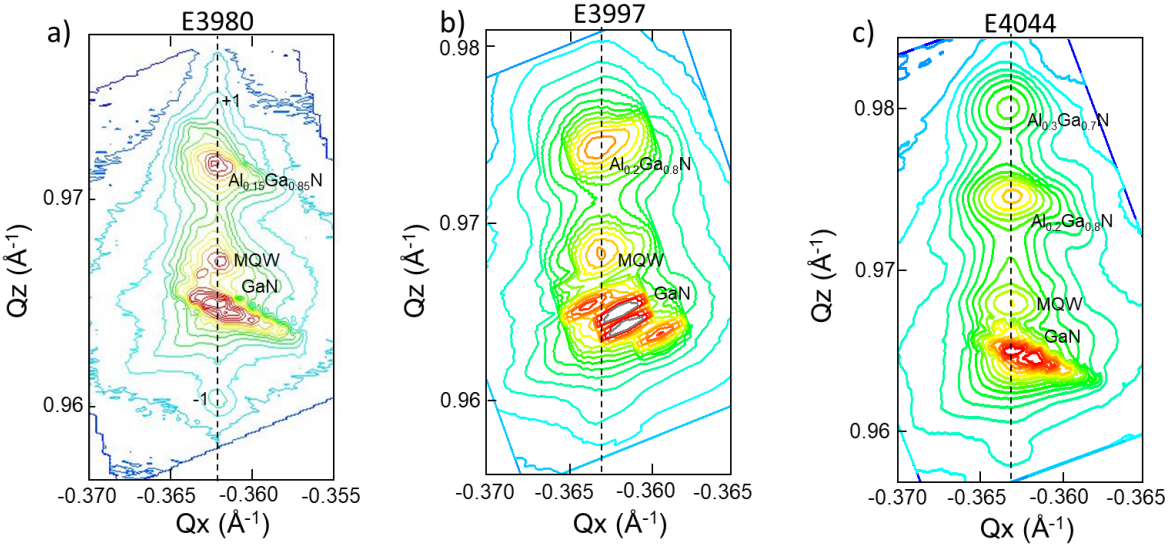

Figure 4.12. *Reciprocal space map around the (10-15) reflection of GaN for samples (a) E3980, (b) E3997 and (c) E4044. Note that for this reflection, the in-plane reciprocal vector is* $Q_x = -2/(a\sqrt{3})$*, where "a" is the in-plane lattice parameter, and the out-of-plane reciprocal vector is* $Q_z = 1/(5c)$*, where "c" is the out-of-plane lattice parameter.*

Complementary studies of the AlGaN molar fraction of the layers were performed by energy-dispersive X-ray spectroscopy (EDX) in STEM by Florian Castioni (CEA-LETI). EDX is a characterization technique that consists in exciting the material with an electron beam and collecting the X-ray generated due to radiative electronic transitions between core electron levels in the atoms. The emitted wavelength is characteristic of each atomic element. Figure 4.13(a) shows a HAADF STEM image together with EDX intensity maps for Al, Ga and N for samples E3997 and E4044. The progressive decrease of signal in the topmost layer of E4044, leading to a blurry area, is due to the fact that the edge of the lamella was damaged during FIB preparation, despite the use of protective layers, and the proximity of vacuum can cause artefacts on X-ray absorption. Figure 4.13(b) presents the atomic fraction of Al, Ga and N extracted from the EDX measurements

along the [0001] growth direction for both samples, calibrated with stoichiometric reference samples of known thicknesses [196]. From them, we confirm that the Al concentration in the outer cladding layers is slightly higher than nominal, as observed in the XRD measurements, attaining 0.25 and 0.38 in the BOC and TOC cladding layers of E4044, respectively. Note that the values of the top cladding layer must be taken as a rough estimation, due to their proximity to the deposited protective layers or to vacuum.

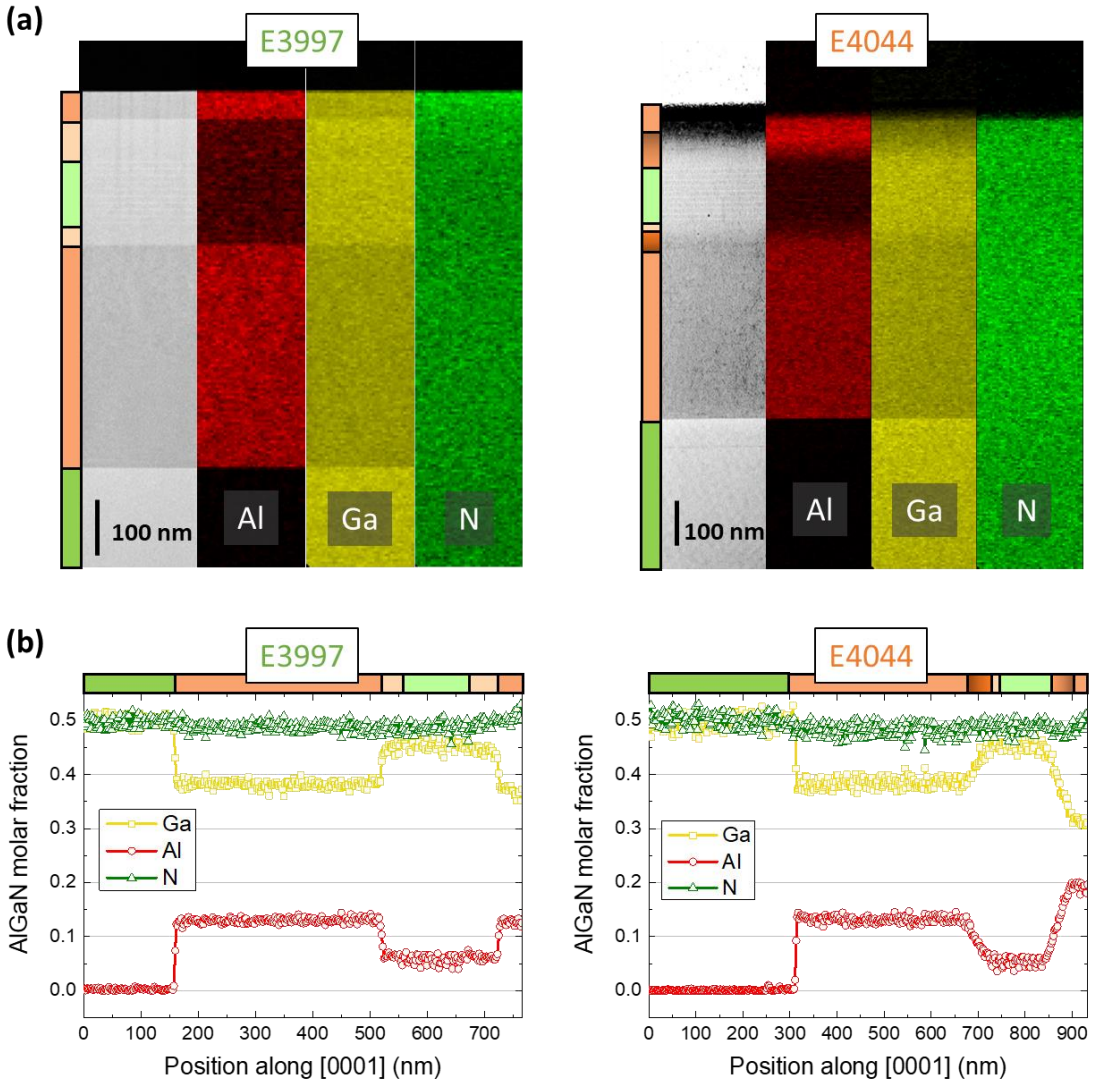

Figure 4.13. *(a) HAADF STEM image and EDX measurement of Al-K_α, Ga-K_α and N-K_α transitions in E3997 and E4044. (b) Quantitative EDX results of Al, Ga and N mole fractions along the growth direction for samples E3997 and E4044. Note that the mole fraction notation $Al_xGa_yN_{(1-x-y)}$ given in the graph is different from the relative concentration between III-atoms $Al_xGa_{(1-x)}N$ used in the rest of the manuscript.*

The relaxation of misfit strain can take place by generation of dislocation or propagation of cracks. In our samples, the latter mechanism is clearly observed in an optical microscope, as illustrated in Figure 4.14. Cracks appear parallel to the cleaved edge and forming 60° angle, which confirms that they propagate along the *m*-planes. Such cracks are generated in AlGaN layers grown under tensile stress, as it is the case here due to the lattice mismatch with the GaN

substrate. The presence of cracks is not catastrophic for the device performance, since the distance between cracks is large enough to allow the fabrication of devices.

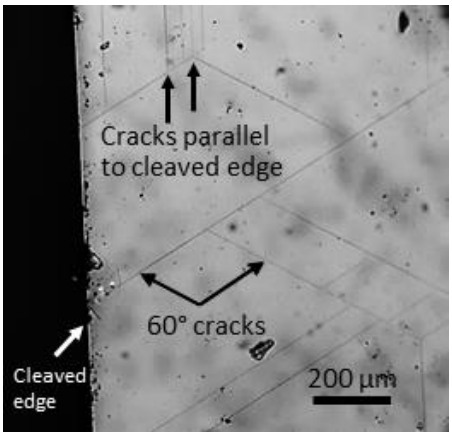

Figure 4.14. *Top view of sample E3980 in the proximity of a cleaved edge following the m-plane. Cracks propagate either parallel to the cleaved edge or forming an angle of 60°.*

4.3 Optical properties of the AlGaN/GaN heterostructures

In this section, I describe the spontaneous emission of the various AlGaN/GaN heterostructures under electron beam or optical excitation. The section includes calculations of the internal quantum efficiency and net gain.

4.3.1 Spontaneous emission under electron beam excitation

Since the final purpose of these AlGaN/GaN heterostructures is to operate under electron beam excitation, we performed cathodoluminescence measurements as a function of the acceleration voltage, V_a, to study the penetration of the beam on the samples. Figure 4.15 presents the cathodoluminescence spectra for the 4 samples under study. Increasing V_a implies increasing the penetration depth of the electron beam, as described in section 2.3.3. Electron-hole pairs generated by impact ionization in the surface layer or deep inside the structure have to diffuse towards the MQW to emit at the desired wavelength. Therefore, the evolution of the CL as a function of V_a gives information about the efficiency of the carrier collection process. This measurement is performed with the injection current remaining approximately constant. The CL spectra are normalized by dividing by the acceleration voltage and injection current, so that their comparison provides a direct view of the evolution of the conversion efficiency. The CL measurements presented here were recorded using a CL-SEM system, which does not reach high enough current densities to attain the amplified spontaneous emission regime. Furthermore, the

experiments were performed in as-grown material, without mirror processing, so that lasing is not expected.

The CL spectra for sample E3980 (see Figure 4.15(a)) presents a main peak coming from the MQW at 360 nm, in good agreement with the targeted wavelength, and a less intense peak at 350 nm attributed to the BIC/TIC $Al_{0.07}Ga_{0.93}N$ layers. A third peak arising at high voltages, attributed to the BOC $Al_{0.15}Ga_{0.85}N$ layer, is consequence of a long penetration depth of the electron beam, which reaches the BOC at a depth longer than the electron-hole pair diffusion length, preventing them to reach the active region.

The CL spectra for sample E3997 (see Figure 4.15(b)) at low acceleration voltages is dominated by recombination in the MQW (peak at 353 nm, shorter than the peak emission of E3980, as targeted). This means that carriers generated close to the surface are efficiently transferred to the MQW. However, a very weak signal around 322 nm is visible for V_a = 5 kV, and it is assigned to the recombination in the $Al_{0.2}Ga_{0.8}N$ TOC layer. In view of the intensity of the curves, the efficiency of the device is maximum in the range of V_a = 7-10 kV. At higher acceleration voltages, a secondary peak at 342 nm assigned to recombination in the $Al_{0.1}Ga_{0.9}N$ inner cladding layers appears, and it becomes dominant for V_a > 12 kV. This behavior points out that carriers generated in the BIC layer have problems to diffuse to the MQW. The origin of this issue becomes evident when looking at the band diagram in Figure 4.8(a). The strong band bending at the $Al_{0.1}Ga_{0.9}N/Al_{0.2}Ga_{0.8}N$ heterointerfaces sets potential barriers (marked with red arrows in the figure) that hinder the carrier transfer to the MQW.

The effect of the incorporation of a GRINSCH region is observable in the CL spectra from sample E4025 (see Figure 4.15(c)). The spectra present a main peak at 352 nm assigned to the MQW and a secondary peak at 339 nm attributed to recombination in the $Al_{0.1}Ga_{0.9}N$ inner cladding layers. A third peak appearing at 324 nm under high acceleration voltage (V_a > 10 kV) is assigned to emission from the $Al_{0.2}Ga_{0.8}N$ BOC layer when the energy of the injected electrons is high enough to penetrate deeper than the GRINSCH region (penetration depth represented in the right panel in Figure 4.9(a)). At the same time, the integrated intensity starts to decrease, probably due to reabsorption of the luminescence from the BOC by the upper layers. In comparison with the CL data from E3997 (SCH design), the intensity of the emission from the $Al_{0.1}Ga_{0.9}N$ for V_a > 10 kV is considerably lower when compared with the MQW line. This confirms an improvement on the transfer from the BIC to the MQW. However, the line at 339 nm is clearly resolved at low accelerating voltages, which implies that carriers recombine in the TIC layer, in the region outlined with a dashed circle in Figure 4.8(b), without diffusing to the MQW.

The emission peaks from E4025 are significantly narrower than those from E3997, although both samples have the same alloy composition, approximately the same QW thickness and they

emit at the same wavelength. The reduction of the FWHM can be attributed to a lower defect density in the structure with GRINSCH due to the smooth change in the lattice parameter between cladding layers. This is consistent with the discussion on the FWHM of the X-ray Δω from section 4.2.2.

In summary, the CL data of sample E4025 represents an improvement with respect to sample E3997 thanks to the enhanced carrier diffusion from the bottom layers. However, further efforts are needed to reduce the carrier recombination rate in the top cladding layers. Sample E4044 addresses this issue by incorporating an asymmetric GRINSCH model, where the top graded layer extends to the edge of the MQW region and attains a higher Al content at the surface (see in Figure 4.8(c)). The CL spectra for E4044 in Figure 4.15(d) shows the predominance of the MQW peak at 351 nm. A peak at 323 nm, assigned to the $Al_{0.2}Ga_{0.8}N$ BOC layer, appears only at high acceleration voltage, when the carriers penetrate deeper than the collection region of the GRINSCH. For operation with $V_a \leq 7$ kV, 99% of the emission comes from the MQW. For comparison purposes, in the case of E4025, at the same acceleration voltage, the light emitted from the MQW was around 75% of the total emission.

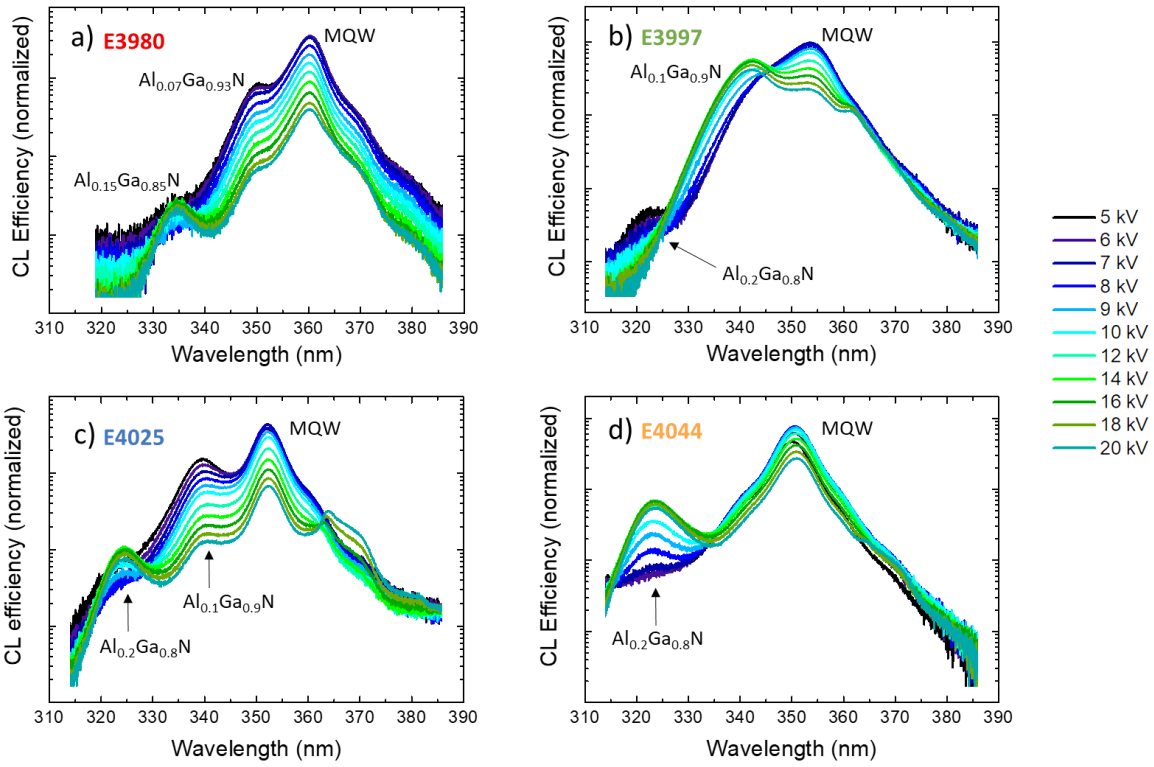

Figure 4.15. *CL spectra recorded at different acceleration voltages for (a) E3980, (b) E3997, (c) E4025 and (d) E4044. The CL spectra are normalized by dividing by the acceleration voltage and injection current.*

4.3.2 Study of the internal quantum efficiency

The performance of a UV emitter can be described by its external quantum efficiency (EQE), which is the ratio between the number of photons detected and the number of photons (optical pumping) or electrons (electrical pumping) injected into the device, as already introduced in section 2.3.2. Also, in the case of a laser, a relevant parameter is the differential EQE, Δ_{EQE}, extracted from the slope of the output power vs the pumping power curve above the lasing threshold. However, to assess the material properties, it is also interesting to refer to the internal quantum efficiency (IQE), which is defined as the product between the injection efficiency and the recombination efficiency as $IQE = \eta_{inj} \times \eta_{rad}$.

The IQE is generally extracted from temperature-dependent PL measurements. It is often assumed that the IQE at a certain temperature (T) can be calculated as

$$\mathrm{IQE(T)} = \frac{I_{PL}(T)}{I_{PL}(T = 0\ K)} \tag{4.1}$$

where $I_{PL}(T)$ is the integrated PL intensity at T. This estimation is based on the hypothesis that the PL intensity saturates at low temperatures, since carrier freeze out prevents them from reaching non-radiative recombination centers.

To obtain the intrinsic IQE associated with the material properties, the excitation should introduce as little perturbation as possible. For this reason, we have performed low-injection temperature-dependent PL measurements (continuous-wave laser at 10 µW) with results presented in Figure 4.16. The multiple MQW peaks are attributed to longitudinal-optical (LO) phonon relaxations, as all the peaks are separated by the characteristic energy of these phonons in GaN, being $E_{LO} \approx 92$ meV. To understand the spectra, we must keep in mind the penetration depth of the pumping laser. In view of the absorption coefficient of GaN, 80% of the absorption occurs in the TOC+TIC layers, and carriers have to diffuse towards the MQW, as depicted in Figure 4.17. Therefore, the observed transitions can be assigned to recombination in the TOC and TIC layers, in the MQW, and to a low energy band due to donor-acceptor pair (DAP) recombination, as indicated in the figures. In all the samples under study, the ratio of the integrated PL intensity from the MQW at room temperature and at low temperature is systematically lower than 1%. Such values are generally observed in GaN-based MQWs measured under low injection conditions [197,198].

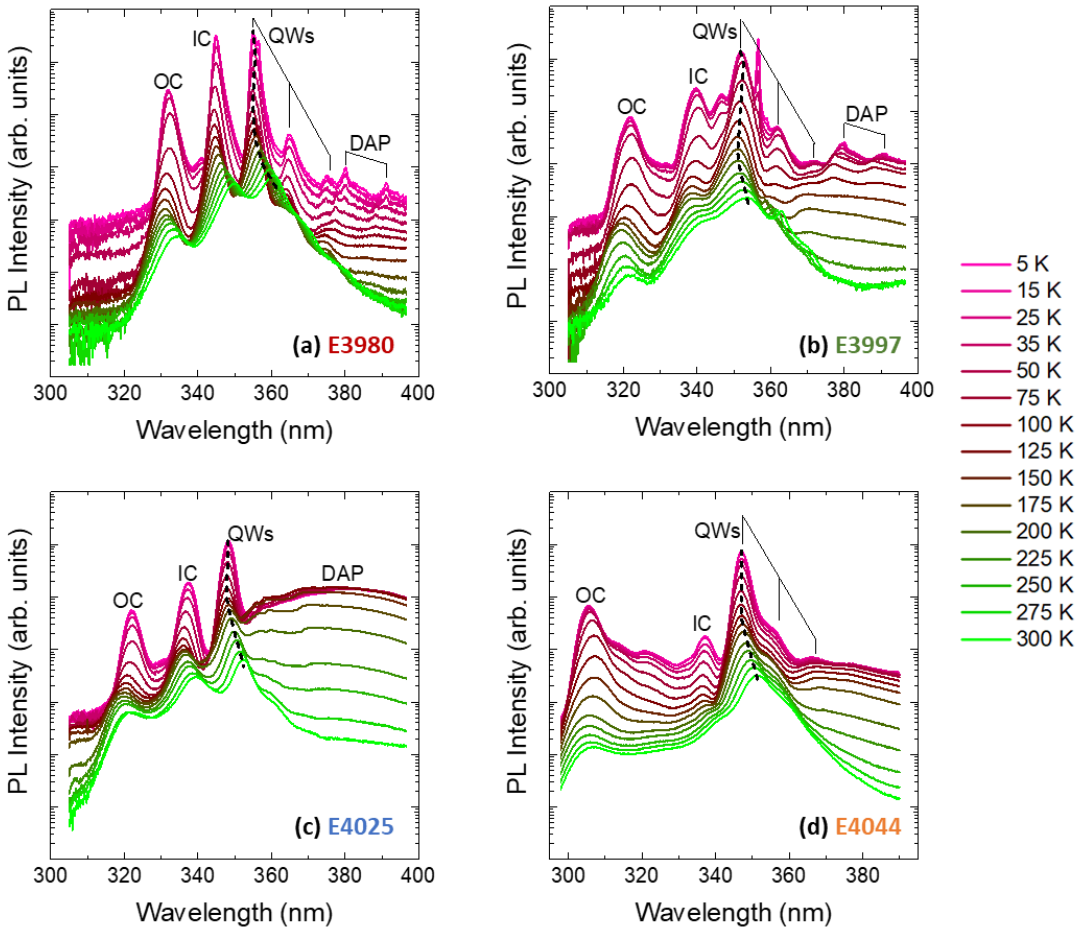

Figure 4.16. *PL spectra at low injection conditions for samples (a) E3980, (b) E3997, (c) E4025 and (d) E4044. The emission assigned to the outer claddings (OC), inner claddings (IC), MQW, and donor-acceptor pair (DAP) recombination are indicated in the figures. Solid lines associate the MQW line with its first and second phonon replicas. Dashed curves describe the evolution of the MQW emission with temperature.*

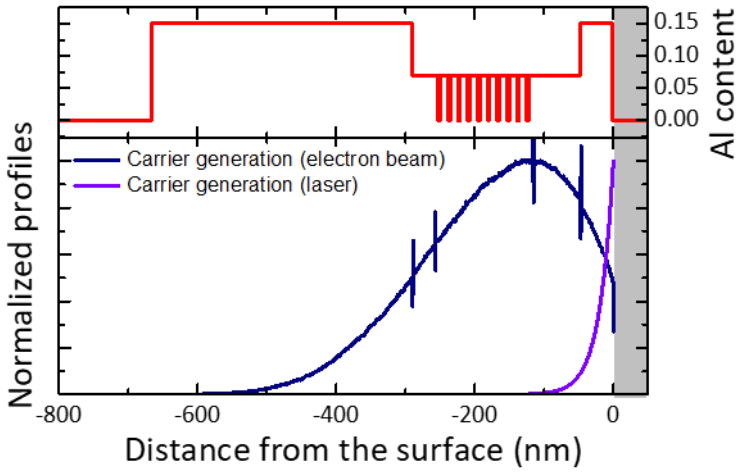

Figure 4.17. *Calculations of the carrier generation a function of depth, normalized to its maximum, in the cases of pumping with an electron beam (acceleration voltage V_a = 10 kV) or with a UV laser (wavelength λ = 266 nm). The calculation used the absorption coefficients reported by Muth et. al. in [191]. The alloy concentration profile corresponds to sample E3980.*

Looking at the PL line assigned to the MQW in Figure 4.16, the spectral evolution of the PL peak presents an S shape, outlined with dashed lines in the figures. This behavior is assigned to the

localization of carriers in potential fluctuations in the QWs [199], which can be due to fluctuations of the QW thickness or alloy inhomogeneities in the QW barrier. Figure 4.18 shows the evolution of the MQW PL peak energy as function of temperature for the four samples, and the high temperature trend is fitted with Varshni's equation [82], introduced as equation (2.9) in section 2.1.4, which defines the theoretical evolution of the material band gap as a function of temperature.

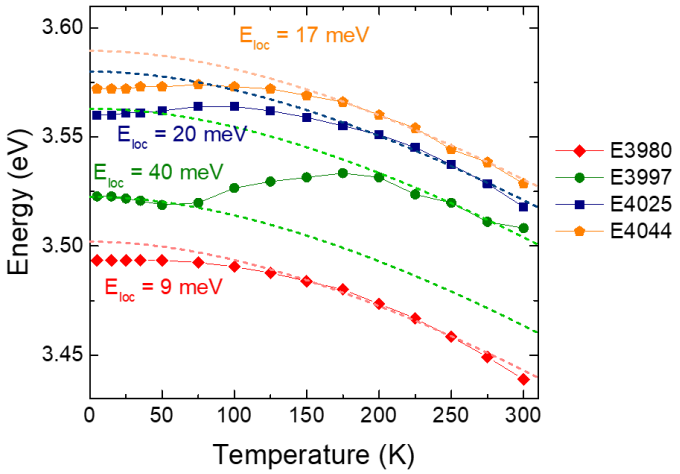

Figure 4.18. *Variation of the MQW peak energy as a function of temperature, compared with the trend given by the Varshni equation (dashed lines) to estimate the carrier localization energy, E_{loc}.*

The deviation from Varshni's trend observed at low temperatures provides an estimation of the carrier localization energy, by extracting the difference between the trend and the experimental results at low temperatures. In some works it has been stated that carrier localization is directly related to the crystal quality of the material [200], since structural irregularities can translate into alloy inhomogeneities or thickness fluctuations in nanostructures. In our samples, if we compare the two SCH designs, the localization energy varies from E_{loc} = 9±0.5 meV for E3980 to 40±2 meV for E3997, which means higher localization in the sample with thinner QWs.

If we compare the samples with the same QW size, where the localization energy varies from E_{loc} = 40±2 meV for E3997 to 20±1 meV for E4025 and 17±1 meV for E4044. In the QWs, localization can be due to alloy inhomogeneities in the barriers or fluctuations of the QW thickness. A similar study applied to the TIC line, assigned to recombination in the $Al_{0.1}Ga_{0.9}N$ inner cladding, leads to E_{loc} = 42±4 meV for E3997 to 37±4 meV for E4025 and 19±3 meV for E4044. In the TIC, localization should be associated with alloy fluctuations. The trends are consistent with the results of energy dispersive X-ray analysis (EDX) measurements in TEM, presented in Figure 4.19, which show that E3997 presents both more thickness fluctuations in the QWs and larger alloy inhomogeneities in the barriers than E4044.

We also note that the localization energy in the TOC layers, with higher Al content, increases to the range of 44-53 meV in all the samples, which hinders the diffusion of carriers toward the MQW at low temperature and explains the presence of the TOC-related lines in all the spectra in Figure 4.16.

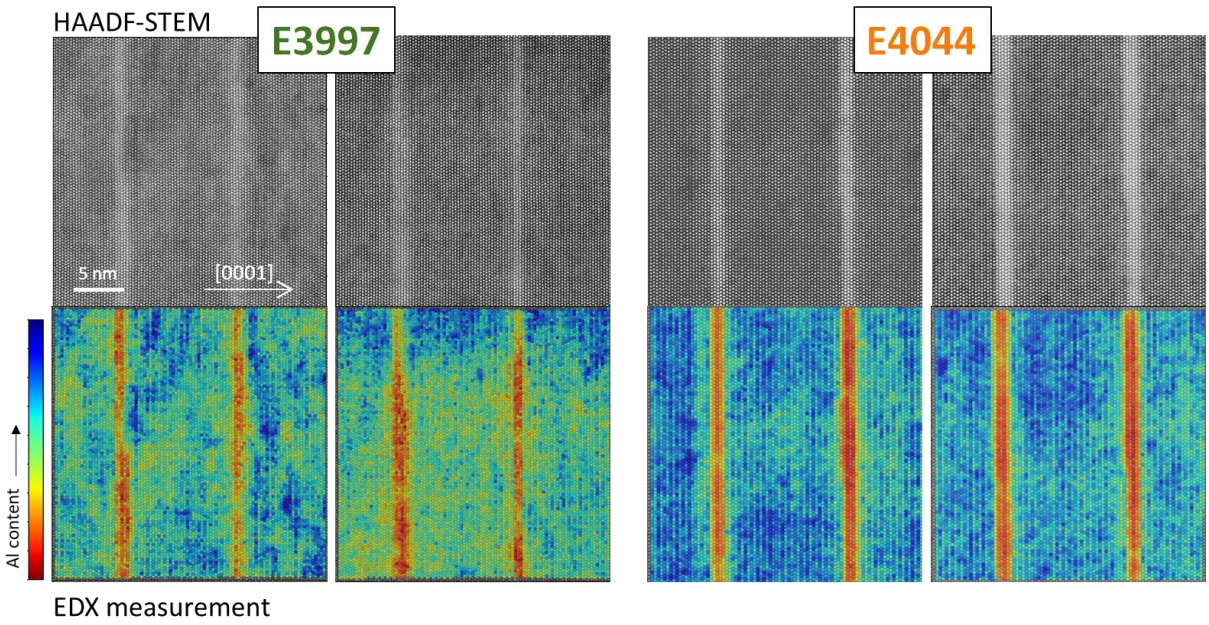

Figure 4.19. *HAADF-STEM images and EDX measurements of two QWs for samples E3997 and E4044. The Al content is illustrated using a color map.*

The IQE of III-nitrides depends strongly on the injection intensity [201–203]. Under operating conditions, the carrier density in the structure is high enough to saturate non-radiative recombination paths and screen potential barriers associated with defects or interfaces. Emulating such conditions requires relatively high pumping densities. Therefore, we have studied the IQE of the heterostructures as a function of temperature and excitation power density using the method described by Yamada *et al.* [204]

$$\mathrm{IQE_{SCH}(T)} = \frac{\eta_{\mathrm{PL}}(T)}{max[\eta_{\mathrm{PL}}(T = 0\ K)]} \tag{4.2}$$

where η_{PL} is the PL efficiency, defined as the integrated PL intensity divided by the excitation power. The PL spectra were measured for various excitation powers, as presented in Figure 4.20 at 6 and 300 K. The narrow lines labeled "*" that appear at high excitation power are assigned to stimulated emission. Such phenomenon is not expected in a sample without cleaved facets, but it occurs due to the feedback provided by reflection at parallel cracks appearing due to the strong lattice mismatch between different layers (see section 4.2.2).

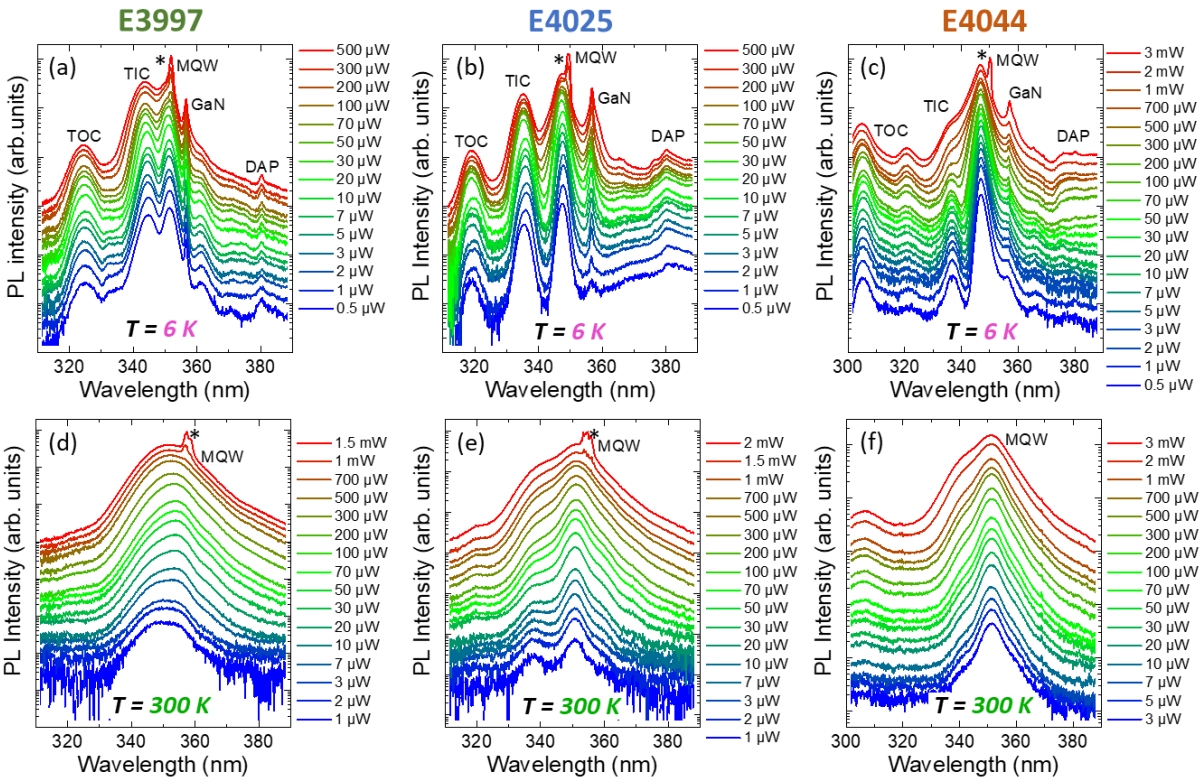

Figure 4.20. *Variation of the PL spectra as a function of excitation power, measured at 6 K and 300 K. The narrow line labeled as "*" that appears at high pumping powers is assigned to stimulated emission.*

The calculation of IQE_{SCH} considers the integrated intensity of the whole PL spectrum. However, the contribution of recombination in the cladding layers to the total intensity can be important, particularly at low temperatures, due to poor carrier diffusion to the MQW. In view of lasing, radiative recombination in the cladding layers should be considered as losses. Therefore, we have calculated IQE_{MQW} integrating only the optical signal from the MQW, which can be extracted using a Lorentzian fit to remove the other contributions (i.e. cladding and lasing lines) with the maximum PL efficiency still given by the integrated PL over the whole spectrum at low temperatures, that is

$$IQE_{MQW}(T) = \frac{\eta_{PL\,MQW}(T)}{max[\eta_{PL}(T = 0\ K)]} \tag{4.3}$$

where $\eta_{PL\,MQW}$ is the integrated PL intensity of the MQW divided by the pumping power and η_{PL} is the total integrated PL intensity divided by the pumping power. Note that the maximum $IQE_{MQW}(T = 0\ K)$ is not necessarily 100%, in contrast with $IQE_{SCH}(T = 0\ K)$, which was assumed to attain 100% as maximum value. Comparing IQE_{SCH} and IQE_{MQW}, we can extract information about the efficiency of the carrier transfer from the waveguide to the MQW. Figure 4.21 displays IQE_{SCH} and IQE_{MQW} as a function of temperature for E3997, E4025 and E4044. The maximum IQE_{SCH} and IQE_{MQW} data is summarized in Table 4.6. At 6K, the highest IQE_{MQW} is about 49%, 56% and 86% for E3997, E4025 and E4044, respectively. Their band diagram can explain the difference between

samples: The GRINSCH in E4025 and E4044 promotes the diffusion of carriers along the growth axis towards the MQW, which is one of the factors that limit the IQE_{MQW} at cryogenic temperatures. However, at 300 K, the trend is reversed compared to that at 6 K, i.e., the IQE_{MQW} is about 22%, 11% and 5% for E3997, E4025 and E4044, respectively. This suggests that the higher carrier mobility at room temperatures promotes not only carrier collection in the MQW, due to the enhanced diffusion length along the growth axis, but also their trapping in non-radiative centers, due to the enhanced in-plane diffusion length. As the acceleration of non-radiative processes is higher in samples with lower carrier localization, the performance of E4044 is penalized with respect to E4025 and E3997.

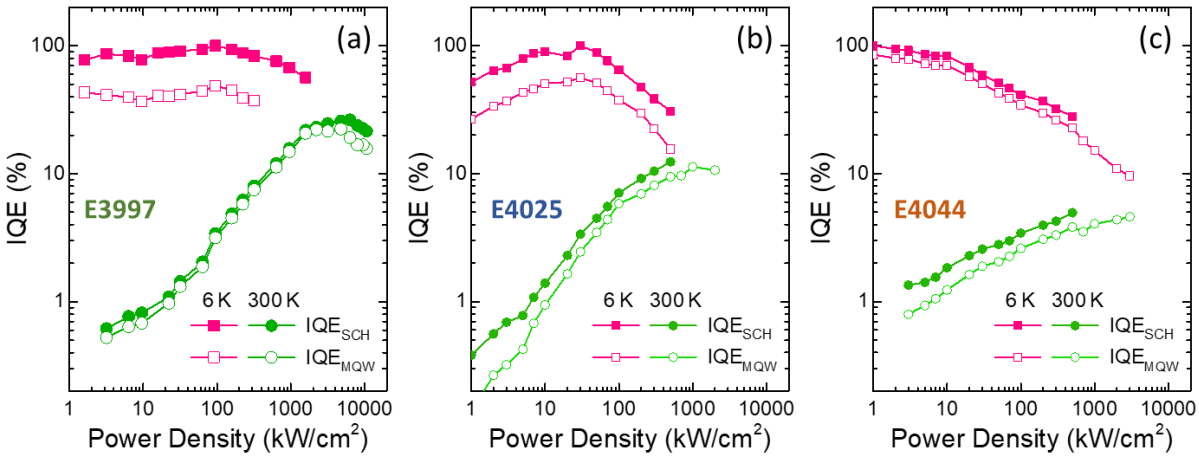

Figure 4.21. *Estimation of the IQE_{SCH} and IQE_{MQW} as a function of the excitation power density for sample (a) E3997, (b) E4025 and (c) E4044, at 6 K and 300 K.*

Table 4.6. *Maximum IQE_{MQW} at 6 K and room temperature and maximum IQE_{SCH} at room temperature (note that the maximum IQE_{SCH} at 6 K is considered to be 100%).*

	E3997	**E4025**	**E4044**
max[IQE_{MQW} (T = 6 K)] (%)	49	56	86
max[IQE_{MQW} (T = 300 K)] (%)	22	11	5.0
max[IQE_{SCH} (T = 300 K)] (%)	26	13	5.5

In general, as the excitation power increases, we can distinguish three different regimes in the IQE:

- Regime A: Starting from low excitation power, when the injection increases, the non-radiative recombination paths start to saturate, leading to an increase of the IQE.
- Regime B: For a certain range of power densities, the non-radiative centers are saturated thus, the maximum IQE is achieved.
- Regime C: When the excitation is even higher, the radiative recombination paths also start to saturate and Auger or thermal effects appear, in detriment of the IQE.

Therefore, the evolution of the IQE with the excitation power presents an inverted U shape. Attaining the maximum IQE (regime B) at room temperature requires higher pumping power than at low temperature. This is due to the larger probability of escape towards non-radiative recombination paths at high temperatures.

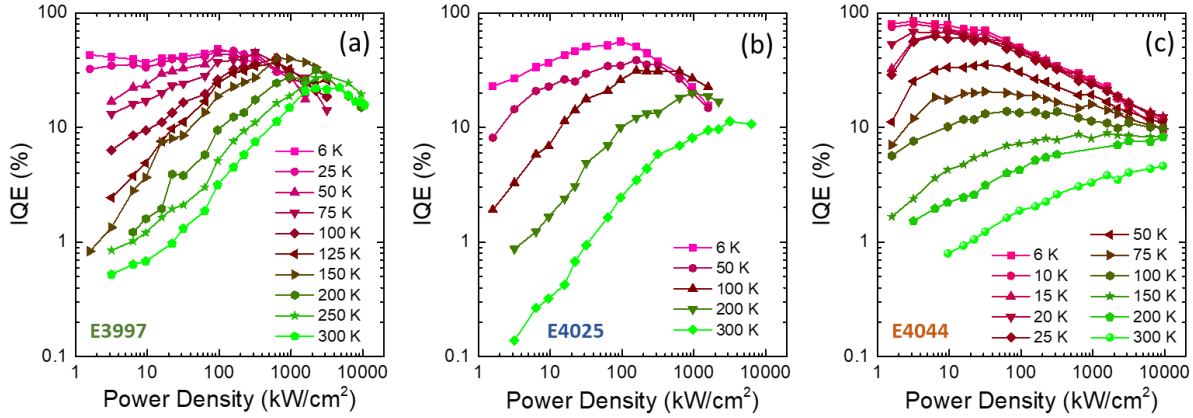

Figure 4.22. *IQE_{MQW} as a function of the excitation power density at different temperatures for (a) E3997, (b) E4025 and (c) E4044.*

Figure 4.22 shows the IQE_{MQW} as a function of the pump power and temperature for the three architectures with comparable QW size and Al content. From the curves, we have extracted the variation of the maximum IQE_{MQW} as a function of temperature in the three samples, with the result illustrated in Figure 4.23. The IQE_{MQW} remains constant at low temperatures and drops sharply for higher temperatures due to the activation of non-radiative recombination paths. The most severe thermal quenching is observed in sample E4044, which features the highest IQE_{MQW} at 6 K. The dashed lines in the figure are fits assuming the dominance of a monoexponential non-radiative process, so that the variation with temperature is described by

$$\mathrm{IQE(T)} = \frac{\mathrm{IQE}(T=0)}{1 + A\, exp(-E_a/kT)} \qquad (4.4)$$

where E_a is the activation energy of the non-radiative process, A is a fitting parameter that is determined by the ratio between the radiative and the non-radiative recombination times [205], and kT is the thermal energy. In the figure, E_a = 22±5 meV, 16±9 meV, and 14±2 meV for samples E3997, E4025 and E4044, respectively. Even if the energy values are smaller than the carrier localization energy extracted from the variation of the PL peak energy with temperature (see Figure 4.18), which can be explained by the different excitation conditions, the trend obtained here is consistent with the trend of the carrier localization energy extracted. On the other hand, the values of A extracted from the fits are A = 2.4±0.6, 6±3, and 12±3 for samples E3997, E4025 and E4044, respectively. Even if the error bars are large, the trend points to an acceleration of non-radiative phenomena in sample E4025 and particularly in sample E4044 with respect to

E3997, which might indicate a higher density of point defects behaving as non-radiative recombination centers. These results suggest that the enhanced mobility of carriers at room temperature in E4025 and E4044 promotes not only carrier collection in the MQW, but also their reaching to non-radiative traps, which are more effective due to the reduced localization in the MQW. The particularly high value of A in E4044 might indicate a higher density of point defects in the structure, which could be explained by the higher aluminium content in the upper layers.

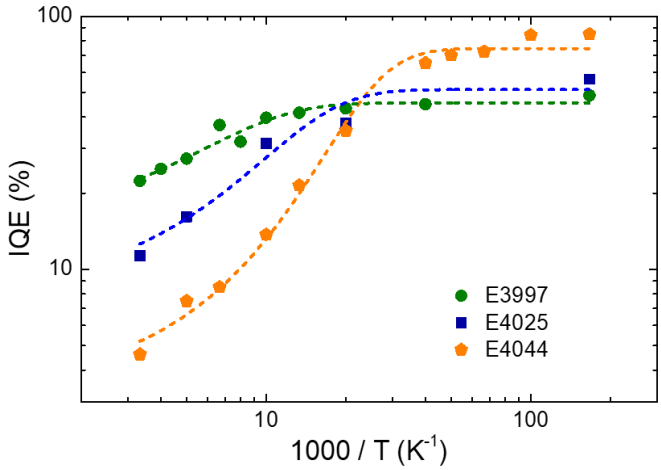

Figure 4.23. *Maximum IQE_{MQW} as a function of the inverse temperature for E3997, E4025 and E4044.*

4.3.3 Assessment of the optical net gain

One of the fundamental conditions to reach lasing is the presence of gain in the active area of the heterostructure. For that reason, an assessment of the optical net gain of the structure can provide an indication on the necessary power to reach gain regime. A study on the optical net gain of sample E3980 was performed in collaboration with Institute Lumière Matière (iLM) - Université Lyon 1. The experimental set-up and the optical measurements were performed by Quang Mihn Thai (iLM).

The measurement of the net optical gain is performed with the variable stripe length (VSL) method [206–208]. This method consists in exciting optically the sample with a stripe-shape beam whose length is controlled with the insertion of a slit or blade in the stripe beam path (see Figure 4.24(a)). The intensity of the edge emitted photoluminescence (I_λ) is measured as a function of the stripe length (L), at fixed excitation power. The variation is described by a one-dimensional optical amplifier model:

$$I_\lambda(L) = \frac{I_s A}{g_\lambda}(e^{g_\lambda L} - 1) \tag{4.5}$$

where I_s is the spontaneous emission rate per unit volume, A is the cross-section area of the excited volume and g_λ is the net gain at a certain wavelength λ. By plotting the PL intensity and then fitting with equation (4.5), we can extract the optical net gain.

The experimental set-up for this measurement is illustrated in Figure 4.24(b). The pump source was a 193 nm ArF excimer laser (Compex 102 from Coherent), operated in pulse mode (20 ns pulse width, with a frequency capped at 20 Hz). Such pump laser was already used in several studies of optical gain in AlGaN-based MQW [209–211]. Since the ArF laser beam dimension is relatively large (10 mm x 24 mm), to create a narrow laser stripe on the sample, we insert a rectangular slit (0.05 mm x 3 mm) in front of the laser beam, then recreate its image on the sample using two fused silica spherical lenses. The laser stripe on the sample has a width of 25 µm and a maximum length of 1500 µm. A mobile slit is positioned in front of the sample to modify the stripe length. Both the sample and the laser stripe can be imaged by reflection on a CMOS camera (Thorlabs DCC1240M). The beam intensity can be modified by using fused silica refractive optical densities. PL signals are collected using an optical fiber and then analyzed with a Horiba Triax 320 spectrometer (grating of 1200 groves/mm, with blaze wavelength at 330 nm), coupled with a cooled CCD camera (Symphony STE).

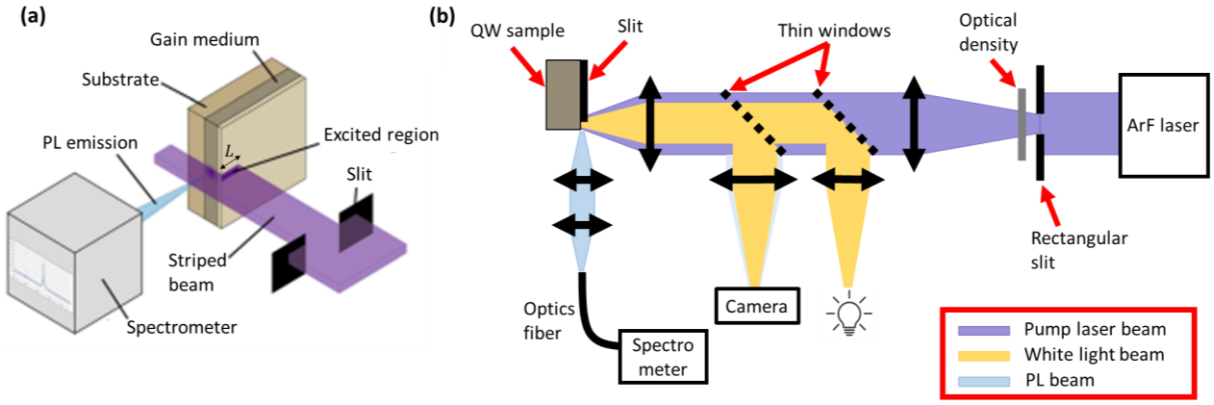

Figure 4.24. *(a) Schematic of the VSL method excitation geometry (modified from [210]). (b) Experimental set-up for net gain measurements using the VSL method.*

To perform the VSL experiment, one of the edges of the sample was mechanically cleaved along the *m*-plane of the GaN substrate, to provide the output facet. Note that lasing is undesired for this kind of measurement, therefore, the back facet was not cleaved. The lateral confinement of the light is obtained by gain guiding, i.e. by the fact that the population-inverted region is determined by the width of the pumping laser stripe, which generates a gain gradient in the structure. To study the homogeneity of the sample, we performed gain measurements on different areas, from which we identified two different behaviors.

Figure 4.25(a) and (b) presents the PL spectra recorded at two different positions labelled as position 1 and position 2, respectively, measured with a pumping power of 743 kW/cm^2, as a

function of the stripe length between 40 μm and 400 μm. At position 1 (Figure 4.25(a)), the PL intensity increases systematically as the stripe length increases. At position 2 (Figure 4.25(b)), the behavior is similar for stripes shorter than 240 μm, and then, the PL intensity increases rapidly in the range between 240-360 μm, and the shape and width of the peak changes. Finally, for the 400 μm long stripe, the intensity saturates. The evolution of the intensity and the FWHM of the peak is shown in Figure 4.25(c). For stripes longer than 240 μm, the FWHM at position 2 becomes narrower than that at position 1, decreasing down to 1.5 nm at position 2 compared to 2.6 nm at position 1. The superlinear increase of the PL intensity with the stripe length, along with the spectral narrowing, confirm the presence of amplified spontaneous emission (ASE).

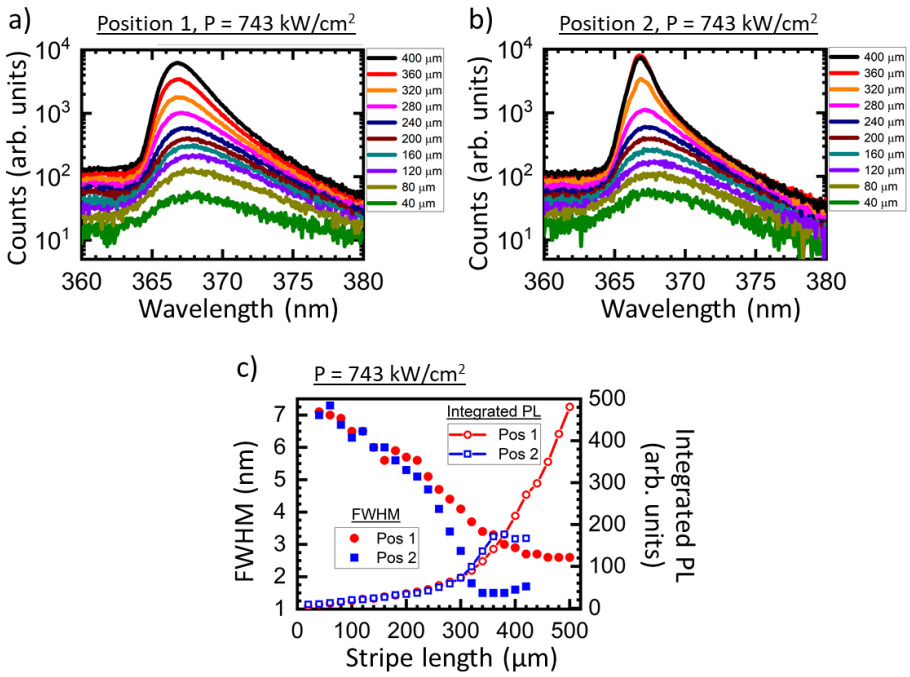

Figure 4.25. *PL spectra obtained from sample E3980 for different stripe lengths, at (a) position 1 and (b) position 2. (c) PL peak FWHM and intensity at position 1 and position 2 as function of the stripe length.*

Figure 4.26(a) shows the evolution of the PL intensity at λ = 367 nm as a function of the stripe length for position 1, for several pumping power values. The fitted net gain varies from -24 cm^{-1} at 218 kW/cm^2, up to 129 cm^{-1} at 743 kW/cm^2. A negative value of net gain occurs when absorption is predominant, while a positive value indicates gain regime. The curve shape is different between the case of absorption (negative gain), where the signal starts to saturate at long stripe length, and in the case of net gain (positive gain), with an exponential increase of the PL intensity. By repeating the fitting process at different wavelengths, we obtain the net gain as function of the wavelength and pumping power, presented in Figure 4.26(b). Positive net gain exists for pumping power higher than 218 kW/cm^2, with highest value equal to 131 cm^{-1} at λ = 366.5 nm for a pumping power of 743 kW/cm^2. The peak net gain shifts from 371 nm at

218 kW/cm² to 366.5 nm at 743 kW/cm², as a consequence of band filling. At longer wavelengths, the net gain becomes negative as absorption internal losses dominate. On the other hand, the response observed for wavelengths shorter than 365 nm might come from the mixed optical response of the top cladding layers.

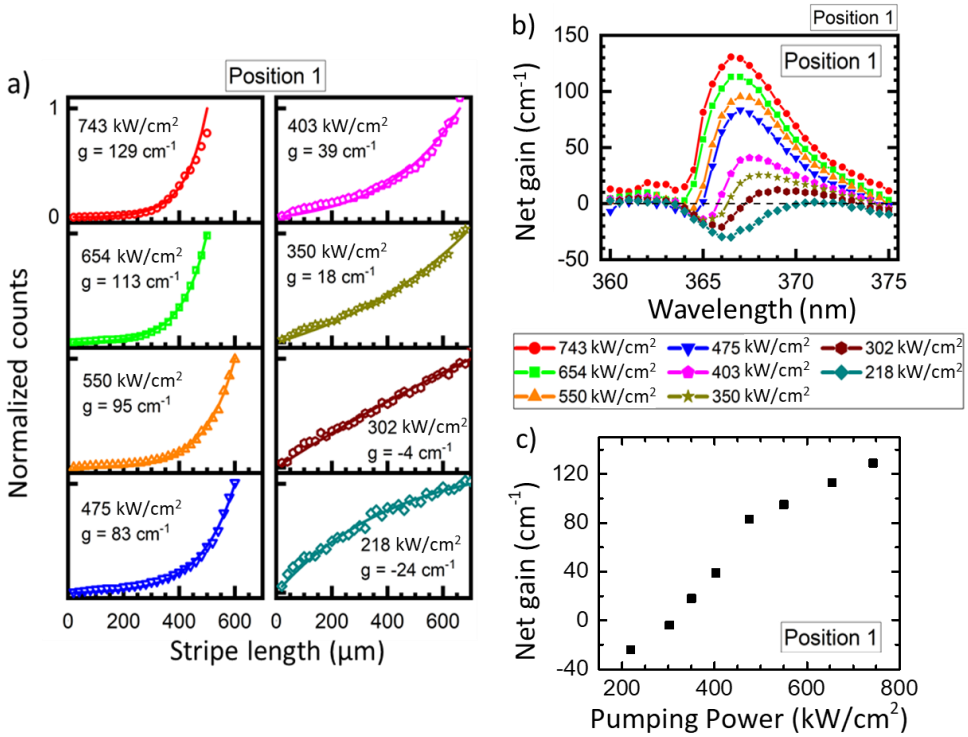

Figure 4.26. *Net gain measurements performed at position 1: (a) PL intensity at λ = 367 nm, as a function of the stripe length, for pumping power between 218 kW/cm² and 743 kW/cm². Raw data are presented as symbols and fits are presented as solid lines. (b) Net gain as function of the wavelength at different pumping powers. Positive values indicate presence of net gain, while negative values indicate absorption. (c) Variation of the maximum net gain at 367 nm as a function of the pumping power.*

In order to compare our results with literature, we have compared the maximum reported net gain divided by the number of QWs in the structure. For this calculation, we assume that all the QWs are active, which is unlikely in our case due to the poor penetration depth of optical pumping into the active region (see Figure 4.17). The carrier density in the wells depend on the carrier diffusion process, so that most probably only the topmost QWs reach population inversion, meaning that we are underestimating our net gain when dividing by the total number of QWs. Nevertheless, the maximum net gain obtained here is 13 cm⁻¹/QW, which is in the range of the results in literature around 12-15 cm⁻¹/QW [212–214]. However, the comparison with gain values in literature is delicate, since the designs have not only different number of QWs, but also different thicknesses or Al composition. In addition, representing the net gain as a function of the pumping power in Figure 4.26(c), we observe that gain saturation is not reached yet at the highest pumped power used in this experiment, so that the maximum net gain for structure E3980 might be slightly higher.

The same measurement was repeated for position 2, with the results shown in Figure 4.27. Compared to position 1, the PL intensity at 367 nm at high powers shows a sharper increase followed by a saturation at large values of the stripe length (see Figure 4.27(a)). To clarify, the saturation part of the graphs was excluded (if present) during the fitting process to extract the gain. The net gain curves as function of the wavelength are plotted in Figure 4.27(b). In this position, the net gain threshold (i.e. the power density necessary to reach positive gain) is 403 kW/cm^2, higher than position 1 with 218 kW/cm^2. However, the maximum net gain at 743 kW/cm^2 is 240 cm^{-1}, significantly higher than 131 cm^{-1} for position 1. In addition, the shape of the curve changes for the three highest pumping power values, resembling a peak rather than the rounded profile expected in gain measurements.

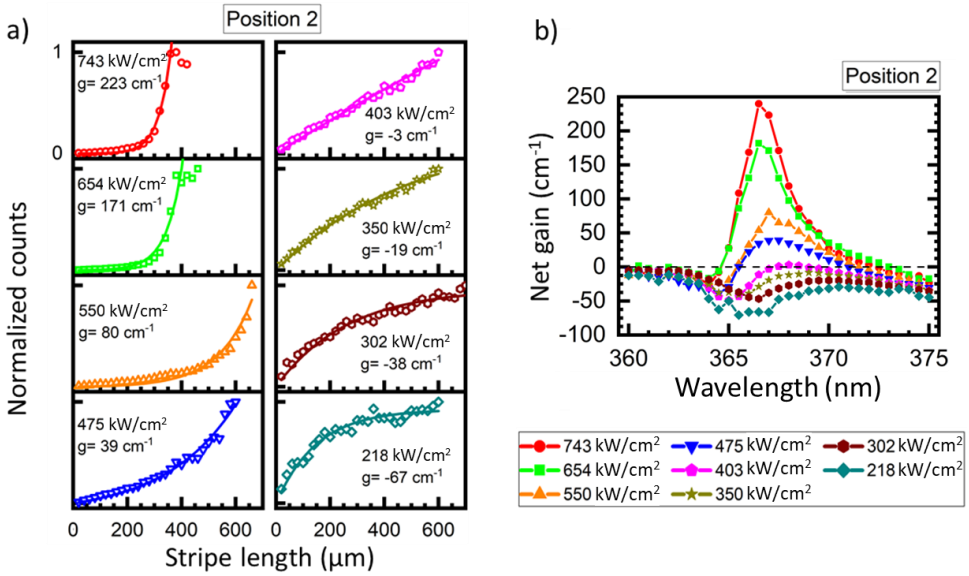

Figure 4.27. *Net gain measurements at position 2: (a) PL intensity at λ = 367 nm, as a function of the stripe length, for pumping power between 218 kW/cm² and 743 kW/cm². Raw data are presented as symbols and fits are presented as solid lines. (b) Net gain as function of the wavelength at different pumping powers.*

From these results, we notice several important differences between the results at positions 1 and 2. The maximum net gain is higher at position 2, but the spectral distribution of the gain is unusual, the PL emission is particularly narrow and there is evidence of gain saturation at long stripe lengths. To understand the mechanisms behind this optical response, we analyzed the evolution of the emission characteristics (intensity and FWHM) as a function of the pumping power for a fixed stripe length, namely 400 μm, and presented them in Figure 4.28. The response is similar for pumping power lower than 550 kW/cm^2. At higher pumping power, for position 2, there is a larger superlinear enhancement of the PL intensity, with a collapse of the FWHM. These features together suggest the onset of lasing, which would be expected for a material with gain within an optical cavity, but is not expected for a sample with only one facet cleaved. However, the presence of the straight cracks that propagate along the *m*-planes revealed by optical microscope in Figure 4.14 from section 4.2.2, might explain the lasing feature. These cracks appear parallel to

the cleaved edge and also forming 60° angle. Therefore, partial reflection from the cracks parallel to the cleaved edge could provide the optical cavity feedback that amplifies the PL intensity, resulting in the anomalous behavior of the emission characteristics observed in position 2. In this case, equation (4.5) is no longer valid.

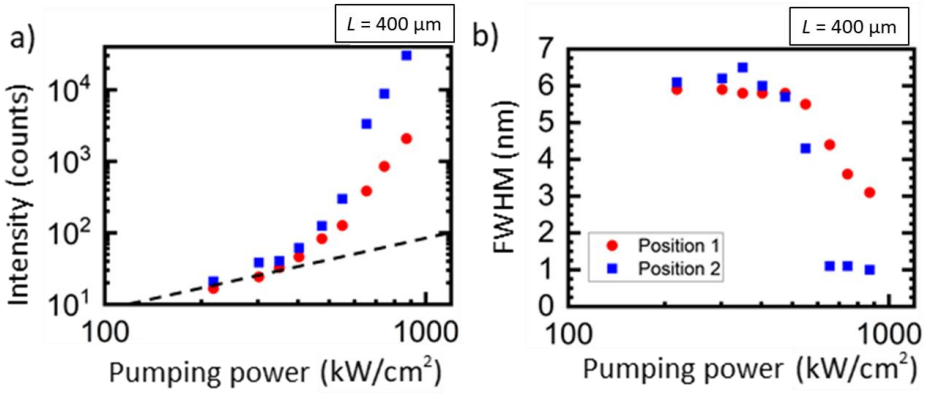

Figure 4.28. *Variation of (a) the PL intensity and (b) the PL peak FWHM as a function of the pumping power measured at position 1 and position 2, for a stripe length of 400 µm.*

Due to the interaction between cracks, the distance between the cleaved edge and the first crack is not constant along the sample (between 300 µm and 600 µm in the microscope image). The length scale of this distance is comparable with our maximum stripe length, which explains the different behavior in different areas of the sample. Thus, it can be concluded that position 1 has the typical behavior expected in a reliable net gain measurement, whereas position 2 presents an amplification of the response for long stripes due to the optical feedback provided by a crack. By changing the measurement point along the sample, we observe locations with the behavior of position 1 and 2. The high density of cracks makes that domains with response described as "position 2" are relatively dominant.

Attempts to perform similar measurements in the samples emitting at shorter wavelength (350 nm such as E3997) encountered higher difficulties: it was hardly possible to find spots without optical amplification due to the shorted distance between cracks originated by the higher misfit strain derived from higher Al concentration in the AlGaN layers. Therefore, gain measurements were systematically overestimated. Solving this issue would require advanced strain management during the growth process, either growing in patterned substrates or on bulk AlN. Even if for these emission wavelengths, AlN substrates present larger lattices mismatch than GaN, the resulting strain in the structure is compressive, which favors relaxation by dislocation instead of crack propagation (tensile strain).

4.3.4 Estimation of the lasing threshold from the net gain

In the case of an optical cavity with very low mirror losses (for example in very long Fabry-Perot cavities), the presence of optical net gain can be used as an indicator to estimate the threshold power required for lasing under electron beam pumping. To compare lasing thresholds measured with different types of carrier injection in the same active region, i.e. optical pumping, electrical injection or electron beam pumping, we estimate their energy cost to achieve the same carrier density threshold. In this study of the optical gain, under optical pumping with an ArF laser (λ = 193 nm), the energy cost to generate an electron-hole pair is the laser photon energy, E_{laser} = 6.42 eV. In the case of electron beam pumping, as mentioned in section 2.3, the energy required to generate an electron-hole pair is about 3 times the band gap [215], i.e. $E_{ebeam} \approx 3 \times 3.6$ eV = 10.8 eV. For this calculation, we consider that the majority of the electron-hole pairs are generated in the barriers of the active region and diffused towards the QWs, thus we consider the band gap energy of $Al_{0.07}Ga_{0.93}N$ being 3.6 eV. With this data, the threshold for electron beam pumping, P_{th}^{ebeam}, can be estimated from the optical net gain threshold, P_{th}^{gain}, using

$$P_{th}^{ebeam} = \frac{E_{ebeam}}{E_{laser}} P_{th}^{gain} \tag{4.6}$$

For E3980, with a net gain threshold of 218 kW/cm², we estimate a lasing threshold $P_{th}^{ebeam} \approx$ 370 kW/cm² under electron beam pumping at room temperature. However, it should be kept in mind that the net gain threshold obtained in this study is overestimated, since measurements were performed by optical pumping, meaning that only the topmost QWs are expected to attain population inversion, and the others contribute to enhance the absorption losses. Therefore, the calculated lasing threshold is indeed an upper limit.

To compare this lasing threshold with values in the literature, we must keep in mind that the gain depends not only on the pumping procedure but also on the number of QWs. Therefore, to take this factor in to account, we will also compare the carrier density per QW at the threshold, N_{th}. This parameter is in the range of state-of-the-art of UV laser diodes based on an SCH (see Table **4.7** and Figure 4.29). A reduction of N_{th} can be obtained by modifying the structure to be specifically adapted for optical pumping, approaching the QWs to the surface [216–218]. However, such designs are not compatible with electron beam pumping.

Table 4.7. *Reported values of lasing wavelength (λ), threshold current (I_{th}) or threshold power density (P_{th}) at room temperature and surface carrier density (N_{th}) injected per QW and per second at the lasing threshold for several UV laser diodes. The active region structure (MQW = multi-quantum well, SQW = single quantum well) and heterostructure design are also indicated*

Ref.	Year	λ (nm)	I_{th} (kA/cm²)	P_{th} (kW/cm²)	N_{th} per QW (×10²² s⁻¹cm⁻²)	Active region	Heterostructure design
[219]	2009	354.4 - 359.6 336.0 - 342.3	8 17.6	-- --	1.7* 3.7*	GaN/AlGaN MQW AlGaN/AlGaN MQW	SCH, 5 µm ridge, 500 µm cavity SCH, 5 µm ridge, 500 µm cavity
[220]	2008	355.4 - 361.6	19.1±5.5	--	4	3×GaN/AlGaN	SCH, 5 µm ridge, 1000 µm cavity
[221]	2004	365	3.5-4.5	--	0.83*	2-7×GaN/AlGaN	SCH, 2 µm ridge, 500 µm cavity
[222]	2001	366.9	3.5	--	2.2	SQW GaN/AlGaN	SCH, 2.5 µm ridge, 600 µm cavity
[223]	2020	278.9	19.6	--	12.3	SQW AlGaN/AlGaN	SCH, 4 µm ridge, 400 µm cavity, HfO_2/Al_2O_3 DBR
[224]	2019	271.8	25	--	15.5	SQW AlGaN/AlGaN	SCH, 4 µm ridge, 400 µm cavity HfO_2/SiO_2 DBR
[225]	2007	355.4 - 361.6	19.1±5.5	--	4	3×GaN/AlGaN	SCH, 5 µm ridge, 1000 µm cavity
[226]	2021	300	14.2	--	4.4	2×AlGaN/AlGaN	SCH, 10 µm ridge, 2000 µm cavity
[227]	2015	350	56	--	11.7*	GaN/AlGaN MQW	SCH, 1.5 µm ridge, 300 µm cavity
[228]	2020	298	41	--	25.6	SQW AlGaN/AlGaN	SCH, 300 µm cavity
[229]	2004	350.9	7.3	--	1.5	3×GaN/AlGaN	SCH, 5.5 µm ridge, 500 µm cavity
[230]	2012	267	--	126	5.2**	3×AlGaN/AlGaN	SCH, 160 µm ridge, 1 mm cavity
[216]	2018	267	--	6	0.2**	3×AlGaN/AlGaN	QWs at the surface
[217]	2019	245	--	190	0.5**	40×GaN/AlGaN	QWs at the surface
[218]	2014	256	--	61	1.2**	5×AlGaN/AlGaN	QWs at the surface
This work	2022	367	--	218	2.1**	10×GaN/AlGaN	SCH designed for electron beam pumping, 50 µm ridge, 1 mm cavity (E3980)

* N_{th} per QW estimated assuming 3 active QWs.
** N_{th} per QW estimated as the photon flux divided by the number of QWs, considering the optical pumping wavelength.

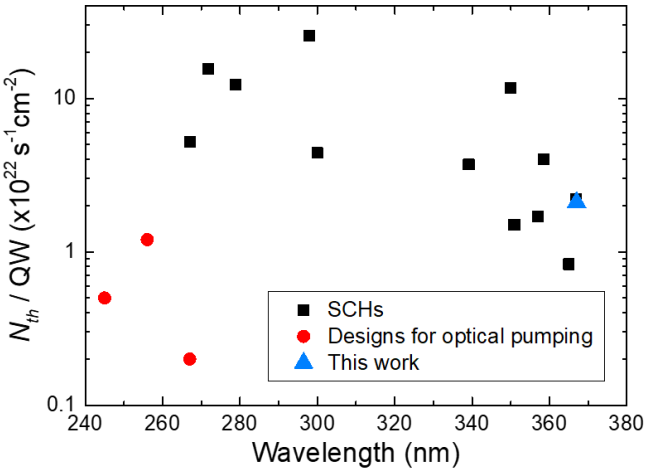

Figure 4.29. *Variation of N_{th} per QW as a function of the emission wavelength (data from Table 4.7). Data corresponding to SCHs and heterostructures optimized for optical pumping are represented with different symbols and colors.*

4.4 Conclusions

In this chapter, I have presented the design, growth, and structural and optical characterization of AlGaN/GaN heterostructures dedicated to operate as active media for electron beam pumped UV-A lasers.

The samples presented in this chapter have been designed to operate at relatively low acceleration voltages ($V_a \leq 10$ kV) in comparison with previously reported structures (e.g. Hayashi *et al.* [51]) by reducing the top cladding layers thickness. This approach allows an efficient confinement of the optical mode inside the waveguide. Optical leakage losses are prevented by a proper selection of thickness and Al concentration in the cladding layers. The samples are designed to emit in the range between 350-365 nm, corresponding to the UV-A spectral region, by tuning the GaN QWs thickness. The implementation of a GRINSCH improves the collection of carriers towards the active region without any negative impact in the quality of the waveguide. Furthermore, the smooth transition between ternary alloys in the compositionally graded layers favors the structural quality of the active MQW. In addition to that, an asymmetric design of the GRINSCH is introduced, to further improve the transfer of carriers towards the active region.

The designed samples were grown by PAMBE. Optical measurements confirm optimal operation around 7-10 kV and superior carrier collection of the GRINSCH. At low temperature, the samples with GRINSCH present superior IQE due to the enhanced carrier transfer towards the MQW. However, the room-temperature IQE is higher in the SCH sample (without graded layers). This fact is attributed to alloy inhomogeneities and QW thickness fluctuations, which favor carrier localization and reduce the non-radiative recombination probability.

Finally, we report the challenge of performing optical net gain measurements at room temperature by VSL method for an SCH designed for electron beam pumping. Due to the electron penetration profile, these structures host multiple QWs within hundreds-of-nanometers thick active region. Characterizing with optical pumping under these conditions is complex, since the optical excitation is restricted to the proximity of the surface, thus, only the topmost QWs can attain population inversion. In spite of these limitations, the results are at the state of the art. Interestingly, we observed an anomalous amplification in some areas of the sample that occurs for long stripe lengths and high pumping powers, and also present higher net gain threshold. We attributed these phenomena to the optical feedback provided by the reflection at cracks, which appear due to plastic relaxation of misfit strain in AlGaN-based structures grown on GaN substrates. The cracks are not catastrophic for the laser device performance; however, they can induce an overestimation of the gain measurements, which can be identified from the spectral variation of the gain.

Chapter 5
Laser emission and device optimization

In this chapter, laser cavities from the studied samples are processed and characterized. Lasing emission under optical pumping is reported at low (5 K) and room temperature, and an estimation of the electron beam pumping threshold is provided. The results reveal a decorrelation between the lasing threshold and the internal quantum efficiency results, which is discussed in the second section. The quality of the mirrors is identified as a limiting factor. Therefore, in the third section, a two-step process to obtain smooth and vertical cavity facets is presented and compared to the mechanically cleaved facet cavities. Finally, we discuss the possibility to implement a DBR mirror to further reduce the lasing threshold.

The measurements under electron beam were performed in collaboration with Steve Purcell (Univ. Claude Bernard Lyon 1). I fabricated the laser cavity and the facet mirrors in the facilities of PTA Grenoble. The MATLAB code to simulate the DBR reflectivity was written by Bruno Gayral, the mirrors were deposited by Eric Delamadeleine, and the experimental reflectivity was measured with the support of Lou Denaix.

Part of the results presented in this chapter have been published in:

(1) "AlGaN/GaN asymmetric graded-index separate confinement heterostructures designed for electron-beam pumped UV lasers", S. Cuesta et al. Opt. Express 29, 13084-13093 (2021) [186]

(2) "Development of AlGaN/GaN heterostructures for e-beam pumped UV lasers", S. Cuesta Arcos et al. Proc. SPIE 11686, Gallium Nitride Materials and Devices XVI, 116860S (2021) [187]

(3) "Decorrelation of internal quantum efficiency and lasing threshold in AlGaN-based separate confinement heterostructures for UV emission", S. Cuesta et al. Appl. Phys. Lett. 119, 151103 (2021) [188]

(4) "Reduction of the lasing threshold in optically pumped AlGaN/GaN lasers with two-step etched facets", S. Cuesta et al. Semicond. Sci. Technol. 37, 075013 (2022) [231]

5.1 Demonstration of lasing

In order to assess the lasing performance of the heterostructures, it is necessary to define a cavity to provide some optical feedback to the gain media. Therefore, a set of laser bars with 1 mm resonator length were prepared by mechanical cleaving along the (10-10) *m*-plane of GaN for each sample. First tests were performed under optical pumping with an Nd:YAG laser emitting at 266 nm. The excitation was perpendicular to the *m*-plane facet and to the surface, and the edge emission was collected as described in the set-up B in section 3.2.5.

5.1.1 Room temperature measurements

Figure 5.1(a) presents the room-temperature PL edge emission from a 1-mm-long laser bar of sample E3980, at various pumping power densities. At low excitation power, the spectrum is dominated by a broad peak centered at 365 nm, assigned to spontaneous emission from the QWs.

However, for power densities higher than 192 kW/cm², a sharp and intense peak arises, which is assigned to lasing emission. For further evidence of lasing, Figure 5.1(b) presents the variation of the main peak PL intensity (left axis) and its FWHM (right axis) as a function of the pumping power density, showing an abrupt superlinear increase in the emission at the threshold, together with a sharp drop of the FWHM. Figure 5.1(c) shows the polarization properties of the stimulated and spontaneous emission from sample E3980. The stimulated emission displays clear dependence on the polarization angle, with a transverse electric (TE) : transverse magnetic (TM) output power ratio = 15:1.

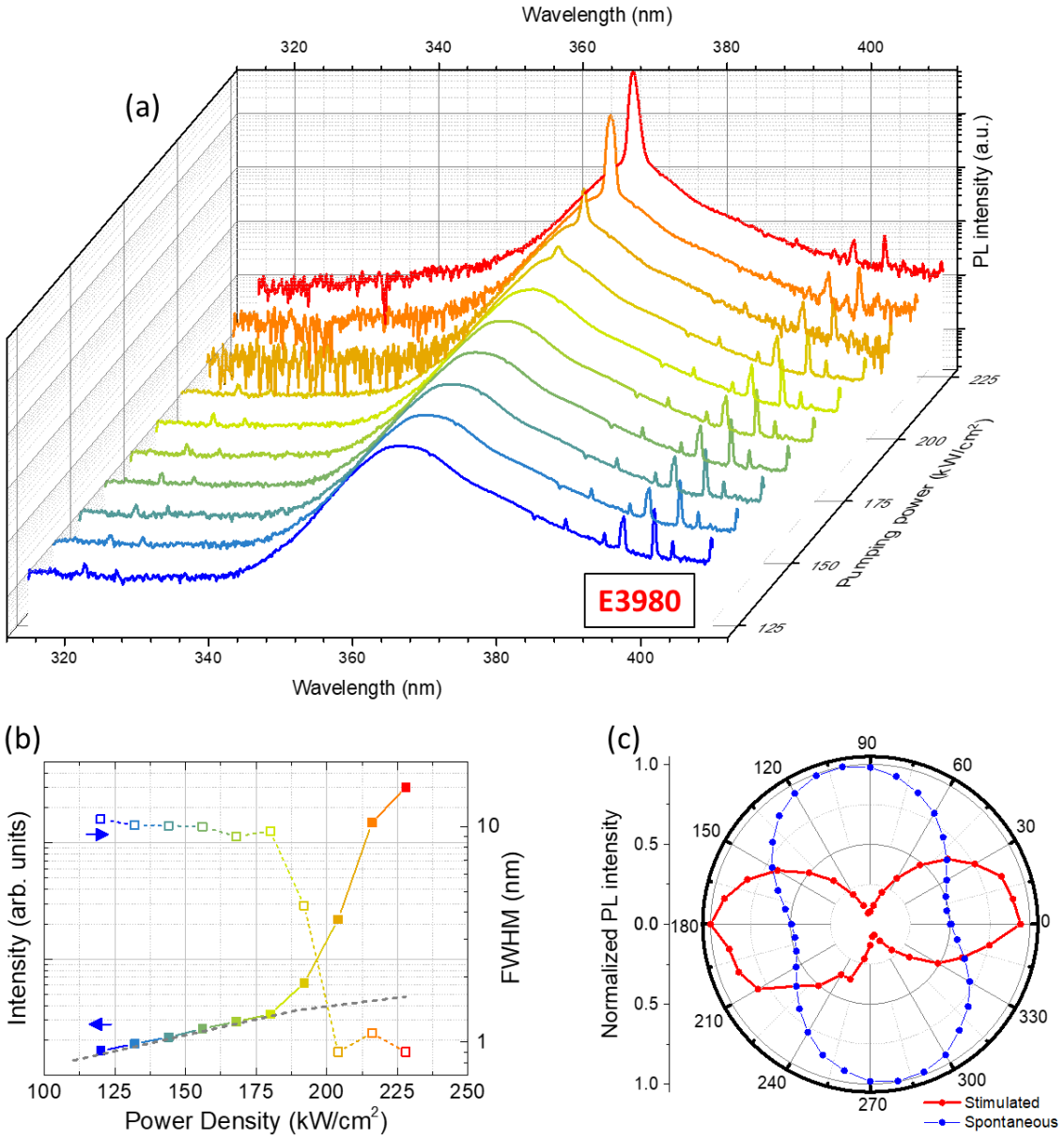

Figure 5.1. *(a) Room temperature PL spectra in semi-logarithmic scale of sample E3980 (cavity length = 1mm) at different pumping power. (b) PL intensity (full markers) and FWHM (hollow markers) as a function of the excitation power density. The grey dashed line represents a linear tendency. Note that 1 nm is the resolution limit of the setup when using a grating with 600 groves/mm. (c) PL intensity collected as function of the polarization angle (0° corresponds to TE polarization).*

Figure 5.2(a) presents the room-temperature PL edge emission of 1 mm long cavity from sample E3997. The spontaneous emission observed at low pumping powers is governed by a broad peak centered at 355 nm, blue-shifted with respect to sample E3980 due to the thinner QWs in E3997. The intense and narrow peak from lasing emission arises at a power density threshold of 210 kW/cm^2. Observing the variation of the PL intensity and FWHM as a function of the pumping power density in Figure 5.2(b), a superlinear increase in the emission together with a drop of the FWHM by several orders of magnitude occur at the threshold. The polarization dependence of the stimulated emission is summarized in Figure 5.2(c), presenting an output ratio TE:TM = 30:1.

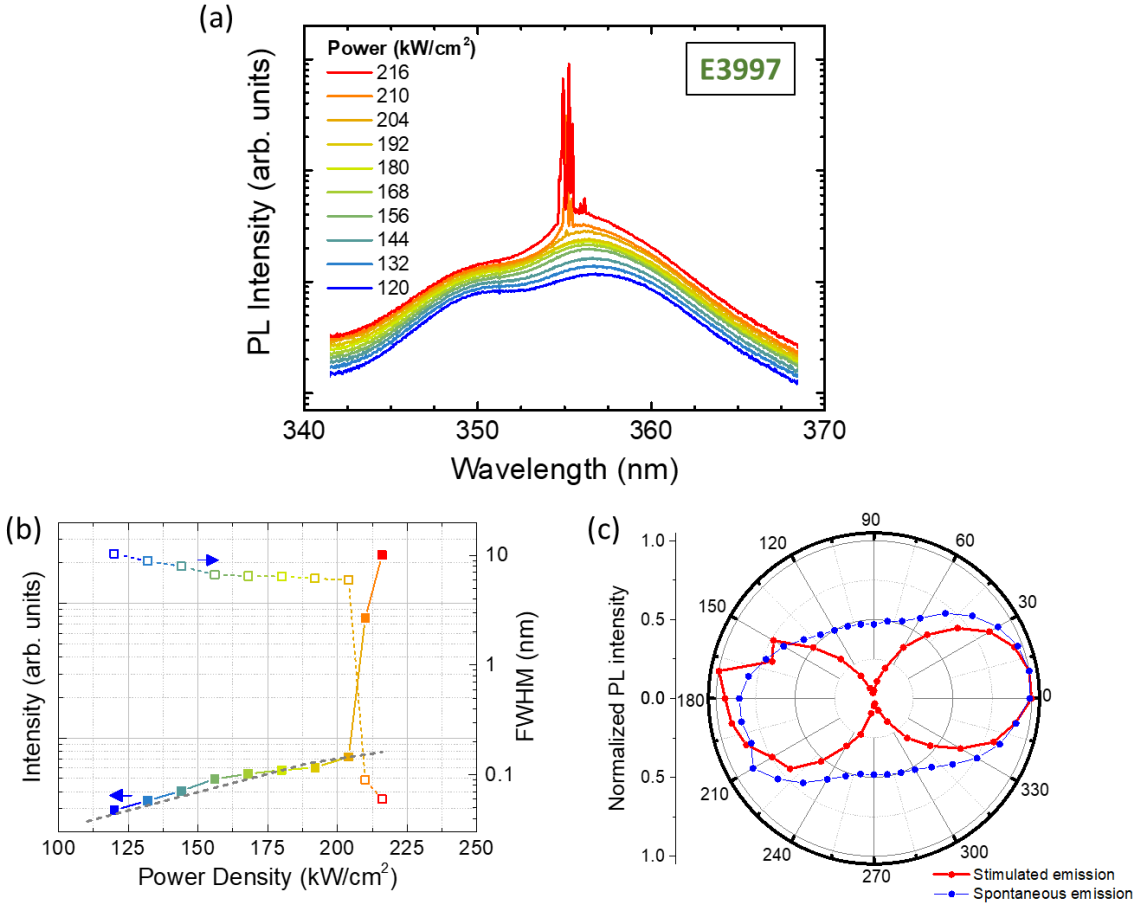

Figure 5.2. *(a) Room temperature PL spectra in semi-logarithmic scale of sample E3997 (cavity length = 1mm) at different pumping power. (b) Emitted photoluminescence intensity (full markers) and FWHM (empty markers) in function of the excitation power density. The grey dashed line represents a linear tendency. Note that 0.1 nm is the resolution limit of the setup when using a grating with 1800 groves/mm. (c) PL intensity collected as function of the polarization angle (0° corresponds to TE polarization).*

Figure 5.3(a) shows the room-temperature PL edge emission of 1 mm long cavity from E4025, with GRINSCH. The stimulated emission appears at 358 nm with a power density threshold of 180 kW/cm^2. The polarization of the emitted light is illustrated in Figure 5.3(b). The stimulated emission is clearly defined in the TE mode direction, and vanishes in the perpendicular TM mode

direction (TE:TM = 30:1). In contrast, spontaneous emission is not polarized, as expected. Figure 5.4(a) shows the room temperature PL edge emission spectra of 1-mm-long cavity from sample E4044 with asymmetric GRINSCH. The spectra shows stimulated emission at 353 nm with a power density threshold of 180 kW/cm^2. The polarization feature in Figure 5.4(b) presents the same behavior as E4025, with the stimulated emission clearly polarized in the TE direction.

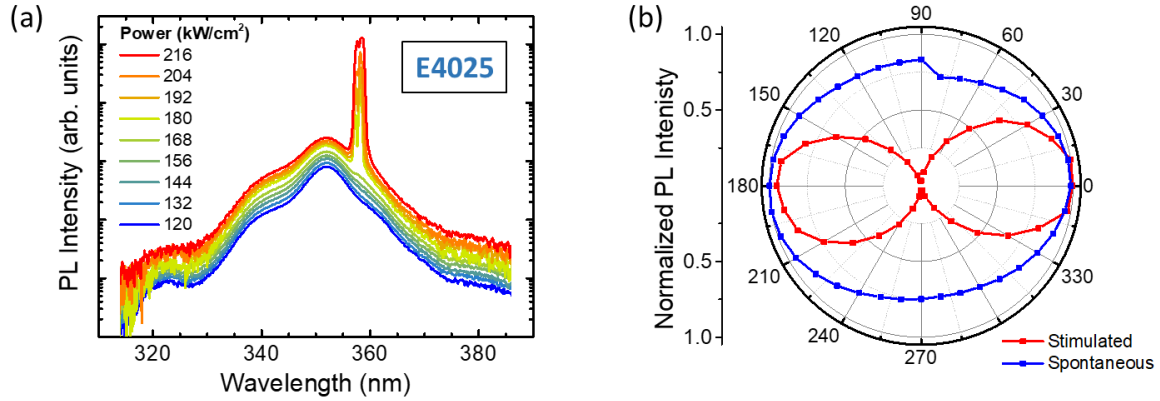

Figure 5.3. *(a) Room temperature PL spectra in semi-logarithmic scale of sample E4025 (cavity length = 1mm) at different pumping power. (b) PL intensity collected as function of the polarization angle (0° corresponds to TE polarization).*

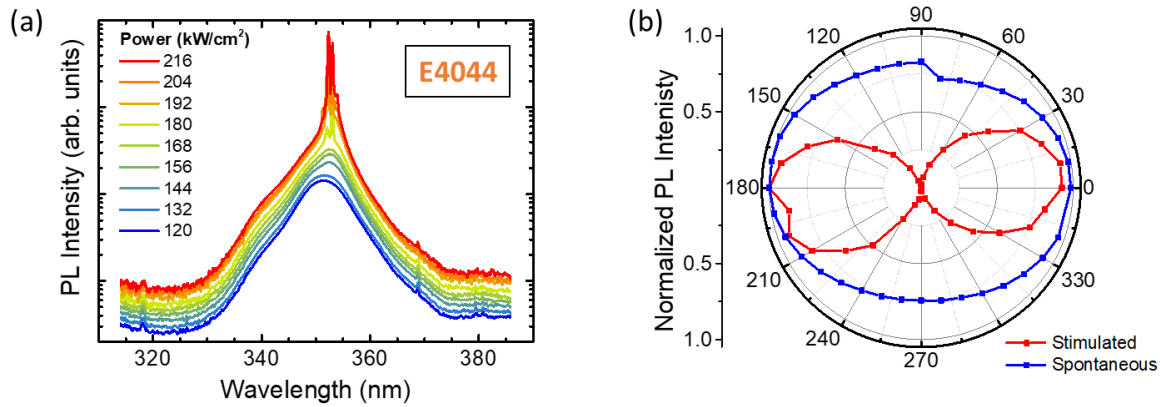

Figure 5.4*. (a) Room temperature PL spectra in semi-logarithmic scale of sample E4044 (cavity length = 1mm) at different pumping power. (b) PL intensity collected as function of the polarization angle (0° corresponds to TE polarization).*

A comparison of the lasing threshold at room temperature between samples E3997, E4025 and E4044 is presented in Figure 5.5. Note that sample E3980 has different MQW composition and thickness, thus it is not directly comparable. For the three samples in the figure, the implementation of the GRINSCH (E4025, blue in figure) leads to an improvement of the lasing performance in comparison with the SCH design (E3997, green in figure), reducing by 15% the threshold power density. The asymmetric GRINSCH (E4044, orange in figure) follows the same tendency as the symmetric GRINSCH. Note that the lasing thresholds compared here are the best performance attained from each sample, from a set of different measurements.

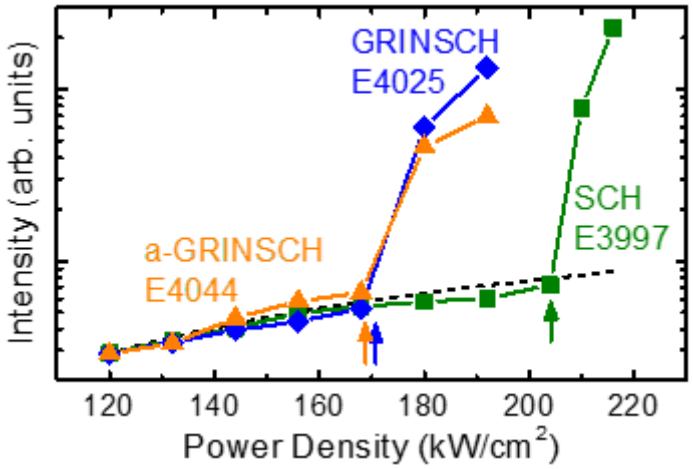

Figure 5.5. *PL peak intensity as a function of the excitation power density for samples E3997 (SCH), E4025 (GRINSCH) and E4044 (a-GRINSCH). The dark dashed line represents a linear tendency.*

5.1.2 Temperature dependent measurements

Figure 5.6 depicts the variation of the lasing threshold as a function of the temperature for samples E3997, E4025 and E4044 (1-mm-long cavities). The evolution of the threshold with temperature follows an exponential trend (expected empirical dependence [85]) with an activation energy E_{th} = 12-13 ± 2 meV for samples E3997 and E4025, increasing to E_{th} = 38 ± 5 meV for E4044. To understand the relatively high threshold of E4044 at low temperatures, we must remind that most of the absorption in PL occurs in the TOC+TIC layers. Therefore, the higher losses that appear when cooling down can be related to alloy fluctuations and higher density of non-radiative point defects in the Al-rich topmost AlGaN layer. In contrast, at high temperatures, carriers have enough energy to follow the potential ramp created by the GRINSCH and diffuse efficiently to the MQW.

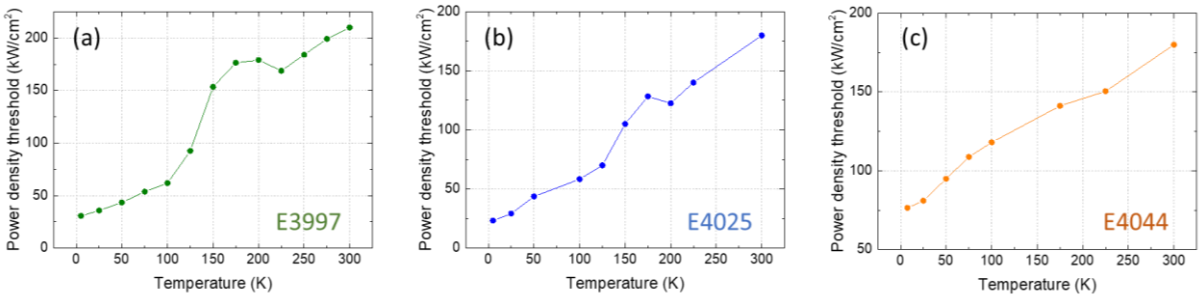

Figure 5.6. *Variation of the lasing threshold as a function of temperature for samples (a) E3997, (b) E4025 and (c) E4044.*

5.1.3 Estimation of lasing threshold under electron beam

The optically pumped threshold power densities presented here can be decreased by eliminating the top cladding layers, facilitating the pumping of the entire MQW stack. This is due to the fact that most of the optical absorption occurs in the top-most ≈100 nm of the structure (as discussed previously in Figure 4.17). However, this would result in a degradation of the performance under electron pumping, which is the target of these structures, due to the different carrier distribution between optically pumped and electron-beam pumped device. Nevertheless, the measurement of the optical threshold provides comparative information about the carrier transfer from the top layers to the active region and the optical losses in the waveguides. For instance, our experiments demonstrate that the implementation of a GRINSCH results in a relevant improvement of the collection of carriers generated by impact-ionization while maintaining laser emission at 353 nm with a threshold power density lower than that of the equivalent SCH design.

We can also use the optical threshold to make an estimation of the electron beam threshold. To compare lasing thresholds measured with different types of carrier injection in the same active region, we estimate their energy cost to achieve the same carrier density threshold, as in section 4.3.4. In the case of optical pumping with an Nd:YAG laser (λ = 266 nm), for each photon absorbed with energy higher than the band gap energy, an electron-hole pair is created; thus, the energy cost to generate an electron-hole pair is the energy of the laser, E_{laser} = 4.66 eV. In the case of electron beam pumping, the energy required to generate an electron-hole pair is about 3 times the band gap energy $E_{ebeam} = 3 \times 3.68$ eV $= 11.04$ eV. With this data, the threshold for electron beam pumping can be estimated from the optical threshold as $P_{th}^{ebeam} = E_{ebeam}\, P_{th}^{laser}/E_{laser}$, with the results summarized in Table 5.1. Note that these lasing thresholds might be overestimated, since measurements were performed under optical pumping, meaning that only the topmost QWs are expected to attain population inversion, while the others contribute to enhance the absorption losses. Therefore, the calculated lasing threshold can be understood as an upper limit.

Table 5.1. *Optical and estimated electron beam pumping lasing power density threshold at room temperature for the samples under study.*

	Optical threshold (kW/cm²)	**Estimated e-beam threshold (kW/cm²)**
E3980	192	455
E3997	210	498
E4025	180	426
E4044	180	426

5.2 Tests under electron beam pumping

The final target of our heterostructures is to work as the active region in an electron beam pumped device, as depicted in Figure 5.7(a). The device consists of a vacuum tube containing the AlGaN dice mounted on a heat sink (anode). In the original design of the project, the cathode consists of carbon nanotubes or carbon fibers, developed by the team of Prof. S. T. Purcell in Univ. Claude Bernard Lyon I (see Figure 5.7(b)).

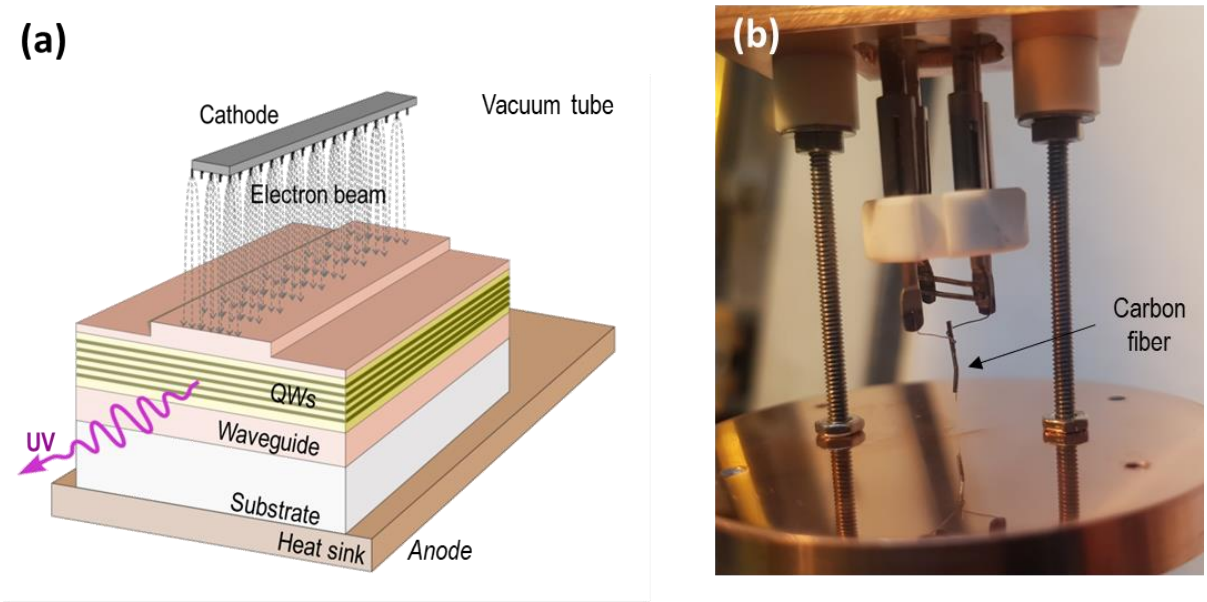

Figure 5.7. *(a) Schematic of the targeted UVLASE prototype. (b) Cathode from Univ. Claude Bernard Lyon I.*

For the first experiments, a commercial thermionic cathode was incorporated into a home-made experimental set-up built by our collaborators in Lyon, which allowed us to perform some preliminary measurements of our samples under electron beam pumping (continuous excitation) at room temperature. Figure 5.8(a) shows the experimental set-up. The laser bars were glued on a copper holder and introduced in the vacuum chamber, which is pumped down to $\approx 10^{-8}$ Torr. The copper holder is placed on a micromanipulator with movement in the X-, Y- and Z-axes. Outside the vacuum chamber, an optical set-up collects the edge emission from the sample, which is focused on an optical fiber connected to a spectrometer (see Figure 5.8(b)). During the last part of my PhD work, a liquid N_2 cooling system and a pulsing gun were integrated in the set-up.

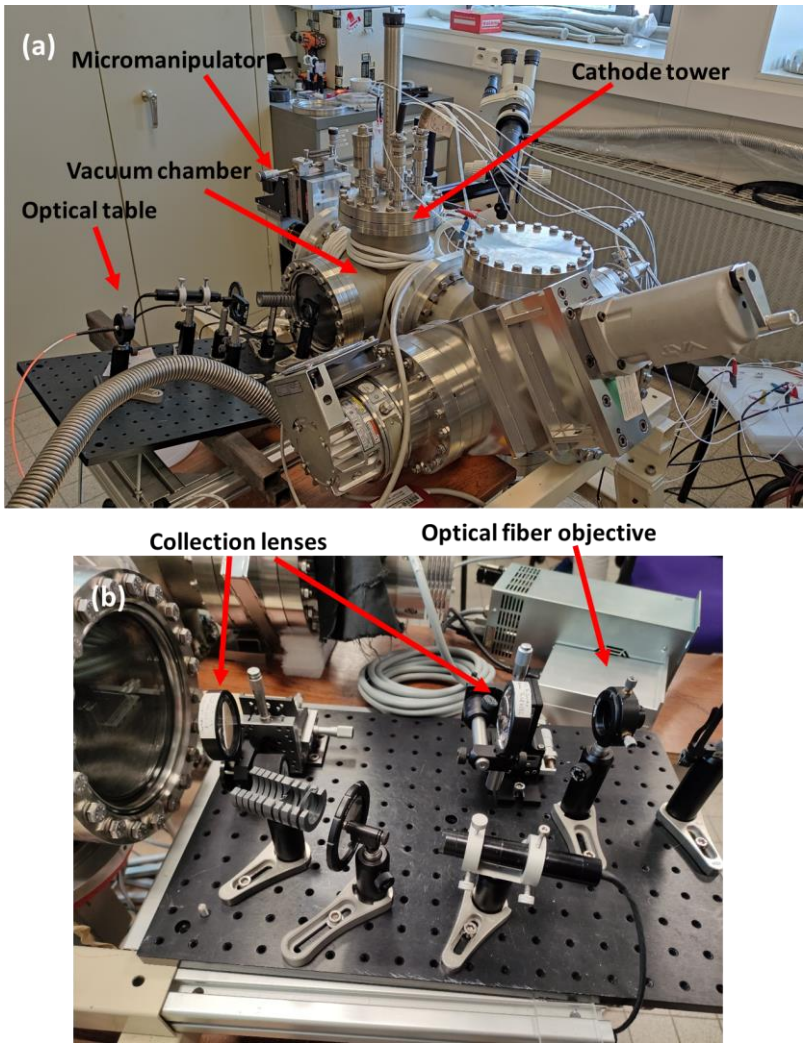

Figure 5.8. *(a) Experimental set-up at Univ. Claude Bernard Lyon I for cathodoluminescence. (b) Optical collection set-up.*

Figure 5.9(a) and (b) are a photograph and a scheme of the set-up inside the vacuum chamber. The cathode is polarized at the desired high voltage ($V_a = V_p$ in the scheme), with respect to the anode, and an additional power supply (V_f, I_f) is used to produce a current in the filament. In order to drive the electrons away from the space charge that is generated on the surface of the cathode, an external voltage (V_c and V_w) is applied to the Wehnelt cylinder (see Figure 5.9(c)) that contains the thermionic cathode (see Figure 5.9(d)). Empirical tests determined that the optimal value for these external voltages in our measurement conditions were $V_c = V_w = V_p$, but they can be tuned independently. An electromagnetic lens (V_{ext}) and three Einzel lenses (V_{Ez}) focus the electron beam into a round spot of 1 mm diameter, without changing its energy. The spot was measured replacing the anode by a phosphor screen. The current of the beam is labelled I_e. The beam impinges on the sample located at the anode, which at the same time is slightly polarized (V_{SE}) in order to attract the secondary electrons and reduce the difference between I_e and the real current through the sample, I_s.

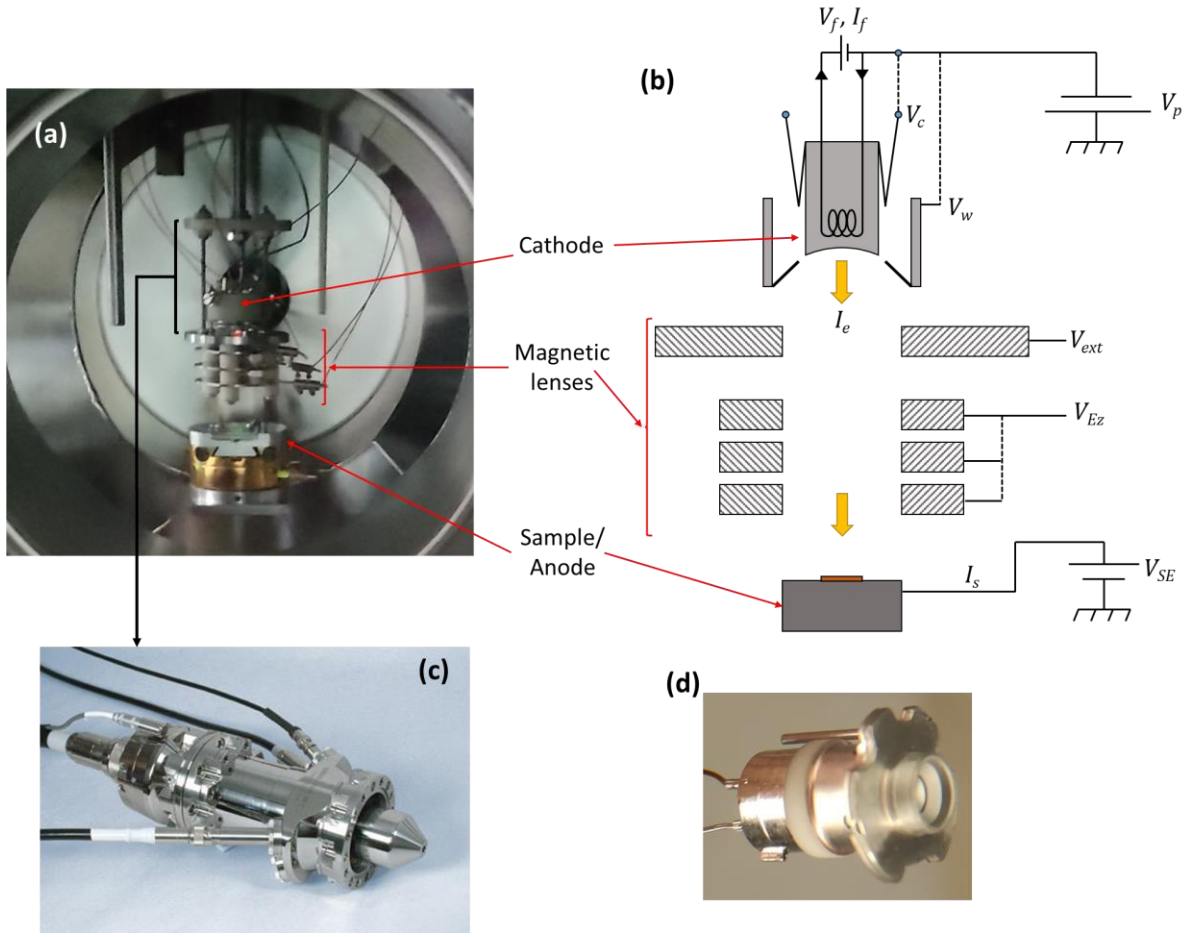

Figure 5.9. *Set-up inside the vacuum chamber: (a) photograph and (b) schematic view. (c) Electron gun. (d) Thermionic cathode.*

Figure 5.10(a) presents CL measurements of a 1.5-mm-long laser bar of sample E3980, as a function of the beam current at 130 K. The measurements were performed in the above-described set-up at room temperature and at 130 K, and with $V_p = 5$ kV and $V_{SE} = 500$ V. The emission was collected from the edge of the sample. The maximum injected current was limited to $I_s = 2$ mA. The main peak at 360 nm, corresponding to emission from the QWs, scales linearly with the injected current at room temperature, showing no evidence of stimulated emission for the range of pumping powers under study. This result is due to the fact that the maximum output of the electron beam in the current conditions is equivalent to 2.5 kW/cm^2, approximately two orders of magnitude lower than the lasing threshold estimated from our optical measurements. A positive result is that we do not find any evidence of saturation thermal effects for these excitation levels. On the other hand, at 130 K we observe a superlinearity in the CL intensity at a certain pumping power (see Figure 5.10(b)). This superlinearity did not come together with a drop in the peak width, which remains almost unchanged. Therefore, we attribute this behavior to the presence of amplified spontaneous emission, which is a promising result towards the lasing achievement. Further tests in the estimated threshold pumping powers are required to demonstrate the feasibility of lasing at room temperature with this technology in our samples.

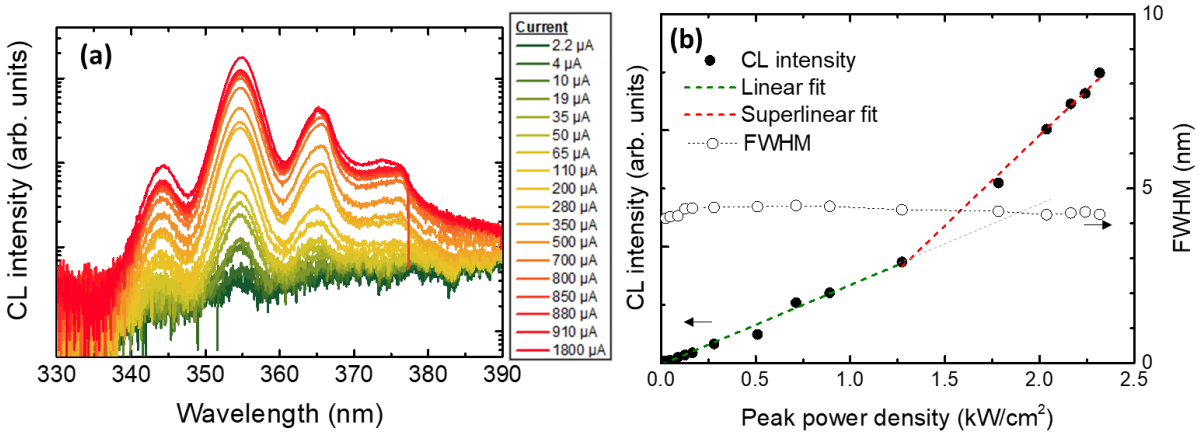

Figure 5.10. *(a) CL emission from E3980 as a function of the electron beam current (I_s) at 130 K. (b) Evolution of the CL intensity and FWHM of the MQW peak as a function of the electron beam pumping power at 130 K.*

5.3 Decorrelation of IQE and lasing threshold

In order to understand which sample design is more favorable as active media for electron beam pumped UV-A lasers, we compare the IQE_{MQW} results from Chapter 4 with the lasing threshold measurements in section 5.1. All these values are summarized in Table 5.2. Figure 5.11 compares the maximum IQE_{MQW} and lasing threshold as a function of temperature for samples E3997, E4025 and E4044. A relevant feature that we observe when comparing these values is that the two parameters are not correlated. At room temperature, E3997 is the sample that presents highest IQE_{MQW}, but at the same time the highest lasing threshold. Paradoxically, sample E4044, which presented the lowest IQE_{MQW}, exhibits at the same time the lowest lasing threshold. A similar situation occurs at low temperature but with an inversed tendency: E4044 is the sample with the highest IQE_{MQW} but the highest lasing threshold. This tendency also occurs when we compare the IQE_{MQW} values at threshold conditions.

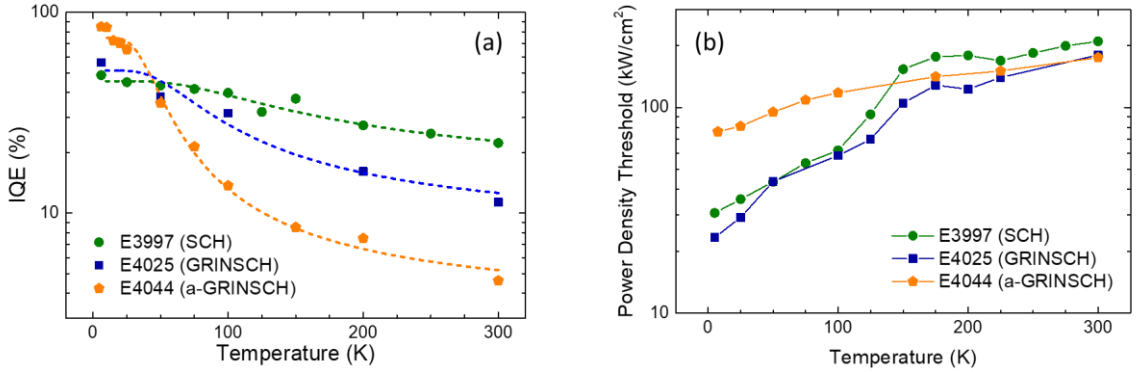

Figure 5.11. *(a) Maximum IQE_{MQW} as a function of temperature for E3997, E4025 and E4044. (b) Variation of the lasing threshold as a function of temperature.*

From the decorrelation between IQE_{MQW} and lasing threshold, we infer that there exist different physical phenomena governing each one of these parameters. Higher IQE_{MQW} at room temperature is associated with higher in-plane carrier localization in the MQW, which is explained by the fact that potential fluctuations prevent carriers from reaching non-radiative centers, as discussed in section 4.3.2. A decorrelation of the lasing threshold and the IQE_{MQW} is expected in samples presenting potential fluctuations in the wells, since they lead in inhomogeneous broadening of the gain spectrum [232]. In that case, higher pumping power is required to attain a high-enough gain to overcome the losses, consequently increasing the lasing threshold, even if the MQW is more radiative efficient. Inhomogeneous spectral broadening of the gain generally manifests as inhomogeneous broadening of the photoluminescence. However, this is not the case in our samples. If we compare the FWHM of the MQW PL peaks in Figure 4.16(b-d) with the lasing power density threshold, displayed in Table 5.2, the values do not follow the same tendency. For example, E4025 has a narrower emission line than E4044 in spite of having the same lasing threshold.

Table 5.2. *Lasing power density threshold at room temperature (RT) and at 6 K (LT) measured in 1-mm-long mechanically cleaved cavities when optically pumped with a Nd-YAG laser. Maximum IQE_{MQW} at room temperature and at 6 K. FWHM of the MQW PL peak from the spectra in Figure 4.16.*

	E3997	**E4025**	**E4044**
Design model	SCH	GRINSCH	a-GRINSCH
RT Lasing threshold (kW/cm²)	210	180	180
LT Lasing threshold (kW/cm²)	31	23	76
max[IQE_{MQW}(T=300 K)] (%)	22	11	5.0
max[IQE_{MQW}(T=6 K)] (%)	49	56	86
RT FWHM MQW PL peak (nm)	10	5	9
LT FWHM MQW PL peak (nm)	4	3	3.5

The lasing threshold depends on more factors, namely, the attainment of a carrier concentration high enough to ensure population inversion and a gain level that compensates the optical losses. In the three structures, the waveguide was designed to present similar optical confinement. The laser bars were cleaved in the same manner, and the cavity length was the same, long enough to ensure that the distributed mirror losses are relatively small. Therefore, the variation of the threshold should not be associated with the optical properties of the waveguide but rather to the difference in carrier injection and material quality. As discussed above, higher losses that appear when cooling down can relate to the alloy fluctuations and higher density of non-radiative point defects in the Al-rich topmost AlGaN layers. In contrast, at high temperature, carriers have enough energy to follow the potential ramp created by the GRINSCH and diffuse efficiently to the MQW.

Overall, at room temperature, carrier localization in the quantum wells leads to an enhancement of the radiative efficiency. However, lasing threshold appears to be more sensitive to carrier injection efficiency than to radiative efficiency. Therefore, designs including graded alloys that enhance the carrier injection are capable of overcoming the lower internal quantum efficiency.

5.4 Threshold reduction with two-step etched facets

5.4.1 Threshold dependence with cavity length

To assess the dependence of the threshold with the cavity length [233], I prepared a set of laser bar cavities with resonator lengths between 0.5 mm and 1.5 mm by mechanical cleaving along the (10-10) *m*-plane of GaN for samples E3997 and E4025. Figure 5.12 presents the lasing thresholds at room temperature under optical pumping, as a function of the cavity length. Note that E4025 has systematically lower power density threshold than E3997 due to the improved carrier transfer to the active MQW discussed in previous sections. Additionally, 0.5-mm-long laser bar from sample E3997 did not attain the lasing threshold with the maximum pumping power density achievable in our set-up (< 250 kW/cm^2).

The power density threshold is the pumping power density required to compensate the optical losses in the structure, including the internal (α_i) and the mirror (α_m) losses. Therefore, as previously discussed in section 2.2.2, the dependence of the threshold (P_{th}) on the cavity length (L) can be expressed as:

$$P_{th} = k(\alpha_i + \alpha_m) = k\left(\alpha_i - \frac{1}{2L} ln(R_1 R_2)\right) \tag{5.1}$$

where k is a proportionality constant and R_1 and R_2 are the reflectivity of the two cavity mirrors. In our case, we can assume that both cleaved facets are identical ($R_1 = R_2 = R$). Looking at the equation, in the case of long cavities, the contribution of the mirror losses becomes negligible compared to the internal losses. In our samples, we observe that for long cavities, the lasing threshold is smaller for the GRINSCH, indicating lower internal losses, which can be associated to the better crystallographic quality of the graded samples. On the contrary, the mirror losses become dominant in short cavities. In Figure 5.12, the cleaved cavities follow the tendency described in equation (5.1) (dashed lines in the figure). The fact that data follow the $1/L$ dependence indicates that the cavity losses are dominated by mirror losses.

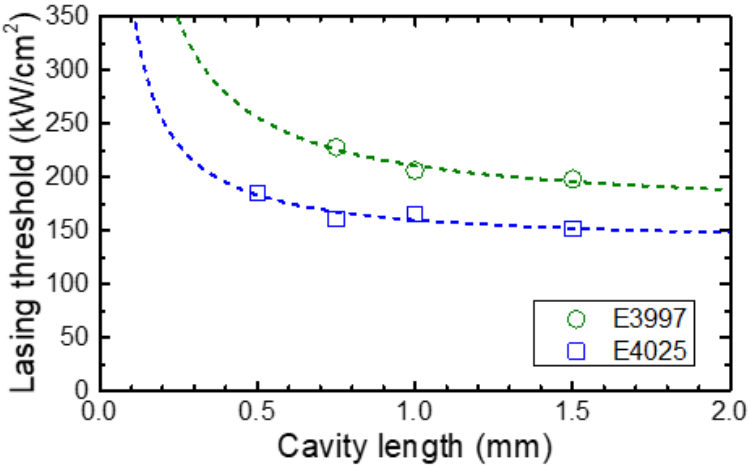

Figure 5.12. *Power density threshold at room temperature as a function of the cavity length for mechanically cleaved cavities from samples E3997 and E4025. Dashed lines represent fits to equation (5.1).*

5.4.2 Mirror fabrication

In order to reduce the lasing threshold of our samples, it is crucial to reduce the optical losses. In the case of edge emitting lasers, the fabrication of very smooth and vertical mirror facets is critical to the laser performance [234]. Mechanical cleaving is a common method for the fabrication of lasers for its good performance for a relatively simple process [17,235,236], although it is not practical for mass production and it sets a bottom limit to the cavity length. Furthermore, the strain fields due to the lattice mismatch in GaN/AlGaN SCH can result in non-ideal cleaved facets, due to the surface roughness induced by stress relaxation during the cleaving process. Also, mechanical cleaving is difficult to apply when the epilayers are grown heteroepitaxially on substrates whose cleaving planes are not aligned with those of the active layers, e.g. AlGaN on *c*-sapphire.

An alternative method for the definition of the cavity is using lithography and etching [237–239], which grants a precise geometry control, independent of the substrate. However, reactive ion etching (RIE) does not provide the vertical walls required for lasing, and complementary crystallographic selective etching process is required to reduce the mirror losses. In this sense, in spite of the high chemical resistance to etching of nitrides to common solvants, the exposure of AlGaN to tetramethylammonium hydroxide (TMAH), sodium hydroxide (NaOH) or potassium hydroxide (KOH) is known to lead to crystallographic selective etching rates [236,240–243]. It is often reported that the fabrication of UV laser cavities include a wet etching step, most often with TMAH [29,51,226,234,244] or KOH [238]. With this idea in mind, here I present the methodology developed in this work in order to obtain vertical and smooth facets with a two-step etching process.

First step is to define a cavity pattern on our sample by optical lithography. For this purpose, I designed the photolithography masks depicted in Figure 5.13, with the software KLayout [245]. The pattern consist in a stepped mesa, with a total height of 1500 µm, and a variable width between 100 µm and 500 µm, stepped every 300 µm. The mesa was defined like that in order to dispose of five different cavity sizes within the same sample. The length of the cavity will be defined by the width of the mesa along the *m*-direction. Therefore, the mesa has to be aligned with the m-plane of the AlGaN/GaN heterostructure. The design was printed in a 4" × 4" mask by the company Compugraphics Photomask. In addition to the mesa pattern, the mask includes several markers that were added to identify the mesa along the sample after fabrication, and to align a second mask in a future processing step that would define a ridge on top of the mesa.

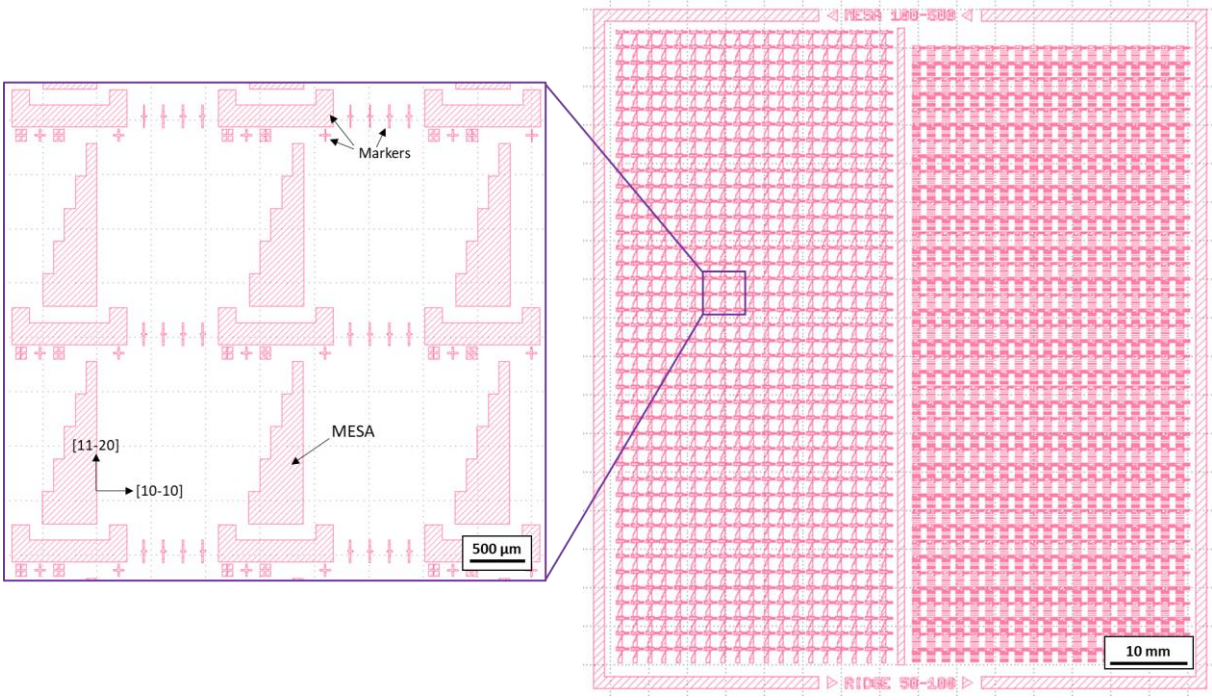

Figure 5.13. *Photolithography mask design. The mesa pattern will define the laser cavities.*

In a first approach in the lithography step, positive photoresist (AZ-5214E) was used as a mask for the definition of the cavities. Since the AlGaN surface resulted to be hydrophobic for the photoresist solution, an intermediate promoter thin layer of hexamethyldisilazane (HMDS) was spin-coated beforehand (4000 rpm, 60 s). The spin-coating recipe for the photoresist deposition was optimized to 2000 rpm during 60 s in order to obtain a photoresist film of 2.2 µm. It was observed that thinner photoresist films were completely consumed by the end of the ICP etching (approximately 1 µm of the photoresist mask is etched during a 5 min process), failing in their task to protect the patterned area. The sample with the photoresist was pre-baked at 100 °C during 90 s, for later be aligned with the photolithography mask and exposed to UV lamp during 30 s. After the exposure, the photoresist was developed with a solution of AZ developer 1:1 during 40 s. At the end of the dry etching process, the photoresist was removed with acetone.

For dry etching by ICP-RIE, samples with the patterned mask were glued on a Si wafer in order to be compatible with the equipment sample holder. The dry etching was performed with a Cl_2/BCl_3 (10/25 sccm) chemistry [246], optimized for GaN. The radiofrequency (RF) power was 220 W, the ICP power was 990 W, the sample temperature was 50 °C and the pressure in the chamber was 10 mTorr.

An initial test was carried out with a GaN-on-sapphire template, for an etching time of 5 min. The height of the resulting mesa was measured with a profilometer, with the results summarized in Table 5.3. We observe that 1.07 µm of GaN were etched during the 5 min, leading to an etching rate of 214 nm/min for this recipe. On the other hand, the photoresist is also etched by the chemistry selected, with an etching rate of 198 nm/min. The deposited photoresist is thick enough (originally 2 µm) to withstand until the end of the procedure. Figure 5.14 presents a SEM image of the etched mesa. The pattern is clearly defined, but the etched sidewalls form an angle of 50° with the direction normal to the surface.

Table 5.3. *Mesa thickness at each step of a 5 min dry etching of a GaN-on-sapphire template.*

	Thickness (µm)
Resist mask after development	2.18
Mesa after etching (with resist)	2.06
Mesa after photoresist removal (without resist)	1.07

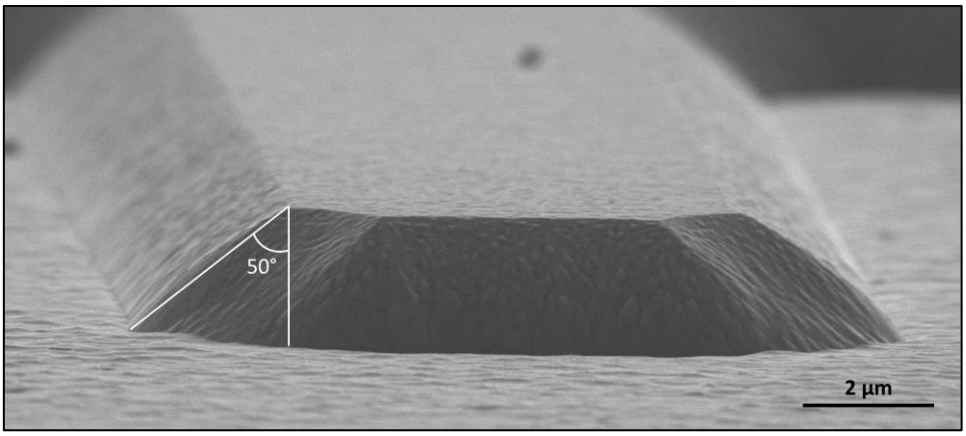

Figure 5.14. *SEM image of the dry etched facet of a GaN template after photoresist removal.*

To reduce this tapering, a second approach consisted in the implementation of a SiO_2 hard mask. For this purpose, a 500-nm-thick SiO_2 layer was deposited by chemical vapor deposition (CVD). Then, the same photolithography process was implemented on the SiO_2 layer with the positive photoresist procedure. Next, the pattern was etched on the SiO_2 hard mask with a CF_4/CH_2F_2 chemistry (25/25 sccm, RF power = 125 W, ICP power = 600 W, pressure in the chamber = 5 mTorr). The etching rate was 80 nm/min, for a total of 7 min to etch the 500 nm.

Afterwards, the photoresist is lifted-off and the GaN heterostructure is dry etched with the same conditions as before. Unfortunately, the resulting mesa revealed that the 500 nm from the SiO_2 hard mask were completely etched with the Cl_2/BCl_3 chemistry. Consequently, the top-most nanometers of the GaN mesa were also etched. This is critical for our AlGaN heterostructures, since the top-most nanometers constitute the top cladding layers of the waveguide.

In order to overcome this problem, a third approach was considered, in which the hard mask was consisted in a SiO_2/Ni (500 nm/150 nm) layer. With this combination, SiO_2 acts as a hard mask for AlGaN while protected from the Cl_2/BCl_3 chemistry by the Ni overlayer. At the end of the process, the SiO_2 hard mask can be easily removed with hydrofluoric acid (HF). Therefore, for this new approach, the SiO_2 layer was deposited on the sample by CVD, but AZ-5214E was used as negative photoresist to define the cavities by photolithography. This is the same resist that we used as positive photoresist in the previous approaches, however, it has the particularity that it is a reversible resist, meaning that depending on the preparation process, it can act as a positive or negative resist. In this case, we choose the negative procedure, that consisted in spin-coating the resist at 4000 rpm during 60 s (thickness ≈ 1.4 µm). After baking at 100 °C during 120 s, the sample was aligned with the mask and exposed to the UV lamp during 5.5 s. Immediately after, the sample underwent a second baking at 120 °C during 120 s, to later be flood exposed during 32 s (without the photolithography mask). Finally, the resist is developed with AZ developer 1:1 during 40 s. The resulting sample presents a layer of photoresist with exposed SiO_2 presenting the patterned shape. Next, a thin Ni layer is deposited by electron-beam evaporation, followed by lift-off. At the end, the sample has a Ni hard mask with the desired pattern. From here onwards, the process is the same as before, starting by etching the SiO_2 layer with the CF_4/CH_2F_2 chemistry, followed by the etching of the GaN mesa with the Cl_2/BCl_3 chemistry. The SEM image of the resulting mesa after dry etching in an AlGaN GRINSCH sample is presented in Figure 5.15. The top dark layer corresponds to the SiO_2/Ni hard mask. With this mask, the facet angle was reduced to 15°. The mask was subsequently removed by washing in HF.

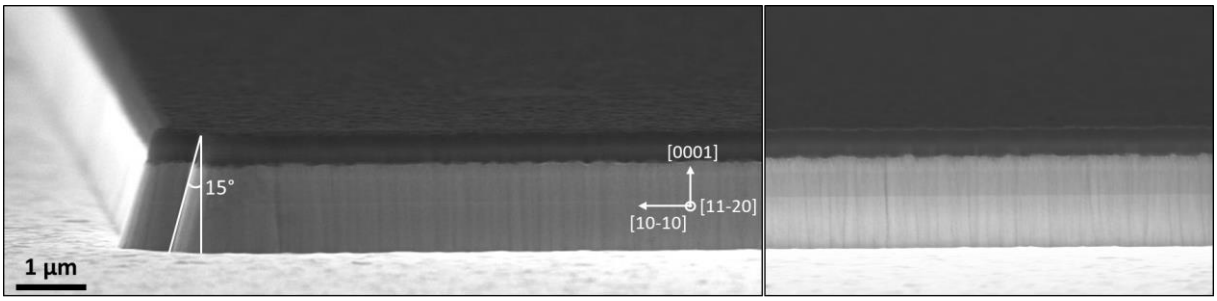

Figure 5.15. *SEM images of the dry etched facet of an AlGaN/GaN GRINSCH sample, before removing the SiO_2/Ni mask.*

Table 5.4 presents the etched depth measured by profilometry compared to the height of the SCH, verifying that the complete stack has been exposed. The as-dry-etched samples did not display any laser emission under optical pumping, which is explained by the imperfection of the optical cavity due to the tilted facet [236,247]. As modelled by van Deurzen *et al* [234], short wavelength emitters based on cavity optics have a high sensitivity to boundary imperfections. Therefore, a crystallographic-selective wet etching process is required to further reduce the facet tilt. The wet chemical etching of AlGaN in KOH-based solutions is highly anisotropic [242], and can be used to reduce tapering.

Table 5.4. *Etched mesa thickness for sample E3997 and E4025 compared to the structure stack height.*

	Mesa (nm)	**SCH (nm)**
E3997	1120	606.4
E4025	897	597.8

For the optimization of the wet etching process, initial tests were performed on a 4 µm-thick GaN-on-sapphire template. The layer was first dry etched following the above-described procedure, with the result shown in Figure 5.16 (top row) after removal of the hard mask. Then, the sample was dipped in a deionized water solution of AZ400K developer (KOH-based developer from AZ Electronic Materials USA Corp.), AZ400K:H_2O = 1:4, stabilized at 65°C. Figure 5.16 show the resulting facets after 1, 2, 3, 4, 6, 8 and 10 h of chemical treatment. The images reveal how the facets evolve under wet etching. In a first step, the areas damaged during the dry etching process are rapidly removed, and we observe the emergence of nanofacets at the sidewalls (first 4 hours), mostly *c*-(0001) and *m*-{10-10} planes. Increasing the etching time, the vertical facets become larger and the presence of (0001) nanofacets is restricted to the part of the sidewall closer to substrate (6-8 hours). For longer etching time (10 hours), vertical facets are obtained. Note that for convex geometries, the etching of the nanofacets is slightly slower.

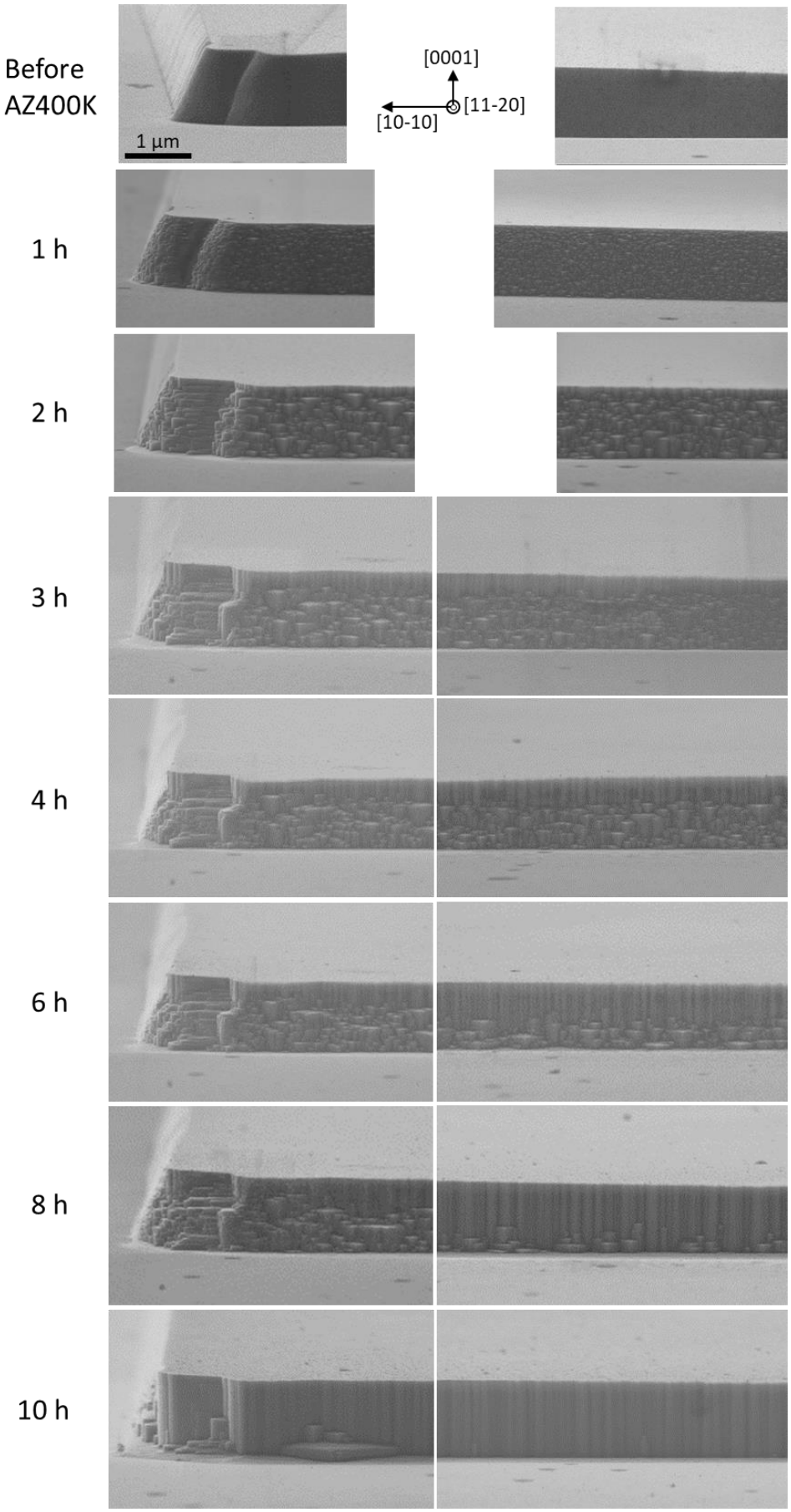

Figure 5.16. *SEM images of the dry etched facets of a GaN-on-sapphire template after a certain wet etching time in AZ400K:H_2O (1:4) at 65 °C. The scale and crystallographic axis are the same in all the images.*

Figure 5.17 presents a top-view SEM image of the resulting facets, showing the straight morphology of the *m*-{10-10} planes and the roughness of *a*-{11-20} planes due to the presence of *m*-{10-10} nanofacets. In contrast with convex geometries, concave areas etch at a faster rate. The shape that results from the etching process is explained by the Wulff-Jaccodine model [248], which can predict the 3D geometry over time [249–251]. This geometrical model, which can be considered the inverse of a growth model, idealized the crystal facets as mathematical planes, neglecting real surface structures. It considers that facets with slow etch rate appear in concave geometries, leading to better quality etched planes than in convex areas. In KOH-based solutions, AlGaN *m*-{10-10}, *a*-{11-20} and *c*-(0001) planes have etching rates with order of magnitude slower (nm/s) than those of semipolar and (000-1) planes (µm/s). Therefore, vertical facets are exposed, particularly those with the slowest etching rate, i.e. *m*-{10-10} planes [252].

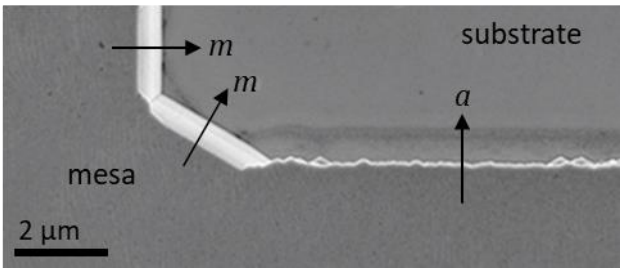

Figure 5.17. *Top-view of the etched sample showing straight, vertical m-facets and rough a-walls showing m-nanofacets.*

The above-described experiment was useful to visualize the process leading to smooth *m* facets. However, for device fabrication, the method must be accelerated. Therefore, for the fabrication of the laser mirrors, we have used non-diluted AZ400K stabilized at 80°C, with the results illustrated in Figure 5.18 for sample E4025. Note that the facets are vertical and there is no significant differences in the etching rate for the various layers in the stack. In fact, it exists a dependence of the etching rate on the Al molar fraction [253]. However, it is negligible for short etching times and low Al molar concentration such as in our case. This effect is not visible in the 10 h process from Figure 5.16 because the sample was bulk GaN.

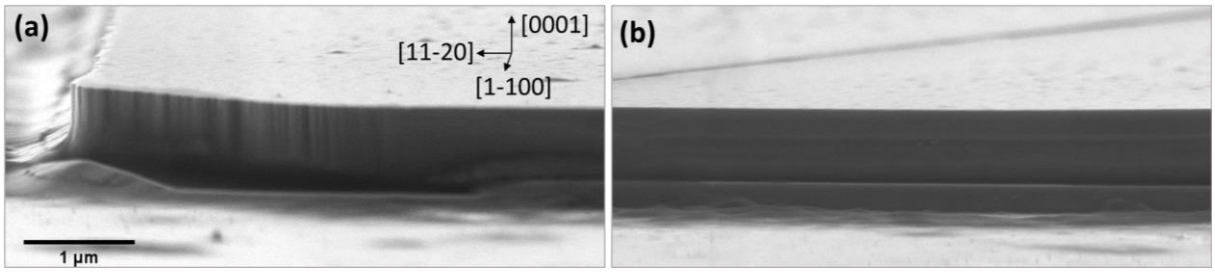

Figure 5.18. *SEM image of the m facet of a laser cavity from sample E4025 after the two-step etching process (dry etching + crystallographic selective etching).*

5.4.3 Comparison between cleaved and etched facets

In the previous section, we developed a two-step etching process to obtain vertical and smooth facets for our laser cavities. However, the question remains if this process can lead to comparable or improved mirror facets with respect to mechanical cleaving, or to what point it might limit the device performance. With that purpose, the profile of the cleaved bars from section 5.4.1 were imaged by SEM, in Figure 5.19(a), and AFM, in Figure 5.19(b), showing that the mechanical cleaving leads to tilted faceting due to the stress relaxation of the AlGaN/GaN heterostructure. The root mean square (rsm) roughness of the facet at the level of the heterostructure is in the order of 20 nm, while the rms roughness of the facet generated at the level of the GaN substrate is in the order of 0.4 nm.

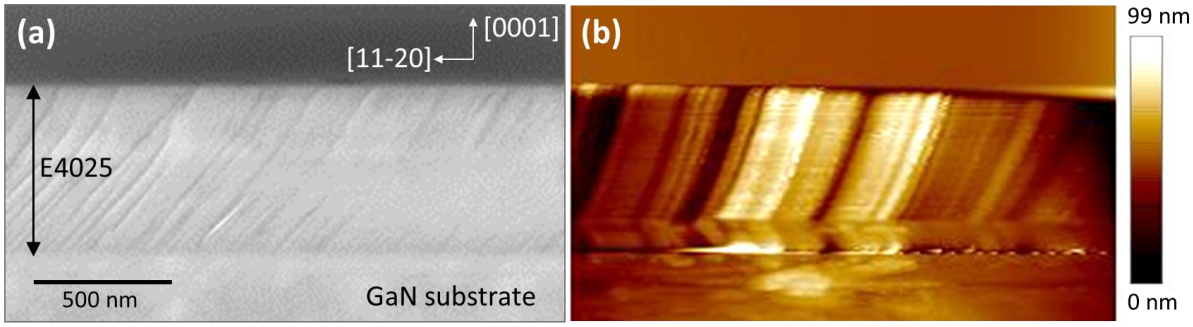

Figure 5.19. *(a) SEM and (b) AFM images of the m facet of sample E4025 laser cavity after mechanical cleaving.*

Top-view SEM images of the etched facet (see Figure 5.20(a)) and the cleaved facet (see Figure 5.20(b)) of E4025 provide further evidence of the higher quality of the etching process, with straight facet, in comparison with the mechanically cleaved facet, whose irregularities are clearly visible at the scale of the image. Lasing was demonstrated in cleaved laser bars above, but the enhanced roughness at the heterostructure can surely produce significant light scattering when operating at short wavelengths, leading to important optical losses due to the mirror quality.

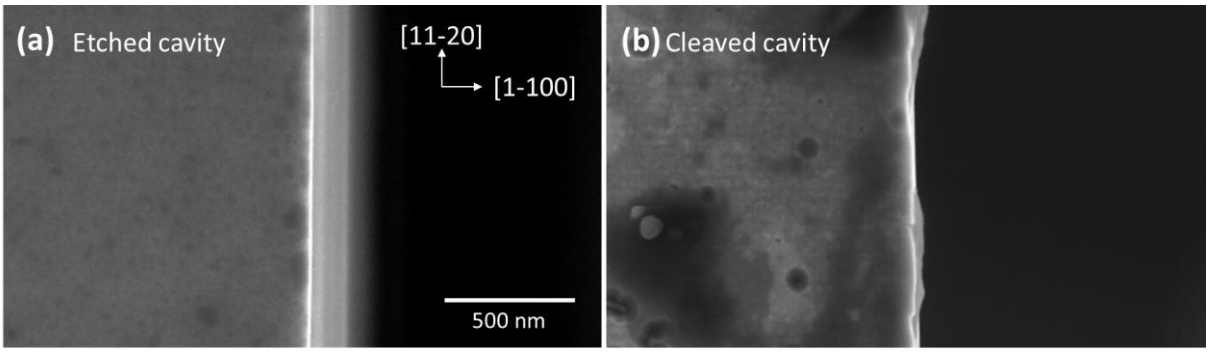

Figure 5.20. *Top-view SEM images of (a) an etched facet and (b) a mechanically cleaved facet of an E4025 laser cavity. The scale is the same in both images.*

PL measurements were performed with the etched cavities in order to compare them with the results obtained with mechanically cleaved cavities. Figure 5.21 show the PL spectra for a 0.3 mm-

long mesa cavity with etched facets and 1 mm-long cavities with cleaved facets for sample E3997 and E4025. Figure 5.21(e) presents the PL intensity as a function of the excitation power density for sample E3997, showing a superlinear dependence for pumping power densities higher than the lasing threshold, which is 200 kW/cm² for the etched cavity (L = 0.3 mm) and 210 kW/cm² for the cleaved cavity (L = 1 mm). Figure 5.21(f) presents the same measurement for sample E4025, showing also a superlinear dependence above the lasing threshold, which is 100 kW/cm² for the etched cavity (L = 0.3 mm) and 180 kW/cm² for the cleaved cavity (L = 1 mm). In both cases, the etched facets cavities present lower threshold than the cleaved facet cavities, in spite of the shorter cavity length, which accentuates the optical mirror losses, by approximately halving the lasing threshold that would be obtained by the cleaved tendency.

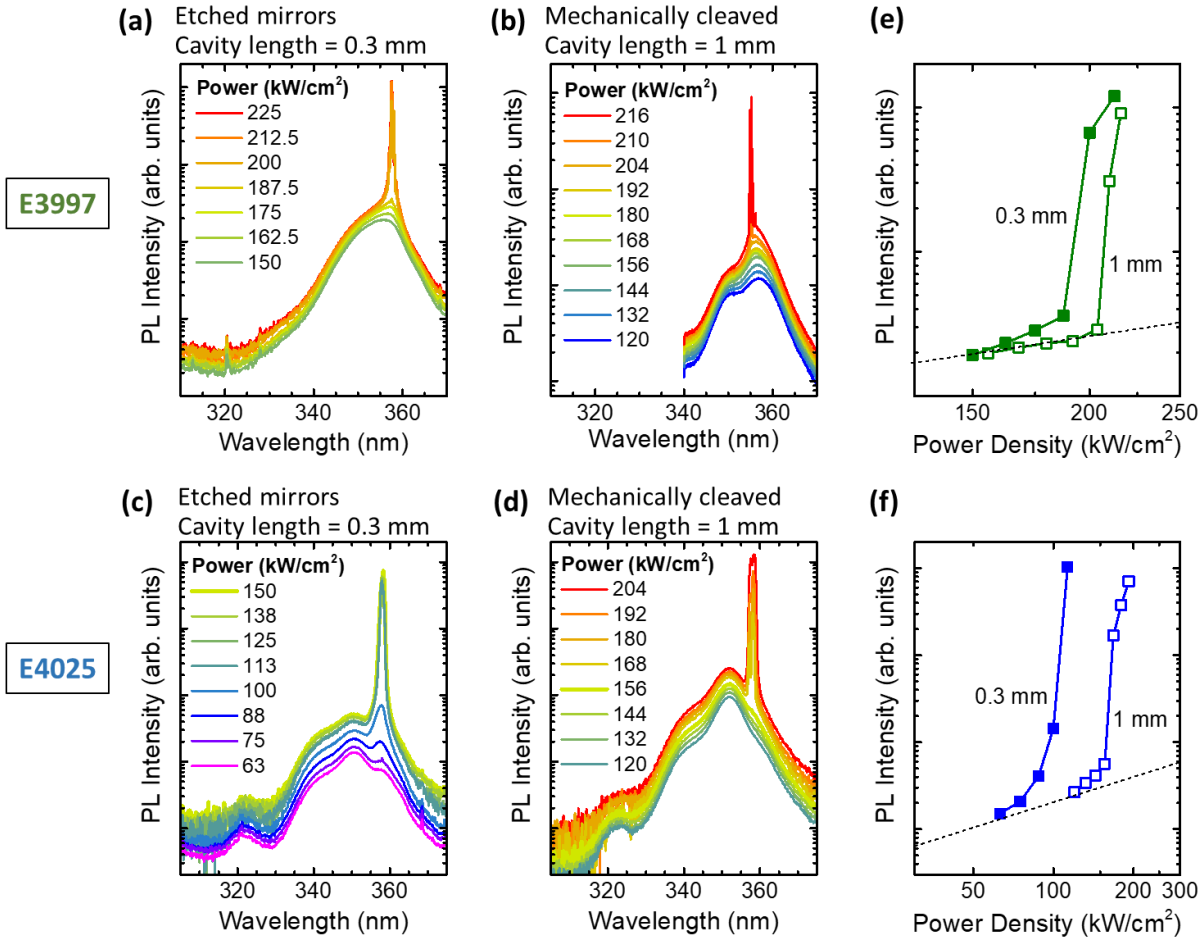

Figure 5.21. *PL spectra as a function of the pumping power density: (a) E3997 with etched facets and a cavity length L = 0.3 mm; (b) E3997 with mechanically cleaved facets and L = 1 mm; (c) E4025 with etched facets and a cavity length L = 0.3 mm; (d) E4025 with mechanically cleaved facets and L = 1 mm. (e-f) Variation of the PL intensity as a function of the pumping power density for cavities with etched facets (L = 0.3 mm) and mechanically cleaved (L = 1mm) for samples (e) E3997 and (f) E4025. The dashed line shows the slope of a linear trend.*

To get a deeper insight on the improvement of the optical performance using etched facets, Figure 5.22 summarizes the evolution of the lasing threshold as a function of the cavity length, as

presented in Figure 5.12, but with the addition of the etched facets cavity of 0.3 mm length (solid symbols in the graph). As seen before, the data follows the tendency $1/L$ described by equation (5.1) (dashed-lines in the graph), indicating that the cavity losses are dominated by mirror losses. The etched cavities, with a length of 0.3 mm, are significantly shifted with respect to that trend, showing a much lower lasing threshold than cleaved cavities. As the internal losses are expected to be the same in both cleaved and etched cavities, coming from the same sample wafer, the different lasing threshold is due to the improved reflectivity of the mirrors in etched cavities.

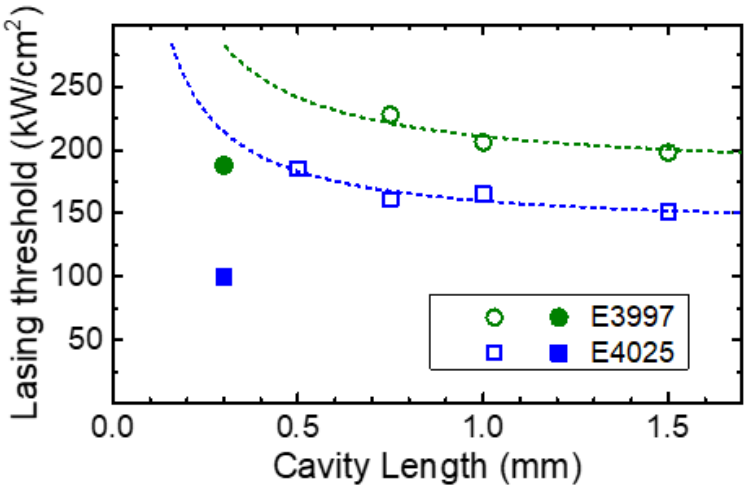

Figure 5.22. *Power density threshold as a function of the cavity length for E3977 and E4025, including mechanically cleaved (hollow symbols) and etched (solid symbols) samples. Dashed lines illustrate the trend given by equation (5.1).*

The stimulated emission of the heterostructures develops on the fundamental mode of the waveguide formed by AlGaN layers due to amplification in quantum wells, which is due to the effective absorption of the higher-order modes in the GaN substrate material. Therefore, in the first approximation, the reflection coefficient can be estimated as the reflection coefficient of a plane wave incident perpendicularly on the plane of the Fabry-Perot resonator. Since the facets are non-coated, the maximum reflectivity (R_{max}) achievable is determined by the contrast between the refractive index of the active media and the external media, as predicted by Fresnel equation:

$$R_{max} = \left(\frac{1 - \left(\frac{n_2}{n_1}\right)}{1 + \left(\frac{n_2}{n_1}\right)} \right)^2 \tag{5.2}$$

where n_1 and n_2 are the refractive indices of the inner and external media, respectively. In our case, taking the refractive index of GaN (n_{GaN} = 2.6915) [254] and air (n_{air} = 1) at the emission wavelength (λ = 355 nm) results in an ideal reflectivity for a perfect facet of R_{max} = 21%. Assuming that the reflectivity of the etched facets is close to the ideal value, we can estimate the reflectivity of the mechanically cleaved mirrors using equation (5.1) to be $R_{cleaved} \approx 3.2\%$. This reflectivity

value is the maximum obtained from the cleaved facets, since it was extracted from the lowest lasing threshold for each cavity. Along the cleaved cavities, the lasing threshold varies typically by ± 13%, which is explained by the inhomogeneity of the facet roughness. Therefore, the value of $R_{cleaved} \approx 3.2\%$ must be understood as an upper limit of the reflectivity of the cleaved mirrors.

In summary, we can conclude that in these strongly strained heterostructures, cleavage causes surface roughness due to stress relaxation that translates in boundary imperfections for the optical cavity. Therefore, the implementation of a two-step etching process for the fabrication of the laser mirrors has proved to be beneficial for the laser performance.

5.5 Design of a distributed Bragg reflector (DBR) coating

5.5.1 Modelling the DBR

Lasing threshold is directly related to the laser cavity optical losses, including internal losses (intrinsic to the heterostructure material and crystal quality) and mirror losses (directly related to the cavity mirror reflectivity). A considerable improvement of the facet reflectivity should decrease the lasing threshold. As we have seen in the previous section, the maximum reflectivity of the facets comes defined by the refractive index contrast between the two sides of an interface. The laser cavity facets presented in this chapter resort to the refractive index contrast between the GaN QWs and the external media (air) to provide optical feedback, which according to equation (5.2), provides a maximum reflectivity of 21%. The achievement of quasi-ideal facets by two-step etching process brings the reflectivity of the cavity mirrors close to this maximum value. However, from 21% to a perfect reflectivity there is still room to improve. In order to raise the reflectivity to further extends, it is possible to add coatings to the facets such that there is an extra interface with strong refractive index variation to reflect the light. Here, we consider the possibility of incorporating a distributed Bragg reflector (DBR), which consists of a multilayered stack that alternates layers of high and low refractive indices, resulting in a periodic variation as depicted in Figure 5.23(a). At each interface, the light is partially reflected. For a given wavelength (λ_0), there is a particular layer thickness (t) for which constructive interference occurs between reflections, given by the expression

$$t = \frac{\lambda_0}{4n} \tag{5.3}$$

where n is the refractive index of the layer. At this thickness, the structure behaves as a high quality reflector for the selected wavelength.

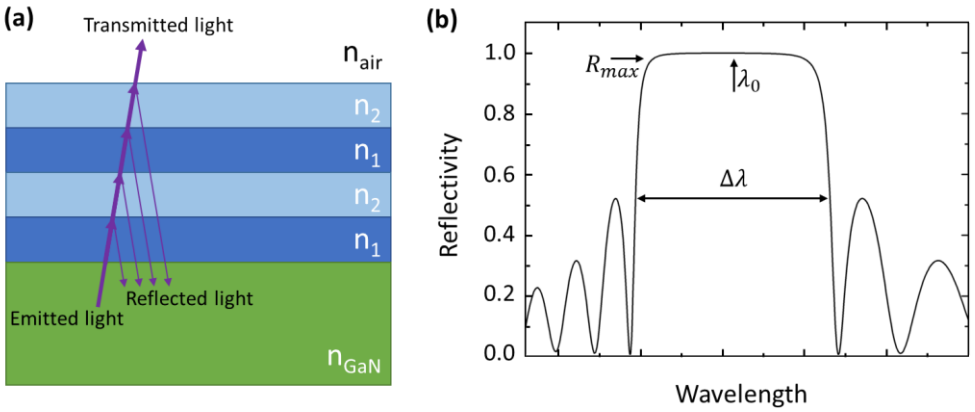

Figure 5.23. *(a) Schematic description of a DBR with an alternation of layers with high refraction index (n_H) and low refraction index (n_L). (b) Calculated reflectivity of a general DBR structure.*

Figure 5.23(b) shows the typical spectral response of a DBR under normal incidence illumination. The peak reflectivity, R_{max}, is given by the following expression [255]:

$$R_{max} = \left(\frac{1 - \left(\frac{n_t}{n_i}\right)\left(\frac{n_1}{n_2}\right)^{2N}}{1 + \left(\frac{n_t}{n_i}\right)\left(\frac{n_1}{n_2}\right)^{2N}} \right)^2 \tag{5.4}$$

where n_t and n_i are the refractive indices of the transmitted and incident media, respectively; n_1 and n_2 are the refractive indices of the first and second layer from the DBR (in the order of incidence of the light); and N is the number of repeated pairs of high and low refractive index layers. The reflectivity raises by incrementing the number of repetitions and the contrast between refractive indices. Peak reflectivities exceeding 99% can be achieved by this approach [256]. The high reflectivity window, $\Delta\lambda$, also called stop band, can be calculated from

$$\Delta\lambda = \frac{4}{\pi}\frac{(n_1 - n_2)}{(n_1 + n_2)}\lambda_0 \tag{5.5}$$

In our case, we target to fabricate a DBR resonant at the emission wavelength λ_0 = 355 nm, to be deposited on the cavity facet to reduce the optical losses related with the mirrors. The materials that constitute the DBR layers must be transparent in that spectral region. We chose to use silicon oxide (SiO_2) as low index material and tantalum peroxide (Ta_2O_5) as high index material [257]. The refractive index of SiO_2 and Ta_2O_5 were available from ellipsometry measurements from reference [257]. With this information, we can calculate the corresponding layer thickness to obtain quarter-wavelength mirrors. The data is summarized in Figure 5.24. According to these calculations, to obtain maximum reflectivity at a wavelength of 355 nm, the nominal thicknesses of the DBR layers must be 60 nm for the SiO_2 and 38 nm for the Ta_2O_5.

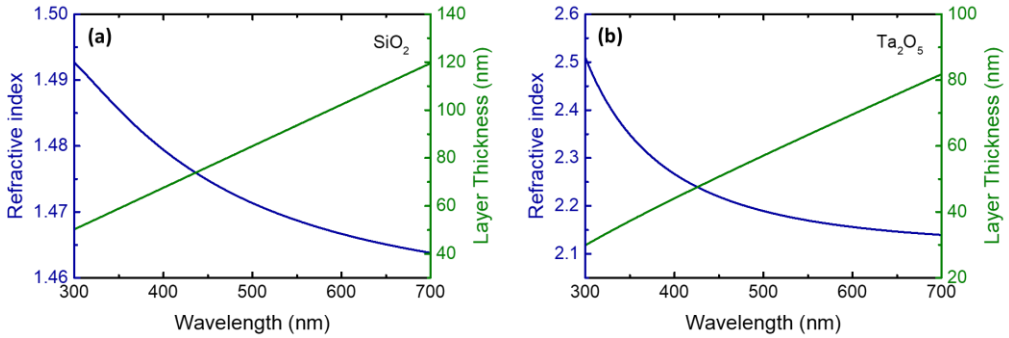

Figure 5.24. *Refractive index (blue) and corresponding layer thickness to obtain maximum reflectivity (green) as a function of wavelength for (a) SiO_2 and (b) Ta_2O_5.*

The last parameter to choose when designing the DBR mirrors is the number of SiO_2/Ta_2O_5 pairs to be deposited. As stated above, a larger number of repetitions would considerably increase the reflectivity of the facets, however, it can be detrimental for the quality of the deposited layers. In fact, thick deposits could lead to deposition on the top of the laser structure and fracture of the mirrors. To optimize the number of pairs to deposit, we calculate the maximum reflectivity as a function of N using equation (5.4). The dependence of the maximum reflectivity as a function of the number of pair repetitions N is illustrated in Figure 5.25(a). In our system, we are considering the GaN QWs as the incident media through where the light travels to hit the DBR ($n_i = n_{GaN}$ = 2.5417) [258], being the air the transmitted media ($n_t = n_{air}$ = 1). For the DBR layers, we considered two options: the dark blue curve represents a DBR system that has Ta_2O_5 as the first layer of the stack ($n_1 = n_{Ta_2O_5}$ = 2.3381), while the bright blue line corresponds to a DBR system that starts with a SiO_2 layer ($n_1 = n_{SiO_2}$ = 1.4848). Note that the refractive indices correspond to a wavelength of 355 nm. As expected, the DBR system with SiO_2 as first layer offers better reflectivity capabilities due to the larger contrast of refractive indices with respect to the GaN. We can also observe how when the number of pair repetitions is high enough, the reflectivity tends to 100% in both cases. For our case, we chose to go for the Ta_2O_5/SiO_2 system with N = 5, which offers a reflectivity >95%, while keeping a compromise with the thickness of the mirror. To reinforce our choice for N, we also performed calculations of the spectral reflectance with a MATLAB implementation of the transfer matrix method [259] (original code written by Bruno Gayral, CEA/PHELIQS). Figure 5.25(b) shows the spectral reflectance expected in our system for N = 4, 5 and 6. The results show that the stopband is compatible with the spectral range of our samples (350-365 nm) and a maximum reflectivity of 98%.

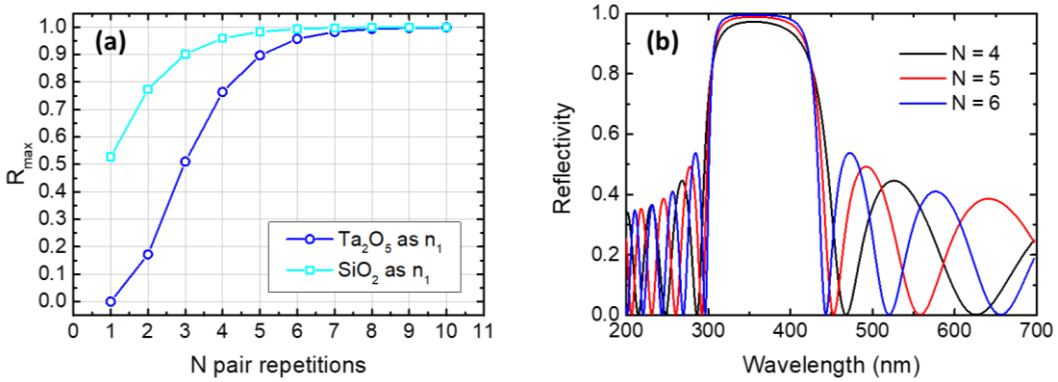

Figure 5.25. *(a) Maximum reflectivity as a function of the N pair repetitions. Dark line represents a DBR where the first layer is Ta_2O_5, while bright line represents a DBR with SiO_2 as first layer. (b) Spectral reflectance of the DBR mirror on sapphire for different number of pairs.*

5.5.2 Testing the DBR on sapphire

To calibrate the deposition of our mirrors, we use first a sapphire substrate as reference sample ($n_{sapphire}$ = 1.7959) [260]. The multilayered stack was deposited by electron beam evaporation at 150°C manipulated by Eric Delamadeleine (CEA/PHELIQS) with the technique described by Amargianitakis *et al*. [257]. Figure 5.26(a) shows a SEM view of the DBR cross section, where we can distinguish the different layers. Figure 5.26(b) shows an AFM measurement of the DBR surface. The topography presents a grainy surface, which is characteristic of sputtered materials. The rms roughness is about 0.7 nm, confirming the good quality of the deposition.

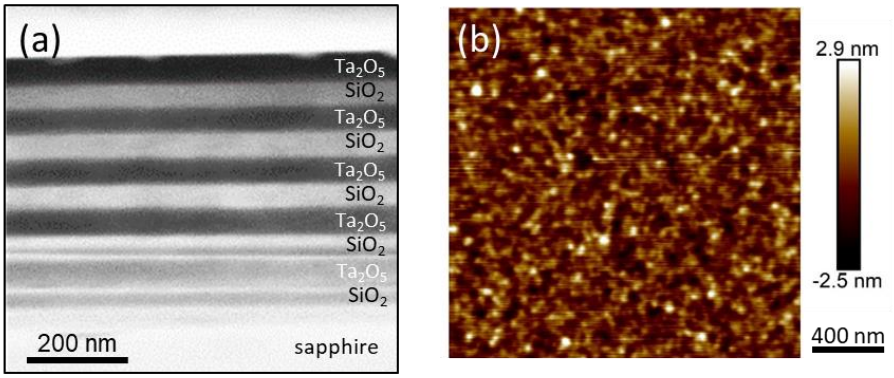

Figure 5.26. *(a) SEM image of the DBR cross section. (b) AFM image of the DBR surface.*

In order to estimate the reflectivity of the deposited mirrors, we measured the reflectivity of the reference sample. Figure 5.27 describes the experimental setup: a Xe lamp is coupled to a Gemini 180 monochromator, which can select specific wavelengths from the broad lamp spectrum. The light is pulsed using an optical chopper. A convergent lens is used to obtain a parallel light beam that will be reflected on an aluminum mirror and imping the sample surface with almost normal incidence. A UV-enhanced high-speed silicon photodetector will collect the light reflected by the DBR sample surface. The electrical signal of the detector feeds a SR830DSP

lock-in current amplifier, which uses the chopper signal as a reference for synchronous detection. The spectral reflectivity is calculated as

$$R(\lambda) = \frac{I_r(\lambda)}{I_i(\lambda)} \tag{5.6}$$

where $I_r(\lambda)$ is the spectral intensity of the light reflected by the sample surface and $I_i(\lambda)$ is the spectral intensity that impinges the sample, which we measure by placing the silicon detector in the sample place.

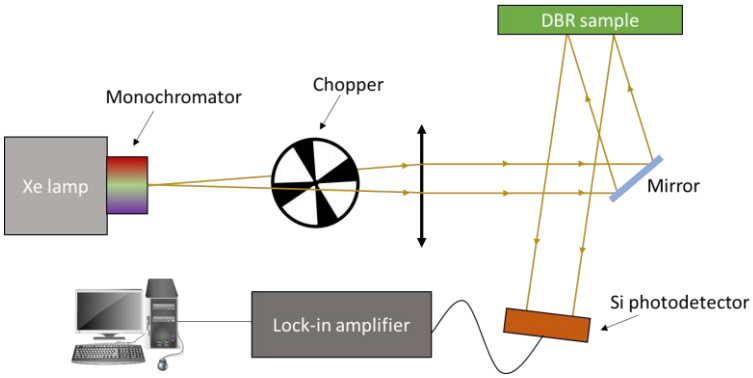

Figure 5.27. *Set-up for reflectivity measurements.*

Figure 5.28 presents the reflectivity measurements, compared with theoretical calculations. The DBR reflectivity is higher than 90% from 340 to 425 nm, including our targeted wavelength of 355 nm in the optical stopband. However, we observe a red shift of the experimental refeltion band compared with the calculation. The spectral location of the band corresponds to a DBR with layers 8% thicker than the nominal structure. The deviation of thickness is consistent with the SEM image in Figure 5.26(a): the total DBR thickness is 536 nm thick instead of the nominal 490 nm.

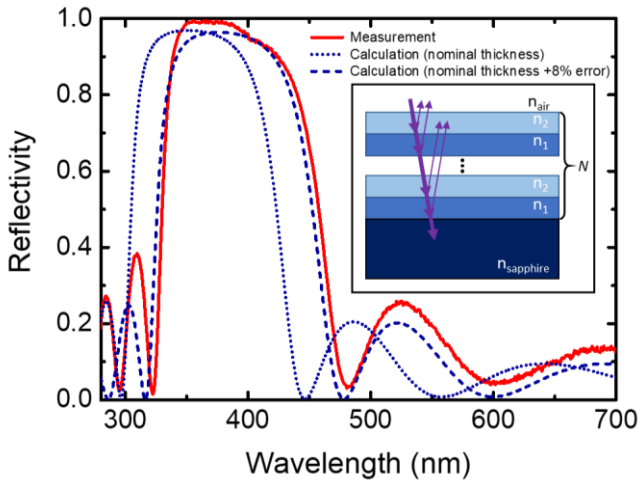

Figure 5.28. *Reflectivity measurement of a DBR with N = 5 repetitions of SiO_2/Ta_2O_5 (60 nm / 38 nm), deposited on sapphire. The dotted line represents a theoretical calculation with the nominal thicknesses, while the dashed line represents a theoretical calculation with an increment of 8% in the layer thicknesses.*

5.5.3 Implementing the DBR on cleaved laser bars

The tested mirrors were also deposited on the rear facet of a 1.5-mm-long mechanically cleaved laser bar from sample E4019 (duplicate of sample E3997). To restrict the deposition to the facet, the top of the laser bar was protected with kapton tape. The laser bar was glued on a sample holder so that the deposition impinged perpendicular to the facet. The PL spectra of the laser bar at room temperature are presented in Figure 5.29(a) before the DBR deposition (recorded with a 600 groves/mm grating) and in Figure 5.29(b) after the DBR deposition (recorded with a 1800 groves/mm grating). The PL spectra with DBR is recorded with a higher resolution grating, which allows resolving different lasing modes that are excited. We can observe oscillations in the peak due to the interference between reflections. However, when we compare the lasing thresholds, we do not find any improvement with the incorporation of the DBR mirrors. In fact, the threshold is even degraded, increasing from 248 kW/cm^2 without DBR to 308 kW/cm^2 with DBR.

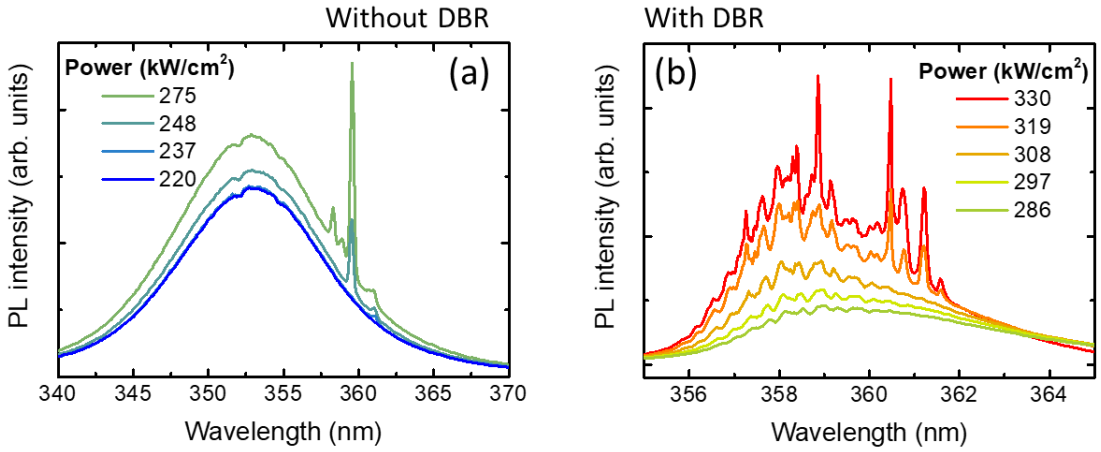

Figure 5.29. *Room temperature PL spectra a 1.5-mm-long E4019 laser cavity (a) before and (b) after DBR deposition.*

To understand this result, we observed the edge of the cleaved laser bar with the deposited mirror in the SEM. The images in Figure 5.30 reveal that the deposition does not reach the edge of the sample, where the MQW layers are located. The deposition seems quite homogeneous along the facet, but the edges are irregular and leave about 2 µm uncoated, which explains that the lasing threshold does not improve. Therefore, the deposition process must be improved, and it must also be adapted to render it compatible with mesa structures.

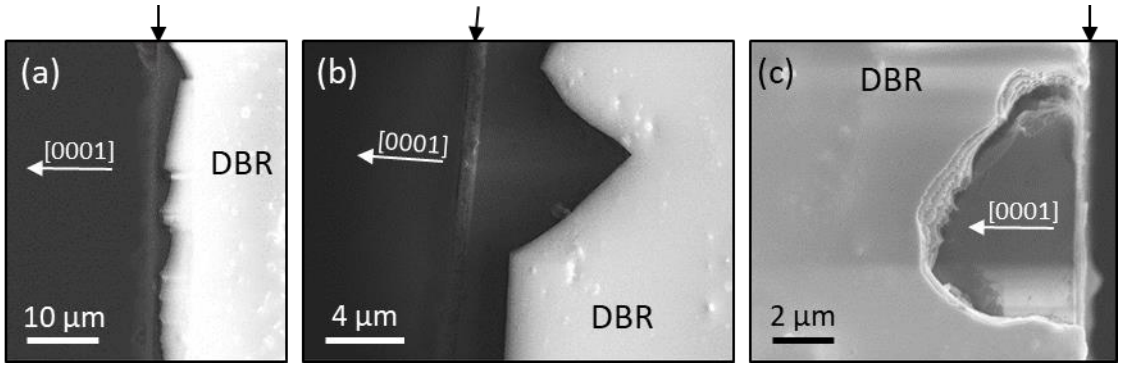

Figure 5.30. *SEM images of a cleaved laser bar (sample E4019) after deposition of the DBR. Images (a) and (b) show the topmost area of the laser bar, containing the MQW epitaxial layers. Image (c) shows the bottom part of the laser bar, corresponding to the substrate. Black arrows on top of the images mark the location of the surface. White arrows indicate the growth direction.*

5.6 Conclusions

In this chapter, I have presented the demonstration of stimulated emission in mechanically cleaved laser bars, under optical pumping. The lasing threshold was lower in samples with graded layers compared to the SCH with abrupt interfaces, due to the enhanced carrier collection. The lasing threshold was 210 kW/cm^2 for the SCH E3997 and 180 kW/cm^2 for the GRINSCH E4025 and the a-GRINSCH E4044. We estimate the lasing threshold under electron beam pumping to be ≈ 2.4 times larger than the optical threshold, although this value could be overestimated since optical pumping does not show all the potential of electron beam pumped lasers. Unfortunately, the first tests under electron beam pumping in the CL set-up demonstrated that the current conditions of the measurement system are still far from the estimated lasing threshold range. However, the presence of amplified spontaneous emission even for low pumping powers is promising towards the achievement of lasing with this technology.

An interesting feature revealed during the stimulated emission measurements is the decorrelation between the IQE and the lasing threshold. At room temperature, carrier localization in the quantum wells leads to an enhancement of the radiative efficiency. However, our results show that the lasing threshold is more sensitive to the injection efficiency than to the radiative efficiency. Therefore, designs including graded alloys result in a reduction of the lasing threshold, in spite of their lower internal quantum efficiency.

Mechanically cleaved cavities present a $1/L$ dependence of the lasing threshold with the cavity length, pointing to a dominance of optical losses related to the mirror quality. In fact, mechanically cleaved facets present high surface roughness due to the stress relaxation in strained heterostructures. In order to obtain smooth and vertical facets, we have developed a two-step

process combining ICP-RIE and KOH-based crystallographic-selective wet etching. Optical measurements confirm that the optical losses derived from the mirror quality are significantly reduced by using the two-step etching process, leading to a reduction of the lasing threshold by almost half in comparison with structures with cleaved facets. We have demonstrated mesa cavities with an optical threshold of 100 kW/cm^2, thus we estimate an electron beam threshold in the order of 240 kW/cm^2 at room temperature. As a reference, this is the value of lasing threshold reported by Meijo University during the first demonstration of lasing under electron beam pumping with an In-free AlGaN heterostructure at 107 K [51]. Here, we are estimating the threshold at room temperature.

Finally, the possibility to deposit a DBR mirror in the rear facet of the cavities has been explored. The reflectivity achievable by the DBR mirror can exceed the 95% at λ = 355 nm. However, in spite of our promising preliminary results testing the mirror on a reference sample, the deposition process gave rise to experimental difficulties that prevented us from properly implementing the DBR in the laser samples.

Chapter 6
Towards e-beam pumped UV-C lasers

This chapter is a starting point towards the achievement of electron beam pumped UV-C lasers based on AlGaN nanostructures, to serve as a base for future progress in this field. Here, I introduce a design targeting emission at 280 nm, and some preliminary results of all-AlGaN separate confinement heterostructures grown on AlN-on-sapphire templates and free-standing AlN substrates.

6.1 Targeting emission at 280 nm

The previous chapters were focused on electron beam pumped AlGaN/GaN lasers emitting in the UV-A range, with important applications in UV curing, UV lithography, and UV sensing [261]. For achieving emission wavelengths of around 360 nm, the laser structure can be grown on bulk GaN, and have an active region consisting of GaN QWs. Moving towards the UV-C range unlocks a whole set of interesting applications in the domain of sterilization/disinfection [262,263] and medical treatments [261]. In order to achieve emission at shorter wavelengths, we must rely on $Al_xGa_{1-x}N/Al_yGa_{1-y}N$ heterostructures with a high Al content for both the QWs and barriers. However, growing ternary AlGaN with a high Al concentration is more challenging than growing binary compounds such as GaN and AlN, or low Al content AlGaN [264]. Also, to prevent severe cracking, the structures must be grown on bulk AlN substrates. In this section, I present some preliminary results on the growth of AlGaN-based laser active regions designed to work under electron beam pumping at 280 nm. This study includes the design and modeling, and first experimental results.

Figure 6.1 presents the heterostructure design targeting emission at 280 nm. A graded BOC acts as buffer layer between the AlN substrate and the active region. This graded layer should help to accommodate the lattice mismatch between layers with different Al content, to reduce the density of misfit defects and prevent surface roughening during the growth. A BIC layer of $Al_{0.7}Ga_{0.3}N$ precedes the MQW composed by ten repetitions of $Al_{0.4}Ga_{0.6}N/Al_{0.7}Ga_{0.3}N$. On top, a TIC graded layer softens the transition between the last barrier and the TOC layer of $Al_{0.8}Ga_{0.2}N$.

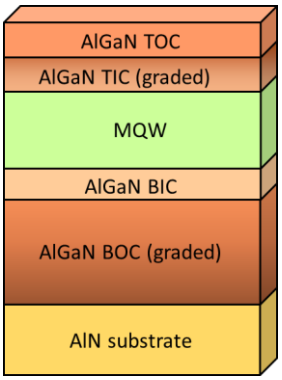

Figure 6.1. *Schematic view of the design.*

Table 6.1. *Description of the designs in terms of thickness and Al content on the layers, following the general design in Figure 6.1.*

	v5
TOC	39 nm $Al_{0.8}Ga_{0.2}N$
TIC	30 nm gradient $Al_{0.7}Ga_{0.3}N \rightarrow Al_{0.8}Ga_{0.2}N$
MQW	10×(1.5 nm $Al_{0.4}Ga_{0.6}N$/ 11 nm $Al_{0.7}Ga_{0.3}N$)
BIC	31 nm $Al_{0.7}Ga_{0.3}N$
BOC	110 nm gradient $AlN \rightarrow Al_{0.7}Ga_{0.3}N$

The design takes into account the considerations discussed in section 4.1. Thus, we tried to avoid potential barriers due to the polarization difference between the various layers, as illustrated in Figure 6.2, which compares a design with constant concentration in all layers, and the final design including graded layers. The strong difference in polarization between the AlN substrate and the $Al_{0.7}Ga_{0.3}N$ BIC layer generates a huge potential barrier that can block the carriers when diffusing to the QWs. The graded BOC solves this issue while providing a buffer layer to the heterostructure to accommodate the lattice mismatch. Furthermore, since AlN has larger absorption bandgap than the QW emission wavelength, the optical mode should not be absorbed by the substrate, thus the BOC can be thinner than in the samples designed for UV-A emission. Finally, a smaller barrier appears at the MQW/TIC interface, which can also be smoothed out using a graded layer.

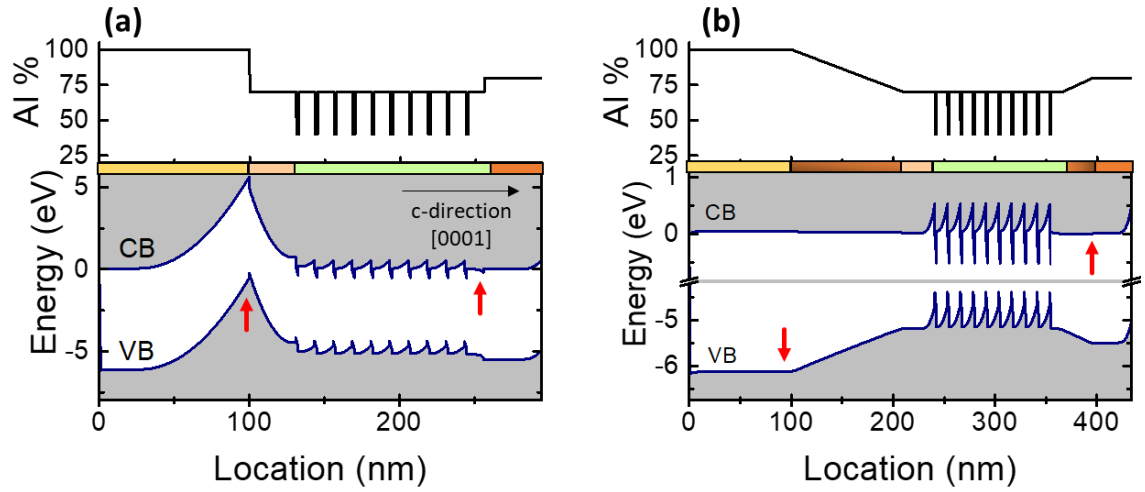

Figure 6.2. *Aluminium concentration along the growth direction and simulated conduction and valence band profile (CB and VB, respectively) for a design targeting emission at 280 nm (a) without and (b) with graded layers. Red marks aid to identify the main differences in the band profiles.*

COMSOL modelling was used to optimize the location of the QWs to maximize the optical confinement, as presented in Figure 6.3(a), attaining an OCF of 6.4% in the QWs (69.8% if the barriers are included in the calculation). Finally, Figure 6.3(b) shows the distribution of electrons

injected into the heterostructure at 8 kV. The thicknesses of the layers were chosen so that the maximum energy loss of the beam overlaps with the location of the active region, while preserving the optical confinement properties of the waveguide. Electron penetration depth is larger in AlN than in GaN, thus, the top cladding layers were thinner than those in previous designs.

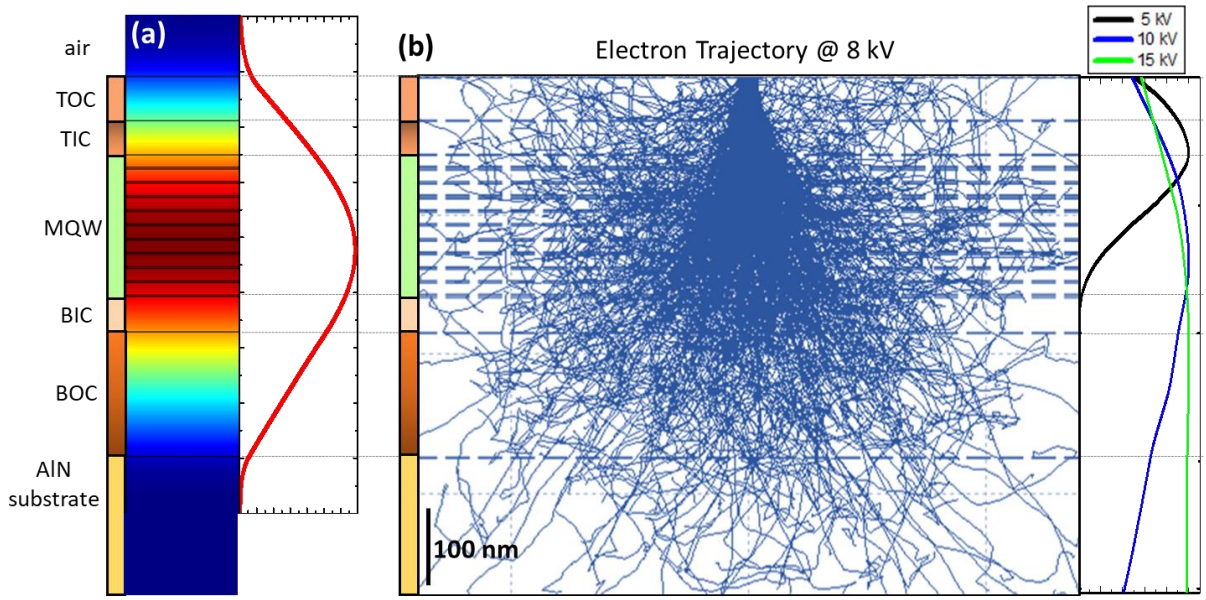

Figure 6.3. *(a) Simulation of the first optical mode distribution and (b) simulation of the electron beam penetration for the design targeting 280 nm.*

6.2 Preliminary results: growth on single crystal AlN

The above-mentioned design was synthesized by MBE on two different substrates, both cut in rectangular pieces of ≈ 1 cm × 1.5 cm. Sample E4208 was grown on an AlN-on-sapphire template and sample E4211 was grown on an AlN(0001) bulk substrate. Before introducing the substrate in the MBE chamber, the surface was degreased with organic solvents, as described in section 4.2.1. The growth conditions were the same for both epitaxial structures. The substrate temperature was T_S = 700 °C, and the growth rate was 0.63 ML/s. As explained in section 3.1.5, the Al/N flux ratio is fixed to the targeted Al mole fraction, while the Ga flux is used in excess to obtain a self-surfactant effect. In order to remain in the group-III-rich regime but preventing Ga droplet accumulation, the Al and Ga fluxes were calibrated individually beforehand, and the evolution on the III/N ratio was monitored in real time by RHEED during the growth.

The study of the UV-A samples (check section 5.3) revealed that in-plane carrier localization in the QWs is favorable for high radiative efficiency. A slightly rough well can promote carrier localization. Therefore, we slightly reduced the III/N ratio in the QWs to favor roughening. The possibility of synthesizing quantum dots (QDs) instead of QWs was also considered. However, for

lasing we aim to accumulate the maximum gain in a narrow spectral range. Incorporating QDs would spread the emission wavelength range due to the fluctuations in QDs size, thus increasing the lasing threshold.

Figure 6.4 presents the XRD θ-2θ scan around the (0002) reflection of AlN for samples E4208 and E4211, together with a theoretical calculation for the design in Table 6.1. From the comparison, we confirm that the experimental Al contents show a good agreement with the nominal values. The $Al_{0.7}Ga_{0.3}N$ reflection from the cladding layers is clearly visible, and overlaps with a broad peak that expands towards the reflection from bulk AlN. This broad reflection is attributed to the graded layers and the $Al_{0.8}Ga_{0.2}N$ TOC. From the analysis of the satellite peak, we extract a period of 12.2 nm for E4208 and 11.6 nm for E4211 (note that the nominal period was 12.5 nm). In general, the peaks from E4211 appear narrower than E4208, which could be associated to a better crystal quality thanks to the bulk AlN substrate.

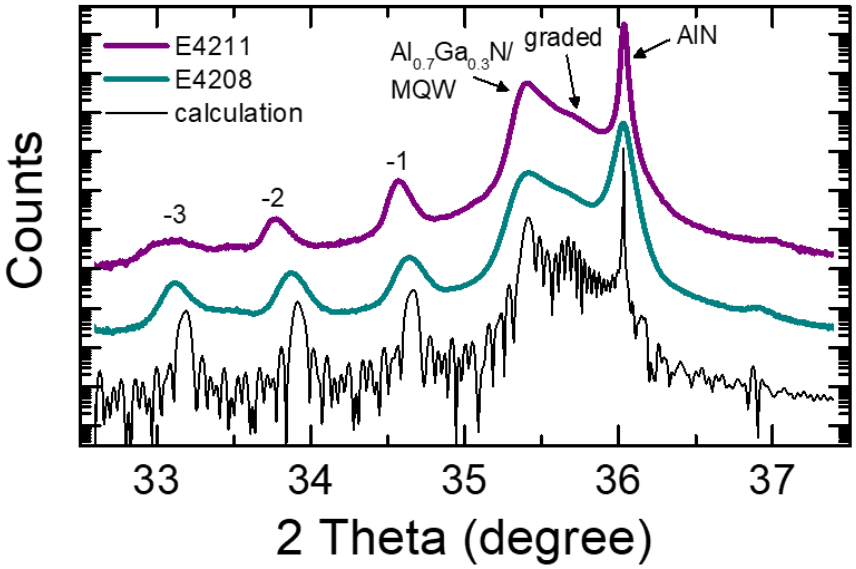

Figure 6.4. *XRD θ-2θ scan around the (0002) reflection of AlN for samples E4208 (AlN-on-sapphire template) and E4211 (bulk AlN substrate). Labels identify the reflections originating from the AlN substrate, $Al_{0.7}Ga_{0.3}N$, graded layers, and MQW, with several satellites. Experimental results are compared with a theoretical calculation of the diffractogram for the design in Table 6.1.*

The photoluminescence of the as-grown samples was characterized at room temperature using a continuous-wave frequency-doubled solid-state laser (λ = 244 nm) with a pumping power of ≈ 500 μW. A spectrally sharp long-pass filter at 248 nm was used to prevent the laser from damaging the CCD camera. The results are presented in Figure 6.5. The main peaks are attributed to the emission from the MQW, located at 292 nm for E4208, and 286 nm for E4211. The spectral shift between both samples is due to the thinner MQW in E4211 compared to E4208. There is no significant variation in the FWHM. A small emission bump was observed at 260-270 nm, and it is attributed to recombination in the $Al_{0.7}Ga_{0.3}N$ layers. Indeed, the location of the bump is the same as the peak emission from a 500-nm-thick $Al_{0.7}Ga_{0.3}N$ layer (dashed line in the figure).

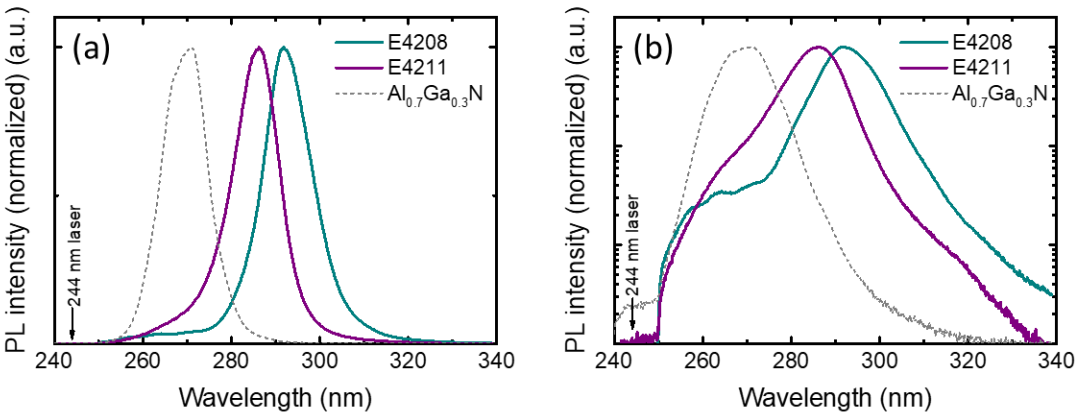

Figure 6.5. *Normalized PL spectra for E4208 and E4211 under continuous wave excitation at λ = 244 nm in (a) linear and (b) semilogarithmic scale. The black arrow indicates the wavelength of the excitation laser. The dashed line corresponds to the PL spectra of a 500-nm-thick $Al_{0.7}Ga_{0.3}N$ layer.*

The CL emission under different acceleration voltages was studied at room temperature. Figure 6.6 shows the CL normalized by the acceleration voltage and injection current for sample E4208 and E4211. The main peak in the range between 5-20 kV corresponds to the emission from the MQW (at 292 nm for E4208, and 286 nm for E4211), which demonstrates that there is a good collection towards the active region thanks to the graded layers. In sample E4208, for acceleration voltages between 8-14 kV, we observe the peak from the $Al_{0.7}Ga_{0.3}N$ layers at 260 nm. However, its intensity is several times smaller than the emission from the MQW. This peak is not resolved in sample E4211.

Figure 6.6(c) shows the maximum CL intensity of the MQW peak as a function of the acceleration voltage. Sample E4211 has an optimal operation voltage between 5-10 kV, while E4208 optimal conditions shift to voltages between 8-13 kV. In addition, at 5 kV the amount of carriers reaching the MQW in sample E4208 is almost zero, while for sample E4211 we collect MQW emission under the same conditions. Since both samples have identical top cladding layer compositions, and the location in depth of the MQW is the same, the discrepancy seems associated to surface recombination or, more probable, charging effects. Due to the insulating nature of the sample, the surface gets negatively charged, which acts as a repulsive potential for the incoming electrons. Thus, higher acceleration voltages are required to overcome this additional potential, which results in the shift observed in the figure.

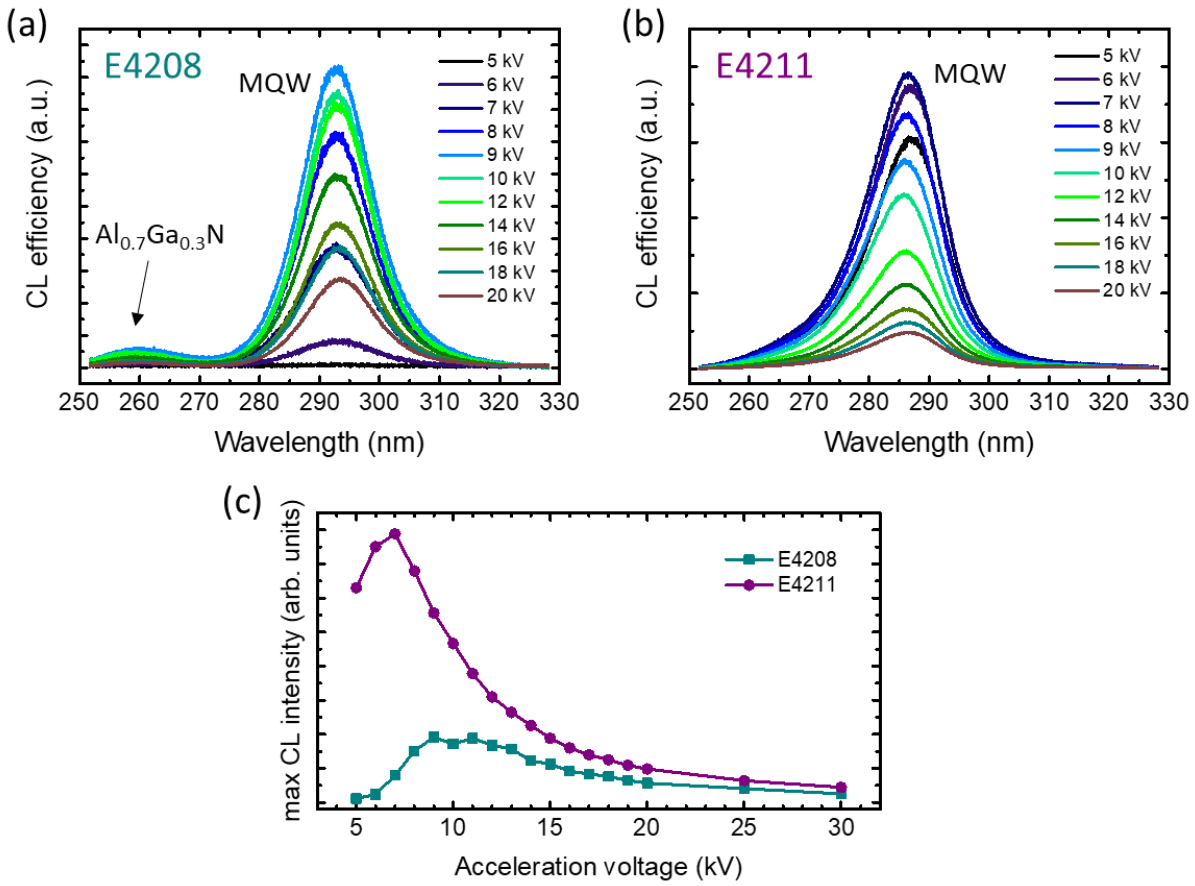

Figure 6.6. *CL spectra recorded at different acceleration voltages for (a) E4208, (b) E4211. The CL spectra are normalized by dividing by the acceleration voltage and injection current. (c) Maximum CL efficiency of the MQW peak as a function of the acceleration voltage.*

In view of the good carrier collection of the design, we fabricate a 1-mm-long laser bar with sample E4211 and we perform PL measurements exciting the cavity with a Nd:YAG (λ = 266 nm) laser stripe, as described in the set-up B from section 3.2.5. The edge PL emission as a function of the temperature is presented in Figure 6.7. For this measurement, we used the maximum pumping power achievable in our setup with the Nd:YAG laser (≈ 250 kW/cm² at 266 nm). Despite that, the sample did not display lasing emission even at low temperature (6 K). Instead, a second peak was observed at longer wavelength (≈ 320 nm). This peak was completely unexpected, since none of the epitaxial layers should emit at such low energy. This peak has already been reported before in literature as an emission involving point defects from the AlN substrate [265]. This was confirmed by performing PL measurements on a piece of the bulk AlN wafer, which displayed emission in the same wavelength range (see dashed line in figure).

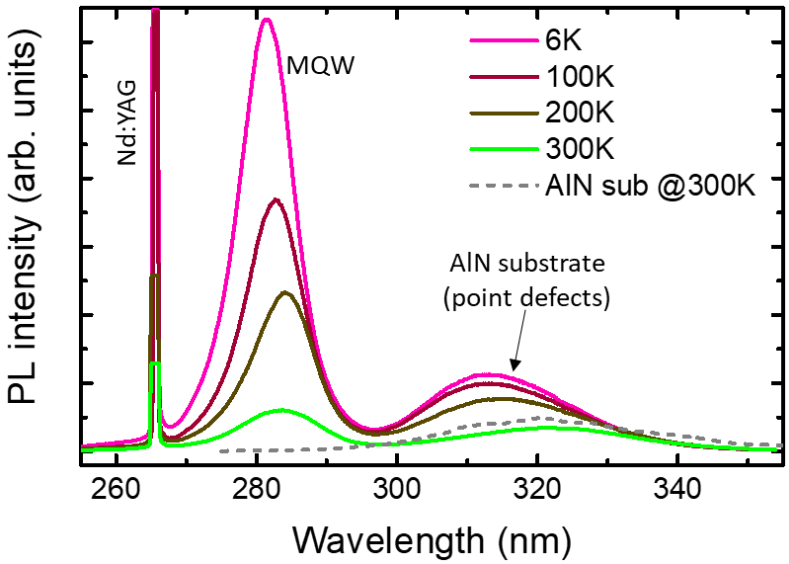

Figure 6.7. *PL spectra for sample E4211 as a function of temperature at a pumping power of ≈ 250 kW/cm² (cavity length = 1mm). Dashed line is the surface PL emission of a bulk AlN substrate at room temperature.*

From these results, we extract some relevant information. The fabrication of high-quality AlN substrates is still under development, thus, the bulk AlN wafers that we can find in the market nowadays can present point defects absorbing in the UV-C, mostly due to C pollution [266]. This is critical for the performance of our AlGaN-based lasers. Our assumption that the AlN substrate is transparent to the light emitted by the QWs is no longer valid; therefore, the design of the optical waveguide must ensure that the optical mode does not leak into the AlN substrate, to prevent a negative impact on the lasing threshold. New AlN substrates with relatively low absorption coefficients have been demonstrated by compensating the C point defects with Si [267], although their prices are several times higher than the wafer used in this work.

Another point to take into account is that the absorption of the $Al_{0.7}Ga_{0.3}N$ barriers at 266 nm is relatively low. Therefore, the amount of carriers injected into the QWs by diffusion is drastically reduced. For this reason, investigations on optically pumped lasing should be performed using, for instance, a 193 nm ArF or 248 nm KrF excimer laser. This problem could also be circumvented under electron beam pumping.

Finally, when working with AlGaN layers on AlN substrates, the strain in the sample becomes compressive, in contrast with the tensile strain when working with GaN substrates. Under compressive strain, the generation of the cracks is prevented (see section 4.2.2). However, let us remind here that these cracks did not result in any important degradation of the laser structure.

6.3 Conclusions

This chapter is a starting point towards the development of AlGaN-based deep-UV lasers pumped by an electron beam. Here, we have applied the experience accumulated from previous experiments at 350-365 nm to perform our first steps towards devices with shorter emission wavelength. To do that, we need all-AlGaN separate confinement heterostructures with high Al content, grown on bulk AlN substrates. We propose a design targeting emission at λ = 280 nm, and incorporating graded layers for enhanced carrier collection. To enhance carrier localization in the QWs, we slightly reduced the III/N ratio during the growth. The change from tensile to compressive strain when changing from GaN to AlN substrate, resulted in the absence of cracks on the sample surface.

The design shows indications of a good carrier collection towards the QWs, as it displays a single emission peak at 286 nm. However, we did not find any evidence of lasing in a 1-mm-long cleaved cavity. This is explained by the fact that the AlN substrate, which was assumed to be transparent in the MQW emission range, was in fact is absorbing due to point defects. Therefore, the optical waveguide must be redesigned to prevent the optical mode to reach the AlN substrate. Testing the lasing capabilities under a higher energy laser or electron beam pumped could lead to better results, since the laser used in our experiment was not fully absorbed by the barriers, thus, generating less carriers that could diffuse towards the wells.

The work presented in this chapter intended to identify the most critical parameters to take into account in order to achieve electron-beam pumped deep-UV AlGaN lasers. New designs, following the advices extracted from our conclusions should lead to heterostructures with improved lasing threshold.

Chapter 7
Conclusion and perspectives

7.1 Conclusions

This work is a contribution to the development of an AlGaN-based electron beam pumped UV laser technology. For the fabrication of efficient devices, it is crucial to understand the mechanisms and parameters that govern their performance. With that purpose, we developed a series of AlGaN/GaN heterostructures with a MQW active area emitting at 365-350 nm and designed to operate at low acceleration voltages (≤ 10 kV). The research aimed to optimize the structures in terms of efficiency and lasing threshold. From these samples, we extracted the following conclusions.

The **design of electron beam pumped lasers** requires taking into account optical and electrical considerations. The emission wavelength is controlled by tuning the GaN QWs thickness, and the optical confinement is fulfilled with a proper selection of thickness and Al composition in the cladding layers. The penetration depth of the electron beam into the structure must be considered to define the location of the active area. In our designs, the thickness of the top cladding layers was adjusted to operate with an acceleration voltage in the range of 7-10 kV.

The **implementation of a GRINSCH** improved the collection of carriers towards the MQW when compared to a standard SCH. Further improvement was obtained with an asymmetric GRINSCH design. An added value for the GRINSCH was the smooth transition between ternary alloys in the compositionally graded layers, which favors the accommodation of misfit stress.

Optical gain measurements under optical pumping were performed using the VSL method. The characterization was complex, since the optical excitation is restricted to the proximity of the surface, which means that only the topmost QWs could attain population inversion. In spite of these limitations, we found values of net gain comparable with the state of the art. We observed anomalous amplification in some areas of the sample due to optical feedback provided by reflections at cracks. These cracks appear due to plastic relaxation under tensile strain in AlGaN structures grown on GaN substrates. The cracks are not catastrophic for the laser performance, but they introduce an overestimation in gain measurements.

Stimulated emission was demonstrated at room temperature under optical pumping in mechanically cleaved laser bars, with lasing thresholds in the range of 180-210 kW/cm^2. We estimate the lasing threshold under electron beam pumping to be ≈ 2.4 times higher than the optical threshold, i.e. around 480 kW/cm^2. Unfortunately, we did not attain lasing in our first tests under electron beam pumping, since the pumping system was still not able to deliver enough current to reach the estimated lasing threshold. Amplified stimulation emission was reported at low pumping powers, which encourages the possibility of lasing at higher powers.

Despite the improved injection properties and crystal quality of the GRINSCH, the SCH sample displayed superior IQE values for spontaneous emission. This was attributed to alloy inhomogeneities and QW thickness fluctuations in the SCH, which favor in-plane carrier localization and reduce the non-radiative recombination probability. However, we observed that the lasing threshold in the graded designs was lower than the lasing threshold in the SCH, thanks to the improved carrier transport along the growth axis. This result reveals a **decorrelation between the lasing threshold and the IQE**.

The lasing threshold in mechanically cleaved cavities presented a $1/L$ dependence with the cavity length, pointing to a huge influence of the mirror losses in our samples. Cleaved facets present high surface roughness due to the stress relaxation in these highly strained heterostructures. In order to **reduce the mirror losses**, we developed a two-step process combining ICP-RIE and KOH-based crystallographic-selective wet etching. The obtained smooth and vertical facets lowered the optical losses at the mirrors, reducing the threshold by half. We demonstrated an optical threshold of 100 kW/cm^2 at room temperature in 0.3 mm long cavities. From this value, we estimate that our lasing threshold under electron beam pumping at room temperature should be in the same range than the electron beam pumping threshold reported at 107 K during the first lasing demonstration of AlGaN heterostructures with this technology.

Finally, the previous results were applied in the **first attempt to develop an AlGaN heterostructure** emitting at 280 nm designed to operate under electron beam pumping. The design took into account the asymmetric GRINSCH concept to improve the carrier collection. The heterostructure was grown by MBE on an AlN bulk substrate. The III/N ratio was slightly reduced in the MQW to promote a soft roughness that favors carrier localization and, consequently, improves the radiative efficiency. The sample displayed good carrier collection, with a dominant emission peak at 286 nm. However, no stimulated emission was detected due to optical absorption of the AlN substrate and reduced pumping efficiency due to the relatively low absorption in the barriers when pumping with a Nd-YAG laser.

7.2 Perspectives

Electron beam pumped lasers are an interesting substitute for laser diodes in certain spectral windows, particularly in the UV range, with the capacity to deliver high power (up to ≈ 100 W). The results of this work contain promising elements for the development of an AlGaN-based electron beam pumped lasing technologies. The 0.3-mm-long GRINSCH sample with etched facets achieved an optical lasing threshold of 100 kW/cm^2, which should lead to lasing under electron beam pumping with a threshold around 240 kW/cm^2 at room temperature. As a reference to compare, the last reported threshold for electron beam pumped AlGaN/GaN heterostructure was 230 kW/cm^2 at 107 K [51]. In both cases, the facets were uncoated, which means that there is still room to improve those values by depositing for instance a DBR mirror in one of the facets, which would lower the optical mirror losses. Understanding the mechanisms behind an efficient carrier collection and recombination is crucial to optimize designs for low threshold devices.

Deep-UV is the spectral range where electron beam pumped AlGaN lasers have more opportunities to shine and compete with conventional laser diodes and where most research efforts should be focused on. The challenges of growing high Al content AlGaN and the quality of the AlN substrates can be a limitation for fabrication high-quality heterostructures with low optical internal losses. However, the AlN wafers are continuously improving, so future structures can only become better. The recommendations that this work can propose for future studies, include:

- Waveguide design: in view of the absorbing AlN substrates, it is important to design an optical waveguide that prevents that the optical mode reaches the substrate, always keeping the MQW at the optimum depth determined by the electron beam penetration.
- GRINSCH implementation: graded layers towards the MQW have proven to be crucial to enhance the carrier collection and reduce the lasing threshold. In addition, the smooth chemical transition between layers can prevent defects derived from the lattice mismatch.
- Favor carrier localization: adding some roughness to the QWs is beneficial to prevent non-radiative recombination and improve the radiative efficiency. This roughness must be moderate, to prevent scattering on the light that would increase the optical internal losses.
- Mirror coating: a proper high-reflectivity mirror can be crucial to reduce the lasing threshold.

Challenges are not only related to the semiconductor active media, but also to the cathode specifications and design. Taking into account that the optimum acceleration voltage is around 8-10 kV, a lasing threshold of 240 kW/cm^2 would require a pumping current of 25-30 A/cm^2. If we consider a cavity length of 0.3 mm, a round electron beam would require injection of around 20 mA. One possibility is to work with smaller cavities (≈ 0.1 mm, which is realistic from the point of view of lithography) or focus the electron beam into a narrow line aligned with the resonator, which would reduce the required current to the range of 2-5 mA. This range of currents can be obtained with commercial pulsed thermionic cathodes.

The final implementation of an actual laser device using our heterostructures as active region requires an additional set of considerations. Regarding thermal management, an analysis of the heat flow in the structure (including the laser, the sample holder and heatsink) was performed by Dr. Gilles Nogues using the COMSOL software, as illustrated in Figure 7.1. In summary, operation at an average power of 5 W can lead to a chip temperature of ≈ 120°C. The glue that links the chip and the Cu holder is the critical element. Therefore, the choice of glue is relevant, and a cooling system must be implemented in the sample holder. However, thermal issues should not impose a critical limitation to the device. The use of a Peltier or a ventilated sink can reduce the chip temperature significantly.

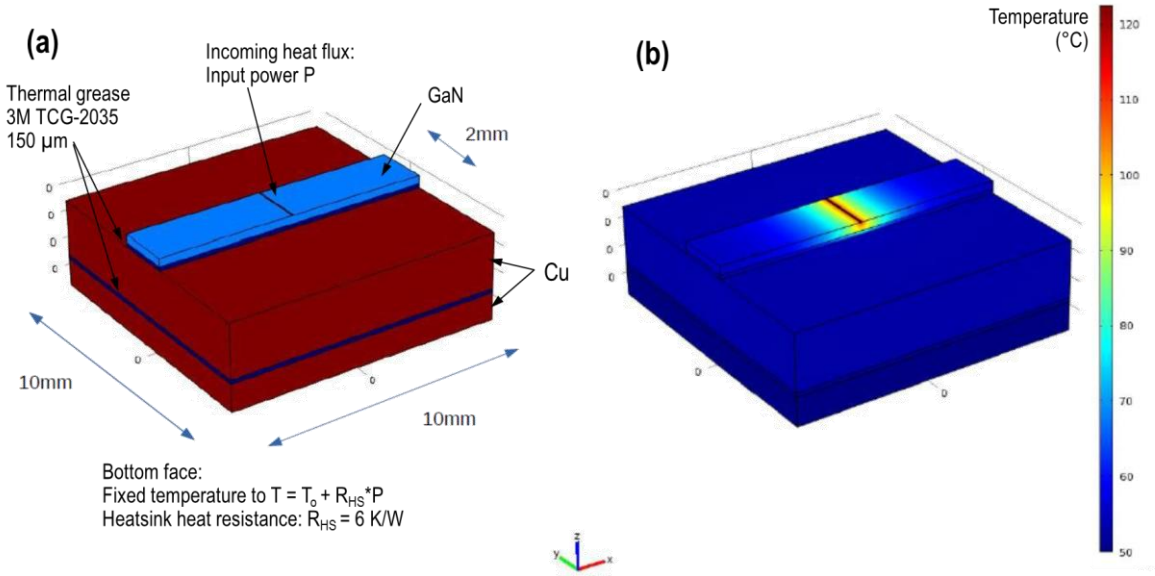

Figure 7.1 *(a) Schematic description of the modelled structure with the main parameters used as input. (b) Results of the simulation showing the temperature distribution in the structure.*

With this information, processed by Prof. Le Si Dang, the design service of Institut Néel has proposed a prototype whose drawings are presented in the Appendix. The laser prototype presents three input ports (for sample, cathode and pumping), a port for the laser output and a visualization port, perpendicular to the laser/pump axis. The sample holder can move in X + Y +

rotation. It can eventually incorporate a liquid cooling circuit. The design allow rapid exchange of samples. The cathode holder can move axially. The construction of such prototype is now under consideration.

In a larger perspective, electron-beam pumping of AlGaN lasers can be considered as a promising alternative, particularly in the deep UV range, where AlGaN laser diodes still present carrier injection problems. The possibility to inject carriers directly into the active media, obviating the need of implementing contacts or inserting doped layers, is an interesting advantage that can simplify the hardest challenges in this field. The adjustment of the penetration depth through the acceleration voltage grants an additional degree of freedom for the design of the optical cavity. By improving the optical cavity, electron beam focusing and further miniaturization of the device components, electron beam pumped AlGaN lasers can lead to compact and efficient systems to overcome current limitations of laser diodes.

References

[1] Ambacher O 1998 Growth and applications of Group III-nitrides *Journal of Physics D: Applied Physics* **31** 2653–710

[2] Kneissl M and Rass J 2016 *III-Nitride Ultraviolet Emitters: Technology and Applications* vol 227 (Cham: Springer International Publishing)

[3] Amano H, Collazo R, Santi C D, Einfeldt S, Funato M, Glaab J, Hagedorn S, Hirano A, Hirayama H, Ishii R, Kashima Y, Kawakami Y, Kirste R, Kneissl M, Martin R, Mehnke F, Meneghini M, Ougazzaden A, Parbrook P J, Rajan S, Reddy P, Römer F, Ruschel J, Sarkar B, Scholz F, Schowalter L J, Shields P, Sitar Z, Sulmoni L, Wang T, Wernicke T, Weyers M, Witzigmann B, Wu Y-R, Wunderer T and Zhang Y 2020 The 2020 UV emitter roadmap *J. Phys. D: Appl. Phys.* **53** 503001

[4] Razeghi M 2011 III-Nitride Optoelectronic Devices: From Ultraviolet Toward Terahertz *IEEE Photonics Journal* **3** 263–7

[5] Cuesta S, Spies M, Boureau V, Donatini F, Hocevar M, den Hertog M I and Monroy E 2019 Effect of Bias on the Response of GaN Axial p–n Junction Single-Nanowire Photodetectors *Nano Lett.* **19** 5506–14

[6] Mishra U K, Parikh P, and Yi-Feng Wu 2002 AlGaN/GaN HEMTs-an overview of device operation and applications *Proc. IEEE* **90** 1022–31

[7] Shen L, Heikman S, Moran B, Coffie R, Zhang N-Q, Buttari D, Smorchkova I P, Keller S, DenBaars S P and Mishra U K 2001 AlGaN/AlN/GaN high-power microwave HEMT *IEEE Electron Device Lett.* **22** 457–9

[8] Yi-Feng Wu, Kapolnek D, Ibbetson J P, Parikh P, Keller B P and Mishra U K 2001 Very-high power density AlGaN/GaN HEMTs *IEEE Trans. Electron Devices* **48** 586–90

[9] Jones E A, Wang F F and Costinett D 2016 Review of Commercial GaN Power Devices and GaN-Based Converter Design Challenges *IEEE J. Emerg. Sel. Topics Power Electron.* **4** 707–19

[10] Fichter Fr 1907 Über Aluminiumnitrid *Z. Anorg. Chem.* **54** 322–7

[11] Johnson W C, Parson J B and Crew M C 1931 Nitrogen Compounds of Gallium. III *J. Phys. Chem.* **36** 2651–4

[12] Manasevit H M, Erdmann F M and Simpson W I 1971 The Use of Metalorganics in the Preparation of Semiconductor Materials *J. Electrochem. Soc.* **118** 1864

[13] Yoshida S, Misawa S and Itoh A 1975 Epitaxial growth of aluminum nitride films on sapphire by reactive evaporation *Applied Physics Letters* **26** 461–2

[14] Amano H, Sawaki N, Akasaki I and Toyoda Y 1986 Metalorganic vapor phase epitaxial growth of a high quality GaN film using an AlN buffer layer *Applied Physics Letters* **48** 353–5

[15] Amano H, Kito M, Hiramatsu K and Akasaki I 1989 P-Type Conduction in Mg-Doped GaN Treated with Low-Energy Electron Beam Irradiation (LEEBI) *Jpn. J. Appl. Phys.* **28** L2112

[16] Nakamura S, Mukai T and Senoh M 1994 Candela-class high-brightness InGaN/AlGaN double-heterostructure blue-light-emitting diodes *Appl. Phys. Lett.* **64** 1687–9

[17] Nakamura S, Senoh M, Nagahama S, Iwasa N, Yamada T, Matsushita T, Kiyoku H and Sugimoto Y 1996 InGaN Multi-Quantum-Well-Structure Laser Diodes with Cleaved Mirror Cavity Facets *Jpn. J. Appl. Phys.* **35** L217–20

[18] Anon Press release of The Royal Swedish Academy of Sciences. (2014) <https://www.nobelprize.org/prizes/physics/2014/advanced-information/>

[19] Barth J 1987 Johann Wilhelm Ritter (1776-1810) and the discovery of ultraviolet irradiation 185 years ago *Hautarzt* **38** 301–3

[20] Kneissl M, Seong T-Y, Han J and Amano H 2019 The emergence and prospects of deep-ultraviolet light-emitting diode technologies *Nature Photonics* **13** 233–44

[21] Anon ISO 21348:2007 Space environment (natural and artificial) — Process for determining solar irradiances

[22] Sun X, Cai W, Alkhazragi O, Ooi E-N, He H, Chaaban A, Shen C, Oubei H M, Khan M Z M, Ng T K, Alouini M-S and Ooi B S 2018 375-nm ultraviolet-laser based non-line-of-sight underwater optical communication *Opt. Express, OE* **26** 12870–7

[23] Totonchy M B and Chiu M W 2014 UV-based therapy *Dermatol Clin* **32** 399–413, ix–x

[24] Wang X, Jiang M, Zhou Z, Gou J and Hui D 2017 3D printing of polymer matrix composites: A review and prospective *Composites Part B: Engineering* **110** 442–58

[25] Einstein A 1917 Zur Quantentheorie der Strahlung *Physikalische Zeitschrift* **18** 121–8

[26] Taylor N 2000 *Laser: the inventor, the Nobel laureate, and the thirty-year patent war* (New York: Simon & Schuster)

[27] Anon Press release of The Royal Swedish Academy of Sciences. (1964) https://www.nobelprize.org/prizes/physics/1964/summary/

[28] Guenther B D and Steel D 2018 *Encyclopedia of modern optics*

[29] Sato K, Yasue S, Yamada K, Tanaka S, Omori T, Ishizuka S, Teramura S, Ogino Y, Iwayama S, Miyake H, Iwaya M, Takeuchi T, Kamiyama S and Akasaki I 2020 Room-temperature operation of AlGaN ultraviolet-B laser diode at 298 nm on lattice-relaxed Al0.6Ga0.4N/AlN/sapphire *Appl. Phys. Express* **13** 031004

[30] Zhang Z, Kushimoto M, Sakai T, Sugiyama N, Schowalter L J, Sasaoka C and Amano H 2019 A 271.8 nm deep-ultraviolet laser diode for room temperature operation *Appl. Phys. Express* **12** 124003

[31] Kneissl M, Kolbe T, Schlegel J, Stellmach J, Chua C, Yang Z, Knauer A, Küller V, Weyers M and Johnson N M 2011 AlGaN-based Ultraviolet Lasers - Applications and Materials Challenges *CLEO:2011 - Laser Applications to Photonic Applications (2011), paper JTuB1* CLEO: Applications and Technology (Optical Society of America) p JTuB1

[32] Epelbaum B M, Bickermann M and Winnacker A 2003 Seeded PVT Growth of Aluminum Nitride on Silicon Carbide *MSF* **433–436** 983–6

[33] Schlesser R and Sitar Z 2002 Growth of bulk AlN crystals by vaporization of aluminum in a nitrogen atmosphere *Journal of Crystal Growth* **234** 349–53

[34] Shi Y, Xie Z Y, Liu L H, Liu B, Edgar J H and Kuball M 2001 Influence of buffer layer and 6H-SiC substrate polarity on the nucleation of AlN grown by the sublimation sandwich technique *Journal of Crystal Growth* **233** 177–86

[35] Balakrishnan K, Iwaya M, Kamiyama S, Amano H, Akasaki I, Takagi T and Noro T 2004 Study on the Seeded Growth of AlN Bulk Crystals by Sublimation *Jpn. J. Appl. Phys.* **43** 7448–53

[36] Kuhn C, Simoneit T, Martens M, Markurt T, Enslin J, Mehnke F, Bellmann K, Schulz T, Albrecht M, Wernicke T and Kneissl M 2018 MOVPE Growth of Smooth and Homogeneous $Al_{0.8}Ga_{0.2}N$:Si Superlattices as UVC Laser Cladding Layers *Phys. Status Solidi A* **215** 1800005

[37] Zhang Z, Kushimoto M, Yoshikawa A, Aoto K, Schowalter L J, Sasaoka C and Amano H 2022 Continuous-wave lasing of AlGaN-based ultraviolet laser diode at 274.8 nm by current injection *Appl. Phys. Express* **15** 041007

[38] Simon J, Protasenko V, Lian C, Xing H and Jena D 2010 Polarization-Induced Hole Doping in Wide-Band-Gap Uniaxial Semiconductor Heterostructures *Science* **327** 60–4

[39] Zhang Z, Kushimoto M, Horita M, Sugiyama N, Schowalter L J, Sasaoka C and Amano H 2020 Space charge profile study of AlGaN-based p-type distributed polarization doped claddings without impurity doping for UV-C laser diodes *Appl. Phys. Lett.* **117** 152104

[40] Zhang Z, Kushimoto M, Sakai T, Sugiyama N, Schowalter L J, Sasaoka C and Amano H 2020 Design and characterization of a low-optical-loss UV-C laser diode *Jpn. J. Appl. Phys.* **59** 094001

[41] Kirste R, Guo Q, Dycus J H, Franke A, Mita S, Sarkar B, Reddy P, LeBeau J M, Collazo R and Sitar Z 2018 6 kW/cm2 UVC laser threshold in optically pumped lasers achieved by controlling point defect formation *Appl. Phys. Express* **11** 082101

[42] Zhang Y, Allerman A A, Krishnamoorthy S, Akyol F, Moseley M W, Armstrong A M and Rajan S 2016 Enhanced light extraction in tunnel junction-enabled top emitting UV LEDs *Appl. Phys. Express* **9** 052102

[43] Martens M 2018 *Optical gain and modal loss in AlGaN based deep UV lasers* (Berlin: Technische Universität Berlin)

[44] Martens M, Kuhn C, Simoneit T, Hagedorn S, Knauer A, Wernicke T, Weyers M and Kneissl M 2017 The effects of magnesium doping on the modal loss in AlGaN-based deep UV lasers *Appl. Phys. Lett.* **110** 081103

[45] Hjort F, Enslin J, Cobet M, Bergmann M A, Gustavsson J, Kolbe T, Knauer A, Nippert F, Häusler I, Wagner M R, Wernicke T, Kneissl M and Haglund Å 2021 A 310 nm Optically Pumped AlGaN Vertical-Cavity Surface-Emitting Laser *ACS Photonics* **8** 135–41

[46] Kang J H, Wenzel H, Hoffmann V, Freier E, Sulmoni L, Unger R-S, Einfeldt S, Wernicke T and Kneissl M 2018 DFB Laser Diodes Based on GaN Using 10th Order Laterally Coupled Surface Gratings *IEEE Photon. Technol. Lett.* **30** 231–4

[47] Deng H, Weihs G, Snoke D, Bloch J and Yamamoto Y 2003 Polariton lasing vs. photon lasing in a semiconductor microcavity *Proc. Natl. Acad. Sci. U.S.A.* **100** 15318–23

[48] Imamog¯lu A, Ram R J, Pau S and Yamamoto Y 1996 Nonequilibrium condensates and lasers without inversion: Exciton-polariton lasers *Phys. Rev. A* **53** 4250–3

[49] Bhattacharya P, Frost T, Deshpande S, Baten M Z, Hazari A and Das A 2014 Room Temperature Electrically Injected Polariton Laser *Phys. Rev. Lett.* **112** 236802

[50] Christmann G, Butté R, Feltin E, Carlin J-F and Grandjean N 2008 Room temperature polariton lasing in a GaN/AlGaN multiple quantum well microcavity *Appl. Phys. Lett.* **93** 051102

[51] Hayashi T, Kawase Y, Nagata N, Senga T, Iwayama S, Iwaya M, Takeuchi T, Kamiyama S, Akasaki I and Matsumoto T 2017 Demonstration of electron beam laser excitation in the UV range using a GaN/AlGaN multiquantum well active layer *Sci Rep* **7** 2944

[52] Cuesta S, Harikumar A and Monroy E 2022 Electron beam pumped light emitting devices *J. Phys. D: Appl. Phys.* **55** 273003

[53] Nalwa H S 2000 *Handbook of nanostructured materials and nanotechnology* (San Diego: Academic Press)

[54] Wonglakhon T and Zahn D 2020 Interaction potentials for modelling GaN precipitation and solid state polymorphism *J. Phys.: Condens. Matter* **32** 205401

[55] Morkoç H, Strite S, Gao G B, Lin M E, Sverdlov B and Burns M 1994 Large-band-gap SiC, III-V nitride, and II-VI ZnSe-based semiconductor device technologies *Journal of Applied Physics* **76** 1363–98

[56] Vurgaftman I and Meyer J R 2003 Band parameters for nitrogen-containing semiconductors *Journal of Applied Physics* **94** 3675–96

[57] Ambacher O, Smart J, Shealy J R, Weimann N G, Chu K, Murphy M, Schaff W J, Eastman L F, Dimitrov R, Wittmer L, Stutzmann M, Rieger W and Hilsenbeck J 1999 Two-dimensional electron gases induced by spontaneous and piezoelectric polarization charges in N- and Ga-face AlGaN/GaN heterostructures *Journal of Applied Physics* **85** 3222–33

[58] Sun C J, Kung P, Saxler A, Ohsato H, Bigan E, Razeghi M and Gaskill D K 1994 Thermal stability of GaN thin films grown on (0001) Al_2O_3, (01$\bar{1}$2) Al_2O_3 and (0001) $_{Si}$ 6H-SiC substrates *Journal of Applied Physics* **76** 236–41

[59] Mastro M A, Kryliouk O M, Anderson T J, Davydov A and Shapiro A 2005 Influence of polarity on GaN thermal stability *Journal of Crystal Growth* **274** 38–46

[60] Sun Q, Cho Y S, Lee I-H, Han J, Kong B H and Cho H K 2008 Nitrogen-polar GaN growth evolution on c-plane sapphire *Appl. Phys. Lett.* **93** 131912

[61] Kim K, Lambrecht W R L and Segall B 1996 Elastic constants and related properties of tetrahedrally bonded BN, AlN, GaN, and InN *Phys. Rev. B* **53** 16310–26

[62] Wright A F 1997 Elastic properties of zinc-blende and wurtzite AlN, GaN, and InN *Journal of Applied Physics* **82** 2833–9

[63] Takagi Y, Ahart M, Azuhata T, Sota T, Suzuki K and Nakamura S 1996 Brillouin scattering study in the GaN epitaxial layer *Physica B: Condensed Matter* **219–220** 547–9

[64] Polian A, Grimsditch M and Grzegory I 1996 Elastic constants of gallium nitride *Journal of Applied Physics* **79** 3343–4

[65] McNeil L E, Grimsditch M and French R H 1993 Vibrational Spectroscopy of Aluminum Nitride *J American Ceramic Society* **76** 1132–6

[66] Deger C, Born E, Angerer H, Ambacher O, Stutzmann M, Hornsteiner J, Riha E and Fischerauer G 1998 Sound velocity of AlxGa1−xN thin films obtained by surface acoustic-wave measurements *Appl. Phys. Lett.* **72** 2400–2

[67] Serrano J, Bosak A, Krisch M, Manjón F J, Romero A H, Garro N, Wang X, Yoshikawa A and Kuball M 2011 InN Thin Film Lattice Dynamics by Grazing Incidence Inelastic X-Ray Scattering *Phys. Rev. Lett.* **106** 205501

[68] Bernardini F, Fiorentini V and Vanderbilt D 1997 Spontaneous polarization and piezoelectric constants of III-V nitrides *Phys. Rev. B* **56** R10024–7

[69] Zoroddu A, Bernardini F, Ruggerone P and Fiorentini V 2001 First-principles prediction of structure, energetics, formation enthalpy, elastic constants, polarization, and piezoelectric constants of AlN, GaN, and InN: Comparison of local and gradient-corrected density-functional theory *Phys. Rev. B* **64** 045208

[70] Ambacher O, Foutz B, Smart J, Shealy J R, Weimann N G, Chu K, Murphy M, Sierakowski A J, Schaff W J, Eastman L F, Dimitrov R, Mitchell A and Stutzmann M 2000 Two dimensional electron gases induced by spontaneous and piezoelectric polarization in undoped and doped AlGaN/GaN heterostructures *Journal of Applied Physics* **87** 334–44

[71] Rezaei B, Asgari A and Kalafi M 2006 Electronic band structure pseudopotential calculation of wurtzite III-nitride materials *Physica B: Condensed Matter* **371** 107–11

[72] Monroy E 1999 Development and Characterization of III-Nitride Based Ultraviolet Photodetectors

[73] Varshni Y P 1967 Temperature dependence of the energy gap in semiconductors *Physica* **34** 149–54

[74] Ochalski T J, Gil B, Lefebvre P, Grandjean N, Leroux M, Massies J, Nakamura S and Morkoç H 1999 Photoreflectance investigations of the bowing parameter in AlGaN alloys lattice-matched to GaN *Appl. Phys. Lett.* **74** 3353–5

[75] Brunner D, Angerer H, Bustarret E, Freudenberg F, Höpler R, Dimitrov R, Ambacher O and Stutzmann M 1997 Optical constants of epitaxial AlGaN films and their temperature dependence *Journal of Applied Physics* **82** 5090–6

[76] Yun F, Reshchikov M A, He L, King T, Morkoç H, Novak S W and Wei L 2002 Energy band bowing parameter in AlxGa1−xN alloys *Journal of Applied Physics* **92** 4837–9

[77] Lee S R, Wright A F, Crawford M H, Petersen G A, Han J and Biefeld R M 1999 The band-gap bowing of AlxGa1−xN alloys *Appl. Phys. Lett.* **74** 3344–6

[78] Levinshteĭn M E, Rumyantsev S L and Shur M 2001 *Properties of advanced semiconductor materials: GaN, AlN, InN, BN, SiC, SiGe* (New York: Wiley)

[79] Morkoç H 2013 *Nitride semiconductor devices: fundamentals and applications* (Weinheim, Germany: Wiley-VCH)

[80] Santic B 2003 On the hole effective mass and the free hole statistics in wurtzite GaN *Semicond. Sci. Technol.* **18** 219–24

[81] Ramos L E, Teles L K, Scolfaro L M R, Castineira J L P, Rosa A L and Leite J R 2001 Structural, electronic, and effective-mass properties of silicon and zinc-blende group-III nitride semiconductor compounds *Phys. Rev. B* **63** 165210

[82] Li Y, Lu Y, Shen H, Wraback M, Brown M G, Schurman M, Koszi L and Stall R A 1997 Temperature dependence of energy gap in GaN thin film studied by thermomodulation *Appl. Phys. Lett.* **70** 2458–60

[83] Schubert E F 2006 *Light-Emitting Diodes* (Cambridge: Cambridge University Press)

[84] Tchernycheva M, Nevou L, Doyennette L, Julien F H, Warde E, Guillot F, Monroy E, Bellet-Amalric E, Remmele T and Albrecht M 2006 Systematic experimental and theoretical

investigation of intersubband absorption in Ga N / Al N quantum wells *Phys. Rev. B* **73** 125347

[85] Pankove J I 1975 *Optical processes in semiconductors* (Mineola [NY]: Dover)

[86] Leamy H J 1982 Charge collection scanning electron microscopy *Journal of Applied Physics* **53** R51–80

[87] Ozol D I 2016 Cascade luminescence as a way to increase the energy efficiency of cathodoluminophores *2016 29th International Vacuum Nanoelectronics Conference (IVNC)* 2016 29th International Vacuum Nanoelectronics Conference (IVNC) (Vancouver, BC, Canada: IEEE) pp 1–2

[88] Ozol D I, Sheshin E P, Danilkin M I and Vereschagina N Yu 2020 Cathodoluminescent UV Sources for Biomedical Applications *4th International Conference on Nanotechnologies and Biomedical Engineering* IFMBE Proceedings vol 77, ed I Tiginyanu, V Sontea and S Railean (Cham: Springer International Publishing) pp 313–7

[89] Everhart T E and Hoff P H 1971 Determination of Kilovolt Electron Energy Dissipation vs Penetration Distance in Solid Materials *Journal of Applied Physics* **42** 5837–46

[90] Colak S, Fitzpatrick B J and Bhargava R N 1985 Electron beam pumped II–VI lasers *Journal of Crystal Growth* **72** 504–11

[91] Bogdankevich O V 1994 Electron-beam-pumped semiconductor lasers *Quantum Electron.* **24** 1031–53

[92] Basov N G, Bogdankevich O V and Devyatkov A G 1964 The excitation of a semiconducting quantum generator by a bundle of fast electrons *Dokl. Akad. Nauk SSSR* **155** 783

[93] Anon 2021 Nicolay G. Basov – Nobel Lecture

[94] Benoit àla Guillaume C and Debever J M 1964 Effet laser dans l'arseniure d'indium par bombardement electronique *Solid State Communications* **2** 145–7

[95] Hurwitz C E and Keyes R J 1964 ELECTRON-BEAM-PUMPED GaAs LASER *Appl. Phys. Lett.* **5** 139–41

[96] Hurwitz C E 1966 ELECTRON-BEAM PUMPED LASERS OF CdSe AND CdS *Appl. Phys. Lett.* **8** 121–4

[97] Hurwitz C E 1966 EFFICIENT ULTRAVIOLET LASER EMISSION IN ELECTRON-BEAM-EXCITED ZnS *Appl. Phys. Lett.* **9** 116–8

[98] Nicoll F H 1966 ULTRAVIOLET ZnO LASER PUMPED BY AN ELECTRON BEAM *Appl. Phys. Lett.* **9** 13–5

[99] Kuklev V P, Petrushenko Y V, Ulasyuk V N and Shubina V V 1979 Sealed scanning semiconductor laser with transverse electronbeam pumping *Sov. J. Quantum Electron.* **9** 206–8

[100] Bogdankevich O V 1994 Electron-beam-pumped semiconductor lasers *Quantum Electron.* **24** 1031–53

[101] Levy U, Gordon E I and Logan R A 1983 Laser cathode ray tube with a semiconductor double-heterostructure screen *IEEE Electron Device Lett.* **4** 155–6

[102] Levy U, Logan R A and Niv Y 1984 Laser cathode ray tube operation at room temperature *Appl. Phys. Lett.* **45** 497–9

[103] Bondar' S A, Borisov N A, Galchenkov D V, Lavrushin B M, Lebedev V V and Strel'chenko S S 1976 Electron-beam-pumped semiconductor laser utilizing multilayer $Ga_{1-x}In_xAs_{1-y}Sb_y$ heterostructures *Sov. J. Quantum Electron.* **6** 50–3

[104] Bogdankevich O V, Borisov N A, Borodulin V I, Pevtsov V F and Shveĭkin V I 1981 Electron-beam-pumped semiconductor laser operating at low acceleration voltages *Sov. J. Quantum Electron.* **11** 675–7

[105] Potts J E, Smith T L and Cheng H 1987 Electron beam pumped lasing in ZnSe grown by molecular beam epitaxy *Appl. Phys. Lett.* **50** 7–9

[106] Cammack D A, Dalby R J, Cornelissen H J and Khurgin J 1987 Electron beam pumped lasing in ZnSe/ZnSSe superlattice structuresn grown by molecular-beam epitaxy *Journal of Applied Physics* **62** 3071–4

[107] Molva E, Accomo R, Labrunie G, Cibert J, Bodin C, Dang L S and Feuillet G 1993 Microgun-pumped semiconductor laser *Appl. Phys. Lett.* **62** 796–8

[108] Hervé D, Accomo R, Molva E, Vanzetti L, Paggel J J, Sorba L and Franciosi A 1995 Microgun-pumped blue lasers *Appl. Phys. Lett.* **67** 2144–6

[109] Ghis A, Meyer R, Rambaud P, Levy F and Leroux T 1991 Sealed vacuum devices: fluorescent microtip displays *IEEE Trans. Electron Devices* **38** 2320–2

[110] Zverev M M, Sorokin S V, Sedova I V, Peregoudov D V, Ivanov S V and Kopev P S 2002 ZnSe-Based Room Temperature Low-Threshold Electron-Beam Pumped Semiconductor Laser *physica status solidi (b)* **229** 1025–8

[111] Zverev M M, Peregudov D V, Sedova I V, Sorokin S V, Ivanov S V and Kop'ev P S 2004 Low-threshold electron-beam-pumped green quantum-well heterostructure semiconductor lasers *Quantum Electron.* **34** 909–11

[112] Zverev M M, Gamov N A, Zhdanova E V, Peregudov D V, Studenov V B, Ivanov S V, Sedova I V, Sorokin S V, Gronin S V and Kop'ev P S 2007 Green lasers based on CdSe/ZnSe nanostructures pumped by electron beams with energies below 10 keV *Tech. Phys. Lett.* **33** 1032–4

[113] Zverev M M, Gamov N A, Peregoudov D V, Studionov V B, Zdanova E V, Sedova I V, Gronin S V, Sorokin S V, Ivanov S V and Kop'ev P S 2008 An efficient electron-beam-pumped

semiconductor laser for the green spectral range based on II–VI multilayer nanostructures *Semiconductors* **42** 1440–4

[114] Zverev M M, Ivanov S V, Gamov N A, Zdanova E V, Studionov V B, Peregoudov D V, Sedova I V, Gronin S V, Sorokin S V, Kop'ev P S and Olikhov I M 2010 Green electron-beam pumped laser arrays based on II-VI nanostructures *phys. stat. sol. (b)* **247** 1561–3

[115] Zverev M M, Sorokin S V, Gamov N A, Zhdanova E V, Studionov V B, Sedova I V, Gronin S V and Ivanov S V 2016 RT ZnSe-based lasers and laser arrays pumped by low-energy electron beam: RT ZnSe-based lasers and laser arrays pumped by low-energy electron beam *Phys. Status Solidi C* **13** 661–4

[116] Kuznetsov P I, Yakushcheva G G, Jitov V A, Zakharov L Yu, Shchamkhalova B S, Kozlovsky V I, Sannikov D A, Skasyrsky Ya K and Tiberi M D 2006 MOVPE growth and study of ZnCdSe/ZnSSe MQW structures for green VCSELs *phys. stat. sol. (c)* **3** 771–5

[117] Klein T, Klembt S, Kozlovsky V I, Zheng A, Tiberi M D and Kruse C 2015 High-power green and blue electron-beam pumped surface-emitting lasers using dielectric and epitaxial distributed Bragg reflectors *Journal of Applied Physics* **117** 113106

[118] Packard J R, Tait W C and Dierssen G H 1971 Two-Dimensionally Scannable Electron-Beam-Pumped Laser *Appl. Phys. Lett.* **19** 338–40

[119] Colak S, Fitzpatrick B J and Bhargava R N 1985 Electron beam pumped II–VI lasers *Journal of Crystal Growth* **72** 504–11

[120] Kozlovskiĭ V I, Korostelin Y V, Nasibov A S, Skasyrskiĭ Y K and Shapkin P V 1984 Ultraviolet ZnS semiconductor laser pumped longitudinally by an electron beam *Sov. J. Quantum Electron.* **14** 420–2

[121] Basov N G, Dianov E M, Kozlovskii V I, Krysa A B, Nasibov A S, Popov Y M, Prokhorov A M, Trubenko P A and Shcherbakov E A 1995 Room-temperature laser cathode-ray tube based on an ZnCdSe/ZnSe superlattice *Quantum Electron.* **25** 726–8

[122] Kozlovsky V I, Shcherbakov E A, Dianov E M, Krysa A B, Nasibov A S and Trubenko P A 1996 Electron-beam pumped laser structures based on MBE grown superlattices *Journal of Crystal Growth* **159** 609–12

[123] Cusano D A 1965 IDENTIFICATION OF LASER TRANSITIONS IN ELECTRON-BEAM-PUMPED GaAs *Appl. Phys. Lett.* **7** 151–2

[124] Bondarev V Y, Kozlovskii V I, Krysa A B, Popov Y M and Skasyrsky Y K 2004 Uniformity of radiation from a laser CRT based on a low-dimensional GaInP/AlGaInP structure with resonance-periodic gain *Quantum Electron.* **34** 919–23

[125] Kozlovsky V I, Krysa A B, Skyasyrsky Y K, Popov Y M, Abare A, Mack M P, Keller S, Mishra U K, Coldren L, DenBaars S, Tiberi M D and George T 1997 Electron Beam Pumped MQW InGaN/GaN Laser *MRS Internet j. nitride semicond. res.* **2** e38

[126] Gamov N A, Zhdanova E V, Zverev M M, Peregudov D V, Studenov V B, Mazalov A V, Kureshov V A, Sabitov D R, Padalitsa A A and Marmalyuk A A 2015 Pulsed electron-beam-pumped laser based on AlGaN/InGaN/GaN quantum-well heterostructure *Quantum Electron.* **45** 601–3

[127] Wunderer T, Jeschke J, Yang Z, Teepe M, Batres M, Vancil B and Johnson N 2017 Resonator-Length Dependence of Electron-Beam-Pumped UV-A GaN-Based Lasers *IEEE Photonics Technology Letters* **29** 1344–7

[128] Nakarmi M L, Kim K H, Khizar M, Fan Z Y, Lin J Y and Jiang H X 2005 Electrical and optical properties of Mg-doped Al0.7Ga0.3N alloys *Appl. Phys. Lett.* **86** 092108

[129] Zhao C-Z, Wei T, Chen L-Y, Wang S-S and Wang J 2017 The activation energy for Mg acceptor in AlxGa1-xN alloys in the whole composition range *Superlattices and Microstructures* **109** 758–62

[130] Mehnke F, Trinh X T, Pingel H, Wernicke T, Janzén E, Son N T and Kneissl M 2016 Electronic properties of Si-doped Al $_x$ Ga1−xN with aluminum mole fractions above 80% *Journal of Applied Physics* **120** 145702

[131] Pampili P and Parbrook P J 2017 Doping of III-nitride materials *Materials Science in Semiconductor Processing* **62** 180–91

[132] Blasco R, Ajay A, Robin E, Bougerol C, Lorentz K, Alves L C, Mouton I, Amichi L, Grenier A and Monroy E 2019 Electrical and optical properties of heavily Ge-doped AlGaN *J. Phys. D: Appl. Phys.* **52** 125101

[133] Bougerol C, Robin E, Di Russo E, Bellet-Amalric E, Grenier V, Ajay A, Rigutti L and Monroy E 2021 Solubility Limit of Ge Dopants in AlGaN: A Chemical and Microstructural Investigation Down to the Nanoscale *ACS Appl. Mater. Interfaces* **13** 4165–73

[134] Gordon L, Lyons J L, Janotti A and Van de Walle C G 2014 Hybrid functional calculations of D X centers in AlN and GaN *Physical Review B* **89** 085204

[135] Wunderer T, Johnson N and Northrup J 2012 Electron beam pumped vertical cavity surface emitting laser

[136] Chen Y R, Zhang Z W, Miao G Q, Jiang H, Li Z M and Song H 2020 AlGaN-based UV-C distributed Bragg reflector with a λ-cavity designed for an external cavity structure electron-beam-pumped VCSEL *Journal of Alloys and Compounds* **820** 153415

[137] Villain J and Pimpinelli A 1999 *Physique de la croissance cristalline* (Eyrolles , Centre d'études nucléaires de Saclay)

[138] Barabási A-L and Stanley H E 1995 *Fractal concepts in surface growth* (New York, NY, USA: Press Syndicate of the University of Cambridge)

[139] Politi P, Grenet G, Marty A, Ponchet A and Villain J 2000 Instabilities in crystal growth by atomic or molecular beams *Physics Reports* **324** 271–404

[140] Daruka I and Barabási A-L 1997 Dislocation-Free Island Formation in Heteroepitaxial Growth: A Study at Equilibrium *Phys. Rev. Lett.* **79** 3708–11

[141] Daruka I and Barabási A-L 1998 Equilibrium phase diagrams for dislocation free self-assembled quantum dots *Appl. Phys. Lett.* **72** 2102–4

[142] Capper P, Irvine S and Joyce T 2006 Epitaxial Crystal Growth: Methods and Materials *Springer Handbook of Electronic and Photonic Materials* ed S Kasap and P Capper (Boston, MA: Springer US) pp 271–301

[143] Cho A Y and Arthur J R 1975 Molecular beam epitaxy *Progress in Solid State Chemistry* **10** 157–91

[144] Lim C B *GaN/AlGaN heterostructures for infrared optoelectronics : polar vs nonpolar orientations*

[145] Mahan J E, Geib K M, Robinson G Y and Long R G 1998 A review of the geometrical fundamentals of reflection high-energy electron diffraction with application to silicon surfaces *Journal of Vacuum Science & Technology A: Vacuum, Surfaces, and Films* **8** 3692

[146] Hestroffer K 2012 *Croissance et caractérisation de nanofils de GaN et d'hétérostructures filaires de GaN/AlN* phdthesis (Université de Grenoble)

[147] Joyce B A, Dobson P J, Neave J H, Woodbridge K, Zhang J, Larsen P K and Bôlger B 1986 RHEED studies of heterojunction and quantum well formation during MBE growth — from multiple scattering to band offsets *Surface Science* **168** 423–38

[148] Ohring M 2001 *Materials Science of Thin Films.* (Burlington: Elsevier)

[149] Adelmann C, Brault J, Mula G, Daudin B, Lymperakis L and Neugebauer J 2003 Gallium adsorption on (0001) GaN surfaces *Phys. Rev. B* **67** 165419

[150] Mula G, Adelmann C, Moehl S, Oullier J and Daudin B 2001 Surfactant effect of gallium during molecular-beam epitaxy of GaN on AlN (0001) *Physical Review B* **64** 195406

[151] Neugebauer J, Zywietz T, Scheffler M, Northrup J, Chen H and Feenstra R 2003 Adatom Kinetics On and Below the Surface: The Existence of a New Diffusion Channel *Physical Review Letters* **90** 056101

[152] Lieberman M A and Lichtenberg A J 2005 Chemical Kinetics and Surface Processes *Principles of Plasma Discharges and Materials Processing* (Hoboken, NJ, USA: John Wiley & Sons, Inc.) pp 285–325

[153] Myoung J M, Gluschenkov O, Kim K and Kim S 1999 Growth kinetics of GaN and effects of flux ratio on the properties of GaN films grown by plasma-assisted molecular beam epitaxy *Journal of Vacuum Science & Technology A: Vacuum, Surfaces, and Films* **17** 3019–28

[154] Kotsar Y, Doisneau B, Bellet-Amalric E, Das A, Sarigiannidou E and Monroy E 2011 Strain relaxation in GaN/AlxGa1-xN superlattices grown by plasma-assisted molecular-beam epitaxy *Journal of Applied Physics* **110** 033501

[155] Bellet-Amalric E, Adelmann C, Sarigiannidou E, Rouvière J L, Feuillet G, Monroy E and Daudin B 2004 Plastic strain relaxation of nitride heterostructures *Journal of Applied Physics* **95** 1127–33

[156] Northrup J, Neugebauer J, Feenstra R and Smith A 2000 Structure of GaN(0001) : The laterally contracted Ga bilayer model *Physical Review B* **61** 9932–5

[157] Kandaswamy P K, Guillot F, Bellet-Amalric E, Monroy E, Nevou L, Tchernycheva M, Michon A, Julien F H, Baumann E, Giorgetta F R, Hofstetter D, Remmele T, Albrecht M, Birner S and Dang L S 2008 GaN/AlN short-period superlattices for intersubband optoelectronics: A systematic study of their epitaxial growth, design, and performance *Journal of Applied Physics* **104** 093501

[158] Adelmann H C 2002 *Growth and strain relaxation mechanisms of group III nitride heterostructures* PhD Thesis (Grenoble: Université Joseph Fourier)

[159] Iliopoulos E and Moustakas T D 2002 Growth kinetics of AlGaN films by plasma-assisted molecular-beam epitaxy *Appl. Phys. Lett.* **81** 295–7

[160] Monroy E, Daudin B, Bellet-Amalric E, Gogneau N, Jalabert D, Enjalbert F, Brault J, Barjon J and Dang L S 2003 Surfactant effect of In for AlGaN growth by plasma-assisted molecular beam epitaxy *Journal of Applied Physics* **93** 1550–6

[161] Harrison W A 1989 *Electronic structure and the properties of solids: the physics of the chemical bond* (New York: Dover Publications)

[162] Kneissl M, Kolbe T, Chua C, Kueller V, Lobo N, Stellmach J, Knauer A, Rodriguez H, Einfeldt S, Yang Z, Johnson N M and Weyers M 2010 Advances in group III-nitride-based deep UV light-emitting diode technology *Semicond. Sci. Technol.* **26** 014036

[163] Ajay A *GaN/AlGaN nanowires for quantum devices* (Université Grenoble Alpes)

[164] Giannuzzi L A, Drown J L, Brown S R, Irwin R B and Stevie F A 1997 Focused Ion Beam Milling and Micromanipulation Lift-Out for Site Specific Cross-Section Tem Specimen Preparation *MRS Proc.* **480** 19

[165] Anon AFM scanning modes – MAX IV

[166] Binnig G, Quate C F and Gerber Ch 1986 Atomic Force Microscope *Phys. Rev. Lett.* **56** 930–3

[167] Smith K K 1981 Photoluminescence of semiconductor materials *Thin Solid Films* **84** 171–82

[168] Knox R S 1983 Introduction to Exciton Physics *Collective Excitations in Solids* ed B Bartolo (Boston, MA: Springer US) pp 183–245

[169] Kornitzer K, Ebner T, Thonke K, Sauer R, Kirchner C, Schwegler V, Kamp M, Leszczynski M, Grzegory I and Porowski S 1999 Photoluminescence and reflectance spectroscopy of excitonic transitions in high-quality homoepitaxial GaN films *Phys. Rev. B* **60** 1471–3

[170] Stępniewski R, Potemski M, Wysmołek A, Pakuła K, Baranowski J M, Łusakowski J, Grzegory I, Porowski S, Martinez G and Wyder P 1999 Symmetry of excitons in GaN *Phys. Rev. B* **60** 4438–41

[171] Park S-H 2000 Crystal Orientation Effects on Electronic Properties of Wurtzite GaN/AlGaN Quantum Wells with Spontaneous and Piezoelectric Polarization *Japanese Journal of Applied Physics* **39** 3478–82

[172] Ambacher O, Dimitrov R, Stutzmann M, Foutz B E, Murphy M J, Smart J A, Shealy J R, Weimann N G, Chu K, Chumbes M, Green B, Sierakowski A J, Schaff W J and Eastman L F 1999 Role of Spontaneous and Piezoelectric Polarization Induced Effects in Group-III Nitride Based Heterostructures and Devices *physica status solidi (b)* **216** 381–9

[173] Vurgaftman I, Meyer J R and Ram-Mohan L R 2001 Band parameters for III–V compound semiconductors and their alloys *Journal of Applied Physics* **89** 5815

[174] Suzuki M and Uenoyama T 1996 Strain effect on electronic and optical properties of GaN/AlGaN quantum-well lasers *Journal of Applied Physics* **80** 6868–74

[175] Park S-H and Chuang S-L 1999 Crystal-orientation effects on the piezoelectric field and electronic properties of strained wurtzite semiconductors *Phys. Rev. B* **59** 4725–37

[176] Yan Q, Rinke P, Janotti A, Scheffler M and Van de Walle C G 2014 Effects of strain on the band structure of group-III nitrides *Phys. Rev. B* **90** 125118

[177] Rinke P, Winkelnkemper M, Qteish A, Bimberg D, Neugebauer J and Scheffler M 2008 Consistent set of band parameters for the group-III nitrides AlN, GaN, and InN *Phys. Rev. B* **77** 075202

[178] Birner S 2011 Modeling of semiconductor nanostructures and semiconductor-electrolyte interfaces

[179] Pastrňák J and Roskovcová L 1966 Refraction Index Measurements on AlN Single Crystals *phys. stat. sol. (b)* **14** K5–8

[180] Kawashima T, Yoshikawa H, Adachi S, Fuke S and Ohtsuka K 1997 Optical properties of hexagonal GaN *Journal of Applied Physics* **82** 3528–35

[181] Rumble J R 2017 *CRC handbook of chemistry and physics* (Boca Raton London New York: CRC Press, Taylor & Francis Group)

[182] Hovington P, Drouin D and Gauvin R 2006 CASINO: A new monte carlo code in C language for electron beam interaction -part I: Description of the program *Scanning* **19** 1–14

[183] Drouin D, Couture A R, Joly D, Tastet X, Aimez V and Gauvin R 2007 CASINO V2.42—A Fast and Easy-to-use Modeling Tool for Scanning Electron Microscopy and Microanalysis Users *Scanning* **29** 92–101

[184] Demers H, Poirier-Demers N, Couture A R, Joly D, Guilmain M, de Jonge N and Drouin D 2011 Three-dimensional electron microscopy simulation with the CASINO Monte Carlo software *Scanning* **33** 135–46

[185] Toth M and Phillips M R 1998 Monte Carlo modeling of cathodoluminescence generation using electron energy loss curves *Scanning* **20** 425–32

[186] Cuesta S, Curé Y, Donatini F, Denaix L, Bellet-Amalric E, Bougerol C, Grenier V, Thai Q-M, Nogues G, Purcell S T, Dang L S and Monroy E 2021 AlGaN/GaN asymmetric graded-index separate confinement heterostructures designed for electron-beam pumped UV lasers *Opt. Express* **29** 13084

[187] Cuesta Arcos S, Thai Q M, Curé Y, Donatini F, Bellet-Amalric E, Bougerol C, Nogues G, Purcell S T, Dang L S and Monroy E 2021 Development of AlGaN/GaN heterostructures for e-beam pumped UV lasers *Gallium Nitride Materials and Devices XVI* Gallium Nitride Materials and Devices XVI ed H Morkoç, H Fujioka and U T Schwarz (Online Only, United States: SPIE) p 15

[188] Cuesta S, Denaix L, Dang L S and Monroy E 2021 Decorrelation of internal quantum efficiency and lasing threshold in AlGaN-based separate confinement heterostructures for UV emission *Appl. Phys. Lett.* **119** 151103

[189] Thai Q M, Cuesta S, Denaix L, Hermelin S, Boisron O, Bellet-Amalric E, Bougerol C, Castioni F, Purcell S T, Dang L S and Monroy E 2022 Optical net gain measurement on $Al_{0.07}Ga_{0.93}N$/GaN multi-quantum wells *Opt. Express* **30** 25219

[190] Jenkins F A and White H E 2001 *Fundamentals of optics* (New York; Montreal: McGraw-Hill)

[191] Muth J F, Lee J H, Shmagin I K, Kolbas R M, Casey H C, Keller B P, Mishra U K and DenBaars S P 1997 Absorption coefficient, energy gap, exciton binding energy, and recombination lifetime of GaN obtained from transmission measurements *Appl. Phys. Lett.* **71** 2572–4

[192] Sun H, Woodward J, Yin J, Moldawer A, Pecora E F, Nikiforov A Yu, Dal Negro L, Paiella R, Ludwig K, Smith D J and Moustakas T D 2013 Development of AlGaN-based graded-index-separate-confinement-heterostructure deep UV emitters by molecular beam epitaxy *Journal of Vacuum Science & Technology B, Nanotechnology and Microelectronics: Materials, Processing, Measurement, and Phenomena* **31** 03C117

[193] Stańczyk S, Czyszanowski T, Kafar A, Goss J, Grzanka S, Grzanka E, Czernecki R, Bojarska A, Targowski G, Leszczyński M, Suski T, Kucharski R and Perlin P 2013 Graded-index separate confinement heterostructure InGaN laser diodes *Appl. Phys. Lett.* **103** 261107

[194] Sato K, Yasue S, Ogino Y, Tanaka S, Iwaya M, Takeuchi T, Kamiyama S and Akasaki I 2019 Light confinement and high current density in UVB laser diode structure using Al composition-graded p-AlGaN cladding layer *Appl. Phys. Lett.* **114** 191103

[195] Simon J, Protasenko V, Lian C, Xing H and Jena D 2010 Polarization-Induced Hole Doping in Wide-Band-Gap Uniaxial Semiconductor Heterostructures *Science* **327** 60–4

[196] Watanabe M and Williams D B 2006 The quantitative analysis of thin specimens: a review of progress from the Cliff-Lorimer to the new zeta-factor methods *J Microsc* **221** 89–109

[197] Gačević Ž, Das A, Teubert J, Kotsar Y, Kandaswamy P K, Kehagias Th, Koukoula T, Komninou Ph and Monroy E 2011 Internal quantum efficiency of III-nitride quantum dot superlattices grown by plasma-assisted molecular-beam epitaxy *Journal of Applied Physics* **109** 103501

[198] Dimkou I, Harikumar A, Donatini F, Lähnemann J, den Hertog M I, Bougerol C, Bellet-Amalric E, Mollard N, Ajay A, Ledoux G, Purcell S T and Monroy E 2020 Assessment of AlGaN/AlN superlattices on GaN nanowires as active region of electron-pumped ultraviolet sources *Nanotechnology* **31** 204001

[199] Roble A A, Patra S K, Massabuau F, Frentrup M, Leontiadou M A, Dawson P, Kappers M J, Oliver R A, Graham D M and Schulz S 2019 Impact of alloy fluctuations and Coulomb effects on the electronic and optical properties of c-plane GaN/AlGaN quantum wells *Sci Rep* **9** 18862

[200] Jeong H, Jeong H J, Oh H M, Hong C-H, Suh E-K, Lerondel G and Jeong M S 2015 Carrier localization in In-rich InGaN/GaN multiple quantum wells for green light-emitting diodes *Sci Rep* **5** 9373

[201] Frankerl C, Hoffmann M P, Nippert F, Wang H, Brandl C, Tillner N, Lugauer H-J, Zeisel R, Hoffmann A and Davies M J 2019 Challenges for reliable internal quantum efficiency determination in AlGaN-based multi-quantum-well structures posed by carrier transport effects and morphology issues *Journal of Applied Physics* **126** 075703

[202] Bryan Z, Bryan I, Xie J, Mita S, Sitar Z and Collazo R 2015 High internal quantum efficiency in AlGaN multiple quantum wells grown on bulk AlN substrates *Appl. Phys. Lett.* **106** 142107

[203] Schlager J B, Sanford N A, Bertness K A and Roshko A 2011 Injection-level-dependent internal quantum efficiency and lasing in low-defect GaN nanowires *Journal of Applied Physics* **109** 044312-044312–7

[204] Yamada Y, Iwamura K, Kuronaka T, Shinomura N, Taguchi T, Kudo H and Okagawa H 2008 Internal Quantum Efficiency of Nitride-based Light-Emitting Diodes *J. Light & Vis. Env.* **32** 191–5

[205] Leroux M, Grandjean N, Beaumont B, Nataf G, Semond F, Massies J and Gibart P 1999 Temperature quenching of photoluminescence intensities in undoped and doped GaN *Journal of Applied Physics* **86** 3721–8

[206] Shaklee K L, Nahory R E and Leheny R F 1973 Optical gain in semiconductors *Journal of Luminescence* **7** 284–309

[207] Shaklee K L and Leheny R F 1971 DIRECT DETERMINATION OF OPTICAL GAIN IN SEMICONDUCTOR CRYSTALS *Appl. Phys. Lett.* **18** 475–7

[208] Barjon J 2002 *Étude d'un laser UV compact à semiconducteurs (Al, Ga)N pompé par micropointes* These de doctorat (Grenoble INPG)

[209] Martens M 2018 *Optical gain and modal loss in AlGaN based deep UV lasers* (Berlin: Technische Universität Berlin)

[210] Guo W, Bryan Z, Xie J, Kirste R, Mita S, Bryan I, Hussey L, Bobea M, Haidet B, Gerhold M, Collazo R and Sitar Z 2014 Stimulated emission and optical gain in AlGaN heterostructures grown on bulk AlN substrates *Journal of Applied Physics* **115** 103108

[211] Guo Q, Kirste R, Mita S, Tweedie J, Reddy P, Moody B, Guan Y, Washiyama S, Klump A, Sitar Z and Collazo R 2019 Design of AlGaN-based quantum structures for low threshold UVC lasers *Journal of Applied Physics* **126** 223101

[212] Heppel S, Hangleiter A, Bader S, Brüderl G, Weimar A, Kümmler V, Lell A, Härle V, Off J, Kuhn B and Scholz F 2001 Systematics of Optical Gain in GaInN/GaN Laser Structures *phys. stat. sol. (a)* **188** 59–63

[213] Oto T, Banal R G, Funato M and Kawakami Y 2014 Optical gain characteristics in Al-rich AlGaN/AlN quantum wells *Appl. Phys. Lett.* **104** 181102

[214] Francesco Pecora E, Zhang W, Yu. Nikiforov A, Zhou L, Smith D J, Yin J, Paiella R, Dal Negro L and Moustakas T D 2012 Sub-250 nm room-temperature optical gain from AlGaN/AlN multiple quantum wells with strong band-structure potential fluctuations *Appl. Phys. Lett.* **100** 061111

[215] Klein C A 1968 Bandgap Dependence and Related Features of Radiation Ionization Energies in Semiconductors *Journal of Applied Physics* **39** 2029

[216] Kirste R, Guo Q, Dycus J H, Franke A, Mita S, Sarkar B, Reddy P, LeBeau J M, Collazo R and Sitar Z 2018 6 kW/cm2 UVC laser threshold in optically pumped lasers achieved by controlling point defect formation *Appl. Phys. Express* **11** 082101

[217] Shan M, Zhang Y, Tran T B, Jiang J, Long H, Zheng Z, Wang A, Guo W, Ye J, Chen C, Dai J and Li X 2019 Deep UV Laser at 249 nm Based on GaN Quantum Wells *ACS Photonics* **6** 2387–91

[218] Li X-H, Detchprohm T, Kao T-T, Satter Md M, Shen S-C, Douglas Yoder P, Dupuis R D, Wang S, Wei Y O, Xie H, Fischer A M, Ponce F A, Wernicke T, Reich C, Martens M and Kneissl M 2014 Low-threshold stimulated emission at 249 nm and 256 nm from AlGaN-based multiple-quantum-well lasers grown on sapphire substrates *Appl. Phys. Lett.* **105** 141106

[219] Yoshida H, Kuwabara M, Yamashita Y, Takagi Y, Uchiyama K and Kan H 2009 AlGaN-based laser diodes for the short-wavelength ultraviolet region *New Journal of Physics* **11**

[220] Yoshida H, Yamashita Y, Kuwabara M and Kan H 2008 A 342-nm ultraviolet AlGaN multiple-quantum-well laser diode *Nature Photonics* **2** 551–4

[221] Edmond J, Abare A, Bergman M, Bharathan J, Lee Bunker K, Emerson D, Haberern K, Ibbetson J, Leung M, Russel P and Slater D 2004 High efficiency GaN-based LEDs and lasers on SiC *Journal of Crystal Growth* **272** 242–50

[222] Nagahama S, Yanamoto T, Sano M and Mukai T 2001 Ultraviolet GaN Single Quantum Well Laser Diodes *Jpn. J. Appl. Phys.* **40** L785–7

[223] Sakai T, Kushimoto M, Zhang Z, Sugiyama N, Schowalter L J, Honda Y, Sasaoka C and Amano H 2020 On-wafer fabrication of etched-mirror UV-Claser diodes with the ALD-deposited DBR *Applied Physics Letters* **116**

[224] Zhang Z, Kushimoto M, Sakai T, Sugiyama N, Schowalter L J, Sasaoka C and Amano H 2019 A 271.8 nm deep-ultraviolet laser diode for room temperature operation *Applied Physics Express* **12**

[225] Yoshida H, Takagi Y, Kuwabara M, Amano H and Kan H 2007 Entirely Crack-Free Ultraviolet GaN/AlGaN Laser Diodes Grown on 2-in. Sapphire Substrate *Jpn. J. Appl. Phys.* **46** 5782–4

[226] Tanaka S, Ogino Y, Yamada K, Omori T, Ogura R, Teramura S, Shimokawa M, Ishizuka S, Yabutani A, Iwayama S, Sato K, Miyake H, Iwaya M, Takeuchi T, Kamiyama S and Akasaki I 2021 AlGaN-based UV-B laser diode with a high optical confinement factor *Appl. Phys. Lett.* **118** 163504

[227] Aoki Y, Kuwabara M, Yamashita Y, Takagi Y, Sugiyama A and Yoshida H 2015 A 350-nm-band GaN/AlGaN multiple-quantum-well laser diode on bulk GaN *Applied Physics Letters* **107**

[228] Sato K, Yasue S, Yamada K, Tanaka S, Omori T, Ishizuka S, Teramura S, Ogino Y, Iwayama S, Miyake H, Iwaya M, Takeuchi T, Kamiyama S and Akasaki I 2020 Room-temperature operation of AlGaN ultraviolet-B laser diode at 298 nm on lattice-relaxed Al0.6Ga0.4N/AlN/sapphire *Applied Physics Express* **13**

[229] Iida K, Kawashima T, Miyazaki A, Kasugai H, Mishima S, Honshio A, Miyake Y, Iwaya M, Kamiyama S, Amano H and Akasaki I 2004 350.9 nm UV Laser Diode Grown on Low-Dislocation-Density AlGaN *Jpn. J. Appl. Phys.* **43** L499–500

[230] Wunderer T, Chua C L, Northrup J E, Yang Z, Johnson N M, Kneissl M, Garrett G A, Shen H, Wraback M, Moody B, Craft H S, Schlesser R, Dalmau R F and Sitar Z 2012 Optically pumped UV lasers grown on bulk AlN substrates *Phys. Status Solidi C* **9** 822–5

[231] Cuesta S, Denaix L, Castioni F, Dang L S and Monroy E 2022 Reduction of the lasing threshold in optically pumped AlGaN/GaN lasers with two-step etched facets *Semicond. Sci. Technol.* **37** 075013

[232] Asryan L V and Suris R A 1996 Inhomogeneous line broadening and the threshold current density of a semiconductor quantum dot laser *Semicond. Sci. Technol.* **11** 554–67

[233] Joullie A, Glastre G, Blondeau R, Nicolas J C, Cuminal Y, Baranov A N, Wilk A, Garcia M, Grech P and Alibert C 1999 Continuous-wave operation of GaInAsSb-GaSb type-II quantum-well ridge-lasers *IEEE J. Select. Topics Quantum Electron.* **5** 711–4

[234] van Deurzen L, Page R, Protasenko V, Huili, Xing and Jena D 2021 Optically Pumped AlGaN Double Heterostructure Deep-UV Laser by Molecular Beam Homoepitaxy: Mirror Imperfections and Cavity Loss *arXiv:2109.10515 [cond-mat, physics:physics]*

[235] Kang J H, Krüger O, Spengler U, Zeimer U, Einfeldt S and Kneissl M 2016 On the formation of cleaved mirror facets of GaN-based laser diodes—A comparative study of diamond-tip edge-scribing and laser scribing *Journal of Vacuum Science & Technology B, Nanotechnology and Microelectronics: Materials, Processing, Measurement, and Phenomena* **34** 041222

[236] Stocker D A, Schubert E F, Grieshaber W, Boutros K S and Redwing J M 1998 Facet roughness analysis for InGaN/GaN lasers with cleaved facets *Appl. Phys. Lett.* **73** 1925–7

[237] Khan F A, Zhou L, Ping A T and Adesida I 1999 Inductively coupled plasma reactive ion etching of Al[sub x]Ga[sub 1−x]N for application in laser facet formation *J. Vac. Sci. Technol. B* **17** 2750

[238] Miller M A, Crawford M H, Allerman A A, Cross K C, Banas M A, Shul R J, Stevens J and Bogart K H A 2009 Smooth and Vertical Facet Formation for AlGaN-Based Deep-UV Laser Diodes *Journal of Elec Materi* **38** 533–7

[239] Shul R J, McClellan G B, Casalnuovo S A, Rieger D J, Pearton S J, Constantine C, Barratt C, Karlicek R F, Tran C and Schurman M 1996 Inductively coupled plasma etching of GaN *Appl. Phys. Lett.* **69** 1119–21

[240] Palacios T, Calle F, Varela M, Ballesteros C, Monroy E, Naranjo F B, Sánchez-García M A, Calleja E and Muñoz E 2000 Wet etching of GaN grown by molecular beam epitaxy on Si(111) *Semicond. Sci. Technol.* **15** 996–1000

[241] Ng H M, Weimann N G and Chowdhury A 2003 GaN nanotip pyramids formed by anisotropic etching *Journal of Applied Physics* **94** 650–3

[242] Zhuang D and Edgar J H 2005 Wet etching of GaN, AlN, and SiC: a review *Materials Science and Engineering: R: Reports* **48** 1–46

[243] Al Taradeh N, Frayssinet E, Rodriguez C, Morancho F, Sonneville C, Phung L-V, Soltani A, Tendille F, Cordier Y and Maher H 2021 Characterization of m-GaN and a-GaN Crystallographic Planes after Being Chemically Etched in TMAH Solution *Energies* **14** 4241

[244] Sakai T, Kushimoto M, Zhang Z, Sugiyama N, Schowalter L J, Honda Y, Sasaoka C and Amano H 2020 On-wafer fabrication of etched-mirror UV-C laser diodes with the ALD-deposited DBR *Appl. Phys. Lett.* **116** 122101

[245] Anon KLayout Layout Viewer And Editor

[246] Valdueza-Felip S, Mukhtarova A, Pan Q, Altamura G, Grenet L, Durand C, Bougerol C, Peyrade D, González-Posada F, Eymery J and Monroy E 2013 Photovoltaic Response of InGaN/GaN Multiple-Quantum Well Solar Cells *Jpn. J. Appl. Phys.* **52** 08JH05

[247] Iga K, Wakao K and Kunikane T 1981 Mode reflectivity of tilted mirrors in semiconductor lasers with etched facets *Appl. Opt.* **20** 2367

[248] Tsai M-C, Leung B, Balakrishnan G and Wang G T 2016 Understanding and Predicting GaN Anisotropic Wet Etch Facet Evolution

[249] Jaccodine R J 1962 Use of Modified Free Energy Theorems to Predict Equilibrium Growing and Etching Shapes *Journal of Applied Physics* **33** 2643–7

[250] Weirauch D F 1975 Correlation of the anisotropic etching of single−crystal silicon spheres and wafers *Journal of Applied Physics* **46** 1478–83

[251] Shaw D W 1979 Morphology analysis in localized crystal growth and dissolution *Journal of Crystal Growth* **47** 509–17

[252] Kazanowska B A, Sapkota K R, Gunning B P, Jones K S and Wang G T 2021 Exploring AlGaN nanostructures fabricated via chemical wet etching *Gallium Nitride Materials and Devices XVI* Gallium Nitride Materials and Devices XVI ed H Morkoç, H Fujioka and U T Schwarz (Online Only, United States: SPIE) p 64

[253] Yasue S, Sato K, Kawase Y, Ikeda J, Sakuragi Y, Iwayama S, Iwaya M, Kamiyama S, Takeuchi T and Akasaki I 2019 The dependence of AlN molar fraction of AlGaN in wet etching by using tetramethylammonium hydroxide aqueous solution *Jpn. J. Appl. Phys.* **58** SCCC30

[254] Barker A S and Ilegems M 1973 Infrared Lattice Vibrations and Free-Electron Dispersion in GaN *Phys. Rev. B* **7** 743–50

[255] Gao B, George J P, Beeckman J and Neyts K 2020 Design, fabrication and characterization of a distributed Bragg reflector for reducing the étendue of a wavelength converting system *Opt. Express* **28** 12837

[256] Muallem M, Palatnik A, Nessim G D and Tischler Y R 2015 Room Temperature Fabrication of Dielectric Bragg Reflectors Composed of a CaF_2/ZnS Multilayered Coating *ACS Appl. Mater. Interfaces* **7** 474–81

[257] Amargianitakis E A, Kazazis S A, Doundoulakis G, Stavrinidis G, Konstantinidis G, Delamadeleine E, Monroy E and Pelekanos N T 2020 Transferrable dielectric DBR membranes for versatile GaN-based polariton and VCSEL technology *Microelectronic Engineering* **228** 111276

[258] Kawashima T, Yoshikawa H, Adachi S, Fuke S and Ohtsuka K 1997 Optical properties of hexagonal GaN *Journal of Applied Physics* **82** 3528–35

[259] Sharhan A A 2020 Transfer Matrix Mathematical Method for Evaluation the DBR Mirror for Light Emitting Diode and Laser *J. Phys.: Conf. Ser.* **1535** 012018

[260] Weber M J 1995 *Optical materials* (Boca Raton: CRC Press)

[261] Ou Y and Petersen P M 2021 Application of ultraviolet light sources for in vivo disinfection *Jpn. J. Appl. Phys.* **60** 100501

[262] Oguma K 2018 Inactivation of feline calicivirus using ultraviolet light-emitting diodes *FEMS Microbiology Letters* **365**

[263] Rattanakul S and Oguma K 2018 Inactivation kinetics and efficiencies of UV-LEDs against Pseudomonas aeruginosa, Legionella pneumophila, and surrogate microorganisms *Water Research* **130** 31–7

[264] Fellmann V, Jaffrennou P, Sam-Giao D, Gayral B, Lorenz K, Alves E and Daudin B 2011 Ternary AlGaN Alloys with High Al Content and Enhanced Compositional Homogeneity Grown by Plasma-Assisted Molecular Beam Epitaxy *Jpn. J. Appl. Phys.* **50** 031001

[265] Tillner N, Frankerl C, Nippert F, Davies M J, Brandl C, Lösing R, Mandl M, Lugauer H-J, Zeisel R, Hoffmann A, Waag A and Hoffmann M P 2020 Point Defect-Induced UV-C Absorption in Aluminum Nitride Epitaxial Layers Grown on Sapphire Substrates by Metal-Organic Chemical Vapor Deposition *Phys. Status Solidi B* **257** 2000278

[266] Dalmau R, Moody B, Schlesser R, Mita S, Xie J, Feneberg M, Neuschl B, Thonke K, Collazo R, Rice A, Tweedie J and Sitar Z 2011 Growth and Characterization of AlN and AlGaN Epitaxial Films on AlN Single Crystal Substrates *J. Electrochem. Soc.* **158** H530

[267] Bickermann M, Epelbaum B M, Filip O, Heimann P, Nagata S and Winnacker A 2010 UV transparent single-crystalline bulk AlN substrates *Phys. Status Solidi (c)* **7** 21–4

Scientific contributions

Publications in international journals

[1] **Effect of bias on the response of GaN axial p–n Junction single-nanowire photodetectors**
S. Cuesta, M. Spies, V. Boureau, F. Donatini, M. Hocevar, M. Den Hertog, E. Monroy
*Nano letters **19** (8), 5506-5514 (2019)*

[2] **AlGaN/GaN asymmetric graded-index separate confinement heterostructures designed for electron-beam pumped UV lasers**
S. Cuesta, Y. Curé, F. Donatini, L. Denaix, E. Bellet-Amalric, C. Bougerol, V. Grenier, Q. M. Thai, G. Nogues, S. T. Purcell, L. S. Dang, and E. Monroy
*Optics Express **29** (9), 13084-13093 (2021)*

[3] **Decorrelation of internal quantum efficiency and lasing threshold in AlGaN-based separate confinement heterostructures for UV emission**
S. Cuesta, L. Denaix, L.S. Dang, E. Monroy
*Applied Physics Letters **119** (15), 151103 (2021)*

[4] **Development of AlGaN/GaN heterostructures for electron-beam pumped UV lasers**
S. Cuesta-Arcos, Q. M. Thai, Y. Curé, F. Donatini, E. Bellet-Amalric, C. Bougerol, G. Nogues, O. Boisron, S. Hermelin, S. T. Purcell, L. S. Dang, and E. Monroy
*SPIE Proc. **11686**, 116860S (2021)*

[5] **Electron beam pumped light emitting devices**
S. Cuesta, A. Harikumar, E. Monroy
*J. Phys. D: Appl. Phys. **55** 273003 (2022)*

[6] **Reduction of the lasing threshold in optically pumped AlGaN/GaN lasers with two-step etched facets**
S. Cuesta, L. Denaix, F. Castioni, L.S. Dang, E. Monroy
*Semicond. Sci. Technol. **37** 075013 (2022)*

[7] **Optical net gain measurement on $Al_{0.07}Ga_{0.93}N$/GaN multi-quantum wells**
Q. M. Thai, S. Cuesta, L. Denaix, S. Hermelin, O. Boisron, E. Bellet-Amalric, C. Bougerol, F. Castioni, S. T. Purcell, L. S. Dang, and E. Monroy
*Optics Express **30** (14), 25219-25233 (2022)*

[8] **Combining atomic-Scale EDX with inelastic multislice simulations for quantitative chemical analysis of AlGaN/GaN 1 nm-thick quantum wells**
F. Castioni, S. Cuesta, N. Bernier, P. Quéméré, E. Robin, V. Delaye, E. Monroy, P. Bayle-Guillemaud
*Microscopy and Microanalysis **28** (S1), 2564-2566 (2022)*

Participation in international conferences

[1] (Oral) **High-performance GaN axial p-n junction single-nanowire photodetectors**
S. Cuesta, M. Spies, V. Boureau, F. Donatini, M. Hocevar, M. Den Hertog, E. Monroy
Nanowire week 2019 (NWW-19), Pisa, Italy. September 2019

[2] (Oral) **Development of AlGaN/GaN heterostructures for e-beam pumped UV lasers**
S. Cuesta, Q. M. Thai, Y. Curé, F. Donatini, E. Bellet-Amalric, C. Bougerol, G. Nogues, S. T. Purcell, L. S. Dang, and E. Monroy
SPIE Photonics West, San Francisco, US. March 2021

[3] (Poster) **AlGaN/GaN heterostructures with asymmetric GRINSCH for e-beam pumped UV lasers**
S. Cuesta, Y. Curé, F. Donatini, L. Denaix, E. Bellet-Amalric, C. Bougerol, V. Grenier, Q. M. Thai, G. Nogues, S. T. Purcell, L. S. Dang, and E. Monroy
Compound Semiconductor Week 2021 (CSW-2021), Stockholm, Sweden (online). May 2021

[4] (Poster) **Study of the optical properties of AlGaN/GaN separate confinement heterostructures for low-threshold e-beam pumped UV lasers**
S. Cuesta, L. Denaix, Q. M. Thai, E. Bellet-Amalric, C. Bougerol, S. T. Purcell, L. S. Dang, and E. Monroy
SPIE Photonics West, San Francisco, US. January 2022

[5] (Oral) **Reduction of the lasing threshold in AlGaN/GaN graded-index separate confinement heterostructures**
S. Cuesta, L. Denaix, F. Castioni, Q. M. Thai, E. Bellet-Amalric, S. T. Purcell, L. S. Dang, and E. Monroy
International Workshop on Nitride Semiconductors (IWN22), Berlin, Germany. October 2022

Other contributions

[1] (Invited talk) **III-nitride based nanowire photodetectors**
M. Spies, I. Dimkou, S. Cuesta, A. Ajay, J. Lähnemann, E. Bellet-Almaric, M. I. den Hertog, and E. Monroy
PDI topical workshop on III-N nanowires, Berlin, Germany. June 2019

[2] (Oral) **High performance GaN axial p-n junction single-NW photodetectors with p^+/n^+ tunnel contacts**
S. Cuesta, M. Spies, V. Boureau, F. Donatini, M. Hocevar, M. I. den Hertog, and E. Monroy
13^{th} International Conference on Nitride Semiconductors 2019 (ICNS-13), Bellevue, Washington, US. July 2019

[3] (Invited talk) **AlGaN Nanostructures for Electron Beam Pumped UV Emitters**
A. Harikumar, S. Cuesta, I. Dimkou, Q.-M. Thai, F. Donantini, Y. Curé, S. T. Purcell, Le Si Dang, and Eva Monroy
UK Nitrides Consortium (UKNC) Winter Meeting, UK (online). January 2021

[4] (Invited talk) **III-nitride based nanowire photodetectors**
S. Cuesta, M. Spies, I. Dimkou, A. Ajay, J. Lähnemann, E. Bellet-Amalric, M. I. den Hertog, and Eva Monroy
Seminar for the University of Cardiff (UK) and University of Bremen (Germany) (online). March 2021

[5] (Oral) **Optical net gain measurements of $Al_{0.07}Ga_{0.93}N$/GaN multi multi-quantum wells for application in cathodo-pumped lasers**
Q. M. Thai, S. Cuesta, L. Denaix, S. Hermelin, O. Boisron, S. T. Purcell, L. S. Dang, and E. Monroy
E-MRS Fall Meeting (online). September 2021

[6] (Invited talk) **Decorrelation of internal quantum efficiency and lasing threshold in AlGaN-based separate confinement heterostructures**
S. Cuesta, F. Castioni, L. Denaix, N. Bernier, L. S. Dang, and E. Monroy
Compound Semiconductor Week 2022 (CSW-2022), Ann Arbor, US. June 2022

[7] (Oral) **Combining atomic-scale EDX with inelastic multislice simulations for quantitative chemical analysis of AlGaN/GaN 1 nm-thick quantum wells**
F. Castioni, S. Cuesta, N. Bernier, P. Quéméré, E. Robin, V. Delaye, E. Monroy, P. Bayle-Guillemaud
Microscopy and Microanalysis (M&M) Meeting, Portland, Oregon, US. August 2022

Appendix

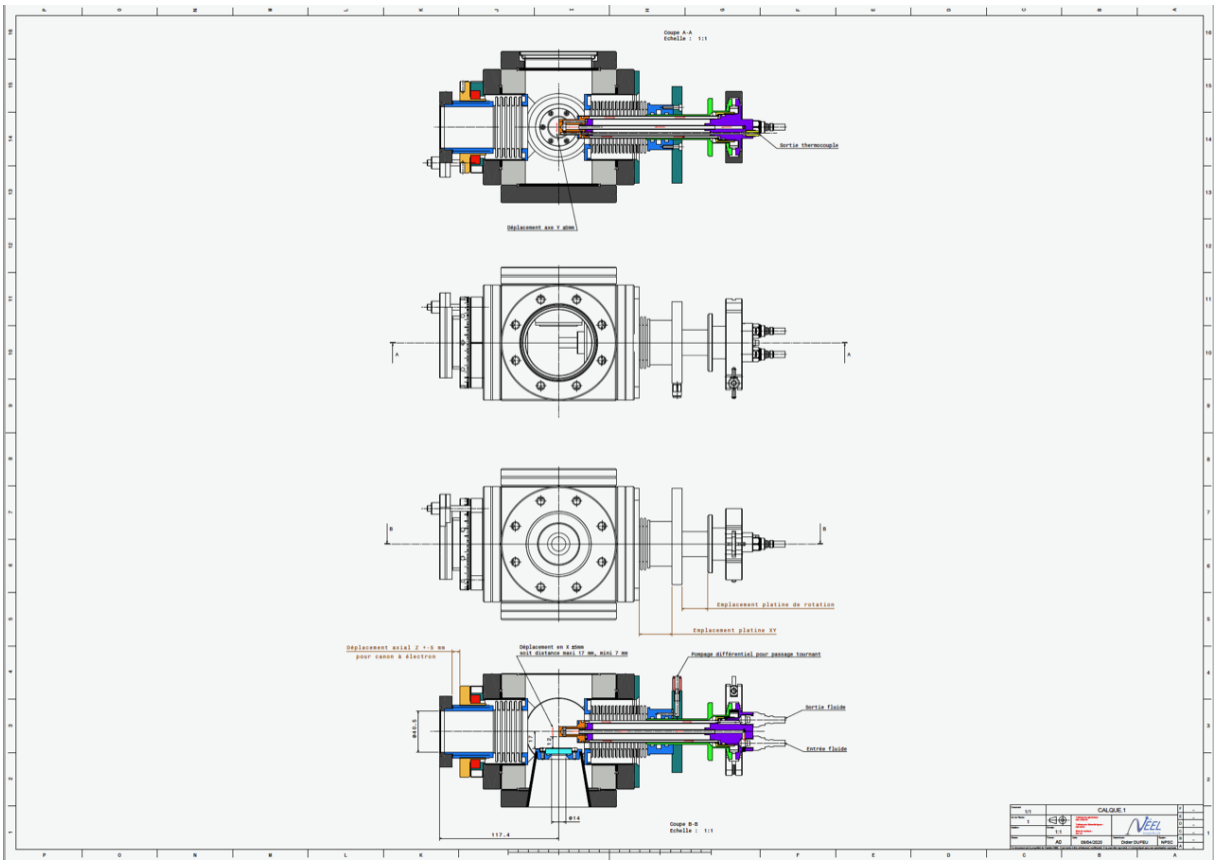
Coupe A-A
Échelle : 1:1
Sortie thermocouple
Déplacement axe Y 40mm
Emplacement platine de rotation
Emplacement platine XY
Déplacement axial Z +-5 mm
pour canon à électron
Déplacement en X 40mm
soit distance maxi 17 mm, mini 7 mm
Pompage différentiel pour passage tournant
Sortie fluide
Entrée fluide
Ø40.5
Ø14
117.4
Coupe B-B
Échelle : 1:1
CALQUE 1
NEEL

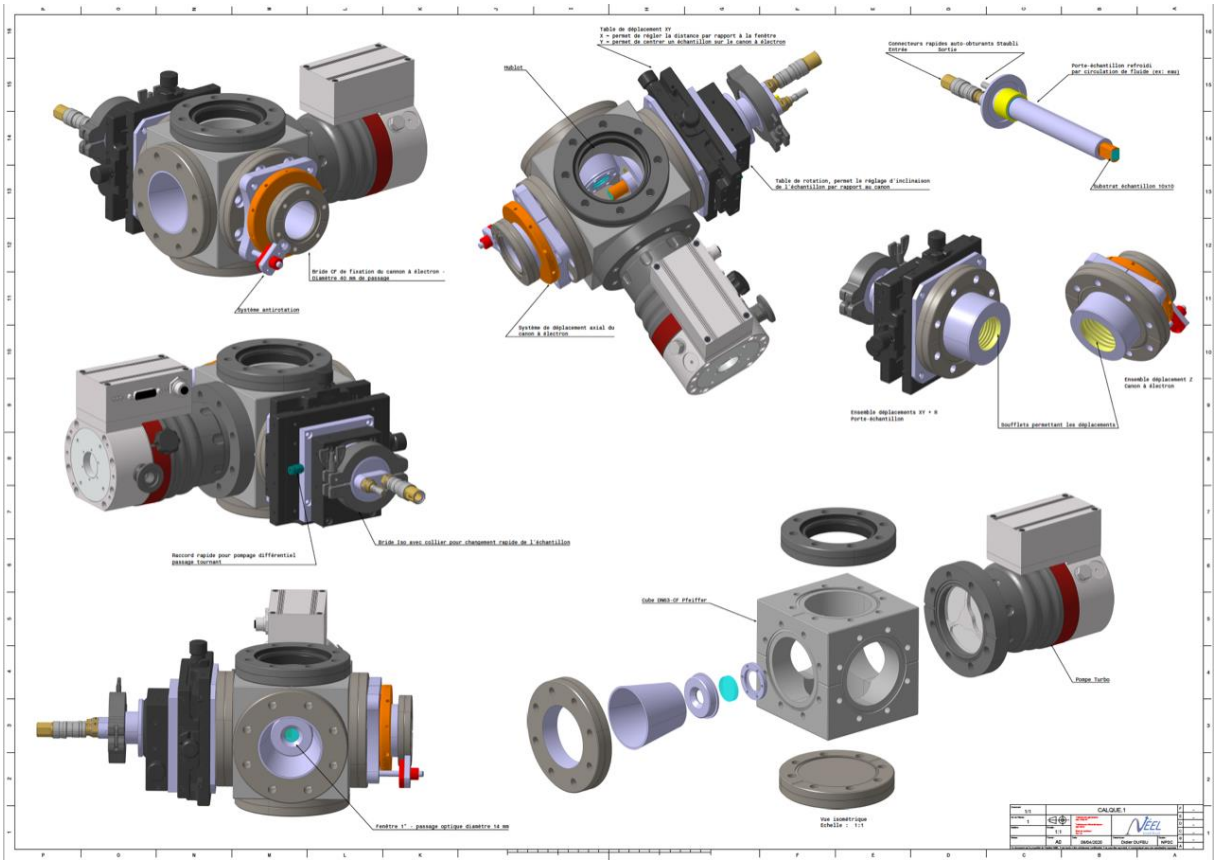
Table de déplacement XY
X = permet de régler la distance par rapport à la fenêtre
Y = permet de centrer un échantillon sur le canon à électron
Connecteurs rapides auto-obturants Staubli
Entrée
Sortie
Porte-échantillon refroidi
par circulation de fluide (eau)
Substrat échantillon tourné
Table de rotation, permet le réglage d'inclinaison
de l'échantillon par rapport au canon
Système de déplacement axial du
canon à électron
Ensemble déplacement Z
Canon à électron
Ensemble déplacements XY + R
Porte-échantillon
Soufflets permettant les déplacements
Bride CF de fixation du canon à électron -
diamètre 40 mm de passage
Système antirotation
Raccord rapide pour pompage différentiel
passage tournant
Bride iso avec collier pour changement rapide de l'échantillon
Cube DN63-CF Pfeiffer
Pompe Turbo
Fenêtre 1" - passage optique diamètre 14 mm
Vue isométrique
Échelle : 1:1
CALQUE 1
NEEL

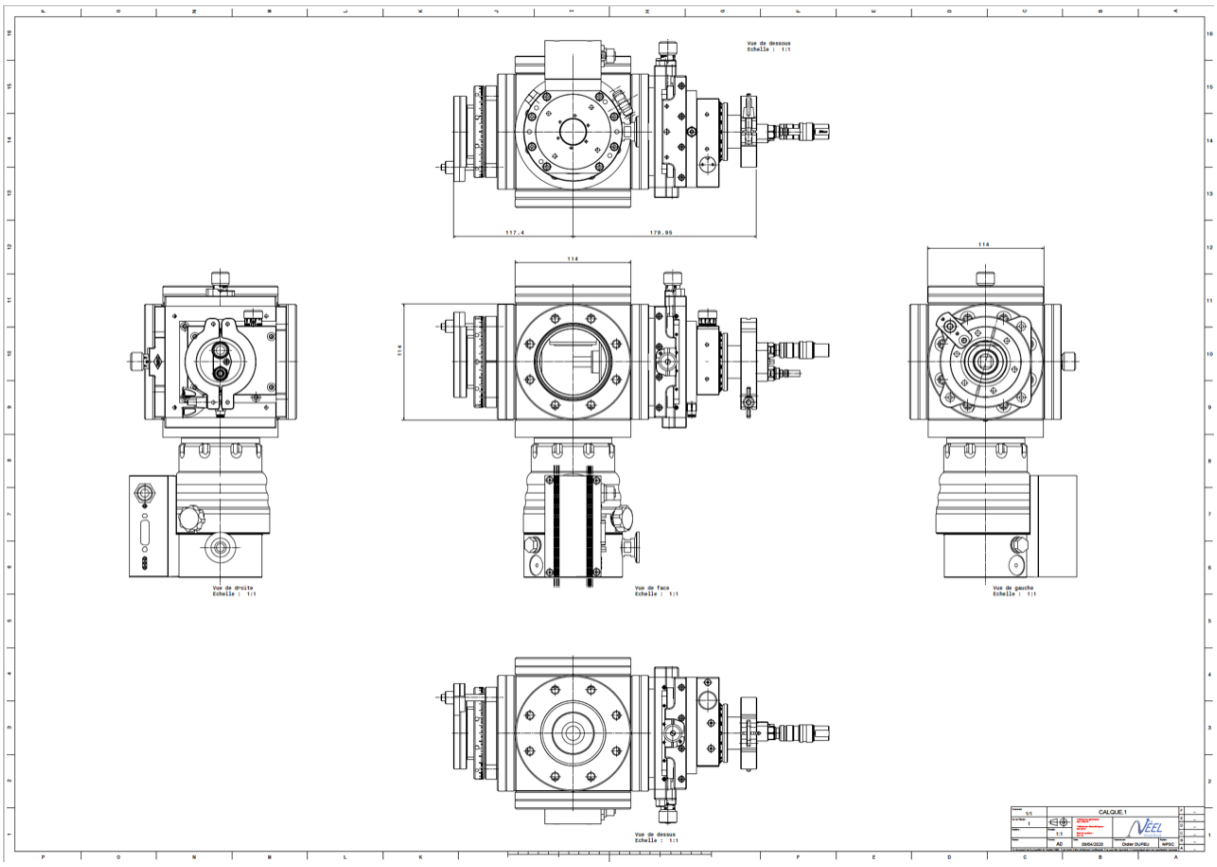
Vue de dessous
Echelle : 1:1
117.4
179.95
114
114
Vue de droite
Echelle : 1:1
Vue de face
Echelle : 1:1
Vue de gauche
Echelle : 1:1
Vue de dessus
Echelle : 1:1
CALQUE.1
A3
SM04CED
Didier DUPEU
NEEL